Pacific Northwest
NATIONAL LABORATORY

PNNL-37528

The Hanford Grout Modeling Framework and Database: Year 1 Summary and Development Guidance

March 2025

PNNL: RM Asmussen, J Anderson, C Curry, M Diaz-Acevedo, M. Enderlin, Y Fang, J Ferrer, S Hu, N Karri, SN Kerisit, JL Lapeyre, Y Li, S Rahmon, SA Saslow, X Song, D Wang

CRESP: K Brown, J Chen, C Gruber, D Kosson

H2C: N. Adams, RS Skeen, U Zaher

Sandia: M Rigali, J Rimsza, J Trageser

SRNL: CA Langton

U.S. DEPARTMENT of ENERGY

Prepared for the U.S. Department of Energy
under Contract DE-AC05-76RL01830

DISCLAIMER

PACIFIC NORTHWEST NATIONAL LABORATORY
operated by
BATTELLE
for the
UNITED STATES DEPARTMENT OF ENERGY
under Contract DE-AC05-76RL01830

Printed in the United States of America

Available to DOE and DOE contractors from
the Office of Scientific and Technical Information,
P.O. Box 62, Oak Ridge, TN 37831-0062
www.osti.gov
ph: (865) 576-8401
fox: (865) 576-5728
email: reports@osti.gov

Available to the public from the National Technical Information Service
5301 Shawnee Rd., Alexandria, VA 22312
ph: (800) 553-NTIS (6847)
or (703) 605-6000
email: info@ntis.gov
Online ordering: http://www.ntis.gov

PNNL-37528

The Hanford Grout Modeling Framework and Database: Year 1 Summary and Development Guidance

March 2025

PNNL: RM Asmussen, J Anderson, C Curry, M Diaz-Acevedo, M. Enderlin, Y Fang, J Ferrer, S Hu, N Karri, SN Kerisit, JL Lapeyre, Y Li, S Rahmon, SA Saslow, X Song, D Wang

CRESP: K Brown, J Chen, C Gruber, D Kosson

H2C: N. Adams, RS Skeen, U Zaher

Sandia: M Rigali, J Rimsza, J Trageser

SRNL: CA Langton

Prepared for
the U.S. Department of Energy
under Contract DE-AC05-76RL01830

Pacific Northwest National Laboratory
Richland, Washington 99354

Executive Summary

Currently, the modeling of grout waste forms (or other structural grouts) varies by site and application. The modeling currently used for grout at the Hanford Site [e.g., grouted secondary waste for the Integrated Disposal Facility (IDF) or tank closure] is simplistic due to prior limitations on data and computing power. Due to these limitations, modeling projections related to the properties and aging of the grout may be unnecessarily conservative and drive overprediction of the loss of material integrity or release of contaminants from grouts (e.g., radionuclides such as Tc-99 and I-129, regulated metals such as Cr, and chemical toxins such as nitrate). In the current modeling approach for the IDF and tank closure, physical and chemical changes to the grout are handled via step function changes, resulting in overly conservative sensitivity cases. In turn, these unrealistically conservative results could limit evaluations of opportunities to implement grout in the mission or require extensive research and development or risk mitigation that may not be needed. Continued conservative analyses of grout will limit the projected benefits in mission cost, duration, vitrification total operating efficiency, worker safety, and long-term environmental management from the expanded use of grout in the Hanford mission.

The *Hanford Grout Modeling Framework* being developed in this project will be composed of the equations and algorithms used to predict waste form behavior in performance assessments. These equations include numerical representations of the aging mechanisms and processes identified in the conceptual model to compare against measured datasets in controlled lab conditions, field experiments, and analogues. The *Hanford Grout Modeling Framework* will contain both the primary waste form release calculations and supporting modeling techniques to build the technical underpinning of grout performance. Components of the *Hanford Grout Modeling Framework* will be supported by a database of Hanford- and waste-relevant datasets that is being developed in this project and will be made available online for future efforts.

This report summarizes the work performed in Year 1 of the "Developing a Hanford Grout Modeling Framework" project, funded by the Laboratory Program Office within the U.S. Department of Energy's Office of Environmental Management. The initial effort was a team workshop to develop the conceptual models for the three main applications of grout at Hanford and a work plan. That workshop and associated information are summarized elsewhere.[1]

The Year 1 development of the *Hanford Grout Modeling Framework* laid the groundwork for forming the full system tool and provided substantial advancement of new tools for modeling grout. Based on conceptual models of the three main applications of grout at Hanford, i.e., liquid waste immobilization, solid waste stabilization/encapsulation, and tank closure as well as the main processes and mechanisms that control grout properties during aging were identified. Five original themes were defined to support the development of the *Hanford Grout Modeling Framework*, and the associated subtasks were initiated during Year 1. The significant developments in each of the subtasks presented in this report are as follows.

- ***Theme 1 Task 1 – Hanford Mineral Network:*** A main component of the *Hanford Grout Modeling Framework* was developed in which the mineral composition of grouts is now defined using a geochemical speciation model. A software link between exascale Subsurface Transport Over Multiple Phases (eSTOMP) and LeachXS - ORCHESTRA (LXO) was developed to facilitate this information transfer.

[1] Asmussen, RM. 2024. *Summary of Developing a Hanford Grout Modeling Framework Initial Workshop*. PNNL-36945. Pacific Northwest National Laboratory, Richland, WA.

- ***Theme 1 Task 2 – Geochemical Modeling of Reactive Grout Phases:*** Predictive dissolution models developed originally for glass waste forms have been successfully applied to predict the early-life dissolution of blast furnace slag, showing promise for a tool to predict long-term dissolution of key reactive phases in the grout microstructure.
- ***Theme 2 Task 1 – Integration of Variably Saturated Flow Modeling to eSTOMP:*** This task demonstrated that previous predictions of moisture pathways and transport times in the IDF using variably saturated flow modeling can be replicated in eSTOMP. These calculations will provide a technical basis for selecting appropriate reaction times in the *Hanford Grout Modeling Framework*.
- ***Theme 2 Task 2 – Integration of Variably Saturated Flow Modeling to Field Experimental Data:*** This task was a first step in validating the *Hanford Grout Modeling Framework* against field data by comparing moisture content model predictions to measurements in the Hanford field lysimeter test.
- ***Theme 3 Task 1 – Application of Geochemical Speciation Modeling to Other Hanford Grout Examples:*** This task further evaluated geochemical speciation models for predicting the behavior of grout components and contaminants. This tool was previously demonstrated with a single grout formulation and this demonstration has now shown success with other Hanford grouts. This tool will be a key component in predicting the chemical state of the grout.
- ***Theme 3 Task 2 – Integration of Key Aging Processes as Spatial Evolution in eSTOMP:*** This task demonstrated, for the first time, the use of a reactive transport representation of oxidation of grout in a Hanford disposal environment, laying the groundwork to capture spatial and dynamic aging processes in the *Hanford Grout Modeling Framework*.
- ***Theme 3 Task 3 – Contaminant Interactions with Microbial Processes:*** This task developed an approach in eSTOMP to represent microbial conversions in grout leachates in disposal conditions using nitrate as an example.
- ***Theme 4 Task 1 – Peridynamic Modeling:*** This task successfully built, for the first time, a peridynamic model of a Hanford-relevant grout (using tank concrete as an example) and compared failure predictions to experimental data. The peridynamics model is being developed as a tool to predict cracking in grout in service.
- ***Theme 4 Task 2 – Maturation of Mesoscale Models for Hanford Grout:*** This task built, for the first time, a Hanford-relevant mesoscale model of silver zeolite solid waste in a grout waste form to model silver migration in the grout matrix. This model will be expanded to contaminant migration and physical evolution.
- ***Theme 5 Task 1 – Grout Database:*** An online hosting tool was developed for a database of Hanford-relevant grout data, and populating with data has been ongoing.

Acknowledgments

The authors would like to thank Ming Zhu, Kaylee Fenker, and John Kelly from the DOE-EM Laboratory Policy Office for programmatic support. We also thank Melanie Chiaradia, Ally Garza, and Andy Ogrinc for internal PNNL support. We thank Hans Meeussen for fruitful discussions and access to ORCHESTRA software variants. We thank Cory Trivelpiece (Savannah River National Laboratory) for sharing experimental data.

Acronyms and Abbreviations

AI	artificial intelligence
API	Application Programming Interface
ARP	American Rock Products
ASPHC	asphalt concrete
ASTM	American Society for Testing and Materials
BFS	blast furnace slag
CDF	cumulative distribution function
CoPC	contaminant of potential concern
CRESP	Consortium for Risk Evaluation with Stakeholder Participation
CS	Cast Stone
DO	dissolved oxygen
DOE	U.S. Department of Energy
DOI	digital object identifier
DP	densely packed
E	elastic modulus
EFRC	Energy Frontier Research Center
EPA	U.S. Environmental Protection Agency
eSTOMP	exascale Subsurface Transport Over Multiple Phases
FA	fly ash
FFTW	Fastest Fourier Transform in the West
FIB	focused ion beam
GCL	geosynthetic clay liner
GDB	grout database
H2C	Hanford Tank Waste Operations and Closure
HD_BACKF	high-density backfill
HDF5	Pandas Hierarchical Data Format version 5
HL	hydrated lime
IDF	Integrated Disposal Facility
L/S	liquid-to-solid (mass) ratio
LAW	low-activity waste
LD_BACKF	low-density backfill
LLM	Large Language Model
LP	loosely packed
LSP	liquid-solid partitioning
LXO	LeachXS - ORCHESTRA
MC	moisture content

ML	machine learning
NNLEMS	Network of National Laboratories for Environmental Management and Stewardship
OCR	Optical Character Recognition
OPC	ordinary Portland cement
OSTI	Office of Science and Technology Information
PA	performance assessment
PD	peridynamics
PDF	probability density function
PHREEQC	PH-Redox-Equilibrium in C
PNNL	Pacific Northwest National Laboratory
ppt	precipitate
PW	pore water
QA	quality assurance
RCRA	Resource Conservation and Recovery Act
SEM	scanning electron microscope
SQL	Structured Query Language
SRNL	Savannah River National Laboratory
SRS	Savannah River Site
TCLP	Toxicity Characteristic Leaching Procedure
UCF	University of Central Florida
VSF	variably saturated flow
VU	Vanderbilt University
W1	grout waste form within eSTOMP oxidation model
WRA	water-reducing additive
WTP	Waste Treatment and Immobilization Plant
XML	Extensible Markup Language
XRD	X-ray diffraction

Contents

Executive Summary iii
Acknowledgments v
Acronyms and Abbreviations vi
1.0 Introduction 1.1
1.1 Project Summary 1.1
1.2 Conceptual Models Summary 1.4
1.2.1 Liquid Waste Immobilization Conceptual Model 1.4
1.2.2 Solid Waste Encapsulation Grout Conceptual Model 1.5
1.2.3 Tank Closure Grout Conceptual Model 1.7
1.3 The Hanford Grout Modeling Framework 1.9
1.4 Project Format 1.10
2.0 Theme 1: Grout Mineralogy 2.1
2.1 Theme 1 Task 1: Hanford Mineral Network 2.1
2.1.1 Team Members 2.1
2.1.2 Background 2.1
2.1.3 Technical Approach 2.2
2.1.4 Results to Date 2.3
2.1.5 Path Forward and Integration 2.4
2.2 Theme 1 Task 2: Geochemical Modeling of Reactive Grout Phases 2.5
2.2.1 Team Members 2.5
2.2.2 Background 2.5
2.2.3 Technical Approach 2.5
2.2.4 Results to Date 2.7
2.2.5 Path Forward and Integration 2.12
3.0 Theme 2: Dynamic Modeling of Moisture Driven Processes 3.1
3.1 Theme 2 Task 1: Integration of Variably Saturated Flow Modeling to eSTOMP (IDF simulations) 3.1
3.1.1 Team Members 3.1
3.1.2 Background 3.1
3.1.3 Technical Approach 3.1
3.1.4 Results to Date 3.7
3.1.5 Path Forward and Integration 3.12
3.2 Theme 2 Task 2: Integration of Variably Saturated Flow Modeling to Field Experimental Data 3.13
3.2.1 Team Members 3.13
3.2.2 Background 3.13
3.2.3 Technical Approach 3.14

3.2.4 Results to Date 3.18
3.2.5 Path Forward and Integration 3.21
4.0 Theme 3: Dynamic Modeling of Processes Impacting Contaminant and Radionuclide Behavior 4.1
4.1 Theme 3 Task 1: Application of Geochemical Speciation Modeling to Other Hanford Grout Examples 4.1
4.1.1 Team Members 4.1
4.1.2 Background 4.1
4.1.3 Technical Approach 4.2
4.1.4 Results to Date 4.7
4.1.5 Path Forward and Integration 4.11
4.2 Theme 3 Task 2: Integration of Key Aging Processes as Spatial Evolution in eSTOMP. 4.12
4.2.1 Team Members 4.12
4.2.2 Background 4.12
4.2.3 Technical Approach 4.13
4.2.4 Results to Date 4.14
4.2.5 Path Forward and Integration 4.16
4.3 Theme 3 Task 3: Contaminant Interactions with Microbial Processes 4.17
4.3.1 Background 4.17
4.3.2 Technical Approach 4.18
4.3.3 Results to Date 4.18
4.3.4 Path Forward and Integration 4.19
5.0 Theme 4: Modeling of Cracking in Grout 5.1
5.1 Theme 4 Task 1: Peridynamics Modeling 5.1
5.1.1 Team Members 5.1
5.1.2 Background 5.1
5.1.3 Technical Approach 5.1
5.1.4 Results to Date 5.5
5.1.5 Path Forward and Integration 5.16
5.2 Theme 4 Task 2: Maturation of Mesoscale Models for Hanford Grout 5.17
5.2.1 Team Members 5.17
5.2.2 Background 5.17
5.2.3 Technical Approach 5.18
5.2.4 Results to Date 5.26
5.2.5 Path Forward and Integration 5.32
6.0 Theme 5: Grout Database 6.1
6.1 Theme 5 Task 1: Grout Database 6.1
6.1.1 Team Members 6.1

6.1.2 Background 6.1
6.1.3 Grout Database Objectives and Approach 6.1
6.1.4 Grout Waste Form Data Needs 6.2
6.1.5 Data Sourcing from Published Literature 6.3
6.1.6 Data Organization 6.5
6.1.7 Database Access 6.6
6.1.8 Data Entry 6.6
6.1.9 Path Forward to Integration 6.10
6.2 Theme 5 Task 2: Completing Data Gaps 6.11
6.2.1 Team Members 6.11
6.2.2 Background 6.11
6.2.3 Target Experiments and Task Integration 6.11
7.0 Summary 7.1
8.0 References 8.1
Appendix A – Python Script to Extract Table Data from XML Files A.1
Appendix B – Python Script for Extracting Data Tables from PDF Files Using LLM API Key B.1
Appendix C – Oxidation Model Inputs C.1
Appendix D – Additional Batch Grout Model Output D.1

Figures

Figure 1.1. Illustrations showing the *Hanford Grout Modeling Framework* and the IDF disposal concept for liquid waste grouts (top) and *Hanford Grout Modeling Framework* simulations (bottom). 1.3

Figure 1.2. Schematic showing the two types of encapsulation used for solid waste grouts. 1.6

Figure 1.3. Schematic showing a closed tank farm at Hanford (Mehta et al. 2016). 1.8

Figure 2.1. Select examples of the comparison between the expected dissolved components controlled by mineral assemblages in grout as predicted by the BIOGEOCHEM (blue) and ORCHESTRA (red)..... 2.3

Figure 2.2. Screenshot of the wrapper written in eSTOMP to facilitate direct call-out to ORCHESTRA to collect geochemical information on mineral compositions and behavior. 2.4

Figure 2.3. Measured and calculated concentrations of Al, Ca, and Si and pH as a function of time for the static dissolution of five slags at 20 °C, l/s = 1,000, and 0.14 M NaOH. Measured concentrations are from Zhang et al. (2022). 2.10

Figure 2.4. Measured and calculated concentrations of Ca, Si, and S and pH as a function of time for the static dissolution of NW slag at room temperature, l/s = 100, and three initial pH values. Measured concentrations are from Asmussen et al. (2015). 2.11

Figure 2.5. Measured and calculated concentrations of Al, Ca, K, Na, S, and Si and pH as a function of time for the static dissolution of a BFS at 50 °C, l/s = 10, and three test conditions (deionized water, pH_0 = 12.5, and 2 M NaOH). Measured concentrations are from Trivelpiece and Hsieh (2021). 2.12

Figure 3.1. Model domain for near-field hydrology model base case, representing the 2-D cross-section of the IDF. This model includes the engineered barrier system, waste disposal layers, and liner system. (a) Full model domain. (b) Enlarged view of the upper layers (blue box in a), highlighting the engineered barrier and liner system. (c) Enlarged view of the side wall and facility bottom (purple box in a), showing details of the waste disposal layers and surrounding materials. 3.3

Figure 3.2. Model domain illustrating spatial variability in waste package placement within the IDF system. (a) Full model domain with a representative waste arrangement. (b) Variations in waste placement, demonstrating the perturbations considered in the analysis. 3.5

Figure 3.3. Model domain for the alternative conceptual model, where all cover layers above the asphalt concrete (ASPHC) layer are degraded and a 3.3-mm/yr infiltration condition is applied to the top boundary. Water flow is assumed to be discharged exclusively at the two bottom sump locations, indicated by the black arrows. 3.6

Figure 3.4. Spatial distribution of saturation after degradation of both the cover and liner for three representative model cases under a 3.5-mm/day infiltration rate through the IDF. The results are shown in a cross-section: (a) baseline case, (b) randomized waste package placement, and (c) alternative test model. 3.8

Figure 3.5. Particle tracking results for three representative model cases under a 3.5-mm/day infiltration rate through the IDF shown in a cross-scetion: (a) baseline case, (b) randomized waste package placement, and (c) alternative test model. Particle

pathlines are colored by travel time, illustrating differences in water flow behavior across the three models. 3.10

Figure 3.6. Probability distribution of particle travel times for three model cases: (a) baseline case, (b) randomized waste package placement, and (c) alternative conceptual model. The shaded blue region represents the histogram of particle travel times, while the red line is the fitted probability density function (PDF) and the green dashed line represents the cumulative distribution function (CDF). The dashed vertical lines highlight the 10th, 50th (median), and 90th percentiles, providing insight into the distribution spread and variability across different model configurations. 3.11

Figure 3.7. Lysimeter configurations at the IDF Test Platform and the detailed waste forms and sensor network in the lysimeter. Co-disposal lysimeters were not installed. 3.14

Figure 3.8. Geometry, boundary, and initial conditions of the 3-D lysimeter model. 3.16

Figure 3.9. Soil-water characteristic curve and unsaturated hydraulic conductivity function of simulated backfill compared with field range curves obtained from the remolded samples. 3.17

Figure 3.10. The (a) hysteresis of soil-water retention curve and (b) soil temperature variation with time and soil depth of the lysimeter ground surface. The air temperature within the lysimeter facility and the temperature measured at the Hanford Meteorological Station for the years 2023 – 2024 are also included. 3.18

Figure 3.11. (a) Cumulative drainage of the lysimeters with 50 cm/yr irrigation and (b) temporal changes in the water storage in the lysimeter from March to November 2024. ..... 3.19

Figure 3.12. Comparison of the models with two backfills (i.e., LP and HP) during irrigation and non-irrigation periods. 3.20

Figure 3.13. Comparison of modeling results incorporating soil temperature variation and hysteresis on three selected days representing irrigation and non-irrigation periods. 3.21

Figure 4.1. Example of the predictive capability of the geochemical speciation model for the release of Tc-99 from grout. 4.1

Figure 4.2. Photo of T6-1 and T6-3 monoliths tested by EPA Method 1315 (Um et al. 2016). 4.4

Figure 4.3. Conceptual LXO model used for tortuosity factor calibration. 4.7

Figure 4.4. Results of EPA Method 1313 tests and the modeled prediction of LSP (liquid-solid partitioning) curves. Red and purple dots are the experimental data of tests T3 and T6 at L/S 10. Blue dashed lines represent the predicted LSP curves for L/S 10. ..... 4.8

Figure 4.5. Predicted solids composition on unit cell basis as a function of pH for EPA Method 1313. ..... 4.9

Figure 4.6. Results of EPA Method 1315 tests for duplicates of T3 and T6 samples. 4.10

Figure 4.7. LXO simulation results for T3 (top) and T6 (bottom) to determine tortuosity factors of these non-binding species. Red and purple dots are experimental data, and the blue dashed line is simulated concentration. 4.11

Figure 4.8. Low- and high-density fill around the grout waste form in the B-25 waste box (left) and the waste burial box (right). 4.15

Figure 4.9. Total solute mass (meq e-) for the B-25 waste box (left) and the waste burial box (right). 4.15
Figure 4.10. Reduction capacity (%) for the B-25 waste box (left) and the waste burial box (right). 4.16
Figure 4.11. B-25 waste box reduction capacity consumption. 4.16
Figure 4.12. High-level design for eSTOMP and ORCHESTRA interaction for dynamically updating oxidation and carbonation. 4.17
Figure 4.13. Comparison of the model results of nitrate release within the IDF from a grouted inventory with and without nitrate reduction. 4.18
Figure 5.1. Representative compressive test curve of CS sample nine from batch one. The slope of the elastic region is used as the elastic modulus (*E*), and the reported compressive strength (σ) is the maximum of that elastic region. 5.3
Figure 5.2. Photos of (a) control (i.e., non-heat treated) concrete samples, (b,c) samples before and after firing at 94 °C, and (d,e) samples before and after firing at 149 °C. Examples of pinhole porosity (solid) and larger cavities (dashed) are circled in panel (a). 5.6
Figure 5.3. (a) Average 28-day compressive strength and (b) average elastic modulus of concrete as heat treatment temperature increases. The standard deviation is represented by the error bars. 5.7
Figure 5.4. Cartoons of typical fracture patterns based on ASTM C39/C39M-24. Here, "caps" are secondary materials like neoprene, sulfur mortar, or high-strength gypsum plaster placed at the ends of samples to facilitate C39/C39M planeness requirements. These secondary materials were not used for these tests. Fracture is not limited to these patterns. 5.8
Figure 5.5. Photographs of representative concrete specimens depicting the different fracture patterns from Figure 5.4. (a) Batch 1 Sample 10 fired at 94 °C pattern 2, (b) Batch 1 Sample 1 fired at 149 °C showing pattern 3, and (c) Batch 2 Sample 2 fired at 94 °C. Patterns 2 and 3 were as prevalent as the resulting pattern, whereas pattern 4 only occurred once during testing. Note: The photo in panel (a) is rotated to better show the fracture pattern. 5.9
Figure 5.6. Photos of (a) non-heat-treated mortar samples, (b,c) samples before and after firing at 94 °C, and (d,e) samples before and after firing at 149 °C. Examples of pinhole porosity (solid) and larger cavities (dashed) are circled in panel (a). 5.10
Figure 5.7. (a) Average 28-day compressive strength and (b) average elastic modulus of mortar samples as heat-treatment temperature increases. The standard deviation is represented by the error bars. 5.11
Figure 5.8. (a) Top surface of control mortar (Batch 1 Sample 2). (b) Fracture surface Batch 2 Sample 3, (c) Fracture surface Batch 2 Sample 1. Blue arrows show fine aggregate deflecting the propagation of a crack whereas green arrows show a crack traversing an aggregate 5.12
Figure 5.9. Representative photos of the 50 mm ∅ × 100 mm CS cylinder (a) before and (b) after type 3 fracture. The green-blue color is commonly observed in BFS-containing mixtures 5.12
Figure 5.10. Probability function vs. natural log of CS compressive strength (i.e., Weibull plot). The *m* and σ_0 parameters (slope and x-axis intercept) were calculated from the linearized dataset. Seventeen samples were tested. 5.13

Figure 5.11. Cumulative probability distribution of the tested CS specimens annotated with IDF and Nuclear Regulatory Commission thresholds. The inset (bottom right) is an enlarged image the intersection of the probability function and the regulatory thresholds. 5.14
Figure 5.12. Discretization for the uniaxial compression test geometry with 20% aggregate packing. 5.15
Figure 5.13. Fracture pattern cross-section for various aggregate packings. 5.15
Figure 5.14. Comparison of percent of broken bonds in the cylinder against the engineering strain for 5%, 10%, 15%, and 20% aggregate packings. 5.16
Figure 5.15. A mesoscale model of adsorption and/or desorption in porous structures during batch and column processes (Li et al. 2022a; Proust et al. 2024). (a) Scanning electron micrograph (SEM) of LTA-zeolite particles, (b) optical images of salt inclusion single crystals, (c) focused ion beam (FIB)-TEM image of geopolymer-based waste-form materials, (d-e) effect of microstructures on radionuclide absorption 5.18
Figure 5.16. (a-d) SEM backscattered electron images of microstructures at magnification levels in the CS matrix with AgM granules. (a) CS matrix with AgM particles; (b) the yellow arrow points to the AgM-CS interface; (c) enlarged image of the AgM particle with mesoscale pores and AgM polycrystalline grains; (d) enlarged image of porous CS with macroscale pores, FA, and BFS particles; the red arrow points to a spherical FA particle while the dashed yellow arrow to a BFS particle; and (e) elemental energy dispersive X-ray spectroscopy dot map near the interface between an AgM granule and CS shown in (c). 5.19
Figure 5.17. Schematic of the simulation cell including AgM, FA, BFS particles, porous CS matrix, and meso-pores inside AgM. The AgM particle is viewed as a cluster of small AgM grains 5.25
Figure 5.18. Temporal evolution of Ag content inside the Ag precipitates and CS matrix. (a) $wAg, pptt,$ and (b) $wAg, Matrixt.$ 5.27
Figure 5.19. Distribution of Ag concentration inside the Ag ppt and CS matrix at normalized time 5820000. (a-b) for $\Delta\mu pq, Ag *= -0.65$ and $\Delta\mu p1q1, Ag *= 0.0$, and (c-d) for $\Delta\mu pq, Ag *= 0.0$ and $\Delta\mu p1q1, Ag *= -0.65$, respectively. 5.28
Figure 5.20. Effect of reaction rates on the temporal evolution of Ag content inside Ag precipitate (ppt) (a) and CS matrix (b). 5.29
Figure 5.21. Temporal evolution of Ag and $Ag +$ concentrations (a) for $rp, Ag +*= 0.4$ and $rp, Ag *= 0.2$ and (b) for $rp, Ag +*= 0.05$ and $rp, Ag *= 0.2.$ 5.30
Figure 5.22. Effect of Ag and Ag+ diffusivity on the temporal evolution of Ag content inside Ag precipitate (ppt) (a) and CS matrix (b). 5.31
Figure 5.23. Effect of AgM particle size on the temporal evolution of Ag content inside Ag precipitate (ppt) (a) and CS matrix (b). 5.31
Figure 6.1. The GDB entry form used when entering single sample or batch data into the GDB. This main window is where document information and sample formulation and curing conditions are logged, except for the liquid composition, which has its own pop-up window that is accessed by the “Add Liquid Waste Data” button at the bottom. Annotations are overlayed describing the type of information being logged for key entry fields. 6.7

Figure 6.2. Examples of the pop-up windows that appear for entering relevant sample or batch test data. (A) The composition of the aqueous (liquid) phase used to formulate the respective batch identified in the main GDB entry form window. (B) The compressive strength of the respective sample or test batch, which can be entered as an average value with the standard deviation identified or as replicate samples with their individual compressive strength values provided. (C) Saturated hydraulic conductivity value(s), entered as an average with a standard deviation or single replicate values. (D) Slurry properties of the formulated batch or sample, including the number of days required to reabsorb residual free liquids, initial and final set times, and flowability measurements using the adapted procedure from Harbour et al. (2005). 6.8

Figure 6.3. Pop-up window for logging EPA 1315 effective diffusivity values. 6.9

Figure 6.4. Pop-up windows for entering (A) Toxicity Characteristic Leaching Procedure (TCLP) concentrations for RCRA metals and (B) sorption partition coefficient test data. Note that the desorption coefficients data entry window (not shown) has the same data entry format used for sorption coefficients. 6.9

Figure 6.5. One control incorporated into the GDB entry form is that the dry blend components' weight percent values must sum to 100 weight percent. (top) Red text appears indicating the current weight percent total and (bottom) turns to green text when the criterion is met. 6.10

Tables

Table 2.1. Example grout properties provided for liquid secondary waste grout in the Liquid Secondary Waste Data Package that supported the 2018 IDF PA. Taken from Table C.1 of Cantrell et al. (2016). 2.2

Table 2.2. Compositions (in mole fractions) of the slags considered in this work. 2.9

Table 2.3. Test conditions and model parameters derived in this work. Parameters $k0$diss and $k0$alt are in $mol_{slag}\ m^{-2}\ s^{-1}$, *SSA* is $m^2\ g^{-1}$, E_a is in kJ mol^{-1}, and the remaining parameters are unitless. 2.9

Table 3.1. Sensitivity analysis cases for infiltration rates, degradation scenarios, and randomized placement of waste packages. 3.4

Table 3.2. Degradation scenarios for asphalt and GCL in sensitivity analysis. 3.4

Table 3.3. Summary of particle travel time percentiles for different model cases. 3.12

Table 3.4. Current data inventory for lysimeter modeling. 3.15

Table 3.5. Physical and hydrological properties of backfill and drainage materials. 3.17

Table 4.1. Liquid secondary waste grout mix designs (Um et al. 2016). 4.2

Table 4.2. Moisture content, dry solids fraction, and XRD analysis for mineral content (Um et al. 2016). 4.3

Table 4.3. List of free liquid diffusivity coefficients (Di^0) that were used in the transport models (Gruber et al. 2022). The uncertainty for the diffusion coefficient is 5%. 4.6

Table 4.4. Comparison of the properties of the two case studies for oxidation testing in this report. 4.13

Table 5.1. Original and fabricated mix design for concrete and mortar samples. 5.2

Table 5.2. Fabricated mix design for Cast Stone samples. 5.2

Table 5.3. Summary of the concrete physical properties: 28-day avg. compressive strength, 28-day avg. elastic modulus, and the fracture patterns measured and observed during testing. 5.7

Table 5.4. Summary of the concrete physical properties: 28-day avg. compressive strength, 28-day avg. elastic modulus, and the fracture patterns measured and observed during testing. Note: Two control specimens broke prematurely before testing. 5.11

Table 5.5. Non-zero model parameters used in the mesoscale simulations. 5.24

Table 5.6. Initial concentrations of species in the AgM-CS mesoscale model 5.25

Table 6.1. Recommended grout waste form data for entry into the GDB. 6.2

Table 6.2. Evaluated PDF data table extraction methods and packages. 6.5

1.0 Introduction

This report summarizes the work performed in Year 1 of the "Developing a Hanford Grout Modeling Framework" project, funded by the Laboratory Program Office within U.S. Department of Energy (DOE) Office of Environmental Management. The initial effort was a team workshop to develop the conceptual models for the three main applications of grout at Hanford and a work plan. That workshop and the associated information are described elsewhere (Asmussen 2024). Based on the work plan in Asmussen (2024), efforts have been ongoing across five themes in the project. This report covers the project background and technical developments for data in each theme and how these fit the target development of the *Hanford Grout Modeling Framework*.

1.1 Project Summary

Cementitious and other ambient-temperature-formed solidification technologies (e.g., geopolymers) play a key role in the nuclear waste management strategies pursued across the globe. These materials are commonly referred to as "grout" within the DOE complex – a term originating from efforts in hydrofracture injection of salt waste mixed with cement and other additives at the Oak Ridge Reservation in the 1960s, in a process similar to borehole "grouting" (Haase et al. 1987). Within the DOE complex, there is extensive experience using grout for solidification of alkaline salt wastes, other liquid wastes, spent solid wastes, tank closure, and facility decommissioning (Lorier and Langton 2019; Bates 2022). At the Hanford Site, grout was the treatment technology originally planned for tank waste using vault designs similar to the Saltstone Disposal Units at the Savannah River Site (SRS) (van Beek and Wodrich 1990).

With the revision to the Tri-Party Agreement in 1993, the focus of grout usage at Hanford shifted to supporting the vitrification mission by grouting the liquid and solid secondary wastes generated by the process. The need for supplemental treatment capacity to complete the low-activity waste (LAW) mission and recent alternative treatment evaluations have renewed efforts to evaluate and consider grout for LAW. Additionally, upon completion of tank retrieval, it is presumed that grouting will be used for closure of the tanks at Hanford, although this is still pre-decisional. Evaluating the benefits and impacts of the various applications of grout at Hanford requires a uniform, and technically defensible, modeling approach.

Currently, the modeling of grout waste forms (or other structural grouts) varies by site and application. The modeling used for grout at the Hanford Site [e.g., grouted secondary waste for the Integrated Disposal Facility (IDF) or tank closure] is simplistic due to prior limitations on data and computing power. Due to these limitations, modeling projections related to the properties and aging of the grout may be unnecessarily conservative and drive overprediction of the loss of material integrity or release of contaminants from grouts (e.g., radionuclides such as Tc-99 and I-129, regulated metals such as Cr, and chemical toxins such as nitrate).

The current modeling approach for the IDF and tank closure handles physical and chemical changes to the grout via step function changes, resulting in overly conservative sensitivity cases. These unrealistically conservative results could limit evaluations of opportunities to implement grout in the mission or require extensive research and development or risk mitigation that may not be needed. Continued conservative analyses of grout will limit the projected benefits in mission cost, duration, vitrification total operating efficiency, worker safety, and long-term environmental management from the expanded use of grout in the Hanford mission. Several multi-lab reviews have identified updating and harmonizing the modeling approach for grout materials at the Hanford Site as a significant mission need, where time-dependent

processes (e.g., carbonation) that control bulk mechanisms (e.g., cracking) in grout can be accounted for (Asmussen et al. 2021; Bates 2022). Moreover, the Network of National Laboratories for Environmental Management and Stewardship (NNLEMS) Roadmap Concepts DL-3, TC-4, and TC-5 identified the need for improved grout modeling in performance assessments (PAs) (NNLEMS 2022). This project is using a multi-organization expert team to produce conceptual models for grout aging at Hanford that can be applied in PAs using a *Hanford Grout Modeling Framework*. Realizing the *Hanford Grout Modeling Framework* will require developing dynamic, reactive front conceptual models, implemented in computational simulations, that better represent the aging processes of the grout in service (see Figure 1.1). The needed conceptual models have been defined for the three main applications of grout at Hanford and are covered in Section 1.2.

The *Hanford Grout Modeling Framework* will be composed of the equations and algorithms used to predict waste form behavior in PAs. These equations include numerical representations of the aging mechanisms and processes (Section 1.2) identified in the conceptual model to compare against measured datasets in controlled lab conditions, field experiments, and analogues. The *Hanford Grout Modeling Framework* will contain both the primary waste form release calculations and the supporting modeling techniques to build the technical underpinning of grout performance. Both components of the *Hanford Grout Modeling Framework* will be supported by a database of Hanford- and waste-relevant datasets that will be developed and made available online for future efforts.

The *Hanford Grout Modeling Framework* will facilitate more accurate performance projections of various grout formulations for both ongoing and future waste processing operations, enabling decision-makers to pursue cost- and time-effective waste disposal strategies at the site, such as whether a grout waste form should be disposed of off site or on site or if specific wastes should be directed to vitrification or would be better candidates for grouting. The project will also help guide development of future formulations by providing a better understanding of the long-term interactions of the multiple aging mechanisms and identifying what data needs to be collected on emerging grout materials while they are being developed to enable proper head-to-head assessments.

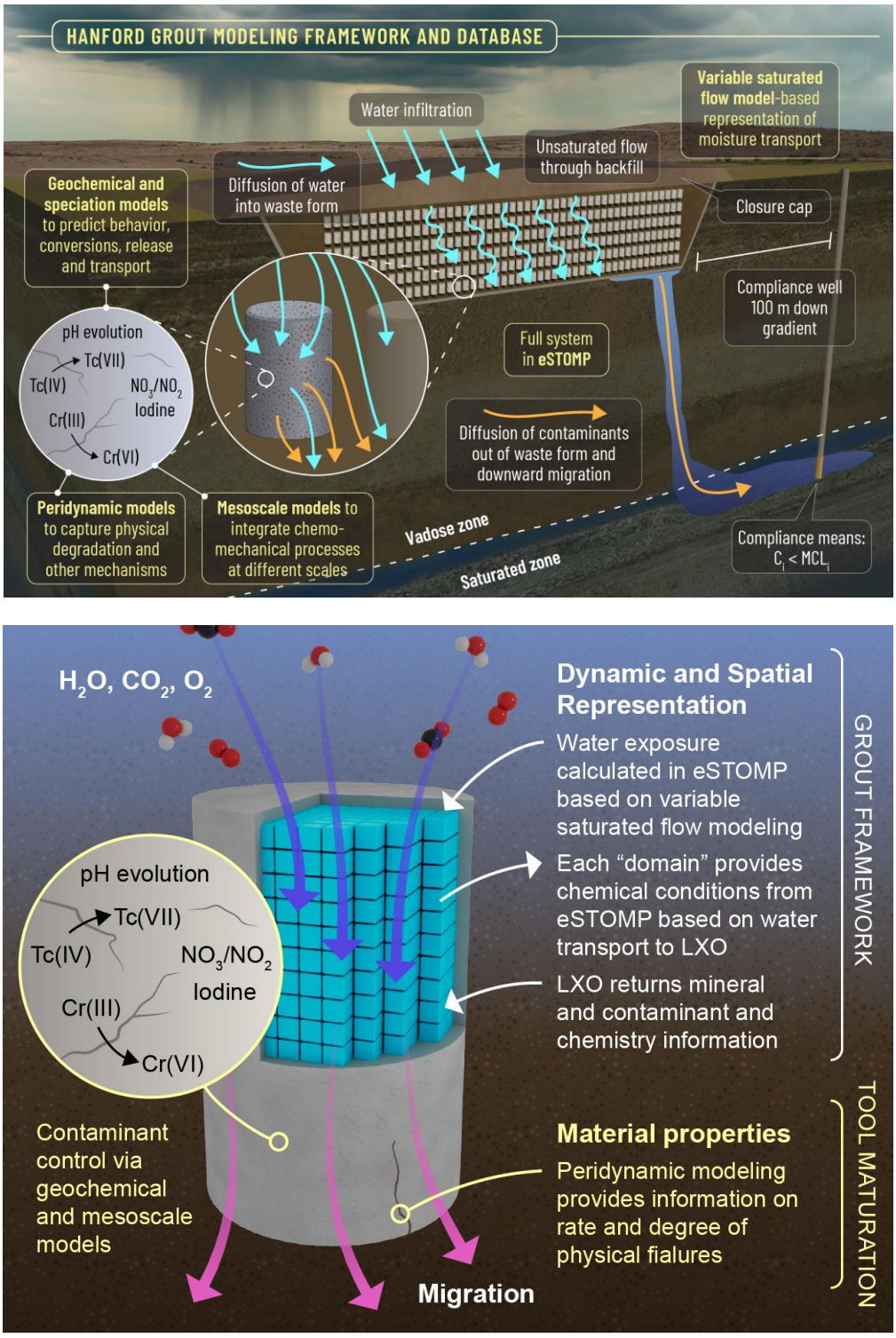

Figure 1.1. Illustrations showing the *Hanford Grout Modeling Framework* and the IDF disposal concept for liquid waste grouts (top) and *Hanford Grout Modeling Framework* simulations (bottom).

1.2 Conceptual Models Summary

The American Concrete Institute defines durability as "the ability of a material to resist weathering action, chemical attack, abrasion and other conditions of service."[1] Unlike conventional concrete structures, waste form durability includes the material's ability to retain contaminants of potential concern (CoPCs) (or in the case of tank closure grout, impede exposure of residuals to infiltrating water). A durable waste form retains CoPCs to limit releases at a rate that protects the surrounding environment. Aging of grout waste forms may degrade their properties, leading to accelerated release of CoPCs, but it could also improve other properties that influence the retention of CoPCs. Predicting grout behavior requires a comprehensive understanding of the different aging mechanisms that either impede or facilitate release of CoPCs. Such understanding would lead to more carefully designed waste forms and disposal strategies that reduce the potential for identified significant degradation processes. These time-dependent aging mechanisms and processes need to be captured in any long-term projection of grout performance. As such, the *Hanford Grout Modeling Framework* is being built on conceptual models that capture the key mechanisms and processes.

This section presents an overview of grout aging mechanisms and processes expected to occur in the IDF (for both liquid waste immobilization grout, Section 1.2.1, and solid waste encapsulation, Section 1.2.2) or in a tank closure scenario (Section 1.2.3) that comprises the proposed conceptual models to be used in this project. Each brief summary lists the project theme under which the process/mechanism is being evaluated. The evaluation criteria and the development of these conceptual models is described in a prior report (Asmussen 2024). Full technical descriptions of the individual mechanisms and processes can be found in other reviews (Pabalan et al. 2009; Asmussen et al. 2021). For this conceptual model development effort, the definitions of processes and mechanisms are as follows and for further descriptions see Asmussen (2024).

- ***Process*:** A material evolution or environmental interaction with the waste form matrix that triggers a mechanism. These interactions can be physical (e.g., freeze thaw) or chemical (e.g., oxidation) in nature.
- ***Mechanism*:** Leads to a behavior or a bulk change in the waste form that is different from the unaltered state and projected aging. Examples include cracking or chemical changes to the radionuclides/CoPC.

1.2.1 Liquid Waste Immobilization Conceptual Model

This application of grout is for the direct stabilization (or immobilization) of liquid waste streams. Here, the water in the liquid waste is used to activate the dry reagents and generate a final solidified waste form. In the scenario considered in the *Hanford Grout Modeling Framework*, the resulting waste form is emplaced in the IDF for disposal. The key processes to be included in a conceptual model for liquid waste grout are described below (in no order of priority) along with the project themes under which the processes will be evaluated.

- ***Moisture-driven cracking:*** A process by which exposure of liquid waste grout to moisture transporting through the disposal facility in the arid Hanford environment could lead to cracking in the waste form. (Theme 2 and Theme 4)
- ***Dimension change:*** A process by which shrinkage of the waste form leads to cracking. (Theme 4)

[1] American Concrete Institute. 2021. Concrete Terminology. CTI-21. Available at: https://www.concrete.org/store/productdetail.aspx?ItemID=CT21

- ***Early exposure conditions:*** Prior to burial in the IDF, a liquid waste grout will experience various environmental factors, including exposure to O_2 and CO_2 (depending on the configuration and packaging for processing, curing and disposal), which can alter the initial condition of the material prior to burial. (Theme 3)
- ***Carbonation:*** A mechanism by which the pH of the grout waste form decreases with time, driving mineralogical and physical changes in the waste form. (Theme 3)
- ***Ca leaching:*** A mechanism by which the network comprising the waste form matrix begins to change due to the flux of Ca and other components out of the waste form. This mechanism is linked to carbonation. (Theme 1 and Theme 2)
- ***Mineral growth:*** Natural aging and contact with infiltrating water can drive mineralogical changes in the waste form that can be deleterious or beneficial to contaminant retention within a liquid waste grout. This process includes delayed ettringite formation. (Theme 1)
- ***Moisture transport:*** The distribution of infiltrating water into the disposal facility and its behavior upon contacting a liquid will factor heavily in the aging processes and leaching of liquid waste grouts and needs to be accurately represented in the disposal facility and in the near field around the grout. (Theme 2)
- ***Oxidation:*** Liquid waste grouts rely on maintaining reducing conditions in the waste form to limit the release of many contaminants and radionuclides. Therefore, the rate of oxidation of the material is key to predicting long-term behavior. (Theme 3)
- ***Radionuclide/contaminant leaching:*** The release of contaminants and radionuclides from liquid waste grouts can be dictated by the physical properties and localized chemistry within the waste form, and these factors need to be captured in a conceptual model. (Theme 3)

Secondary processes that will be considered in the project are as follows.

- ***Early exposure conditions (e.g., temperature):*** Prior to burial in the IDF, a liquid waste grout may experience environmental changes and freeze-thaw cycles in the open atmosphere, which could cause cracks in the material. (Theme 4)
- ***Phase segregation:*** Some liquid waste grouts (e.g., those prepared as geopolymers) may experience phase segregation or crystallization over time. (Theme 1)
- ***Sulfate attack:*** A mechanism by which infiltrating sulfate can lead to expansion, cracking, and deterioration of a liquid waste grout due to mineral conversions. This mechanism is relevant to high-sulfate waste streams to be immobilized as grout. (Theme 1, Theme 3, and Theme 4)
- ***Microbial:*** The Hanford backfill and subsurface are home to microbes that can impact contaminant transport. While material degradation of liquid waste grouts via microbial activity is unlikely, microbial activity can play a crucial role in determining contaminant transport in the near and far fields. It is unknown if the presence of organics or admixtures can drive enhanced activity. (Theme 3)
- ***Environmental conditions:*** While direct effects of evolving climate conditions cannot be predicted, sensitivity cases in modeling efforts should always be considered to identify impacts of possible environmental changes (e.g., higher infiltration rates). (Theme 2)

1.2.2 Solid Waste Encapsulation Grout Conceptual Model

This application of grout is for the encapsulation (either microencapsulation/stabilization or macroencapsulation) of waste particulate or bulk solids, Figure . Here, a slurry is prepared and then

introduced to the solid waste. The grout isolates the contaminated solid waste from infiltrating water and in some cases enhances binding of any contaminants released from the solids. The scenario considered in the *Hanford Grout Modeling Framework* emplaces the waste in the IDF for disposal. The grout formulations of interest in this work are ultra-high performance grout (Nichols et al. 2021), paste, and mortar. The processes identified by the project team to be most relevant to the performance of solid waste encapsulation are described below and were supported by a recent review of this class of grout (Asmussen et al. 2021). The testing theme under which the process will be evaluated is listed as well.

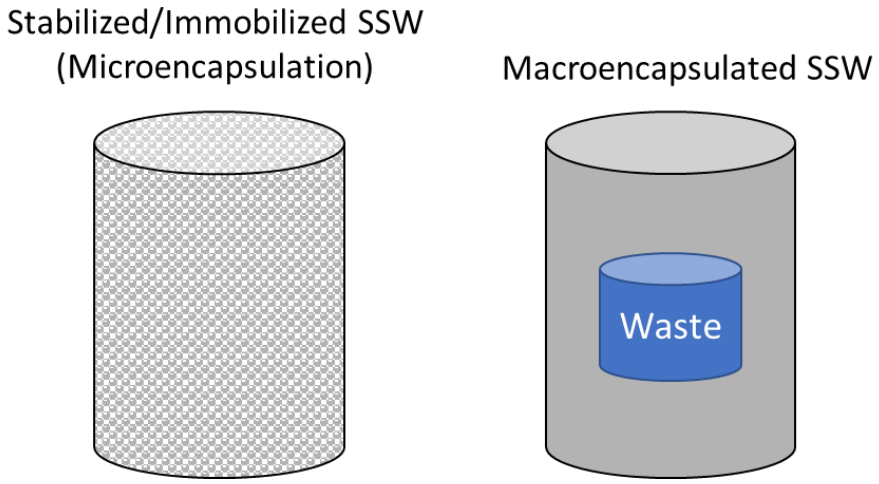

Figure 1.2. Schematic showing the two types of encapsulation used for solid waste grouts.

- ***Moisture-driven cracking:*** A mechanism by which the effects of moisture transport on disposal in the arid Hanford environment could lead to cracking in a solid waste encapsulation grout, including the hydration of unreacted cement. (Theme 2)
- ***Dimension change*****:** A mechanism by which shrinkage of the waste form leads to cracking or the volume of the encapsulated solid changes over time. (Theme 4)
- ***Early exposure conditions:*** Prior to burial in the IDF, a solid waste grout will experience various environmental factors, including exposure to O_2 and CO_2 (depending on the configuration and packaging for processing, curing, and disposal), which can alter the initial condition of the material prior to burial. (Theme 3)
- ***Carbonation:*** A mechanism by which the pH of the liquid waste grout waste form can decrease with time, driving mineralogical and physical property changes in the waste form. (Theme 3)
- ***Ca leaching:*** A mechanism by which the network comprising the waste form matrix begins to change due to leaching of the constituent phases. This mechanism is linked to carbonation. (Theme 3)
- ***Mineral growth:*** Natural aging and contact with infiltrating water can drive mineralogical changes within the waste form that can be deleterious or beneficial to contaminant retention within a solid waste encapsulation grout, including delayed ettringite formation. (Theme 1)
- ***Moisture transport:*** The distribution of infiltrating water into the disposal facility and its behavior upon contacting a liquid will factor heavily in the aging processes and leaching of solid encapsulation grouts. (Theme 2)

Secondary processes that will be considered in the project are as follows.

- ***Early exposure conditions (e.g. temperature):*** Prior to burial in the IDF, a solid waste encapsulation grout may experience environmental changes and freeze-thaw cycles in the open atmosphere, which could cause cracks in the material. (Theme 4)
- ***Oxidation:*** Some solid waste encapsulation grouts are designed with reducing conditions in the waste form; however, reduction is not a primary retention mechanism in these systems. (Theme 3)
- ***Radionuclide/contaminant leaching:*** The release of contaminants and radionuclides from solid waste encapsulation grouts is more strongly influenced by the physical properties of the grout than by leaching from the solid waste material itself. Cracking would be a primary driver of radionuclide/contaminant transport. (Theme 3)
- ***Microbial:*** The Hanford backfill and subsurface are home to microbes that can impact contaminant transport. While material degradation of solid waste encapsulation grouts via microbial activity is unlikely, microbial activity can play a crucial role in determining contaminant transport in the near and far fields. It is unknown if the presence of organics or admixtures can drive enhanced activity. (Theme 3)
- ***Environmental conditions:*** While direct effects of evolving climate conditions cannot be predicted, sensitivity cases in modeling efforts should always be considered to identify impacts of possible environmental changes (e.g., higher infiltration rates). (Theme 2)

1.2.3 Tank Closure Grout Conceptual Model

This pre-decisional application of grout involves the bulk filling of retrieved tanks for closure. Here, the grout is poured into the tank following retrieval and rests on top of any solid residuals in the tank. The grout provides structural fill to the tank void space and limits ingress of water to the residuals, which in turn can limit release of contaminants and radionuclides to the subsurface. Figure 1.3 presents a schematic of a closed tank farm. The processes and mechanisms identified by the project team to be most relevant to the performance of tank closure grout are described below the figure and were influenced by a prior review on closure grout (Pabalan et al. 2009). The testing theme under which the process will be evaluated is listed as well.

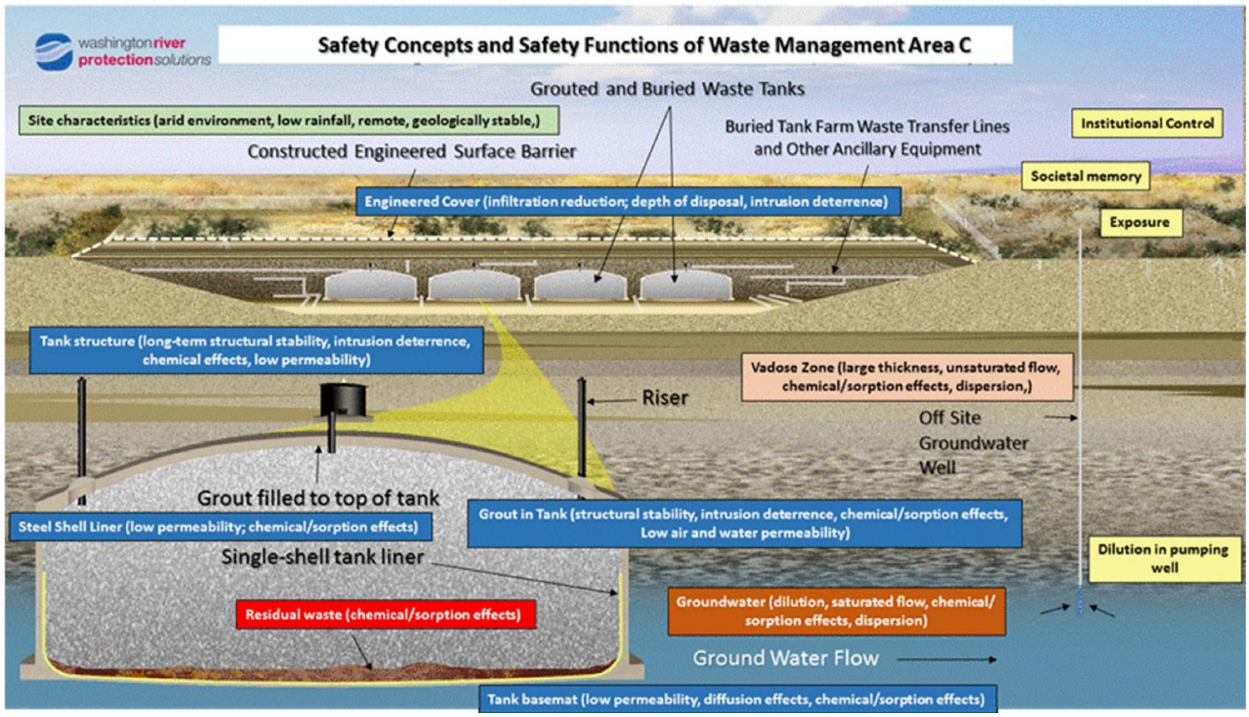

Figure 1.3. Schematic showing a closed tank farm at Hanford (Mehta et al. 2016).

- ***Thermally driven cracking:*** A process by which the thermal history of the existing concrete structures or thermal history of the grout upon emplacement leads to changes in the initial condition of the structures, including extreme heat events. (Theme 4)
- ***Steel corrosion:*** A process that involves the imbedded steel rebar in the tank superstructure corroding, leading to changes in the immediate vicinity of the rebar. This process can also apply to the steel infrastructure (e.g., risers, pipes) within the closed tank. (Theme 4)
- ***Carbonation:*** A mechanism by which the pH of the emplaced grout or concrete structure can decrease with time, driving mineralogical and physical property changes in the matrix. (Theme 2 and Theme 3)
- ***Ca leaching:*** A mechanism by which the network comprising the grout matrix begins to change due to leaching of the constituent phases. This mechanism is linked to carbonation. (Theme 3)
- ***Moisture transport:*** The distribution of infiltrating water into the closed tank and its behavior upon contacting the closure will factor heavily in the aging processes and migration toward residuals. This process includes any hydraulic head that may be present during emplacement. (Theme 2)
- ***Radionuclide/contaminant leaching:*** The release of contaminants and radionuclides from the residuals (or, if any inventory is present in the concrete superstructure, from waste leaks) is a key driver in closure PAs. The release is dictated by both the initial condition of the radionuclides/contaminants and the interfacial behavior between the grout and residuals. (Theme 3)

Secondary mechanisms that will be considered in the project are as follows.

- ***Oxidation:*** Oxidation is relevant in tank closure only if an amendment (e.g., Fe) is placed in the first layer of grout to interact with residuals and impede release. (Theme 3)

- ***Microbial:*** The Hanford backfill and subsurface are home to microbes that can impact contaminant transport. While material degradation of solid waste encapsulation grouts via microbial activity is unlikely, microbial activity can play a crucial role in determining contaminant transport in the near and far fields. It is unknown if the presence of organics or admixtures can drive enhanced activity. (Theme 3)
- ***Environmental conditions:*** While direct effects of evolving climate conditions cannot be predicted, sensitivity cases in modeling efforts should always be considered to identify impacts of possible environmental changes (e.g., higher infiltration rates). (Theme 2)

1.3 The Hanford Grout Modeling Framework

Based on the conceptual models, the *Hanford Grout Modeling Framework* will be constructed to (1) define how to best represent the numerical equations for target processes/mechanisms in reactive transport simulations of grout at Hanford and (2) mature emerging techniques that could further improve the framework. The existing exascale Subsurface Transport Over Multiple Phases (eSTOMP) software is envisioned to carry out the *Hanford Grout Modeling Framework* simulations, with supporting information from other software where needed.

As discussed previously, it is imperative to capture time and spatially dependent processes that impact both the properties of the grout and contaminant release. The proposed construct of the *Hanford Grout Modeling Framework* is designed to capture these dynamic processes (and their causes) by accurate projections of near-field disposal conditions. The *Hanford Grout Modeling Framework* is proposed to have the following components and functions (presented in the order in which the simulations will be performed). The theme (Section 1.4) under which work is being performed is given in parentheses.

1. **Initial Condition**
    a. ***Mineral network:*** The mineral network of the grout will be defined initially using mineral networks calculated with geochemical speciation modeling (ORCHESTRA) that were confirmed using analysis of leaching data (LeachXS, LXO). (Meeussen, 2003) The databases of cement mineral phases (e.g., CEMDATA-18) will be used in the determinations. Evolution of the cured grout between post-burial and first exposure to infiltrating water will be determined using CemGEMS[1]. (Theme 1)
    b. ***Reduction capacity:*** Defined using current calculation methods based on experimental data and pre-burial conditions. (Theme 3)
    c. ***Porosity/tortuosity:*** Defined using LXO-derived tortuosity numbers. (Theme 3)
2. ***Water transport:*** The rate at which water, and associated components like O_2 and CO_2, arrives at and contacts the grout will be determined in eSTOMP using calculations that were originally defined in variably saturated flow (VSF) models. (Theme 2)
3. ***Water ingress:*** The rate at which water moves into the grout and the rate at which associated components diffuse/migrate into the grout will be determined in eSTOMP. This step will determine the initial chemical conditions at different spatial points in the grout (from outer wall to interior). (Theme 2)
4. ***Mineral evolution:*** Based on the water and component ingress to the grout, at discrete spatial units of the grout, eSTOMP will provide information to LXO, and LXO will return the mineral condition based on the current chemistry. (Theme 1)

[1] https://cemgems.org

5. ***Contaminant evolution:*** Based on the water and component ingress to the grout, at discrete spatial units of the grout, eSTOMP will provide information to LXO, and LXO will return the chemical conditions of the contaminant(s) of interest. This step would dictate the availability of a species to migrate in/out of the grout. (Theme 3)
6. ***Diffusion:*** eSTOMP will calculate the migration of contaminant(s) through diffusive release into the near field. (Theme 2)
7. ***Transport from grout:*** The near-field transport through the disposal site will be defined using variably saturated flow modeling. This simulation step includes maturing approaches for microbial conversions in the near and far field. (Theme 2 and Theme 3)
8. ***Material evolution:*** Based on the evolving conditions in the grout and near field, the physical state of the material can be projected. This projection will be done using peridynamics (PD) modeling to predict fracturing of the material (Theme 4) and geochemical speciation modeling for other conditions (Theme 3).

This project is also maturing emerging modeling capabilities that could inform portions of the grout modeling framework or provide expanded toolsets to represent key processes.

1. ***Dataset expansion:*** Building tools to replicate experimental conditions in representative Hanford conditions, with a primary focus on the Hanford field lysimeter test. (Theme 2)
2. ***Microstructure evolution:*** Components of the grout matrix will continually react with time, dictating chemical and mineral makeup. Models can be developed to evaluate the evolution of individual components of the grout that can contribute to chemical and physical changes. These predictive tools are based on models developed for waste glasses. (Theme 1)
3. ***Mesoscale processes:*** Linking chemical and mechanical processes in grout has long been a goal of the cement research community and can be achieved by linking mechanisms at the sub-microscale to bulk material processes. Mesoscale models may be developed to bridge these scales and accurately account for transport behavior, physical state changes, and individual phase evolution. (Theme 4)
4. ***Experimental data availability:*** To support this and future modeling efforts using the *Hanford Grout Modeling Framework*, a centralized database of Hanford-relevant grout properties collected to date will be highly beneficial. An online database is being developed, and the centralized data could enable future evaluations for property trends using machine learning (ML) techniques. (Theme 5)

1.4 Project Format

The development of the *Hanford Grout Modeling Framework* is supported by five individual themes, each containing different subtasks with specific focus areas. The themes were developed based on specific targets identified within the conceptual models.

- ***Theme 1 – Grout Mineralogy:*** Grouts are composed of complex mineral assemblages that dictate many key performance properties of the material. During their lifetimes, these mineral assemblages evolve through continued hydration processes, conversion to other phases, or dissolution based on environmental exposure. These mineral growth and conversion processes are integral to determining the properties of grouts during their service and disposal lifetimes. As such, tracking this continued evolution was identified as a key component of the *Hanford Grout Modeling Framework*. In current Hanford grout modeling, the mineral assemblages are based on the initial cured compositions (i.e., early life from X-ray diffraction, XRD, where a majority of the composition is an amorphous fraction), and within the model these phases can only dissolve through kinetic reactions.

The thermodynamic databases used to assign these reaction rates and properties in current Hanford modeling are not designed for cementitious materials. As such, Theme 1 aims to update the handling of mineral evolutions in Hanford grout modeling. There are two tasks within this theme. The first task is focused on developing a software construct to inform dynamic mineral evolution in grout by informing the reactive transport models using a geochemical speciation modeling approach, which itself is supported by mineral databases designed specifically for cementitious systems. The second task is focused on developing dissolution and reaction models for the individual components of grouts (e.g., slag) based on previously developed geochemical tools designed for the long-term reactions of glass.

- ***Theme 2 – Moisture Driven Processes***: A significant limitation of the modeling of grout currently applied at Hanford is the lack of dynamic processes occurring within the grout and disposal facility. The rate of these dynamic processes (e.g., carbonation, oxidation, contaminant transport) is dictated directly by the transport of key environmental species (e.g., CO_2 , O_2) to and from the grout. After burial, the primary exposure route to environmental conditions is the transport of infiltrating water to the grout. As such, it is crucial to realize the behavior of infiltrating water and moisture in a predictive model. This theme was developed to capture contemporary approaches to moisture transport into the *Hanford Grout Modeling Framework*. A specific focus will be placed on moisture behavior both in the disposal facility and around waste forms coupled with the rates of key processes (e.g., oxidation, carbonation) in confined porous geometries of grout.
- ***Theme 3 – Dynamic Modeling of Processes Impacting Contaminant and Radionuclide Behavior:*** Crucial to the performance modeling of grout is being able to predict the release of contaminants and how the evolution of conditions in the material dictates the release. This theme was defined to capture contemporary approaches for representing the processes and chemistry responsible for controlling contaminant release from grout. This theme encompasses tasks focused on processes within the grout dictated by evolving chemistry, modeling of key aging processes (oxidation, carbonation), and significant subsurface processes (microbial behavior).
- ***Theme 4 – Chemo-mechanical Links to Grout Properties:*** As grouts age, bulk material properties change due to the evolution of hydration products and interactions with the near-field environment. Changes in bulk properties can directly impact the release behavior of contaminants from the grout and are caused by coupled chemical and mechanical processes within the grout waste form. Hence, linking chemo-mechanical processes to grout properties has important implications for grout waste form durability. Cracking remains the prominent mechanism that can drive failure of grout and can be caused by several processes. Yet, predicting and representing cracking in grouts remains a challenge and is rarely pursued for grouts used in waste management applications. This theme was designed to mature emerging approaches to capture the rate and extent of cracking in grout and to develop chemo-mechanical links at the mesoscale.
- ***Theme 5 – Grout Database:*** This theme will assemble a central resource for Hanford grout properties from reports and the peer-reviewed literature and prior reports. The database will be based on an in-progress online database of glass properties. An online interface similar to the glass database interface will be used. The goals of this effort are to provide a centralized reference for grout data to support modeling efforts, identify significant data gaps for key processes that require further research and development, and potentially develop ML assessments for predictions of grout properties. This theme will also encompass experimental efforts to fill data gaps that have already been identified in analysis of the accumulated datasets.
- ***Theme 6 – (New) Assembling the Hanford Grout Modeling Framework:*** This theme will begin in Year 2 by assembling the simulation approach to house the *Hanford Grout Modeling Framework*. The effort will initially use eSTOMP with callouts to other models (e.g., LXO) where appropriate.

2.0 Theme 1: Grout Mineralogy

This section presents overviews of the two tasks performed in Theme 1 during Year 1 of the project. Task 1 is focused on developments toward a dynamic mineral network within reactive transport software. Task 2 highlights the success of applying predictive dissolution models for glass materials toward common reagents in grout.

2.1 Theme 1 Task 1: Hanford Mineral Network

2.1.1 Team Members

Yilin Fang (Pacific Northwest National Laboratory, PNNL), Chen Gruber (Vanderbilt University, VU).

2.1.2 Background

This task has focused on updating the handling of mineral phases within grout modeling in Hanford -specific systems. The current approach to representing the mineral assemblages within grouts is to measure the composition in early age (immediately after curing) with XRD. Table presents an example of mineral compositions proposed to be used in modeling as reported in Appendix C of the Liquid Secondary Waste Data Package (Cantrell et al. 2016) in support of the 2018 IDF PA (USDOE 2018). Only five phases were reported based on the XRD measurements, and the majority (>58%) of the grouts was reported as an undefined amorphous phase. Based on the grout selected, these mineral phases at the reported amounts are input to reactive transport models to define the grout composition. The reactions of the phases are controlled by a thermodynamic database from Lawrence Berkeley National Laboratory designed specifically for subsurface sediments. These reactions are not representative of the expected evolution of the grout's mineral assemblages. Some of the most crucial phase evolutions in grouts correspond to the formation of calcium-sodium-(alumino)-silicate hydrate (C-N0(A)-S-H) phases; however, these phases are indistinguishable from the "amorphous" fraction. As such, there is a significant need to accurately represent these mineral transformations in the *Hanford Grout Modeling Framework*.

To achieve this development in the *Hanford Grout Modeling Framework*, there is a need to define the thermodynamic and chemical properties of assigned mineral phases and move toward an equilibrium phase-based approach, where appropriate. First, the CEMDATA-18 database (Lothenbach et al. 2019) – which was developed specifically for hydrated Portland, calcium aluminate, calcium sulfoaluminate, and blended cements, as well as for alkali-activated materials – will be used instead of the contemporary databases used in Hanford modeling. CEMDATA-18 enables predictions of phase transitions through an equilibrium approach to capture the actual mineral assemblages in grout. Doing this requires integrating reactive transport and geochemical speciation models. This tool will be a primary component of the *Hanford Grout Modelling Framework* and will be used directly in future simulations.

Table 2.1. Example grout properties provided for liquid secondary waste grout in the Liquid Secondary Waste Data Package that supported the 2018 IDF PA. Taken from Table C.1 of Cantrell et al. (2016).

Test Batch #	MC (%)[a]	Dry Solids Fraction	XRD Analysis (wt%)[b]						
			Ettringite	Portlandite	Calcite	Larnite	Hydrocalumite	Quartz	Amorphous
1	27.13	0.729	12	11	9.0	4.2	-	3.0	61
2	25.03	0.750	9.8	14	6.9	4.5	6.1	-	58
3	25.14	0.749	14	11	6.8	4.4	-	-	64
4	30.63	0.694	9.3	12	6.8	4.9	-	-	66
5	29.42	0.706	9.4	12	3.3	6.4	5.4	-	63
6	29.74	0.703	17	9.7	5.4	4.5	-	-	63
7	25.48	0.745	9.7	15	7.2	4.9	5.5	0.3	58
8	29.79	0.702	16	10	9.9	5.1	-	0.9	58
9	27.89	0.721	11	9.1	5.8	2.4	-	0.4	71
10	27.52	0.725	16	8.1	6.8	3.7	-	0.6	65
11	30.44	0.696	15	-	4.5	4.1	-	2.0	75
12	29.63	0.704	14	-	3.7	2.4	-	1.5	78
13	26.64	0.734	12	-	4.2	2.0	-	4.1	78
14	25.77	0.742	8.9	14	8.6	4.6	2.8	1.3	60
15	24.99	0.750	19	8.9	5.7	6.5	-	-	60
16	25.43	0.746	16	11	4.6	4.0	-	0.4	63
17	26.66	0.733	13	7.9	4.1	3.9	-	0.6	70
18	26.46	0.735	13	7.8	4.0	4.1	-	1.2	70
19[c]	26.21	0.738	13	9.5	-	5.3	-	-	72
20[c]	29.74	0.703	15	8.0	-	4.4	-	-	73
21[c]	31.21	0.688	12	-	-	3.7	-	1.8	82

MC = moisture content
Chemical formulas of minerals: ettringite [$Ca_6Al_2(SO_4)_3(OH)_{12}•26H_2O$], portlandite [$Ca(OH)_2$], calcite [CaCO3], larnite [Ca_2SiO_4], hydrocalumite [$Ca_4Al_2(OH)_{12}(OH)_2•6H_2O$)], and quartz [$SiO_2$]
Non-radiological grout monoliths (T19, T20, and T21)

2.1.3 Technical Approach

The approach taken to integrate a representative and evolving mineral network in the *Hanford Grout Modeling Framework* has focused on developing a comprehensive modeling framework that integrates a reaction solver in eSTOMP to simulate flow and reactive transport in the near-field region of grout waste forms. The solver can be used to define the mineral assemblages using CEMDATA-18 based on the key environmental conditions within the grout and near field. Although ORCHESTRA provides a useful basis for comparison, it only simulates equilibrium reactions, meaning that additional work would be required to incorporate kinetic reactions into the Hanford specific applications. To overcome this limitation, the batch reaction solver was developed to capture both kinetic and equilibrium reactions within a single framework.

To establish confidence in the eSTOMP solver, a benchmarking exercise was performed against an equilibrium reaction solver, ORCHESTRA (Meeussen 2003). This benchmarking exercise was performed using an in-house code, herein referred to as BIOGEOCHEM, that can simulate equilibrium mineral phases within grout modeling. As an intermediate step, eSTOMP was coupled directly with

ORCHESTRA (using a C++ version of ORCHESTRA) to provide an additional layer of benchmarking, allowing testing and validation of not only the eSTOMP reaction solver but also the transport modeling. This intermediate benchmarking will help identify any potential issues or discrepancies between eSTOMP and ORCHESTRA/LEACHXS. As eSTOMP is written in FORTRAN90, the team wrote a custom wrapper for eSTOMP to use ORCHESTRA as its reaction solver.

2.1.4 Results to Date

The initial comparison test case of the eSTOMP batch solver involved a reaction network of 269 species and 241 reactions. Twenty-seven of the species are minerals or are related to solid solutions specific to grouts as defined in CEMDATA-18. Note, the project team excluded surface complexation reactions in BIOGEOCHEM; these reactions were included in the corresponding ORCHESTRA model. The results of predicted concentrations from the minerals over a pH range showed good agreement with those obtained from ORCHESTRA, Figure . While some deviations were observed, mainly driven by solid-solution relationships, the predictions within the range of pH values expected in grout waste forms (pH >7) were strong, as shown in Figure for selected species. There are discrepancies in Na and Fe results between ORCHESTRA and BIOGEOCHEM (but not excluded in the ORCHESTRA model). The numerical experiments reveal that Fe is highly sensitive to speciation reactions, suggesting that the exclusion of surface complexation reactions in BIOGEOCHEM may contribute to the observed discrepancy. However, the exact cause of the difference in Na, which could also be attributed to incomplete reaction mechanisms in BIOGEOCHEM, has not been identified to date. Further investigation is needed to resolve these discrepancies.

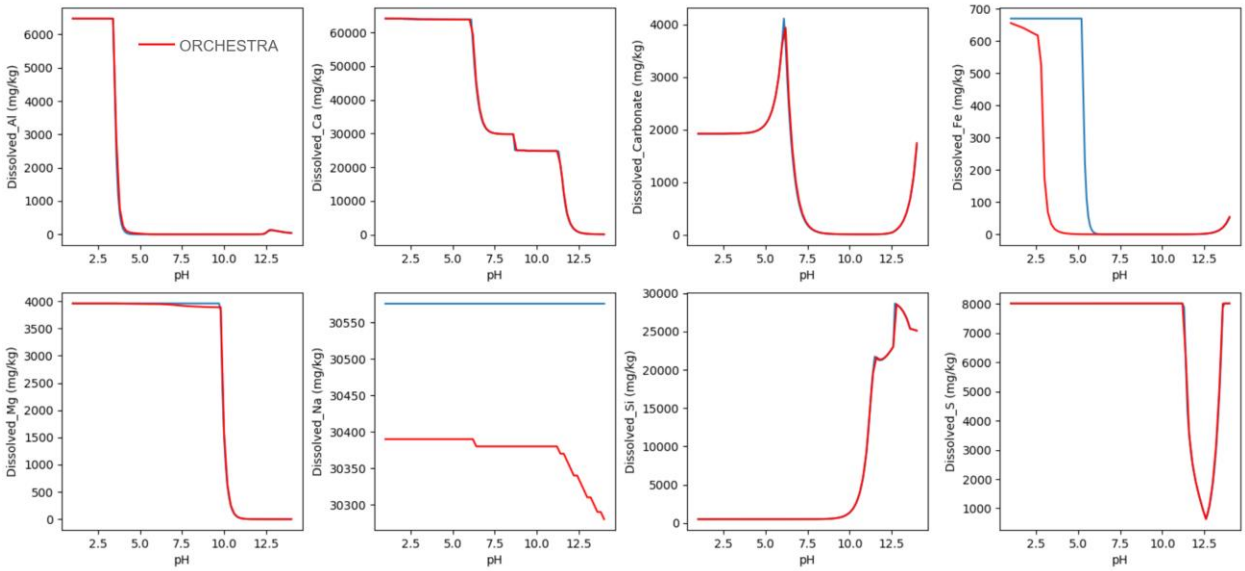

Figure 2.1. Select examples of the comparison between the expected dissolved components controlled by mineral assemblages in grout as predicted by the BIOGEOCHEM (blue) and ORCHESTRA (red).

Additional effort was made to develop a direct call-out between eSTOMP and ORCHESTRA through a wrapper in eSTOMP. Figure shows a screenshot of the wrapper functions that were developed for the integration. Initial tests showed that the code was implemented correctly and that eSTOMP could feed input to ORCHESTRA as well as get output from ORCHESTRA to be used in transport simulations. This development will support benchmarking of the eSTOMP batch solver and will be integral to capturing

other key aging mechanisms and contaminant behavior within eSTOMP under work performed in Theme 3.

```
subroutine get_output_indices(nodeType, outputVariableNames, outputIndx,size) bind(C, name="get_output_indices")
    import :: c_ptr, c_int
    type(c_ptr), value :: nodeType
    type(c_ptr), value :: outputVariableNames
    integer(c_int), intent(out) :: outputIndx(*)
    integer(c_int), value :: size
end subroutine get_output_indices

subroutine get_variable_indices(nodeType, paramList, indices, size)bind(C, name="get_variable_indices")
    import :: c_ptr, c_int
    type(c_ptr), value :: nodeType
    type(c_ptr), value :: paramList
    integer(c_int), intent(out) :: indices(*)
    integer(c_int), value :: size
end subroutine get_variable_indices

subroutine set_node_values_from_stomp(node, numNodes, inputIndx, fortranArray,numVariables) bind(C, name="set_node_values_from_stomp")
    import :: c_int, c_double, c_ptr
    type(c_ptr), value :: node
    integer(c_int), value :: numNodes
    integer(c_int), dimension(*), intent(in) :: inputIndx
    real(c_double), dimension(*), intent(in) :: fortranArray
    integer(c_int), value :: numVariables
end subroutine set_node_values_from_stomp

function create_calculator(fileID) bind(c, name="create_calculator")
    import :: c_ptr
    type(c_ptr) :: create_calculator
    type(c_ptr), value :: fileID
end function create_calculator
```

Figure 2.2. Screenshot of the wrapper written in eSTOMP to facilitate direct call-out to ORCHESTRA to collect geochemical information on mineral compositions and behavior.

2.1.5 Path Forward and Integration

This task achieved two main successes in Year 1: (1) development of a batch solver for mineral assemblage assessments and (2) integration of the reactive transport eSTOMP software with the geochemical speciation modeling in ORCHESTRA. If issues with numerical solver convergence are encountered during simulations of the *Hanford Grout Modeling Framework* in the future, there are now two reaction solver options to overcome such challenges. The solver will be used going forward in predictions of the evolution of mineral phases in full-system simulations of grout in Hanford. The call-out between eSTOMP and ORCHESTRA will serve as a key component of the *Hanford Grout Modeling Framework*, allowing other geochemical speciation information to be pulled into the reactive transport simulations.

Year 2 of this task will have three focus areas.

- ***Subtask 1.1.1:*** First, further benchmarking, calibration, and validation will be performed against experimental data sets for various grouts and analogue systems. This effort will include defining the mineral networks for other grouts – specifically, ultra-high performance grout, ordinary portland cement (OPC) with reductants, and geopolymers (Gong and Pegg 2022).
- ***Subtask 1.1.2:*** Spatial calculations within the grout will be crucial to developing the full *Hanford Grout Modeling Framework*. This task will incorporate this functionality into eSTOMP specific to mineral evolution at different positions within the waste forms. This effort will integrate across Themes 2, 3, and 6 (new).
- ***Subtask 1.1.3:*** This subtask will evaluate the mineral reaction network for the near-field region of grout waste forms in the IDF or closed tanks. This effort will ensure accurate representation of the minerals in the grout and near field.

2.2 Theme 1 Task 2: Geochemical Modeling of Reactive Grout Phases

2.2.1 Team Members

Sebastien Kerisit (PNNL), Matt Asmussen (PNNL)

2.2.2 Background

Unreacted reagents are commonly found in grout waste forms, and their continued hydration can drive mineral changes and impact contaminant release. The evolution of one reagent, blast furnace slag (BFS), is of particular interest. BFS is a supplementary cementitious material that is involved in the core hydration reactions forming the solidified grout. Most importantly for waste form applications, BFS provides reduction capacity to suppress the release of redox-sensitive contaminants and radionuclides (e.g., Cr and Tc). BFS is an amorphous material (glassy) that is ground for use in the cement industry but retains its glassy features. Following the initial hydration processes generating the grout, unreacted BFS particles that remain in the cured material can continually react over disposal timeframes and replenish the species responsible for maintaining a reducing environment (e.g., Fe(II), sulfide). However, little is known about the rate at which this process can occur.

This task focuses on a novel approach of applying glass dissolution models developed for Hanford to predict slag dissolution rates within cured grout waste forms. Identifying and building tools to assess the dissolution and reduction release rates of supplementary cementitious materials will help support predictive capability for oxidation rates of grout waste forms. This effort also lays the foundation for a new tool to predict the rates of reaction and hydration of various supplementary cementitious materials and other additives relevant to grout waste forms. This tool will support the *Hanford Grout Modeling Framework* by providing input to the full simulations.

2.2.3 Technical Approach

A slag dissolution model was developed for use in geochemical calculations that simulate the aqueous concentrations of dissolved slag components in static dissolution tests. The model parameters were varied to optimize agreement with the measured aqueous concentrations of key elements such as Ca, Al, S, and Si as a function of time. Experimental data from static dissolution tests was used to determine the best-fit model parameters. This section describes the slag dissolution model, the approach used to perform the geochemical calculations, and the model parameters.

2.2.3.1 Slag Dissolution Model

The model used in this work is composed of two coupled processes: dissolution and alteration/hydration.

Dissolution: This process is modeled by the following dissolution rate equation, which describes the slag dissolution rate, r_{diss}, as a function of distance from equilibrium:

$$r_{\text{diss}} = k_0^{\text{diss}} a_{\text{H}^+}^{-\eta} \exp\left(\frac{-E_a}{RT}\right)\left[1 - \left(\frac{Q}{K}\right)\right] \qquad \text{Eq. 2.1}$$

where r_{diss} is the slag dissolution rate ($mol_{slag}\ m^{-2}\ s^{-1}$), k_0^{diss} is the intrinsic rate constant ($mol_{slag}\ m^{-2}\ s^{-1}$), a_{H+} is the hydrogen ion activity (unitless), η is the pH power law coefficient (unitless), E_a is the activation

energy (J mol^{-1}), R is the ideal gas constant (8.314 J K^{-1} mol^{-1}), T is the temperature (K), Q is the ion activity product for slag (unitless), and K is the equilibrium constant for slag (unitless).

Alteration/Hydration: This process is modeled by a time-dependent rate, r_{alt}, to form an altered/hydrated slag overlayer. The altered slag dissolves according to the same dissolution rate equation and with the same parameters as the pristine slag (Eq. 2.1). The altered slag is represented as an oxide of aluminum, calcium, and silicon. The altered slag is formed by alteration of the pristine slag whereby some fractions of Al, Ca, and Si in the pristine slag are retained. Simplifying the composition of the pristine slag to the Al, Ca, and Si oxide components, the chemical reaction for slag dissolution can be written as:

$$\mathrm{Al}_a\mathrm{Ca}_b\mathrm{Si}_c\mathrm{O}_{x\,(s)} + y\,\mathrm{H_2O}_{(aq)} \leftrightarrow a\,\mathrm{Al^{3+}}_{(aq)} + b\,\mathrm{Ca^{2+}}_{(aq)} + c\,\mathrm{H_4SiO_4}_{(aq)} + z\,\mathrm{OH^-}_{(aq)} \qquad \text{Eq. 2.2}$$

where a, b, and c are the stoichiometric coefficients of the Al, Ca, and Si oxide components. Similarly, the chemical reaction for dissolution of the altered slag can be written as:

$$\begin{aligned}\mathrm{Al}_{a\times rf_{\mathrm{Al}}}\mathrm{Ca}_{b\times rf_{\mathrm{Ca}}}\mathrm{Si}_{c\times rf_{\mathrm{Si}}}\mathrm{O}_{x'\,(s)} + y'\,\mathrm{H_2O}_{(aq)} \\ \leftrightarrow a\times rf_{\mathrm{Al}}\,\mathrm{Al^{3+}}_{(aq)} + b\times rf_{\mathrm{Ca}}\,\mathrm{Ca^{2+}}_{(aq)} + c\times rf_{\mathrm{Si}}\,\mathrm{H_4SiO_4}_{(aq)} + z'\,\mathrm{OH^-}_{(aq)}\end{aligned} \qquad \text{Eq. 2.3}$$

where rf_{Al}, rf_{Ca}, and rf_{Si} are the Al, Ca, and Si retention factors, which vary from 0 (fully dissolved) to 1 (fully retained). The alteration reaction forms n mol of altered slag for n mol of pristine slag consumed (Eq. 2.2 and Eq. 2.3):

$$\begin{aligned}\mathrm{Al}_a\mathrm{Ca}_b\mathrm{Si}_c\mathrm{O}_{x\,(s)} + (y-y')\,\mathrm{H_2O}_{(aq)} \\ \leftrightarrow \mathrm{Al}_{a\times rf_{\mathrm{Al}}}\mathrm{Ca}_{b\times rf_{\mathrm{Ca}}}\mathrm{Si}_{c\times rf_{\mathrm{Si}}}\mathrm{O}_{x'\,(s)} + a\times(1-rf_{\mathrm{Al}})\,\mathrm{Al^{3+}}_{(aq)} \\ + b\times(1-rf_{\mathrm{Ca}})\,\mathrm{Ca^{2+}}_{(aq)} + c\times(1-rf_{\mathrm{Si}})\,\mathrm{H_4SiO_4}_{(aq)} + (z-z')\,\mathrm{OH^-}_{(aq)}\end{aligned} \qquad \text{Eq. 2.4}$$

The alteration/hydration reaction is modeled using a time-dependent kinetic rate equation:

$$r_{\mathrm{alt}} = k_0^{\mathrm{alt}} \times \frac{1}{t^p} \qquad \text{Eq. 2.5}$$

where k_0^{alt} is the alteration empirical rate constant (mol_{slag} m^{-2} s^{-1}), t is time (s), and p is the time power coefficient (unitless).

The pristine slag is consumed by dissolution and alteration/hydration:

$$r_{\mathrm{p}} = A_{\mathrm{p}} r_{\mathrm{diss}} + A_{\mathrm{p}} r_{\mathrm{alt}} \qquad \text{Eq. 2.6}$$

whereas the altered slag is consumed by dissolution and formed by alteration/hydration:

$$r_{\mathrm{a}} = A_{\mathrm{a}} r_{\mathrm{diss}} - A_{\mathrm{p}} r_{\mathrm{alt}} \qquad \text{Eq. 2.7}$$

where r_{diss} and r_{alt} are defined in Eq. 2.1 and Eq. 2.5, respectively, and A_p and A_a (m^2) are the surface areas of the pristine and altered slags, respectively, and are defined as:

$$A_{\mathrm{p}} = SSA \times n_{\mathrm{p}} \times MW_{\mathrm{p}} \qquad \text{Eq. 2.8}$$

and

$$A_{\mathrm{a}} = SSA \times n_{\mathrm{a}} \times MW_{\mathrm{a}} \qquad \text{Eq. 2.9}$$

where SSA ($m^2\ g^{-1}$) is the slag specific surface area (assumed to be the same for the pristine and altered slags); n_p and n_a (mol_{slag}) are the number of moles of pristine and altered slags (n_a is zero at the start of each calculation), respectively; and MW_p and MW_a ($g_{slag}\ mol_{slag}^{-1}$) are the molecular weights of the pristine and altered slags, respectively.

Additionally, the aqueous speciation of dissolved slag components is modeled using a thermodynamic database of equilibrium constants. The thermodynamic database, thermo.com.V8.R6.230, is used for the equilibrium constants of all aqueous species.

2.2.3.2 Geochemical Calculations

The geochemical calculation software PHREEQC (PH-REdox-EQuilibrium in C) (Parkhurst and Appelo 2013) was employed to model the dissolution of several slags in static dissolution tests. The geochemical calculations reproduced the conditions of the static dissolution tests reported by Zhang et al. (2022b), Trivelpiece and Hsieh (2021), and Asmussen et al. (2015). The temperatures were 20 °C, 22 °C, and 50 °C for the tests of Zhang et al. (2022), Trivelpiece and Hsieh (2021), and Asmussen et al. (2015), respectively. The initial amount of slag and the solution volume were set to reproduce the respective liquid-to-solid mass ratios of 1,000, 100, and 10. A logarithmic-based integration timestep was used in the calculations: 10×10^{-6} h, 9×10^{-5} h, 9×10^{-4} h, 9×10^{-3} h, 9×10^{-2} h, 9×10^{-1} h, $x \times 1$ h, where x was 79, 239, and 71 for the calculations of the tests from Zhang et al. (2022), Asmussen (2014), and Trivelpiece and Hsieh (2021), respectively, and an additional 53 steps with 1-d intervals were used for the last of the three sets of tests. The slag compositions were those reported by Zhang et al. (2022) for M16, A3, A16, CS2, and S; Westsik et al. (2013) for NW slag; and Trivelpiece and Hsieh (2021) for BFS.

2.2.3.3 Model Parameters

The molecular weights of the pristine and hydrated slags were those calculated using the atomic weights listed in thermo.com.V8.R6.230. The specific surface areas (Table 2.3) were those reported by Zhang et al. (2022) for M16, A3, A18, CS2, and S and by Westsik et al. (2013) for NW slag. For BFS used by Trivelpiece and Hsieh (2021), an approximate value of 1 was used based on the values reported by Zhang et al. (2022). The parameters k_0^{diss}, η, and E_a in Eq. 2.1 (Table 2.3) were calculated using composition–parameter correlation models developed from dissolution tests performed in dilute conditions with the stirred-reactor coupon analysis method for a matrix of 24 enhanced waste glasses. The parameters K, k_0^{alt}, p, rf_{Al}, rf_{Ca}, and rf_{Si} were used as free parameters of the fits.

2.2.4 Results to Date

The slag dissolution model was applied to three datasets that span a wide range of slag compositions and test conditions. These datasets were selected because they provided data amenable to geochemical modeling, namely, solution chemistry data as a function of time. The dissolution test data from Zhang et al. (2022) was obtained for five slags (labeled M16, A3, A18, CS2, and S; see Table 2.2 for compositions) at 20 °C, a liquid-to-solid mass ratio (l/s) of 1,000, and in a 0.14 M NaOH solution (pH = 13.2) with samplings up to 72 h. The high liquid-to-solid mass ratio, high pH, and short sampling times mean that this dataset probes the early dissolution of slags in dilute conditions. Al, Ca, and Si concentrations calculated using the model parameters in Table 2.3 are compared to measured concentrations in Figure 2.3.

The forward-rate model parameters (k_0^{diss}, η, and E_a), which were predicted using composition–parameter correlation models rather than fit to experimental data, successfully reproduced the initial rise in Al, Ca, and Si concentrations within approximately the first 10 hours. The concentrations at later times, which are mostly controlled by the alteration rate, r_{alt}, were well reproduced with empirical rate constants, k_0^{alt}, ranging from 3×10^{-8} to 3×10^{-7} mol_{slag} m^{-2} s^{-1} and time power coefficients, p, from 0.25 to 0.40. Most retention factors were low and ranged from 0.3 to 0.4, as expected based on the dilute conditions of the tests. Two slags (M16 and A18) had high Al retention factors (0.74 and 0.71, respectively). As indicated by Zhang et al. (2022), these two slags had high combined Al_2O_3 and MgO contents and CaO/SiO_2 mass ratios greater than 1. One slag (CS2) had a high Ca retention factor (0.79) and was the slag with the lowest CaO/SiO_2 mass ratio. These correlations between slag composition and model parameters indicate that additional slag dissolution test data would allow the development of composition–parameter correlation models.

Table 2.2. Compositions (in mole fractions) of the slags considered in this work.

Slag	Al_2O_3	CaO	Fe_2O_3	K_2O	MgO	MnO	MnO_2	Na_2O	P_2O_5	SO_3	SiO_2	SrO	TiO_2
M16	0.08568	0.35288	0.00124	0.00129	0.23144	0.00131	0.00000	0.00206	0.00000	0.00007	0.31872	0.00000	0.00531
A3	0.02037	0.42234	0.00025	0.00000	0.15127	0.00000	0.00000	0.00000	0.00000	0.00007	0.40570	0.00000	0.00000
A18	0.10915	0.40227	0.00153	0.00266	0.12114	0.00233	0.00000	0.00365	0.00000	0.00023	0.35060	0.00000	0.00644
CS2	0.10198	0.30381	0.00133	0.00206	0.14572	0.00163	0.00000	0.00304	0.00000	0.00061	0.43306	0.00000	0.00677
S	0.07989	0.40005	0.00135	0.00178	0.12070	0.00254	0.00000	0.00000	0.00000	0.00697	0.37757	0.00000	0.00916
BFS	0.07907	0.45218	0.00153	0.00239	0.09828	0.00077	0.00063	0.00000	0.00003	0.02489	0.33572	0.00038	0.00412
NW	0.07618	0.47000	0.00295	0.00000	0.06026	0.00000	0.00207	0.00000	0.00000	0.04713	0.34100	0.00041	0.00000

Table 2.3. Test conditions and model parameters derived in this work. Parameters k_0^{diss} and k_0^{alt} are in $\mathrm{mol_{slag}\ m^{-2}\ s^{-1}}$, *SSA* is $\mathrm{m^2\ g^{-1}}$, E_a is in kJ $\mathrm{mol^{-1}}$, and the remaining parameters are unitless.

Slag	l/s	T (°C)	pH_0	*SSA*	k_0^{diss}	η	E_a	log *K*	k_0^{alt}	*p*	rf_{Al}	rf_{Ca}	rf_{Si}
M16	1,000	20	13.2	0.96	2.178×10^{5}	0.404	98.1	-8.5	3.0×10^{-7}	0.40	0.74	0.36	0.37
A3	1,000	20	13.2	1.09	1.852×10^{3}	0.334	82.3	-14.2	1.0×10^{-7}	0.25	0.35	0.35	0.37
A18	1,000	20	13.2	0.90	6.190×10^{5}	0.561	112.4	-13.7	3.0×10^{-8}	0.40	0.71	0.49	0.37
CS2	1,000	20	13.2	1.08	1.383×10^{5}	0.582	114.6	-12.6	7.0×10^{-8}	0.30	0.30	0.79	0.10
S	1,000	20	13.2	0.94	9.305×10^{4}	0.489	103.0	-12.2	8.0×10^{-8}	0.25	0.30	0.60	0.30
NW	100	22	7	3.03	6.834×10^{4}	0.463	100.2	-12.0	7.5×10^{-8}	0.50	-	0.68	0.73
NW	100	22	10	3.03	6.834×10^{4}	0.463	100.2	-12.0	7.5×10^{-8}	0.50	-	0.68	0.73
NW	100	22	13	3.03	6.834×10^{4}	0.463	100.2	-12.0	7.5×10^{-7}	0.50	-	0.99	0.94
BFS	10	50	7	1.00	9.143×10^{4}	0.472	100.1	-11.2	1.5×10^{-5}	0.85	1.00	0.90	1.00
BFS	10	50	12.5	1.00	9.143×10^{4}	0.472	100.1	-10.8	1.0×10^{-5}	0.85	1.00	1.00	1.00
BFS	10	50	>13	1.00	9.143×10^{4}	0.472	100.1	-10.8	1.0×10^{-4}	0.85	0.91	1.00	1.00

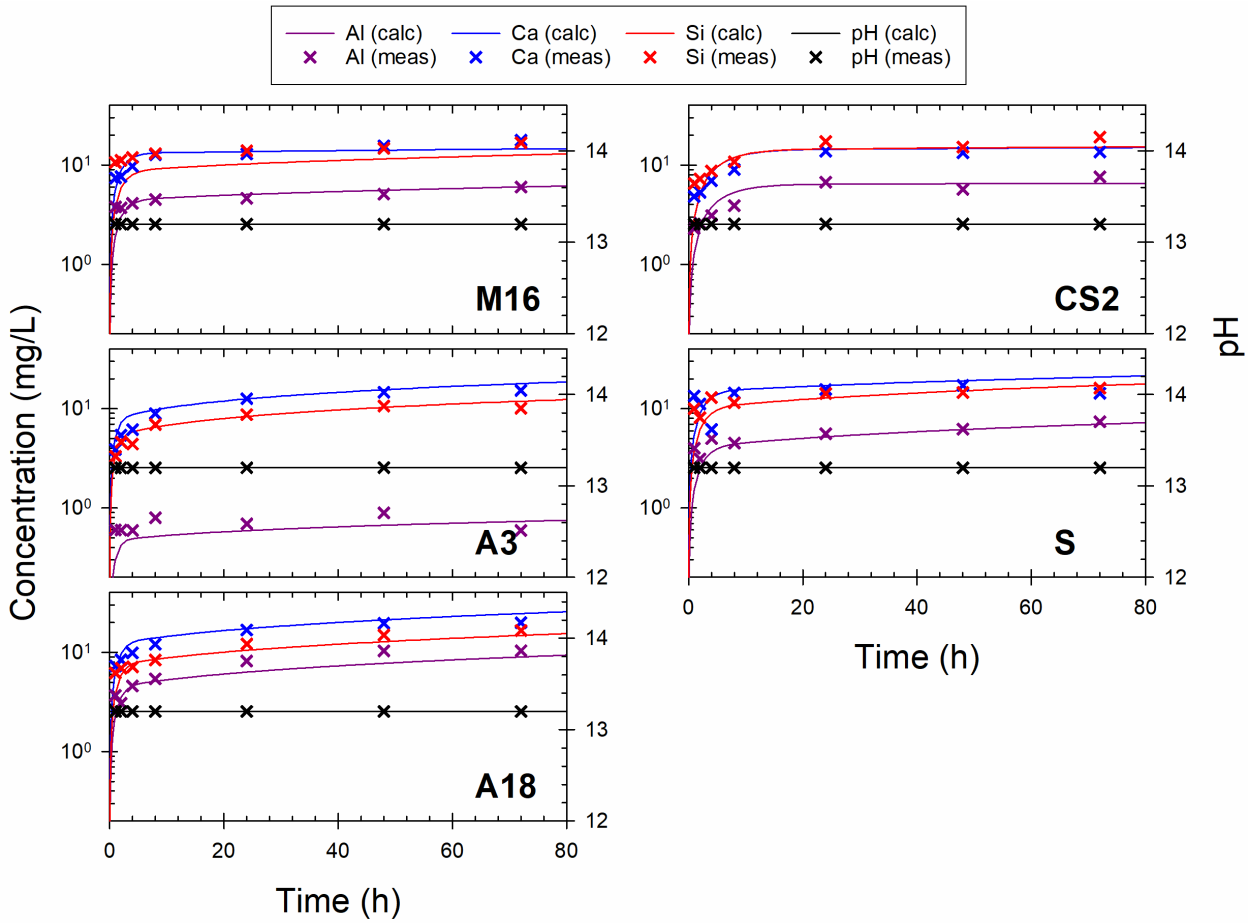

Figure 2.3. Measured and calculated concentrations of Al, Ca, and Si and pH as a function of time for the static dissolution of five slags at 20 °C, l/s = 1,000, and 0.14 M NaOH. Measured concentrations are from Zhang et al. (2022).

The dissolution test data from Asmussen et al. (2015) was obtained for one slag (labeled NW; see Table 2.2 for composition) at room temperature, a l/s value of 100, and with samplings up to 10 d. The lower liquid-to-solid mass ratio and longer sampling times than used by Zhang et al. (2022) mean that this dataset probes the intermediate slag dissolution regime. Ca, S, and Si concentrations calculated using the model parameters in Table 2.3 are compared to measured concentrations in Figure 2.4 for the three initial pH values. The same model parameters gave good agreement with the experimental data obtained at pH_0 = 7 and 10. The results obtained at these two initial values were similar because the slag is a source of alkalinity and the pH of a solution in equilibrium with the slag would be higher than either of the initial pH values. At a higher initial pH of 13, the log *K* and *p* parameters remained the same but k_0^{alt} increased by one order of magnitude, consistent with an expected high rate of alteration in highly alkaline conditions. The Ca and Si retention factors also increased, indicating a greater extent of slag transformation into alteration products.

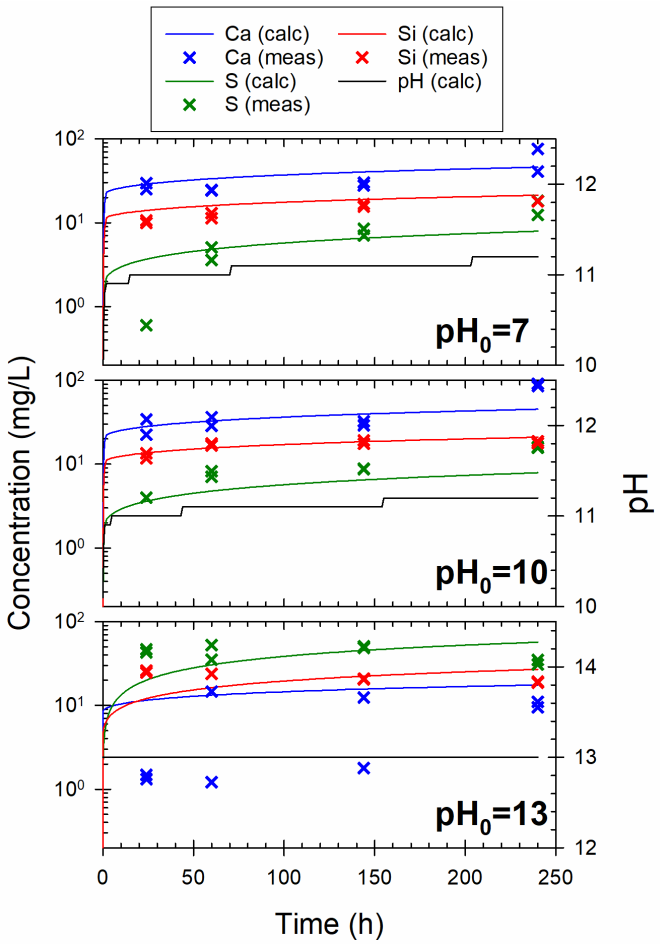

Figure 2.4. Measured and calculated concentrations of Ca, Si, and S and pH as a function of time for the static dissolution of NW slag at room temperature, l/s = 100, and three initial pH values. Measured concentrations are from Asmussen et al. (2015).

The dissolution test data from Trivelpiece and Hsieh (2021) was obtained for one slag (labeled BFS; see Table 2.2 for composition) at 50 °C, a l/s value of 10, and with samplings up to 56 d. The higher temperature, lower liquid-to-solid mass ratio, and longer sampling times than in the other two datasets mean that this dataset probes the later slag dissolution regime. XRD analysis of the slag reported in Trivelpiece and Hsieh (2021) indicated the presence of gypsum ($CaSO_4 \cdot 2H_2O$). Therefore, a small amount of gypsum was assumed to be present initially and to rapidly dissolve. If it is assumed that K and S are not retained in the hydrated slag particles or in secondary phases, the excess S release relative to K can be attributed to gypsum. This amount was small (1 wt%) and consistent across the three conditions considered in this work, supporting this assumption.

Figure 2.5 compares the Al, Ca, K, Na, S, and Si concentrations calculated using the parameters in Table 2.3 to the values reported by Trivelpiece and Hsieh (2021) for tests performed in deionized water, at an initial pH of 12.5, and in a 2 M NaOH solution. Similar to the modeling results obtained with the NW slag, k_0^{alt} was similar for the tests in deionized water and at pH_0 = 12.5 but increased by one order of magnitude for the test in 2 M NaOH solution. The parameter p was independent of test conditions, as found for the NW slag, and was higher than for the other two datasets, consistent with the higher reaction progress probed in these tests. The Al, Ca, and Si retention factors were very high, often reaching 1, indicating extensive slag hydration and transformation into secondary phases.

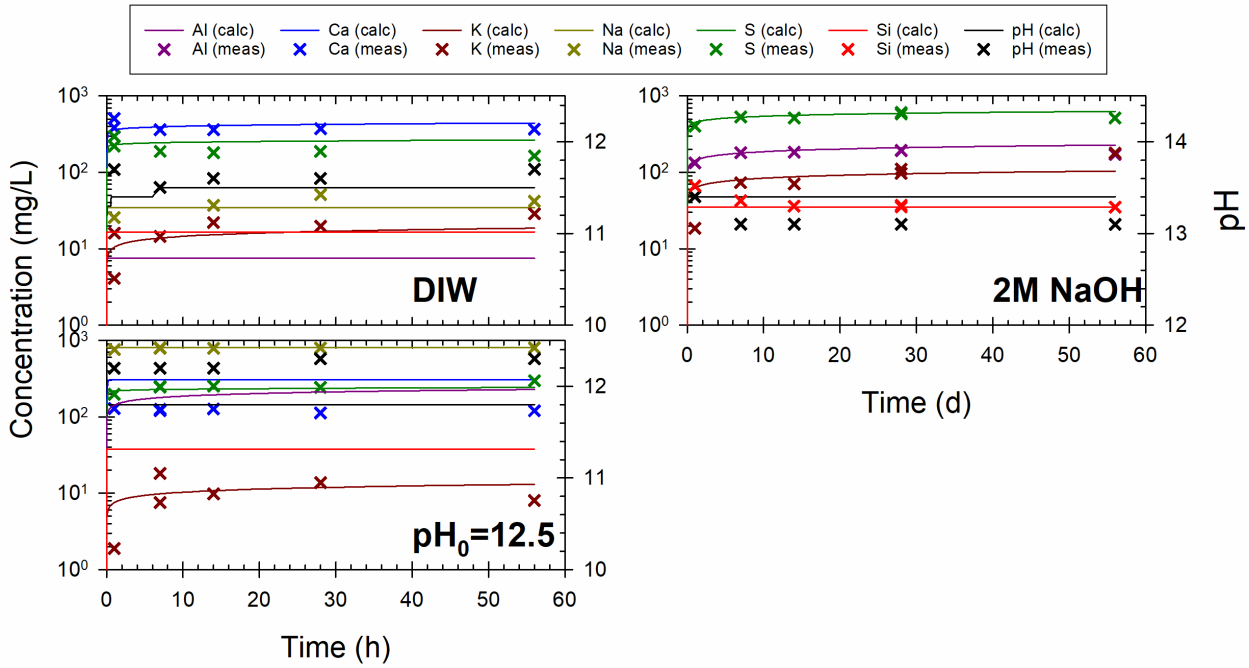

Figure 2.5. Measured and calculated concentrations of Al, Ca, K, Na, S, and Si and pH as a function of time for the static dissolution of a BFS at 50 °C, l/s = 10, and three test conditions (deionized water, pH_0 = 12.5, and 2 M NaOH). Measured concentrations are from Trivelpiece and Hsieh (2021).

In summary, a model of slag dissolution in aqueous conditions has been developed based on existing glass corrosion models. The model combines a linear rate law for dissolution with a time-dependent hydration/alteration rate. Model parameterization was performed using three datasets that covered a range of slag compositions reacted at multiple temperatures, liquid-to-solid ratios (L/S), and pH values and that spanned several dissolution regimes (early, intermediate, and late dissolution regimes). The model accounts for the observed initial rapid dissolution followed by long-term slow alteration and can serve as a source term for reduction capacity in large-scale models of cementitious waste form disposal.

2.2.5 Path Forward and Integration

The work performed in Year 1 and described above focused on developing and parameterizing a dissolution model for slag in aqueous conditions, i.e., in isolation and outside of a grout environment. With this tool developed, in Year 2 the project team will investigate the broader applicability of this approach.

- ***Subtask 1.2.1:*** This subtask will focus on the long-term dissolution of slag particles in grout in terms of both how grout impacts slag dissolution and how slag dissolution influences grout mineralogical evolution and the release of redox-sensitive contaminants and radionuclides. Time-dependent solution chemistry data from the literature and from this project will be collected for slag-containing grout samples for model evaluation. The formation of secondary phases, specifically calcium silicate hydrates, will be modeled using the CEMDATA18 database (Lothenbach et al. 2019). This effort will also use data from a separate Laboratory Policy Office project led by Savannah River National Laboratory (SRNL) to characterize slag particles in cured grout. This subtask will provide information on reaction rate times for long-term slag dissolution in cured grout.

- ***Subtask 1.2.2:*** The slag dissolution model developed in Year 1 can serve as a point source term in higher-scale models, such as the mesoscale model described in Section 5.2 that treats the interplay between diffusion and particle dissolution in an inhomogeneous microstructure of particles inside a grout matrix. Integration of the slag dissolution model into a mesoscale model will be validated against time sequences of electron micrographs of cross sections of reacted slag particles. By linking these two modeling tools, local models of long-term reactivity of key phases on grouts can be developed.
- ***Subtask 1.2.3:*** BFS is one of several conventional supplementary cementitious materials alongside fly ash (FA), silica fume, and calcined clays or other additives such as iron oxides. In Year 2, the project team will apply the geochemical modeling approach described in this section to the dissolution of other materials where data is available. The team will first perform a literature review to identify and collect FA dissolution data amenable to geochemical modeling, specifically, time-dependent solution chemistry data. The team will seek datasets that vary dissolution conditions (temperature, pH, L/S, reaction time, etc.) and FA composition. Following the approach used to correlate the parameters of a dissolution model for Hanford glass, the team will combine the dissolution model parameters derived in Year 1 for BFS and in Year 2 for FA to develop composition–parameter correlation models that can be used to predict dissolution model parameters of supplementary cementitious materials, and thus their long-term dissolution, solely based on material composition.

3.0 Theme 2: Dynamic Modeling of Moisture Driven Processes

This section presents overviews of the two tasks performed in Theme 2 during Year 1 of the project. Task 1 integrated moisture transport predictions in disposal environments using variably saturated flow modeling (VSF) into the reactive transport simulations used at Hanford. Task 2 was focused on assessing the ability of VSF to simulate experimental conditions within the Hanford field lysimeter test, in preparation to use the lysimeter data to verify the *Hanford Grout Modeling Framework*.

3.1 Theme 2 Task 1: Integration of Variably Saturated Flow Modeling to eSTOMP (IDF simulations)

3.1.1 Team Members

Xuehang Song (PNNL), Jiannan Chen (University of Central Florida, UCF).

3.1.2 Background

This task was focused integrating recent developments of VSF developed by the University of Central Florida into the existing eSTOMP construct used at Hanford. The current approach at Hanford assumes a constant infiltration rate that is not affected by seasons or position in the IDF/subsurface. The VSF that has been developed proposes that, within the IDF or in a closed tank scenario, there will be large variations in the degree of saturation across the IDF. This means that the water flux near individual waste forms will vary based on their position within the IDF, and the release of contaminants from the grout (or rate of processes such as oxidation) will vary spatially. In other words, the current projections using constant infiltrating and wetting are overly conservative. This task was used to benchmark between the VSF and eSTOMP. The information produced will be a core component of the *Hanford Grout Modeling Framework* to provide information on the amount of water reaching the grout and degree of surface exposure to it.

3.1.3 Technical Approach

This study employed a 2-D near-field hydrology model developed using eSTOMP to evaluate unsaturated flow dynamics in the IDF. The model assesses infiltration, cover degradation, and liner performance, providing a basis for an eventual 3-D vadose zone flow and transport model as part of the *Hanford Grout Modeling Framework*. To extend the analysis, sensitivity simulations were conducted, incorporating 495 cases that explore varying infiltration rates, degradation scenarios, and spatial variability in waste package placement in the IDF. An alternative scenario was also developed to examine the impact of complete degradation of the IDF cover, where all infiltration discharges at sump locations. Additionally, particle tracking simulations were performed across all cases to analyze flow pathways and travel times. This approach quantifies preferential flow patterns, retention zones, and travel time variability, informing contaminant transport assessments and model resolution considerations.

The following sections detail the baseline model, sensitivity and alternative conceptual models, particle tracking methodology, results, and future integration with reactive transport modeling efforts.

3.1.3.1 Near-Field Hydrology Model Base Case

The near-field hydrology model is a 2-D cross-sectional representation of the IDF (Figure) developed using eSTOMP to simulate unsaturated flow dynamics and evaluate the impact of infiltration scenarios, cover degradation, and liner performance (USDOE 2016). The model assesses water redistribution within and around the IDF, particularly in the vadose zone, and serves as a precursor for a 3-D vadose zone flow and transport model.

The model domain represents an east-west cross-section of the IDF, perpendicular to the north-south-oriented sump lines. The computational grid is discretized into elements with nominal dimensions of 1.25 × 0.25 m, allowing for a detailed representation of the engineered barriers and natural subsurface features. The model includes key components such as the Resource Conservation and Recovery Act (RCRA) Subtitle C barrier, the liner system [geomembrane and geosynthetic clay liner (GCL) composite], and the waste disposal layers, consisting of four lifts of waste package containers, each 2.3 m high, separated by 1-m-thick compacted backfill layers. Hydraulic properties for the different material layers were assigned based on onsite characterization data, with a focus on capturing the influence of low-permeability asphalt and GCL layers, sandy soil backfill, and the drainage layer. Initial conditions assume an intact cover and liner system, with minimal infiltration into the waste layers. The model accounts for long-term degradation by increasing the permeability of the asphalt and GCL layers after 500 years, which affects infiltration rates and water redistribution patterns.

This near-field hydrology model captures the movement of water through the surface barrier, backfill, and liner system within the IDF. As a flow model rather than a contaminant transport model, it evaluates water movement and its interaction with the waste forms. Key outputs include the spatial and temporal distribution of water flow rates within the IDF, the extent of contact with immobilized LAW glass and cementitious waste forms, and the water flow rate through the liner system to the vadose zone, which serves as recharge input for the vadose zone flow and transport model.

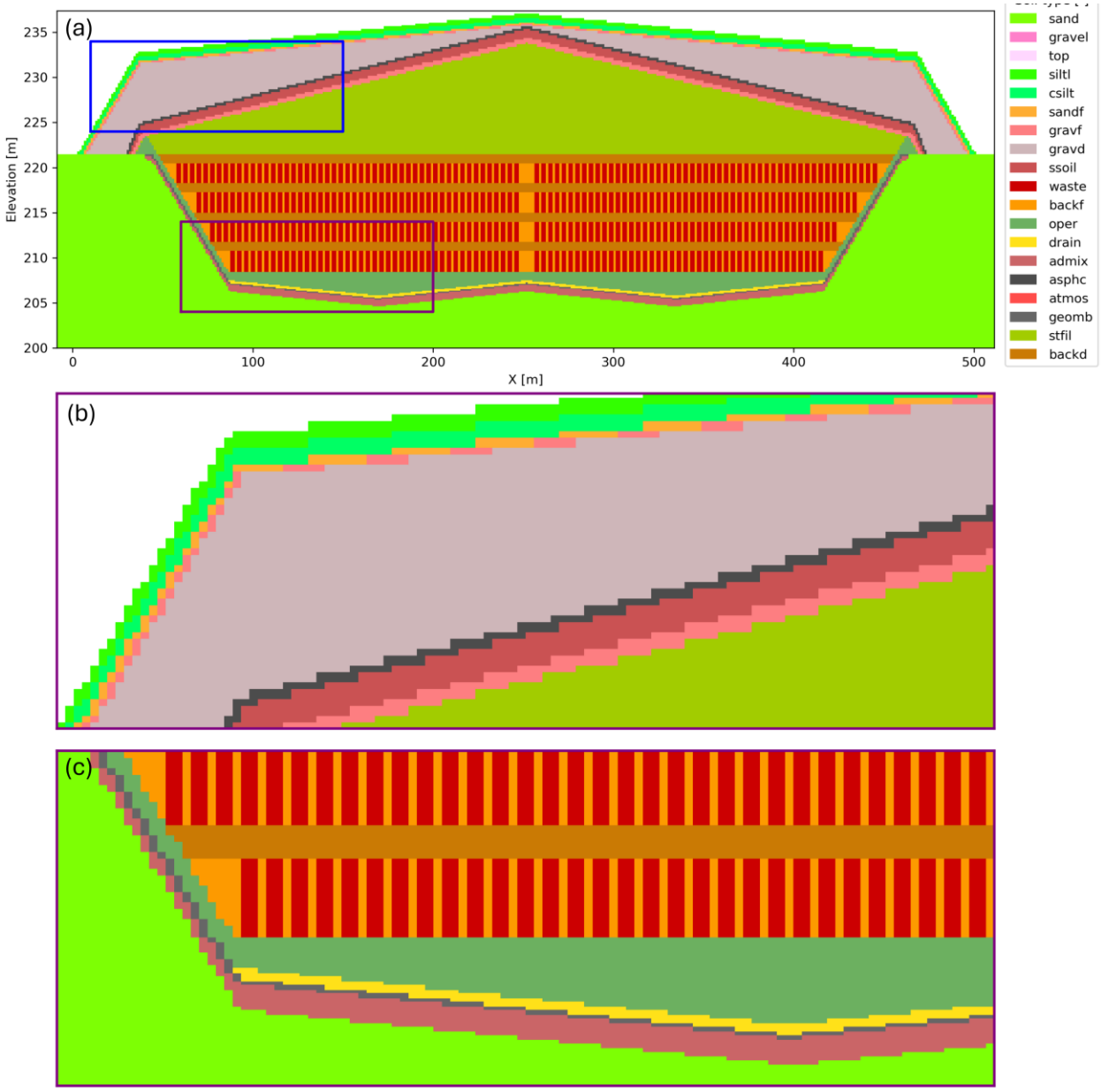

Figure 3.1. Model domain for near-field hydrology model base case, representing the 2-D cross-section of the IDF. This model includes the engineered barrier system, waste disposal layers, and liner system. (a) Full model domain. (b) Enlarged view of the upper layers (blue box in a), highlighting the engineered barrier and liner system. (c) Enlarged view of the side wall and facility bottom (purple box in a), showing details of the waste disposal layers and surrounding materials.

3.1.3.2 Alternative Conceptual Models for Near-Field Hydrology: Sensitivity and Cover Degradation

In the 2018 IDF PA (USDOE 2018), a sensitivity analysis examined the impact of different degradation scenarios on water flow within the IDF by conducting a series of restart simulations with varying assumptions about the integrity of the cover and liner system. The initial steady-state simulation

established baseline conditions, where the IDF trench and surface barrier were represented by a high-permeability uniform fill material, while the liner system maintained its present configuration. Subsequent simulations explored different durations of intact cover and liner conditions (100, 500, and 1,000 years), with degradation events triggering new transient simulations extending to 10,000 years. These cases helped assess how changes in barrier integrity over time influence water redistribution, recharge rates, and potential waste form interactions.

Building on these PA sensitivity analyses, this model expands the approach by incorporating a broader range of infiltration scenarios, degradation assumptions, and spatial variability in waste package placement, enabling a more comprehensive evaluation of long-term water movement within and beyond the IDF. Table 3.1 summarizes the sensitivity analysis cases, where five different infiltration rates (ranging from 0.9 to 33 mm/yr) are evaluated across nine degradation scenarios, with 11 realizations per case, resulting in a total of 495 simulations. The degradation cases, presented in Table 3.2, account for different assumptions about the timing of the asphalt and GCL layer degradation, with variations in the assumptions about when these low-permeability barriers will fail.

Table 3.1. Sensitivity analysis cases for infiltration rates, degradation scenarios, and randomized placement of waste packages.

Factor	Values
Infiltration rate (mm/yr)	0.9, 1.7, 3.5, 5.0, 33 (5 values)
Degradation year (yr)	9 cases (see below)
Randomized realizations	Baseline + 10 realizations (11 total)

Table 3.2. Degradation scenarios for asphalt and GCL in sensitivity analysis.

Case Index	Asphalt (yr)	GCL (yr)
1	100	500
2	100	1,000
3	100	2,000
4	500	500
5	500	1,000
6	500	2,000
7	1,000	1,000
8	1,000	2,000
9	2,000	2,000

To evaluate the impact of spatial variability in waste package placement on near-field hydrology and subsequent contaminant migration, nine randomized realizations were generated by perturbing waste package locations within the IDF model domain. Figure 3.2 presents three example realizations from these nine cases. Incorporating these perturbations into the analysis provides insights into the sensitivity of water flow and release patterns to small-scale variations in waste configuration, complementing the broader sensitivity studies on infiltration rates and degradation scenarios.

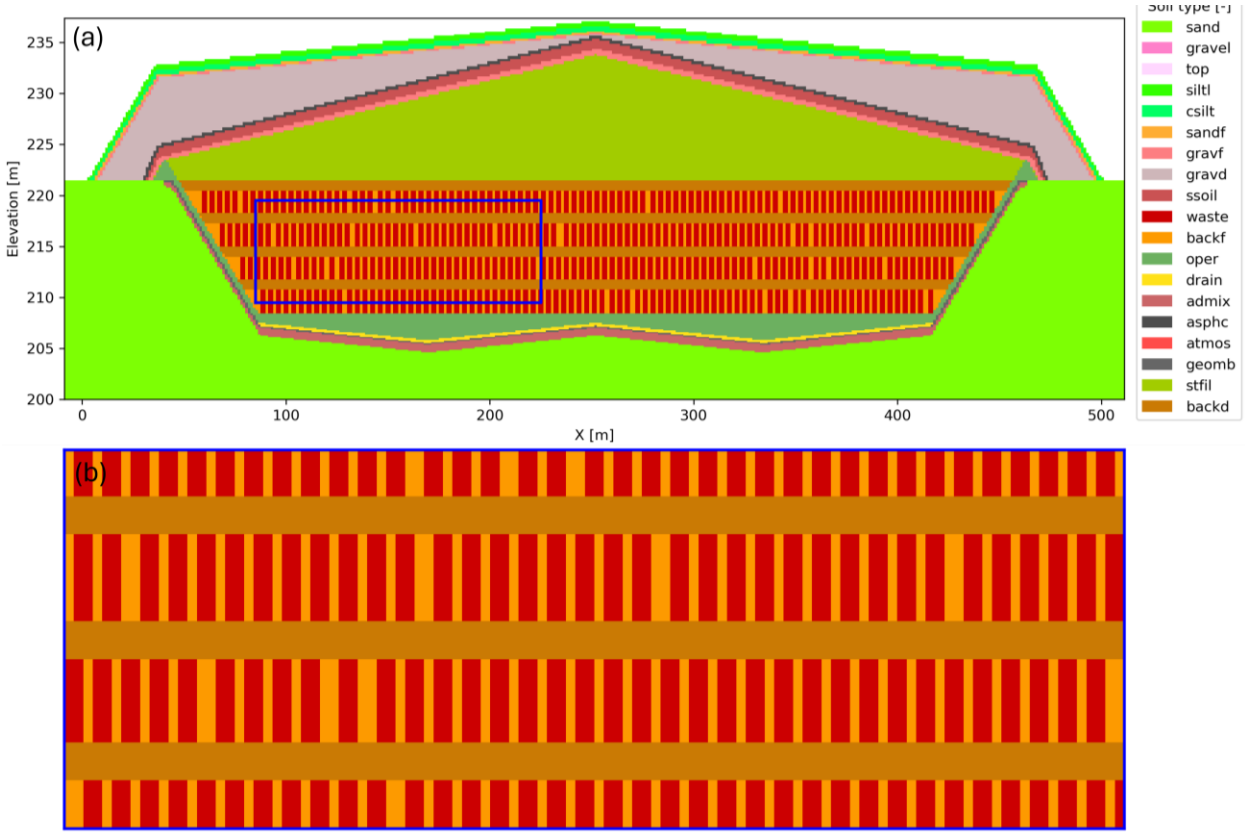

Figure 3.2. Model domain illustrating spatial variability in waste package placement within the IDF system. (a) Full model domain with a representative waste arrangement. (b) Variations in waste placement, demonstrating the perturbations considered in the analysis.

In addition to the sensitivity model, an alternative test model was developed to examine the effects of enhanced cover degradation and preferential flow pathways on near-field hydrology. In this scenario, all cover layers above the asphalt concrete (ASPHC) layer are assumed to be fully degraded, leading to altered water redistribution patterns and reduced travel time. A uniform infiltration rate of 3.3 mm/yr is applied to the top boundary of the model domain to represent long-term recharge conditions (indicated by the top arrows in the model domain). Unlike the sensitivity model, this alternative model assumes that all discharge is directed toward the two bottom sump locations, as shown by the black arrows at the bottom of the model domain, Figure 3.3. This conceptualization explores potential changes in water flow behavior and their implications for vadose zone transport and contaminant migration.

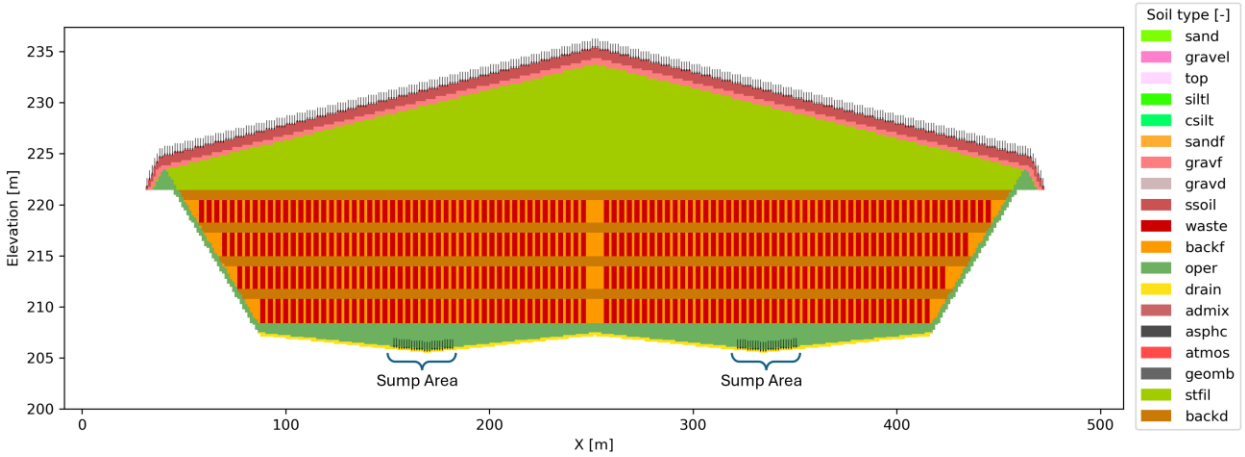

Figure 3.3. Model domain for the alternative conceptual model, where all cover layers above the asphalt concrete (ASPHC) layer are degraded and a 3.3-mm/yr infiltration condition is applied to the top boundary. Water flow is assumed to be discharged exclusively at the two bottom sump locations, indicated by the black arrows.

3.1.3.3 Alternative Conceptual Models for Near-Field Hydrology: Particle Tracking

To investigate the hydrological behavior of water entering the IDF and its interaction with waste packages, a custom particle tracking algorithm was developed to analyze flow paths and travel times. This approach provides a computationally efficient method to evaluate water movement patterns and residence times, offering insights into how infiltration, cover degradation, and engineered barriers influence near-field hydrology. Unlike full reactive transport modeling, particle tracking focuses solely on advective transport, enabling a detailed examination of flow dynamics and potential contaminant transport pathways. This algorithm allows benchmarking comparisons between eSTOMP and VSF modeling.

The particle tracking analysis is based on a cell-centered steady-state velocity field derived from eSTOMP flow simulations and interpolated onto a face-centered grid to improve numerical accuracy. Particles are released at the top boundary of the IDF model, following the infiltration pathways, and tracked forward in time through engineered barriers, waste disposal regions, and the liner system. The particle movement is governed by the advection equation:

$$\frac{dx}{dt} = v_x(x,z), \qquad \frac{dz}{dt} = v_z(x,z) \qquad \text{Eq. 3.1}$$

where (x,z) represents the particle position at time t, and $v_x(x,z)$, $v_z(x,z)$ are the interpolated velocity components at that location. The velocity field is obtained from a steady-state flow simulation, ensuring consistency between flow predictions and transport pathways.

To solve this system, the project team employed explicit time integration with an adaptive time step Δt, determined based on the local velocity and grid resolution:

$$\Delta t = C \cdot min\left(\frac{\Delta x}{|v_x| + \epsilon} + \frac{\Delta z}{|v_z| + \epsilon}\right) \qquad \text{Eq. 3.2}$$

where C is a Courant-like safety factor (set as 0.1) and ϵ is s a small constant to prevent division by zero. This approach ensures that particles remain within stable velocity regions while capturing fine-scale variations in flow paths.

To ensure accurate particle tracking, the velocity field is interpolated using "RegularGridInterpolator" in Python, providing a smooth and continuous representation across the model domain. Particles are initialized at the top surface, aligning with infiltration zones to reflect natural recharge conditions. No-flow boundaries are enforced by setting velocity components to zero at impermeable barriers, preventing unphysical movement through restricted regions. Discharge locations are predefined at the sump points or the bottom of the model domain, where flow exits the system.

By computing particle trajectories and travel times, this analysis identifies preferential flow pathways, evaluates water retention zones, and examines the effects of cover and liner degradation on water movement. The results provide more insights into near-field hydrology, providing a foundation for future contaminant transport modeling and improving the assessment of long-term water flow behavior within the IDF system.

3.1.4 Results to Date

This section presents the results of flow and transport simulations conducted for the IDF. The analysis examines how infiltration, cover degradation, and waste package configurations influence moisture distribution and water movement within the system. These results provide insights into water retention zones, preferential flow paths, and travel time variability, which are critical for understanding long-term hydrological behavior and informing future assessments of contaminant transport. The following subsections detail the moisture content distribution and particle tracking results, highlighting key trends and differences across the scenarios evaluated.

3.1.4.1 Moisture Content Distribution

Moisture content distributions were analyzed across all model cases to evaluate water infiltration and redistribution within the IDF system. Figure 3.4 presents three representative cases under a uniform 3.5-mm/day infiltration rate: (a) the baseline case, where waste packages follow a structured arrangement; (b) a case with randomly placed waste packages, introducing spatial variability in waste distribution; and (c) the alternative test, which assumes full degradation of cover layers above the asphalt and concentrated discharge at the sump locations. These cases illustrate the differences in moisture accumulation and preferential flow patterns arising from variations in waste package configurations and cover integrity.

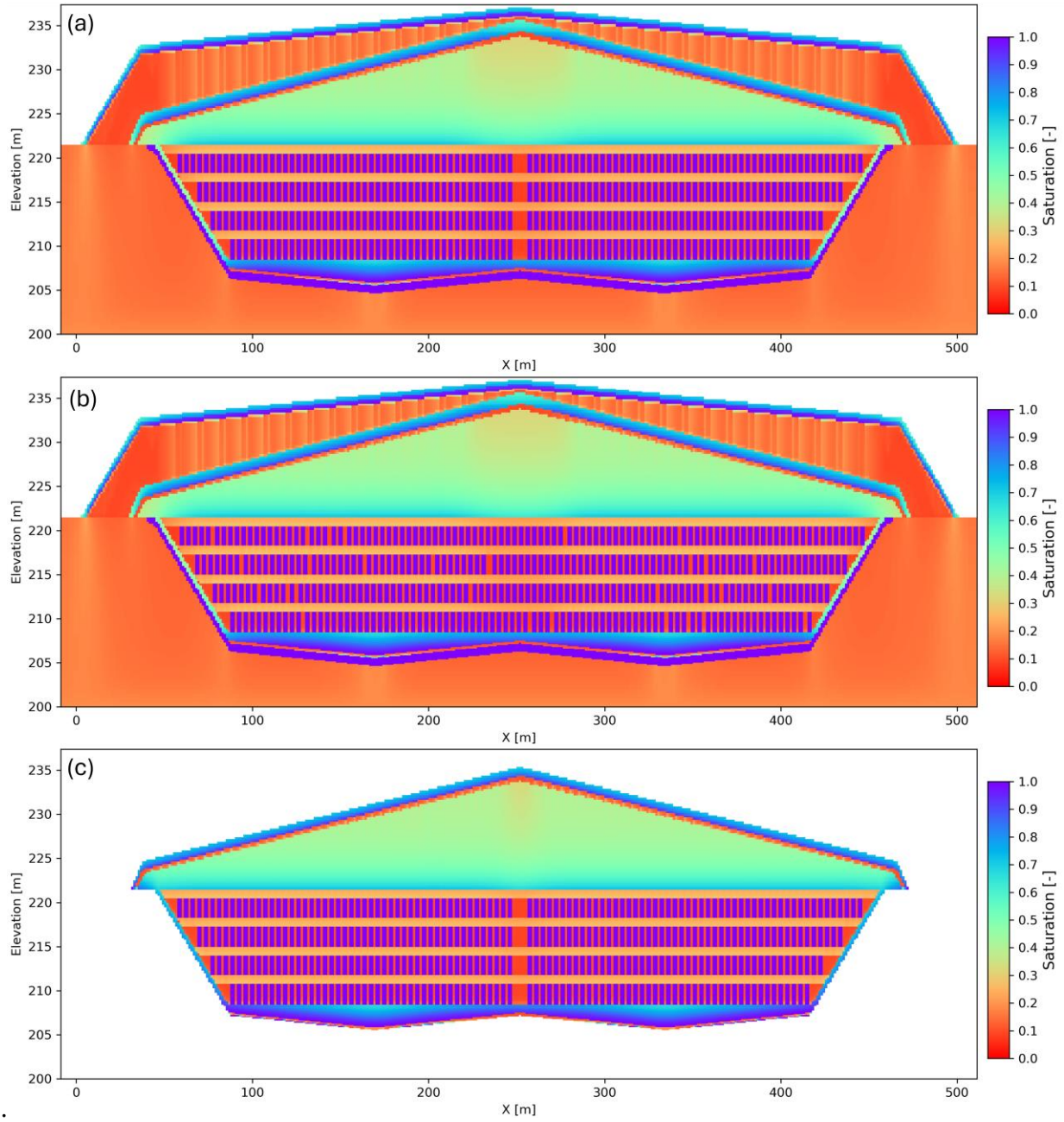

Figure 3.4. Spatial distribution of saturation after degradation of both the cover and liner for three representative model cases under a 3.5-mm/day infiltration rate through the IDF. The results are shown in a cross-section: (a) baseline case, (b) randomized waste package placement, and (c) alternative test model.

Key observations from the results include:

- Overall, the three cases exhibit a similar saturation pattern, with consistent saturation levels within the same material types across different cases.
- Saturation levels are highest within the waste containers, reflecting the low hydraulic conductivity of the waste material and higher matric suction in the waste form, which restricts water movement.

- The spatial distribution of saturation is more variable in the randomized waste package placement case compared to the baseline case. The introduction of randomized waste placement increases spatial heterogeneity, suggesting that variability in waste package configuration can influence near-field hydrology by altering localized retention and flow patterns.
- In the alternative case, the degradation of the cover and liner, combined with concentrated discharge at the sump locations, results in a more direct and uniform infiltration pattern.
- The benchmark of eSTOMP and VSF models showed consistently agreement by the impact of waste emplacement on the hydrological conditions, including water flow patterns and degree of saturation, in the IDF.

3.1.4.2 Particle Tracking Results

Particle tracking simulations were conducted for all model cases to analyze flow paths and travel times. Figure presents three representative examples under a uniform 3.5-mm/day infiltration rate: (a) the baseline structural arrangement, (b) randomized waste package configuration, and (c) the alternative test with degraded cover conditions. For the baseline and randomized waste package models, 10,483 numerical particles were introduced at the top boundary, while the alternative model used 8,902 particles due to its modified domain configuration. Particle path lines are color-coded by travel time, providing a visual comparison of flow behavior across different scenarios.

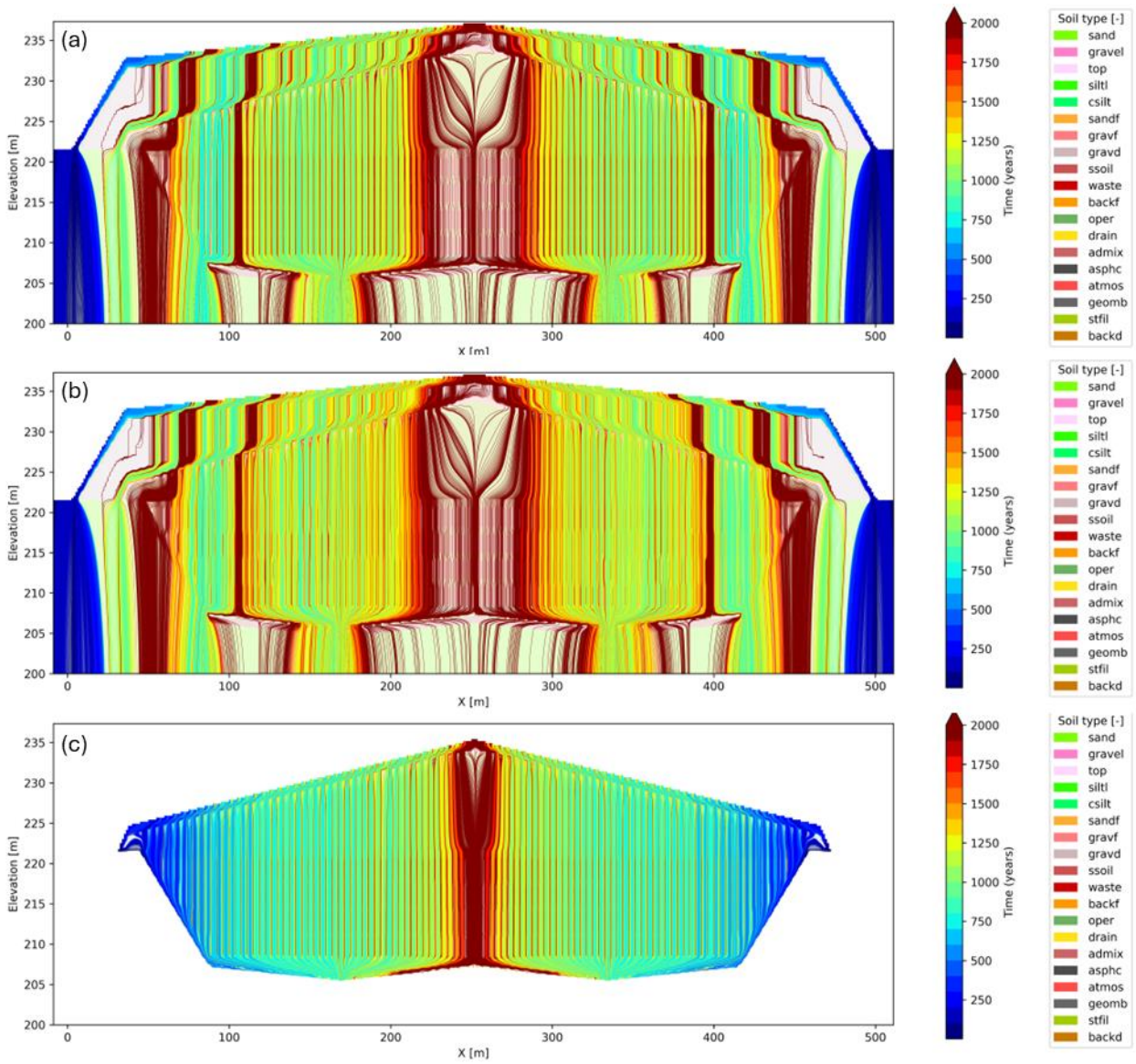

Figure 3.5. Particle tracking results for three representative model cases under a 3.5-mm/day infiltration rate through the IDF shown in a cross-scetion: (a) baseline case, (b) randomized waste package placement, and (c) alternative test model. Particle pathlines are colored by travel time, illustrating differences in water flow behavior across the three models.

Key observations from the results include:

- Travel times are generally longer in the center of the facility model, where flow pathways are more constrained.
- Particles passing through waste packages exhibit significantly longer travel times due to the low hydraulic conductivity of the waste material.
- Randomized waste package placement introduces greater flow path complexity, particularly in the central region of the domain, compared to the baseline case.
- The alternative model produces more uniform and shorter travel paths, reflecting its simpler domain configuration and more direct flow paths toward the sump locations.

- Numerical discretization artifacts in the baseline model create stepwise travel paths and localized irregularities in particle trajectories.
- The benchmarking of eSTOMP and VSF models demonstrated consistency in the spatial variation of water flow and saturation, as well as agreement on the spatial distribution of residence time in modeling the disposal conditions at the IDF.

By summarizing the travel times of particles that passed through the waste package, a probability distribution of particle travel times is obtained, as shown in Figure . The figure presents distributions for the baseline case, the randomly placed waste package case, and the alternative test model, corresponding to the three cases discussed earlier. In each panel, the shaded blue region represents the histogram of travel times, while the red line is the fitted probability density function (PDF) and the green dashed line represents the cumulative distribution function (CDF). The dashed vertical lines highlight the 10th, 50th (median), and 90th percentiles, providing a quantitative measure of travel time variability across different model configurations.

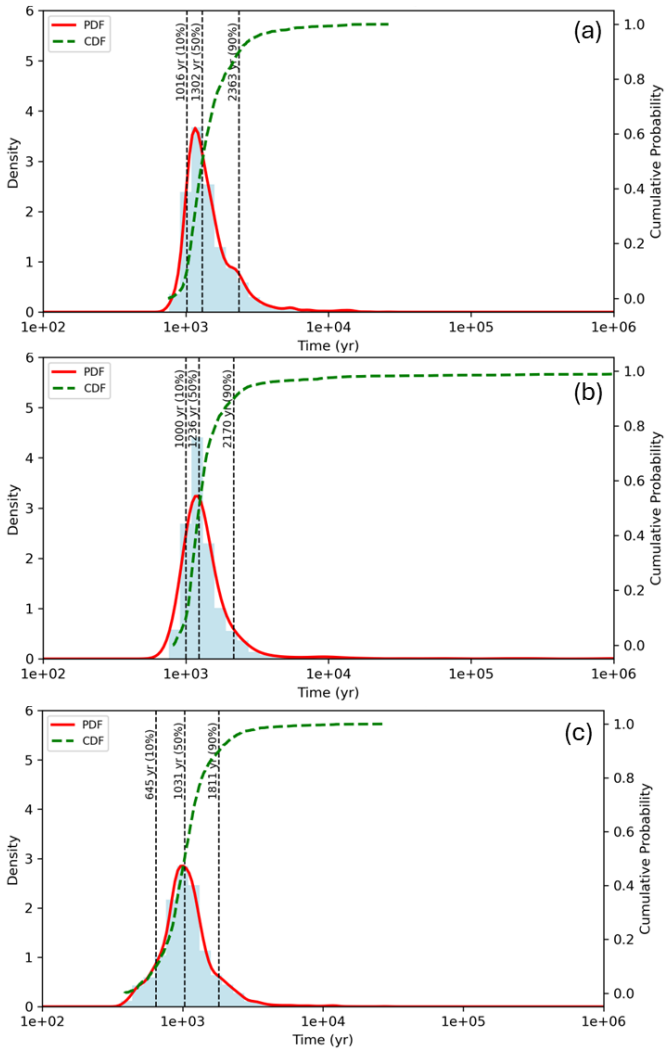

Figure 3.6. Probability distribution of particle travel times for three model cases: (a) baseline case, (b) randomized waste package placement, and (c) alternative conceptual model. The shaded blue region represents the histogram of particle travel times, while the red line is the fitted

probability density function (PDF) and the green dashed line represents the cumulative distribution function (CDF). The dashed vertical lines highlight the 10th, 50th (median), and 90th percentiles, providing insight into the distribution spread and variability across different model configurations.

The alternative test model exhibits a more compact and left-skewed distribution, indicating shorter and more uniform travel times, while the baseline and randomized placement cases show broader distributions with extended tails, suggesting greater heterogeneity and longer retention times. These distributions serve as a basis for further comparative analysis, with a summary of all results provided in Table .

Table 3.3. Summary of particle travel time percentiles for different model cases.

Model Case	Infiltration Rate (mm/yr)	10th Percentile	25th Percentile	50th Percentile (Median)	75th Percentile	90th Percentile
Base case	0.9	3,985	5421	6,955	125,52	78,368
	1.7	2,041	2,270	2,757	4,424	9,096
	3.5	1,016	1,115	1,302	1,657	2,363
	5.0	724	803	937	1,191	1,641
Randomized waste package placement case	0.9	4,049-4,208	4,992-5,297	6,330-6,589	11,020-12,319	79,827-93,125
	1.7	1,991-2,044	2,215-2,256	2,518-2,585	3,393-3,564	7,063-8,347
	3.5	985-10,09	1,085-1,102	1,220-1,239	1,457-1,507	2,097-2,195
	5.0	711-726	791-802	885-902	1,043-1,074	1,403-1,483
Alternative model case	3.5	645	847	1,031	1,285	1,811

These results highlight the travel times of soil moisture within the IDF, being on the order of 1,000 years from top to bottom. This timescale is consistent with variably saturated flow modeling developed by the UCF team, who conducted particle tracking simulations at several locations in a model similar to the alternative case in this study. In their simulations, particles placed near the middle of the slope, approximately 150 m in the x-direction in the eSTOMP model domain, reached the leachate sump in approximately 1,111 years. Correspondingly, the simulation from the alternative case in this study yielded a median travel time of 1,051 years. These two models show strong agreement, reinforcing the reliability of the predicted travel times. These timescales will introduce evaluations of flow times vs. reaction times of key process drivers in the *Hanford Grout Modeling Framework*.

3.1.5 Path Forward and Integration

- ***Subtask 2.1.1:*** The travel time estimation provides a fundamental understanding of moisture transport timescales in the near-field hydrology model. In the second year, collaboration with the reactive transport modeling team will integrate reaction and transport timescales to identify the limiting factors in waste package degradation and reactions. Parameters such as Damköhler numbers will be derived to evaluate the relative importance of reaction kinetics and transport processes in controlling waste package behavior. This will allow calculations of distribution of performance in the disposal facility
- ***Subtask 2.1.2:*** The results indicate that the current PA model domain may still be too coarse to fully capture the hydraulic property contrasts between waste packages and backfill materials. This limitation could lead to an underestimation of travel times and overly conservative transport predictions. To address this, model resolution tests can be conducted, or small-scale, high-resolution

particle tracking simulations can be performed to refine the estimates and improve the representation of flow dynamics in the near-field system. This will include updating, if needed, mass transfer coefficients in backfill and local equilibrium impacts.

- ***Subtask 2.1.3:*** As highlighted in recent studies, the pre-burial and pre-closure conditions can have the most significant impacts on changes to the condition of grout waste forms (Zheng et al. 2022a). This task will develop moisture transport models for these timeframes to allow improved representation of grout prior to closure.

3.2 Theme 2 Task 2: Integration of Variably Saturated Flow Modeling to Field Experimental Data

3.2.1 Team Members

Jiannan Chen (UCF)

3.2.2 Background

This component of the overall effort in Theme 2 was focused on preparing VSF models to replicate moisture transport in a field lysimeter test currently ongoing at Hanford (Meyer et al. 2024). The lysimeter test is providing crucial data to verify predictive corrosion models for glass and grout waste forms. This task is providing a tool to ensure accuracy of all conditions within the lysimeter in future benchmarking studies. This task is structured around two main objectives: (1) understand the hydrological behavior of the backfill surrounding the waste forms by developing and calibrating numerical models and (2) establish hydrological boundary conditions for modeling contaminant release. These conditions are crucial for simulating the release of contaminants from both cementitious and glass waste forms.

Field tests on the hydrological behavior of the IDF backfill provide essential data on the early-stage performance of waste form materials, including key properties such as leaching rates and temperature. However, evaluating the large-scale and long-term behavior of the IDF requires numerical simulations. Sensitivity analyses are necessary to predict IDF performance over extended disposal timeframes that far exceed those that can be performed experimentally. Benchmarking the model against lysimeter field tests will improve the understanding of soil hydrological behavior, enhancing the accuracy of material properties and boundary conditions used for long-term, large-scale predictions. Ultimately, this task will contribute to the long-term environmental management of the IDF and support validation of predictions made using the *Hanford Grout Modeling Framework*.

3.2.2.1 Summary of Field Test Setup and Methodology of Hanford Lysimeters

The field lysimeter test has been in progress at the IDF Test Platform near the Hanford Site's 200 West Area since 2019 (Meyer et al. 2024). This facility comprises 14 cylindrical drainage lysimeters, each 2 m in diameter and 3 m in height, alongside an underground gallery that provides lateral access to the lysimeters. The lysimeters are categorized based on the type of waste they contain and the rate of irrigation applied. Specifically, three lysimeters are filled with cementitious waste forms, and three others contain glass waste forms. Two lysimeters, devoid of waste, function as controls. An automated irrigation system controls the water flow within these lysimeters. The test targets three irrigation rates: 50, 20, and 5 cm/yr (Figure 3.7).

Pan lysimeters are installed beneath each waste form to collect the water that drains through the soil. Drainage is also collected at the base of each lysimeter through a 0.3-meter layer of primarily pea gravel, channeled via a pipeline. Because the control lysimeters do not contain waste forms, they lack pan

lysimeters. The backfill soil was sourced from the IDF excavated soil. In the lysimeters containing cementitious waste forms (15 cm in diameter and 19 cm in height; 10 cm in diameter and 19 cm in height) and glass waste forms (8 cm in diameter and 15 cm in height), these materials are positioned at depths of 1.25 and 2 m below the lysimeter surface, respectively.

To evaluate the spatial-temporal hydrological and thermal behaviors of the backfill soils, a sensor network has been integrated into the lysimeters. This network records moisture content (via neutron probe testing), soil suction (via tensiometers), drainage (via tipping buckets gauge), and soil temperature (via thermistors). The soil surface is maintained approximately 25 cm below the top of each lysimeter to ensure adequate space for irrigation. A fiberglass cover has been installed atop the lysimeters to minimize evaporation, which has not yet been factored into the modeling.

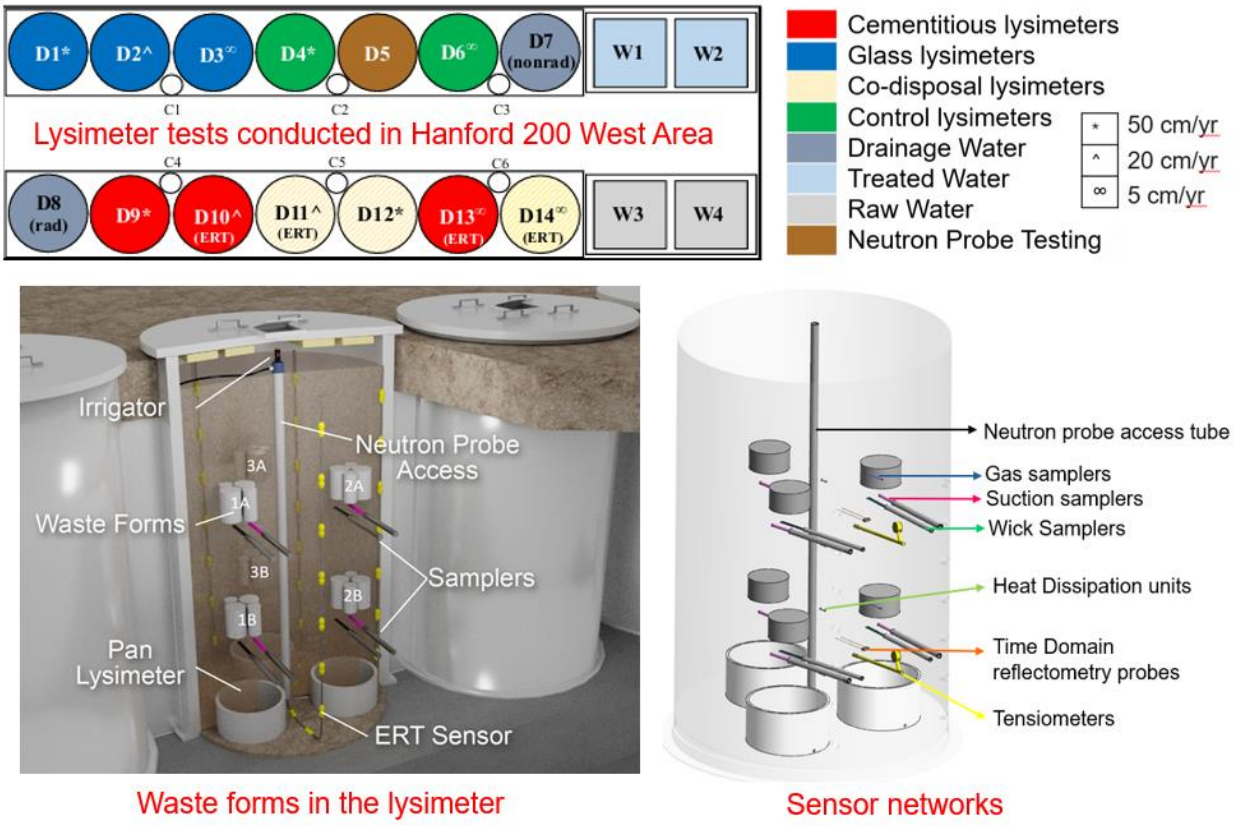

Figure 3.7. Lysimeter configurations at the IDF Test Platform and the detailed waste forms and sensor network in the lysimeter. Co-disposal lysimeters were not installed.

3.2.3 Technical Approach

The primary goal of implementing the UCF/CRESP benchmark model for the lysimeter field test is to generate field-scale hydrological parameters that are pertinent to the long-term performance of waste forms while minimizing uncertainties.

To meet these objectives, a 3-D representation of the lysimeter field test was created using the SEEP/W code (Seequent, Calgary, Alberta, Canada) to model variably saturated flow within the lysimeter. The primary method for modeling moisture transport in soil involves assessing liquid transport driven by water pressure gradients, which follows Richard's equation (Richards 1931) as shown in Eq. 3.3.

Additionally, the soil-water characteristic curve, as proposed by van Genuchten (1980) and outlined in Eq. 3.4, provides the necessary hydraulic properties for calculating unsaturated hydraulic conductivity, detailed in Eq. 3.5.

$$\frac{\partial \theta}{\partial t} = \frac{\partial}{\partial z}[K_w(\varphi)(\partial h/\partial z + 1)] \quad \text{Eq. 3.3}$$

$$\theta_w = \theta_r + \frac{\theta_s - \theta_r}{[1+(\alpha'\varphi)^n]^m} \quad \text{Eq. 3.4}$$

$$K(\varphi) = K_{sat} + \frac{\{1 - (\alpha'\varphi)^{n-1}[1 + (\alpha'\varphi)^n]^{-m}\}^2}{[1 + (\alpha'\varphi)^n]^{m/2}} \quad \text{Eq. 3.5}$$

$$\frac{\partial \theta}{\partial t} = \frac{\partial}{\partial z}[K_w(\varphi)(\partial h/\partial z + 1)] \quad \text{Eq. 3.6}$$

where, $K(\varphi)$ is the unsaturated hydraulic conductivity, θ_r is the residual water content (m^3/m^3), θ_s is the saturated water content (m^3/m^3), K_{sat} is the saturated hydraulic conductivity (m/s), and α, n, and m are the fitting parameters related to the van Genuchten soil water characteristic curve.

The irrigation schedule, hydraulic properties of the backfill, backfill density, volumetric water content, soil temperature, soil suction, sensor outputs, and drainage data from the lysimeters collected from 2021 to 2024 were used to model the lysimeters and benchmark the results. Table 3.4 provides a comprehensive summary of the data available for model calibration, which includes measurements of volumetric water content, saturated hydraulic conductivity, dry bulk density, porosity, van Genuchten parameters, drainage, matric suction, soil temperature, and particle size distribution.

Table 3.4. Current data inventory for lysimeter modeling.

Data		2021	2022	2023	2024
Irrigation	Rate	50 cm/yr, 20 cm/yr, and 5 cm/yr			
	Frequency	1 hour per 7-day week (50 cm/yr and 20 cm/yr) 1 hour every two weeks (5 cm/yr)			
	Date and Time	N/A			
Volumetric water content		Quarterly measurements (neutron probe)			
Material properties	Hydrological	Obtained from bulk and repacked samples			
	Density	Obtained from core samples			
	Thermal	Estimated based on mineralogy and porosity			
Drainage		N/A			Hourly
Temperature		N/A		Hourly	
Other data	Suction	N/A		Hourly	
	TDR	N/A		Hourly	

This dataset was sourced from a PNNL report on the lysimeter study (Meyer et al. 2024), with supplemental data from 2024 provided by PNNL which will be available in the 2025 revision of Meyer et al (2024). The measurements of drainage, soil temperature, and soil suction are continuous, while the volumetric water content is assessed quarterly (in February, May, August, and November) using a neutron probe. This approach ensures a robust dataset for calibrating and validating the hydrological models.

3.2.3.1 Model Domains, Material Properties, and Boundary Conditions

The geometry and hydraulic properties of the backfill and waste forms within the lysimeters were instrumental in constructing the 3-D numerical model. This model was calibrated using data from the control lysimeter D4, which operates under a 50-cm/yr irrigation rate. This calibration process helped identify potential field uncertainties. Subsequent modeling efforts incorporated the waste forms to analyze water flow patterns around the waste forms. The lysimeters are cylindrical, measuring 2 m in diameter and 3 m in height. Their bottom drainage consists of a 0.3-meter-thick layer, which includes a 1-in. sand layer topped by a 1-in. pea gravel layer. The initial compaction density and volumetric water content of the compacted backfill, essential for establishing the initial conditions of the model, were derived from the lysimeter study report (Meyer et al. 2024). Core samples used in the calibration were obtained from depths of 65, 148, and 242 cm from the lysimeter surface, as shown in Figure .

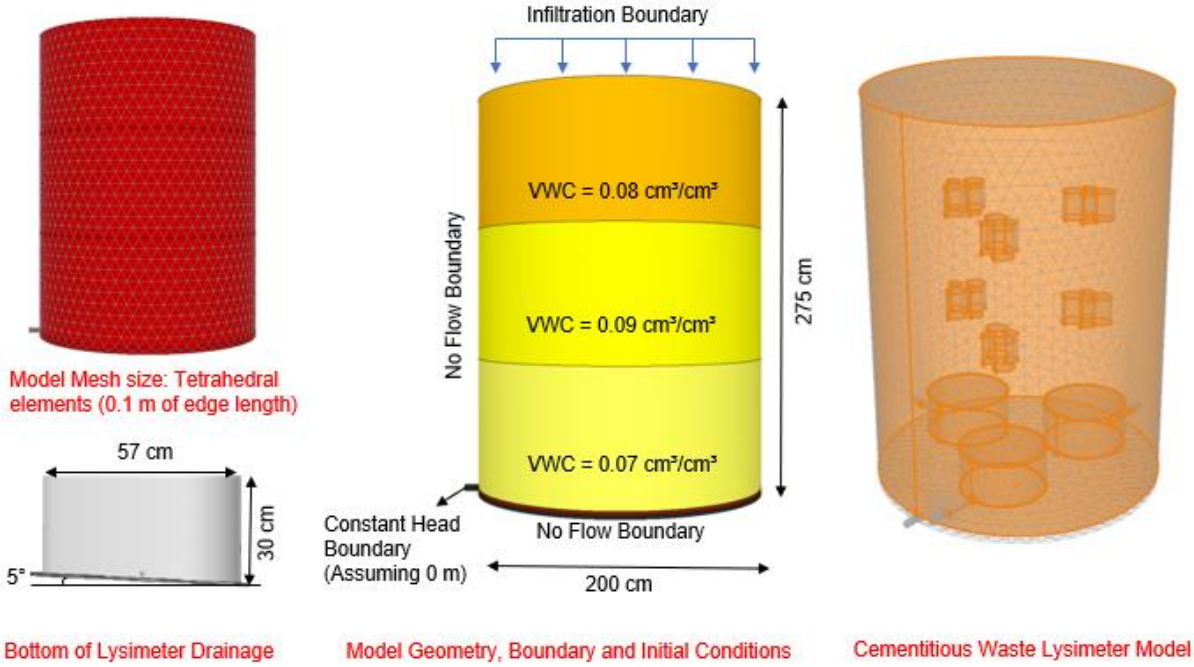

Figure 3.8. Geometry, boundary, and initial conditions of the 3-D lysimeter model.

An evenly distributed infiltration boundary was applied at the top of the model to simulate irrigation at a rate of 50 cm/yr, administered weekly based on the established irrigation frequency. The hydraulic boundary condition at the model's base was set to a constant head at the drainage pipe, facilitating effective drainage at the bottom of the lysimeter while maintaining retained moisture near the drainage layer. A no-flow boundary condition was designated for the vertical edges and the base of the model to mimic the impermeable nature of the container material. Figure illustrates the model's geometry, boundary conditions, and initial conditions.

The hydrological properties of the backfill materials and drainage layers were based on the IDF PA (USDOE 2018), as detailed in Table 3.5. This table includes the saturated hydraulic conductivity, van Genuchten parameters for soil-water characteristic curves, unsaturated hydraulic conductivity, and porosity of the IDF materials, as documented in the IDF PA (USDOE 2019). Although particle size, moisture content, bulk density, and particle size distribution were determined from core samples, the saturated and unsaturated hydraulic properties were derived from remolded bulk samples. Variations in the hydraulic properties of the backfill material may contribute to model uncertainties. Figure 3.9

compares the hydraulic properties of the remolded samples to those specified in the IDF PA (USDOE 2019). The properties measured from remolded materials are highlighted in the red-shaded area, indicating a relatively lower porosity but comparable hydraulic conductivity at various degrees of saturation.

For the numerical modeling, properties of loosely packed (LP) backfill were used to benchmark against the field results. Additionally, modeling with densely packed (DP) backfill was conducted to capture uncertainties associated with material properties.

Table 3.5. Physical and hydrological properties of backfill and drainage materials.

	Hydraulic Parameter	van Genuchten Parameters			
	K_{sat} (m/s)	θ_s	θ_r	α (kPa)	n
Densely compacted backfill (DP)[(a)]	4.9E-05	0.387	0.03	1.54	1.7
Loosely compacted backfill (LP) [(a)]	1.7E-04	0.443	0.03	1.75	2.8
Coarse sand[(b)]	1.10E-01	0.420	0	107.8	9.3
Pea gravel[(c)]	2.80E-01	0.420	0	107.8	1.4

(a) Meyer et al. (2004)
(b) Sanford et al. (1995)
(c) Yeh and Harvey (1990)

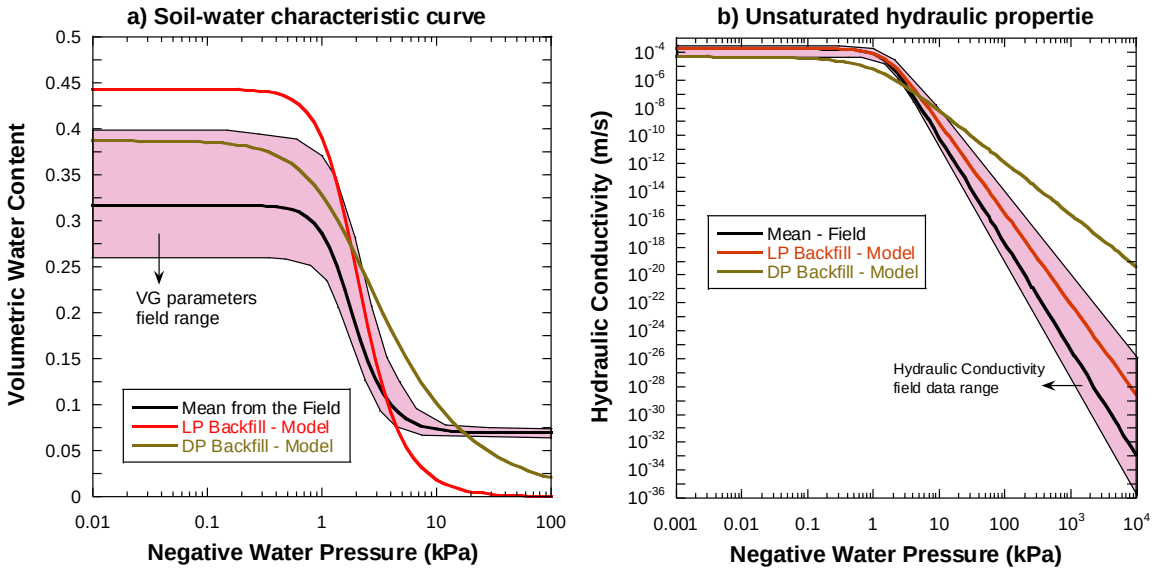

Figure 3.9. Soil-water characteristic curve and unsaturated hydraulic conductivity function of simulated backfill compared with field range curves obtained from the remolded samples.

Additional mechanisms influencing the field hydrology, such as the hysteresis of soil-waste retention and temperature oscillations, have been incorporated into the model. Figure 3.10 displays the hysteresis of the soil-water retention, which illustrates the drying and wetting cycles, alongside the measured soil temperatures and temperature data from the Hanford Meteorological Station. The hysteresis curve follows the methodology outlined by Šimůnek et al. (2006), which assumes that the van Genuchten parameter α during drying is twice as high as during wetting.

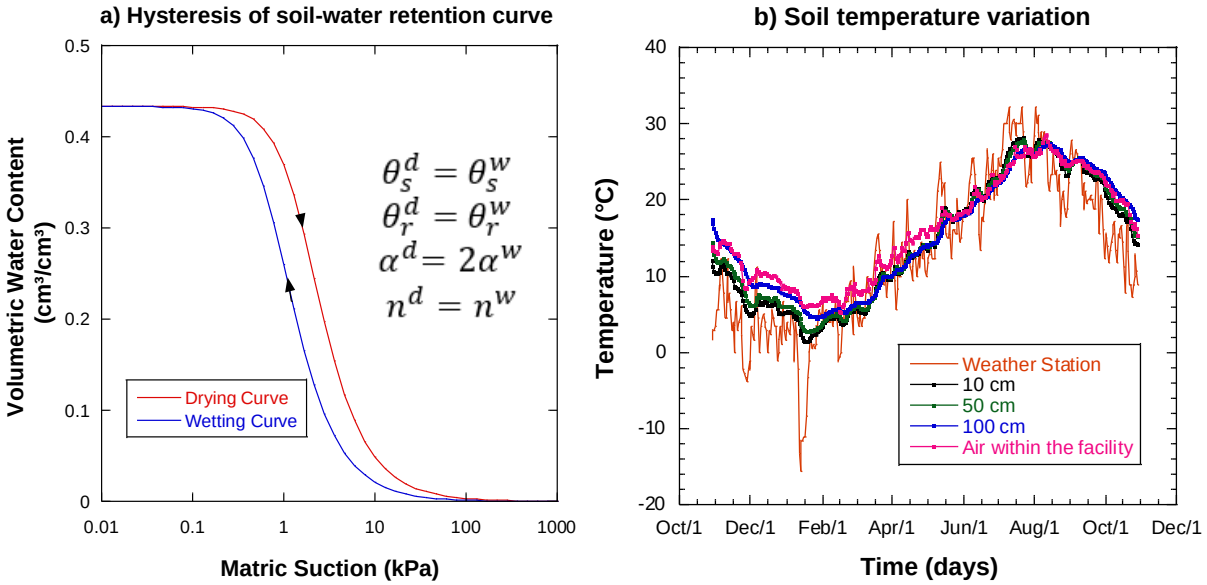

Figure 3.10. The (a) hysteresis of soil-water retention curve and (b) soil temperature variation with time and soil depth of the lysimeter ground surface. The air temperature within the lysimeter facility and the temperature measured at the Hanford Meteorological Station for the years 2023 – 2024 are also included.

3.2.4 Results to Date

3.2.4.1 Water Balance of the Field Lysimeters

The water balance evaluations of the lysimeters were conducted by integrating the irrigation rate, water storage, and drainage data. Evaluations focused on lysimeters irrigated at a rate of 50 cm/yr, aiming to assess potential evaporation loss near the lysimeter surface and the infiltration rate through the lysimeter. Based on the relatively low drainage observed, significant evaporation or insufficient irrigation from lysimeters with 20- and 5-cm/yr irrigation rates was postulated; these were excluded from the current model-field benchmarking.

The analysis included lysimeters D1 (containing glass waste forms), D4 (control), and D9 (containing cementitious waste forms), all operating at the 50-cm/yr irrigation rate. Based on drainage data collected from March to December 2024, the cumulative drainage from the bottom of the lysimeter ranged from 24 to 31 cm, equivalent to 765 to 988 L of infiltration over this period (Figure a). An increase in water storage up to 9 cm was also observed during this period over depth. Figure b shows the increase in water storage in the soil of the control lysimeter D4 from February (non-irrigation period) to November (end of the irrigation period), calculated at 4 cm (126 L). The estimated loss from the irrigated water totaled 456 L, representing 30% of the irrigated water. However, several factors introduce uncertainties into the water balance calculations, including pump accuracy, non-uniform wetting, variations in void ratio due to the compaction of the backfills, and evaporation. Despite these uncertainties, the calculated annual infiltration rate for the lysimeter, based on the drainage data, stands at approximately 32 cm/yr.

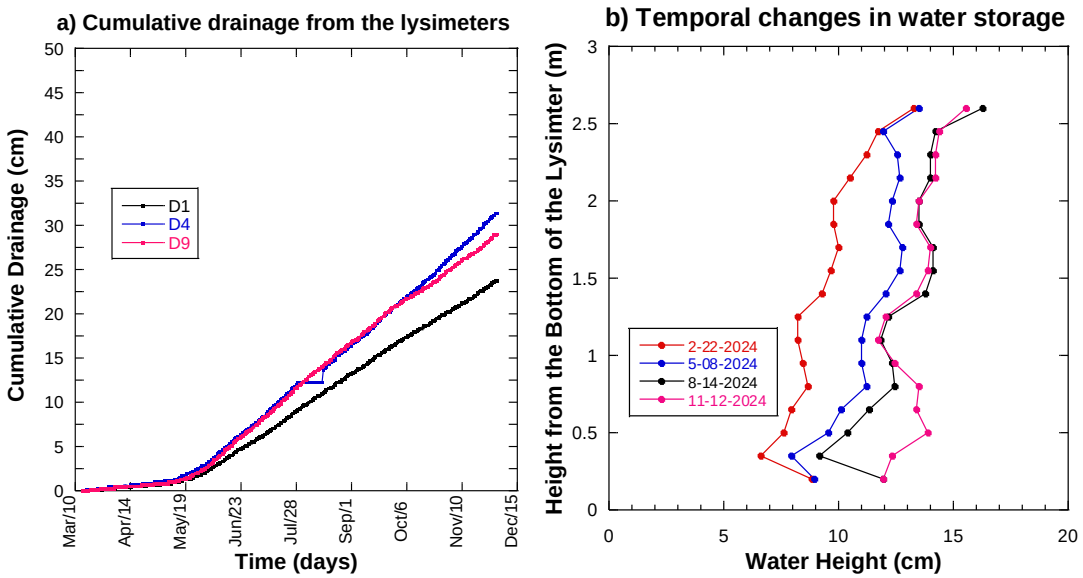

Figure 3.11. (a) Cumulative drainage of the lysimeters with 50 cm/yr irrigation and (b) temporal changes in the water storage in the lysimeter from March to November 2024.

3.2.4.2 Model Benchmarking with the Lysimeter Data

The UCF/CRESP model results for volumetric water content using LP and HP backfills were compared with data from the control lysimeter (D4). As illustrated in Figure 3.12, the modeled and field water profiles generally align well in trend across depth. Results using LP backfill showed an average discrepancy of 36% compared to all field measurements, except for the data recorded on April 22, 2021. Nonetheless, both modeled and field values for volumetric water content typically ranged between 0.05 and 0.12 cm^3/cm^3.

The backfill density significantly influences the volumetric water contents, underscoring that the degree of compaction is a critical factor affecting the hydrological behaviors in the backfill. This is particularly evident in the fitting parameters of the van Genuchten curve and the saturated hydraulic conductivity. Notably, a minor variation between LP and HP backfill can alter the soil volumetric water content profile. Overall, the HP backfill produced a soil profile that was consistently wetter than the field measurements. Conversely, the model using LP backfill aligned more closely with the field data, although further refinements are needed based on the mean-field hydraulic properties detailed in Section 3.2.4.1.

Additionally, the modeled drainage consistently exceeded that observed from the field lysimeter over time. Several factors may contribute to this discrepancy: (1) the model did not account for evaporation from the lysimeter surface; (2) the assumed 50 cm/yr of irrigation as constant infiltration throughout the year did not consider pump accuracy; and (3) the observed bottom drain was not consistently wet, particularly during non-irrigation periods. For the next UCF/CRESP model revision in Year 2, the calculated infiltration rate will be incorporated and boundary conditions will be adjusted to better match the observed drainage data.

The volumetric water content profile for April 2022 underscores the importance of measurement timing. On this specific day, a visible wetting front was present in the shallow soil layer of the lysimeter, contrasting with other dates where the wetting front appeared deeper. This variability can be attributed to the non-constant irrigation schedule and irregular measurement intervals. If measurements are taken shortly after irrigation, the shallow soil layers may present as wetter compared to the rest of the lysimeter.

Because the precise timing of irrigation and measurement was not documented, the modeling for the specified day was calibrated to best match the observed results.

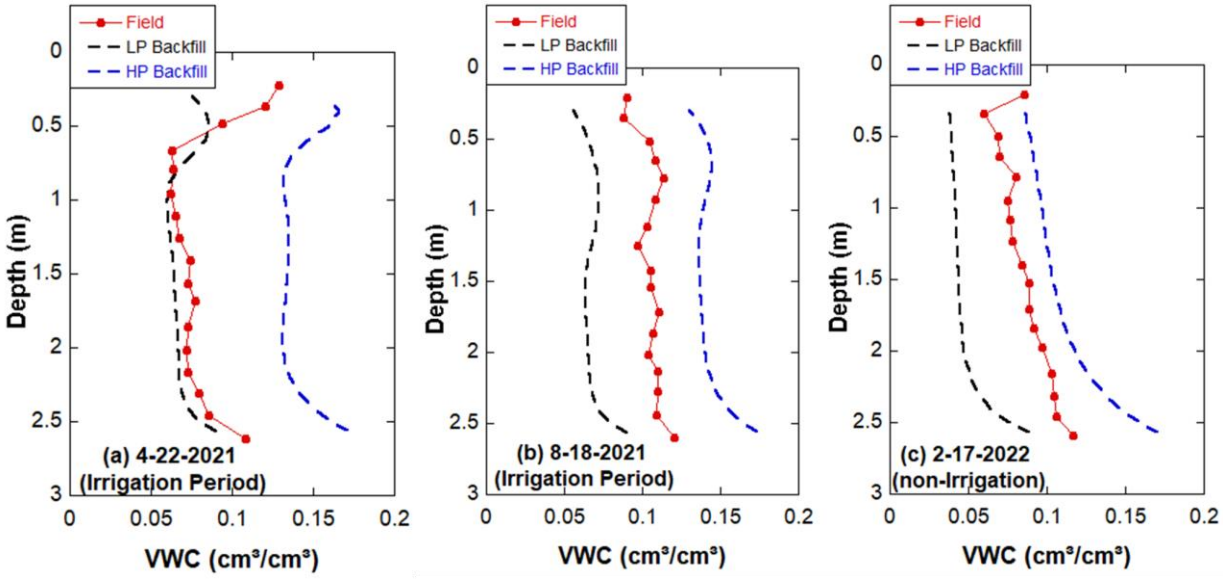

Figure 3.12. Comparison of the models with two backfills (i.e., LP (black) and HP(blue)) during irrigation and non-irrigation periods measured in the field lysimeter test (red).

3.2.4.3 Impact of Temperature and Hysteresis on Modeling Results

To evaluate the impact of temperature fluctuations and soil-water retention hysteresis on modeling results, both factors were integrated into the UCF/CRESP model and compared with simulations that excluded them. The current assessment indicates that differences in volumetric water content profiles with and without temperature and hysteresis effects are minimal in the backfill, particularly beyond the 2.2-m depth, where discrepancies remain within 5% (Figure 3.13). However, hysteresis significantly influences volumetric water content near the bottom drainage, increasing water content in a manner consistent with field observations. Overall, hydraulic properties – including density, porosity, hydraulic conductivity, and soil-water retention – are the primary factors affecting volumetric water content, while hysteresis has only a localized impact near the drain. Given these findings, future Year 2 modeling efforts can simplify simulations by omitting temperature effects, if applicable, to conserve computational resources. Instead, the focus should be on accurately estimating and applying backfill hydraulic properties for improved modeling accuracy.

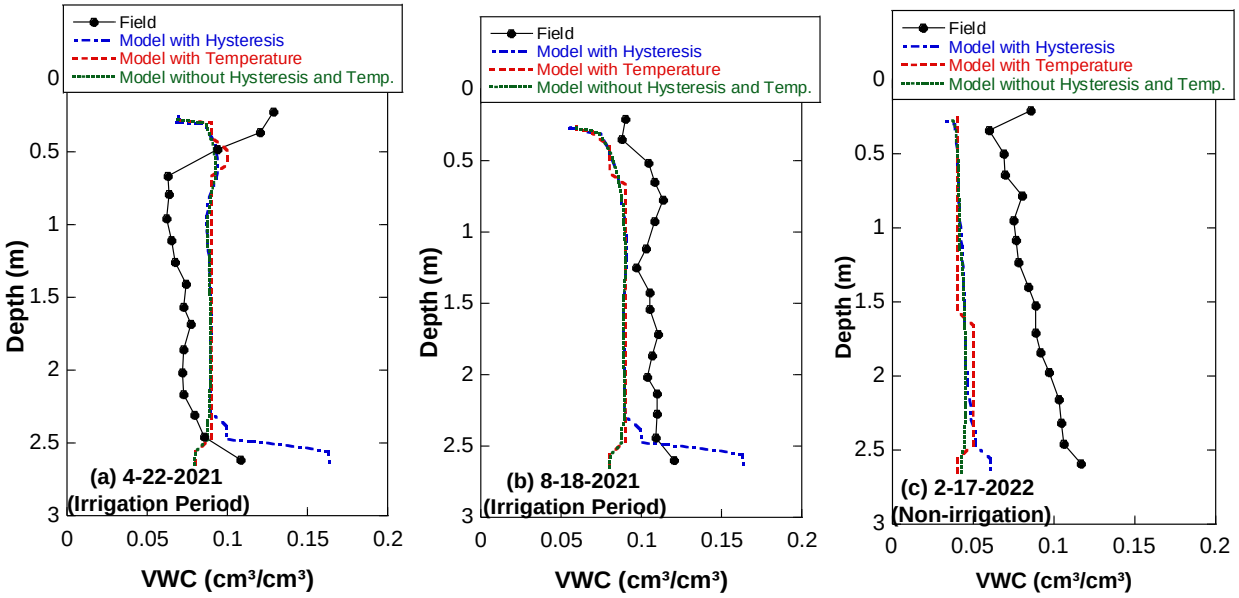

Figure 3.13. Comparison of modeling results incorporating soil temperature variation and hysteresis on three selected days representing irrigation and non-irrigation periods and compared against measured field lysimeter data (black).

3.2.5 Path Forward and Integration

Year 1 saw the successful construction of a moisture tracking model in VSF for the lysimeter tests. Based on the results from Year 1, the proposed agenda for Year 2 includes the following subtasks:

- ***Subtask 2.2.1 – Model Update and Refinement:*** Update the UCF/CRESP model by incorporating revised hydraulic properties and boundary conditions, specifically infiltration and drainage boundaries. These updates aim to enhance model accuracy and reduce discrepancies with field measurements. This applies to both the lysimeter model and supporting IDF model
- ***Subtask 2.2.2 – 3-D Modeling of Lysimeters with Cementitious Waste Forms:*** Execute 3-D models on lysimeters containing cementitious waste forms, incorporating the aforementioned updates based on field observations. These models are intended to derive critical backfill hydrological parameters, such as water saturation, flux, and water residence time near the waste forms. This will also support the establishment of hydraulic boundaries for mass transfer modeling under both pre- and post-closure conditions. An uncertainty analysis will be conducted to address variations in backfill properties, sensor accuracy, and other factors. This task would link with other mechanistic tasks to predict release from the grout waste forms and verify against experimental data.
- ***Subtask 2.2.3 – Localized Modeling Around Waste Packages/Tank Closure:*** This task will build on existing VSF models that describe spatial transport models around grout materials. These will be integrated into eSTOMP as part of the *Hanford Grout Modeling Framework*.

4.0 Theme 3: Dynamic Modeling of Processes Impacting Contaminant and Radionuclide Behavior

4.1 Theme 3 Task 1: Application of Geochemical Speciation Modeling to Other Hanford Grout Examples

4.1.1 Team Members

Chen Gruber (VU), Miroslava Peterson (PNNL), Joelle Reiser (PNNL), Rodney Skeen (H2C), Usama Zaher (H2C)

4.1.2 Background

Previously, a geochemical speciation model for grout was evaluated using a Hanford-specific test case of a Cast Stone (CS) formulation prepared with a liquid secondary waste simulant, Figure 4.1 (Chen et al. 2021). This previous work showed that the geochemical speciation model was able to replicate the release behavior of a multitude of elements from the grout, including Tc-99 (Chen et al. 2021). A geochemical speciation component to the *Hanford Grout Modeling Framework* will likely improve the fidelity of contaminant releases, but further assessment against grout datasets is required. This prior developmental work will be expanded to assess the predictive capability of the geochemical speciation model against other Hanford grout datasets. The approach uses leaching data from U.S. Environmental Protection Agency (EPA) Method 1313 (pH dependent release, *Liquid-Solid Partitioning as a Function of Extract pH Using a Parallel Batch Extraction Procedure*) and EPA Method 1315 (semi-dynamic leaching, *Mass Transfer Rates of Constituents in Monolithic or Compacted Granular Materials Using a Semi-Dynamic Tank Leaching Procedure*) to calibrate mineral sets and a speciation model to determine the chemical state and subsequent leaching behavior.

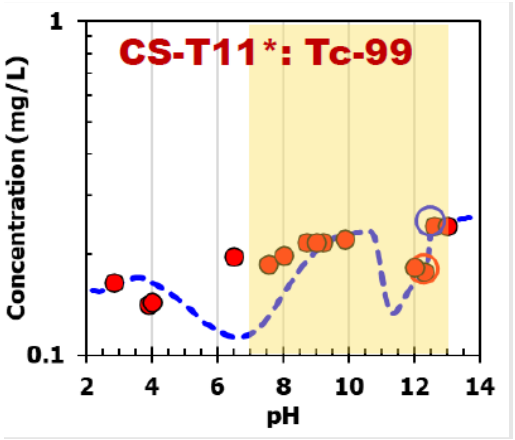

Figure 4.1. Example of the predictive capability of the geochemical speciation model for the release of Tc-99 from grout.

The datasets evaluated will be those reported by Um et al. (2016), who evaluated various grout formulations for the immobilization of secondary liquid wastes at Hanford. The reason for selecting three formulations from this work (T3, T6, T11) was to represent two additional formulations with the same simulant as the original CS data. Most importantly, the Tc-99 leaching behavior of the T3 and T6 samples is unique due to the inclusion of hydrated lime in the formulations. These hydrated-lime-containing formulations provided the lowest Tc-99 releases measured to date from a liquid waste grout (Bourchy et al. 2022).

The overall goal of this task is to develop a component of the *Hanford Grout Modeling Framework* in which speciation information of specific contaminants and radionuclides can be provided dependent on the spatially evolving conditions within a waste form. This information can be retrieved from the geochemical speciation modeling software using a call-out approach similar to that being developed in Theme 1 Task 1 (Section 2.1). This is a significant upgrade from the current approach of using a static,

experimentally estimated distribution coefficient (K_d) for specific contaminants in the grout modeling at Hanford.

4.1.3 Technical Approach

4.1.3.1 Objective

This PNNL and CRESP collaboration is focused on understanding the strength and limitations of eSTOMP and LeachXS/ORCHESTRA (LXO) as platforms for providing geochemical speciation models in reactive transport simulations. To evaluate these impediments to construction of the *Hanford Grout Modeling Framework*, information from the geochemical speciation models in LXO is being targeted for incorporation into eSTOMP. To meet this functionality goal, the specific targets of the first year of effort were:

1. Use LXO reactive transport geochemical speciation models to simulate EPA Method 1313 (EPA 2017a) and EPA Method 1315 (EPA 2017b) results for the T3, T6, and T11 secondary waste grout samples (Um et al. 2016), including development of mineral reaction sets describing the liquid to solid partitioning results.
2. Calibrate a tortuosity factor using EPA Method 1315 results for the T3, T6, and T11 samples using reactive transport geochemical speciation modeling.
3. Simulate Tc geochemical speciation and observed diffusivity for T3, T6, and T11 samples.

4.1.3.2 Sample Preparation

Three mix designs were used for performance testing of grouted liquid secondary waste. Formulations T3 and T6 used the same mix ratios (20 wt% lime, 35 wt% OPC, and 45 wt% BFS) at water-to-binder ratios of 0.5 and 0.6, respectively. Mix T11 used the same three reagents as CS from the original work, but at a different ratio of 20 wt% OPC, 35 wt% FA and 45 wt% BFS. These mix designs were spiked with Tc-99 (Table 4.1). Xypex (Admix C-500, Xypex Chemical Corp) was added to reduce the porosity of the cured grout. Table presents the initial chemical makeup of the grouts measured with XRD.

Table 4.1. Liquid secondary waste grout mix designs (Um et al. 2016).

Test #	Simulant[(a)] (g)	Water-to-Dry-Mix Ratio	Dry Blend Addition[(b)]	Dry Materials	Admix[(c)]	WRA[(d)]	TC-99[(a)] (µg/L)
3	WTP (711.6)	0.5	20%, 35%, 45%	HL, OPC, BFS	--	3,030	14,800
6	WTP (853.9)	0.6	20%, 35%, 45%	HL, OPC, BFS	--	3,030	15,000
11	WTP (853.9)	0.6	20%, 35%, 45%	OPC, FA, BFS	Xypex	3,030	15,100

(a) See Table 3.2 in Um et al. (2016) for simulant compositions. Simulant mass (gram) used is shown in parenthesis.
(b) The three dry blend materials were mixed by placing the dry ingredients into a single plastic bag and manipulating the bag until the dry mixture appeared to be homogeneous.
(c) Xypex was used as additional admixture based on 5 wt% of dry mix.
(d) Water-reducing additive (WRA): MG 3030 was used to enhance the cement rheology based on 0.6 mL of MG 3030 per 100 g of dry mix.
(e) Tc-99 concentration measured in each simulant before mixing with dry ingredients.
HL = hydrated lime; total dry materials mass is 1,167 g; WTP = Waste Treatment and Immobilization Plant.

Table 4.2. Moisture content, dry solids fraction, and XRD analysis for mineral content (Um et al. 2016).

Test #	MC (%)	Dry Solids Fraction	XRD Analyses[(a)] (wt%)						
			Ettringite	Portlandite	Calcite	Larnite	Hydrocalumite	Quartz	Amorphous
3	25.14	0.749	14	11	6.8	4.4	--	--	64
6	29.74	0.703	17	9.7	5.4	4.5	--	--	63
11	30.44	0.696	15	--	4.5	4.1	--	2.0	75

(a) Chemical formulas of minerals: ettringite [Ca6Al2(SO4)3(OH)12•26H2O], portlandite [Ca(OH)2], calcite [CaCl2], larnite [Ca2SiO4], hydrocalumite [Ca4Al2(OH)12(OH)2•6H2O)], and quartz [SiO2]
MC = moisture content

4.1.3.3 EPA Method 1313

Um et al. (2016) provide a detailed description of the EPA Method 1313 tests done for the grout formulations T3, T6, and T11 hydrated lime liquid secondary waste grout samples. In summary, T3, T6, and T11 secondary waste grout samples were characterized using EPA Method 1313. Eluate solutions were prepared with a final target pH ranging from < 2 to 13 using particle-size reduced subsamples of test materials to approach solid-liquid equilibrium in the test. For each material (T3, T6, and T11), a set of parallel batch extractions of a solid material at specified end-point pH conditions were carried out at a L/S of 10 mL/g-dry. Dilute nitric acid and potassium hydroxide were used as reagents for adjusting solutions to their target pH values.

4.1.3.4 EPA Method 1315

EPA Method 1315 is a diffusion mass transfer rate, semi-dynamic leaching test (EPA 2017b). The test consists of continuous leaching of water-saturated monolithic material with periodic renewal of the eluent at predetermined intervals, typically for a minimum of 63 days leaching in deionized water. The concentration of each constituent in the eluate at each interval was used to calculate the interval mass flux across the exposed surface area (mg m^{-2} sec^{-1}) and the cumulative mass release (mg m^{-2}) to the eluate.

The T3, T6, and T11 sample dimensions were 5.08 cm (2 in.) internal diameter × 10.16 cm (4-in.) high right-circular cylindrical forms; examples are shown in Figure 4.2. After the 28-day curing period, monoliths were placed in 2-L plastic buckets with lids and were fully submerged in the leaching solution. Leaching solution exchanges and sampling were done at fixed intervals, at cumulative leaching times of 0.08, 1, 2, 7, 14, 28, 42, 49, and 63 days. Additional leachate exchanges and samplings were conducted at cumulative leaching times of 90 and 140 days, which are beyond the typical times prescribed in EPA Method 1315.

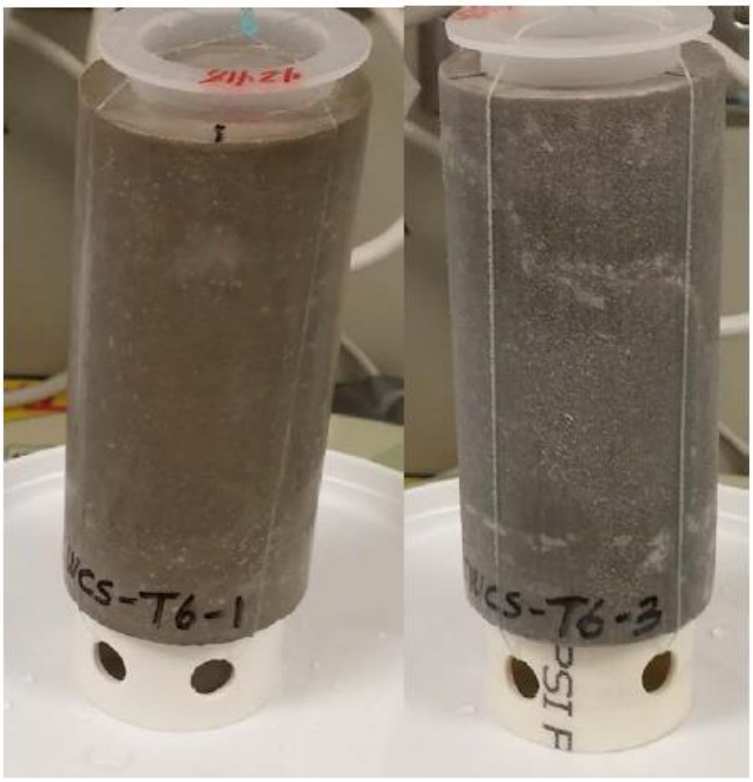

Figure 4.2. Photo of T6-1 and T6-3 monoliths tested by EPA Method 1315 (Um et al. 2016).

4.1.3.5 Geochemical Speciation and Reactive Transport Models

LeachXS (Van der Sloot et al. 2008) with ORCHESTRA (Meeussen 2003) embedded for geochemical speciation and reactive mass transport (hereafter LeachXS/ORCHESTRA, LXO) was used to develop a geochemical reactive transport model that considers geochemical speciation, liquid/solid partitioning, and multi-ionic diffusion (Meeussen 2003). Geochemical speciation modeling was used to simulate the equilibrium liquid-solid partitioning (LSP) of constituents obtained from EPA Method 1313 (i.e., pH-dependent LSP model) and the mass transfer release of constituents in EPA Method 1315 (i.e., monolith diffusion-controlled leaching model).

The aqueous phase speciation and mineral reaction set used in modeling were from the thermodynamic databases minteq.v4 (Eary and Everett 1992) and CEMDATA18 (Lothenbach et al. 2019). Activity coefficients were calculated by adopting the approach of Samson et al. (1999) for ionic strength greater than the range of the extended Debye-Hückel and Davies equations. Log K values of modeled solid phases were calculated for 25 °C using the temperature dependency reported in the minteqv4 and CEMDATA18 datasets.

A set of minerals (i.e., mineral reaction set) that may be present in the system was derived by fitting LSP curves of constituents as a function of pH at equilibrium. Minerals were selected based on (1) identifying phases from the XRD analyses (Table) and (2) minimizing the residuals between the modeled and measured LSP curves by selecting phases that are likely to form under the EPA Method 1313 test experimental conditions (i.e., pH, temperature, and experiment duration).

4.1.3.6 Transport Modeling (multi-ionic diffusion)

Two materials (T3 and T6) were conceptualized in LXO and were represented using a 1-D model consisting of a series of 20 concentric, well-mixed cells (Figure). The surface area at the outermost cell is equal to the sum of the surface areas of faces in contact with the leaching solution. The cells are thickest in the interior of the conceptualized monolith and progressively become thinner in the direction of diffusion, where the innermost boundary is a no-flux boundary. The refresh solution is in contact with the external face of the outermost cell. Constituent diffusion from each cell is based on the fully explicit finite volume scheme described in Meeussen and Brown (2018). In all simulations, the assumptions for local equilibrium conditions were met, i.e., the chemical reactions within a cell were considered much faster than the transport between cells (Samson et al. 1999).

A multi-ionic diffusion approach (Arnold et al. 2017) was used to model constituent specific diffusivity in both monolith diffusion-controlled leaching and rock-cement interface models. The approach uses free liquid diffusivity coefficients, D_i^0, for specific constituents to calculate the diffusivity of the constituent on a per primary-entity (or master species) basis. When D_i^0 could not be found for a particular constituent, the geometric mean of D_i^0 per electron of all the known D_i^0 values was used to calculate the D_i^0 of the constituent. Table summarizes the D_i^0 values used for each primary entity and corresponding constituent.

Table 4.3. List of free liquid diffusivity coefficients (Di^0) that were used in the transport models (Gruber et al. 2022). The uncertainty for the diffusion coefficient is 5%.

Constituent	Primary Entity	D_i^0 (10^{-9} m^2/s)	Reference
Al	$Al[OH]_4^-$	3.120	Mackin and Aller 1983
As	AsO_4^{-3}	3.360[(a)]	average
Ba	Ba^{+2}	1.694	Vanysek 2018
Br	Br^-	2.080	Vanysek 2018
CO_3^{-2}, DIC	CO_3^{-2}	1.846	Vanysek 2018
Ca	Ca^{+2}	1.584	Vanysek 2018
Cd	Cd^{+2}	1.438	Vanysek 2018
Cl	Cl^-	2.032	Vanysek 2018
Co	Co^{+2}	1.464	Vanysek 2018
Cr	CrO_4^{-2}	2.264	Vanysek 2018
Cu	Cu^{+2}	1.428	Vanysek 2018
Fe	$Fe[OH]_4^-$	1.257	Arnold et al. 2017
H^+	H^+	5.273[(b)]	Vanysek 2018
B	$H_2BO_3^-$	1.120[(a)]	Average
Si	$H_2SiO_4^{-2}$	1.697	Arnold et al. 2017
K	K^+	1.957	Vanysek 2018
Li	Li^+	1.029	Vanysek 2018
Mg	Mg^{+2}	1.412	Vanysek 2018
Mn	Mn^{+2}	1.424	Vanysek 2018
Mo	MoO_4^{-2}	3.968	Vanysek 2018
NO	NO_3^-	1.902	Vanysek 2018
Na	Na^+	1.334	Vanysek 2018
Ni	Ni^{+2}	1.322	Vanysek 2018
PO	PO_4^{-3}	2.472	Vanysek 2018
Pb	Pb^{+2}	1.890	Vanysek 2018
SO	SO_4^{-2}	2.130	Vanysek 2018
Sb	$Sb[OH]_6^-$	0.849	Vanysek 2018
Se	SeO_4^{-2}	2.016	Vanysek 2018
Sn	Sn^+	2.240[(a)]	average
Sr	Sr^{+2}	1.582	Vanysek 2018
Th	Th^{+4}	6.120	Yuan-Hui and Gregory 1974
VO	VO_2^+	1.120[(a)]	Average
Zn	Zn^+	1.406	Vanysek 2018

(a) The geometric mean of D_i^0 per electron of all the known D_i^0 values.
(b) D_i^0 of OH^- used because system is alkaline.

Tortuosity factors (τ), representing physical retention of constituents moving through a tortuous pore network, were calibrated for each cell by minimizing the sum of log-squared residuals of the predicted vs. the measured Na^+ and K^+ releases measured for the first 63 days (Skeen et al. 2025). The first exchange at approximately 2 hr is not included in the calibration because typically there is surface wash of soluble constituents (including Na^+) and mold interface effects when a monolith is first submerged in the leachant. Tortuosity factor for the material within the matrix located deeper than the diffusion front at the conclusion of testing was set equal to the tortuosity factor for the most interior cell at the diffusion front. The dependency of the effective diffusivity on tortuosity is described by:

$$D_{i,eff} = D_i^0 \frac{\emptyset}{\tau^2} \quad \text{Eq. 4.1}$$

where $Di_{,eff}$ is the effective diffusivity (m^2 sec^{-1}) and ∅ is the porosity (fraction). Calibration was achieved by minimization of residuals between the simulated and measured values. Arithmetic residuals were calculated as:

$$\sum R = log|\, y - \hat{y}|^2 \qquad \text{Eq. 4.2}$$

where R is the residual, y is the observed value and $\hat{y}$ is the predicted or modeled value.

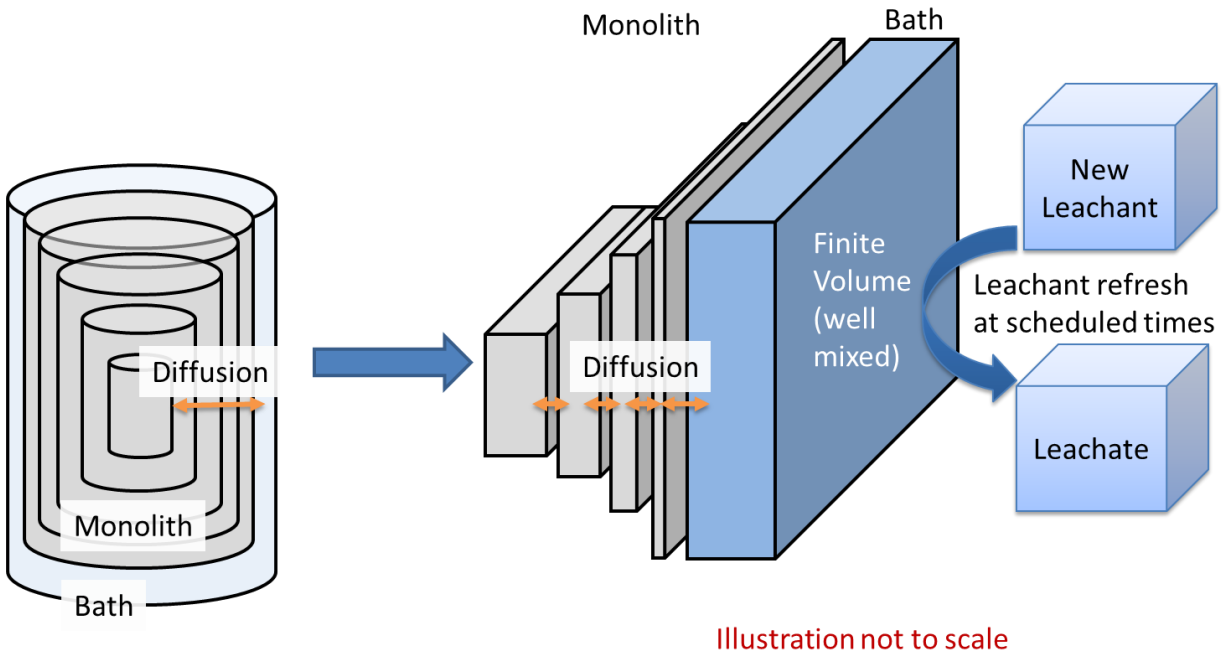

Figure 4.3. Conceptual LXO model used for tortuosity factor calibration.

4.1.4 Results to Date

4.1.4.1 pH Dependent Model

Figure shows the results of EPA Method 1313 and the simulated LSP by LXO for a pH range 1-14 for the T3 and T6 samples. Despite the difference in water-to-dry-materials ratios in the mix designs, the pH dependency of major constituents (Al, Ca, Fe, Si, Mg, Na, and S) is almost identical for both grouts, indicating no significant effect on the mineral composition of the grouts. Therefore, for LSP modeling, T3 and T6 were simulated as duplicates of the same material. The blue dashed line in the panels of Figure show the simulated LSP curves by LXO, and Figure shows the corresponding simulated solid compositions. XRD measurements provided a upper boundary condition for the relative amounts of simulated solids (Table . This condition was met by results for all constituents used in the simulation. While the XRD data provides limited information on some of the solid material composition of the grout, combining EPA Method 1313 test results with LXO modeling allows for the estimation of the solid composition of the material, which is traditionally difficult to determine from XRD (in which materials that are not identified are considered to be amorphous or below detection limits) or other solid characterization methods. Hence, together with further simulation results, it allows the use of the calibrated mineral reaction set to describe how the hydrated lime secondary liquid waste grout interacts with the environment under wide range of pH conditions and porewater compositions.

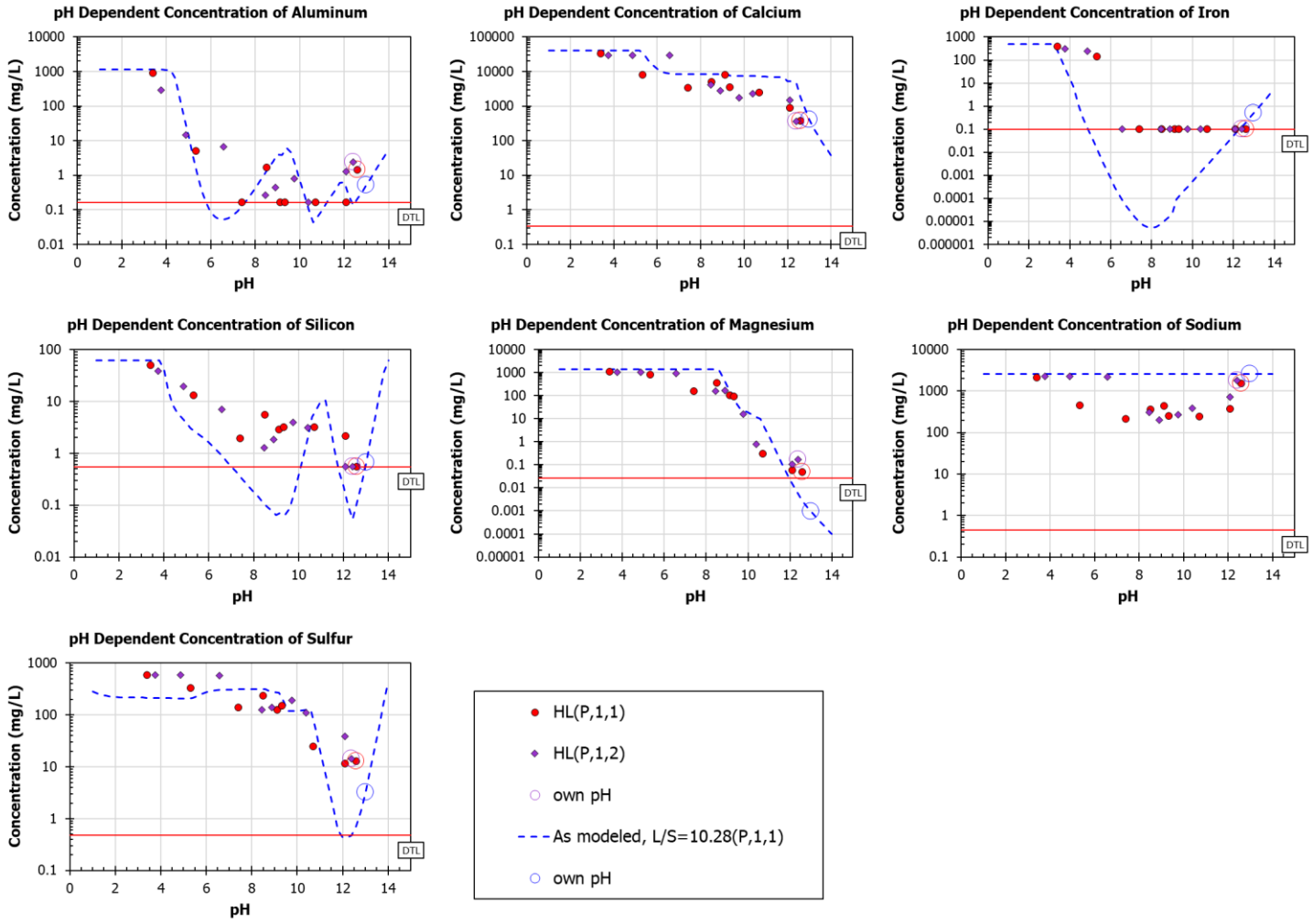

Figure 4.4. Results of EPA Method 1313 tests and the modeled prediction of LSP (liquid-solid partitioning) curves. Red and purple dots are the experimental data of tests T3 and T6 at L/S 10. Blue dashed lines represent the predicted LSP curves for L/S 10.

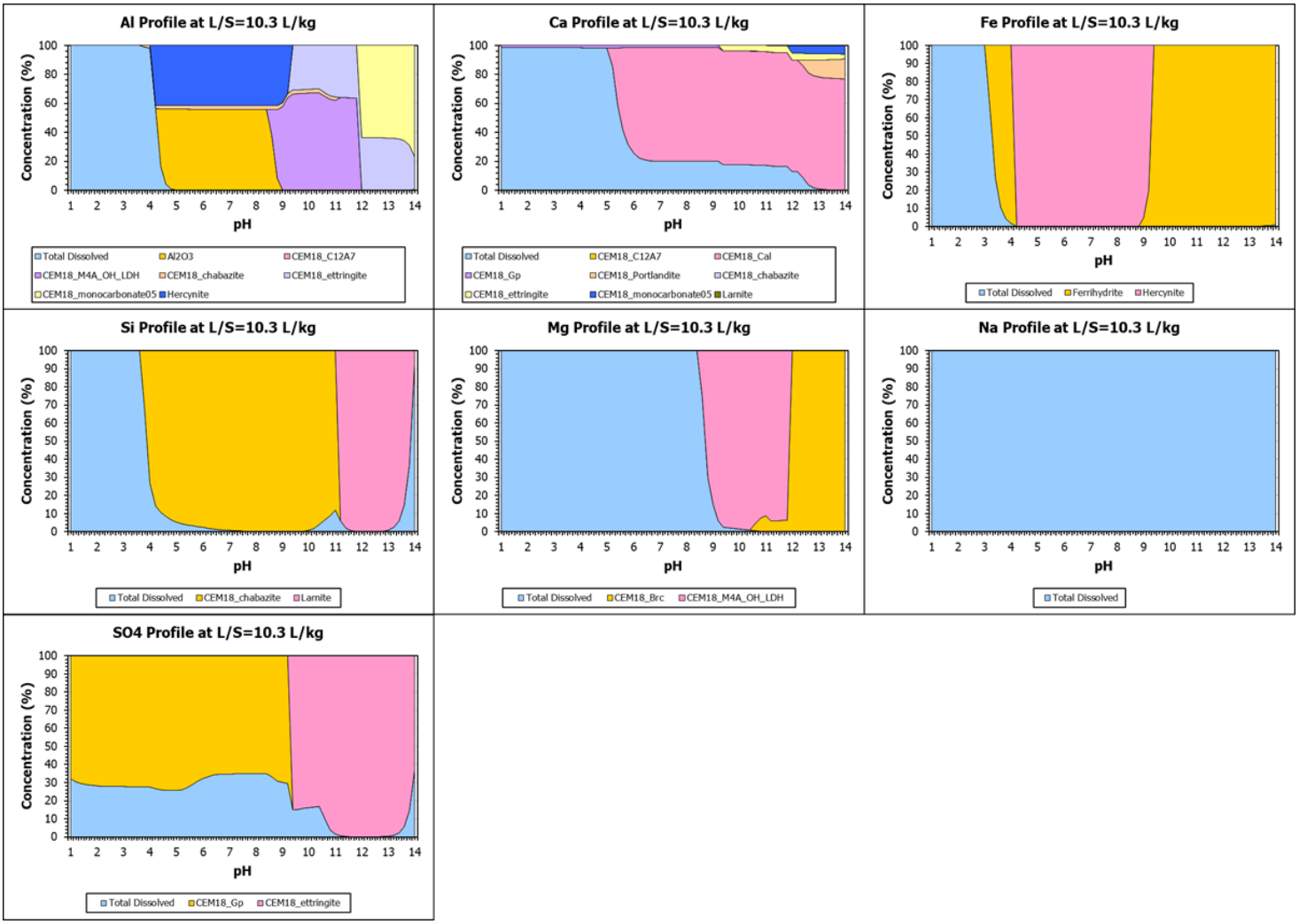

Figure 4.5. Predicted solids composition on unit cell basis as a function of pH for EPA Method 1313.

4.1.4.2 Effective Diffusivity and Tortuosity Factor Modelling

A reactive transport model was used to model the effective diffusivity of close-to-conservative constituents in tests of mass transfer rate tank leaching tests (EPA Method 1315). Non-binding constituents (e.g., sodium, potassium, nitrate, NO_3) can be used to calibrate the tortuosity factor of porous medium as their effective diffusivity is mostly affected by concentration gradient, porosity, and tortuosity factor. In these simulations, values of initial porosity and porewater concentration gradients are based on measurements (e.g., mercury intrusion porosimetry and EPA Method 1313), making tortuosity factor the only unknown in the effective diffusivity equation (Eq. 4.1). Figure shows results of EPA Method 1315 tests for samples T3 and T6. The gray line (slope of -0.5) in each panel demonstrates the theoretical diffusion flux of a fully non-binding constituent. For the duration of the tests, both sodium and potassium exhibited close to conservative flux as being non-binding from the monolith. Hence, tortuosity factor was calibrated using sodium and potassium. While T3 and T6 are similar chemically, the effective diffusivity of T3 was higher than of T6 (for sodium and potassium),this result possibly reflecting differences in the physical properties of the grout samples, including structure, pore size, and pore size distribution.

Figure shows results of LXO simulations for duplicate samples from EPA Method 1315 for T3 and T6 samples. The results are presented as concentrations of sodium and potassium as a function of time. Tortuosity factors of hydrated lime secondary liquid waste grout T3 and T6 samples were calibrated using LXO. Tortuosity factors were estimated to be 40 and 61 for T3 and T6, respectively. The calibrated tortuosity factor range (40-61) is lower than the published range (80-150) for CS materials calibrated by Skeen et al. (2025).

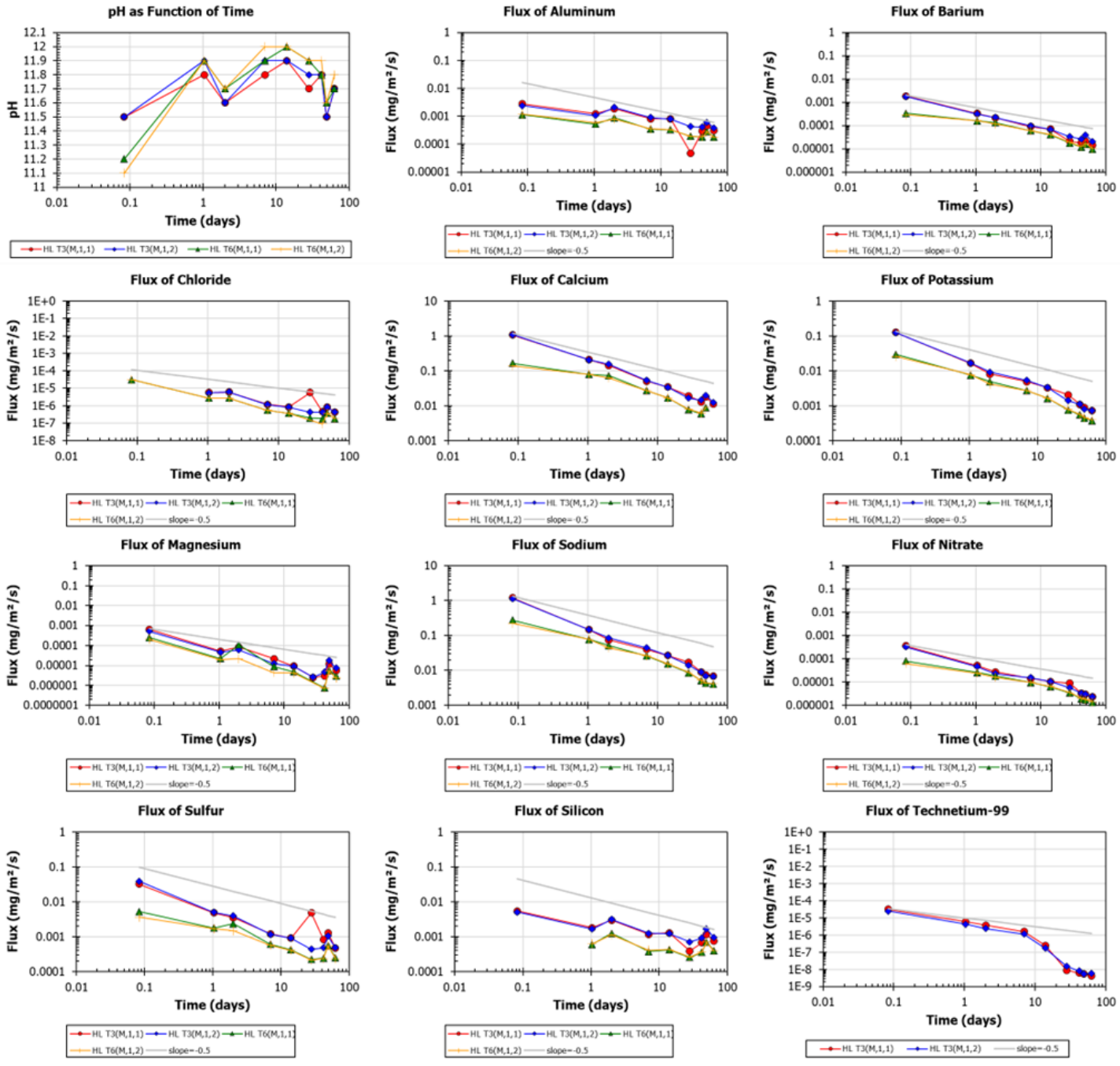

Figure 4.6. Results of EPA Method 1315 tests for duplicates of T3 and T6 samples.

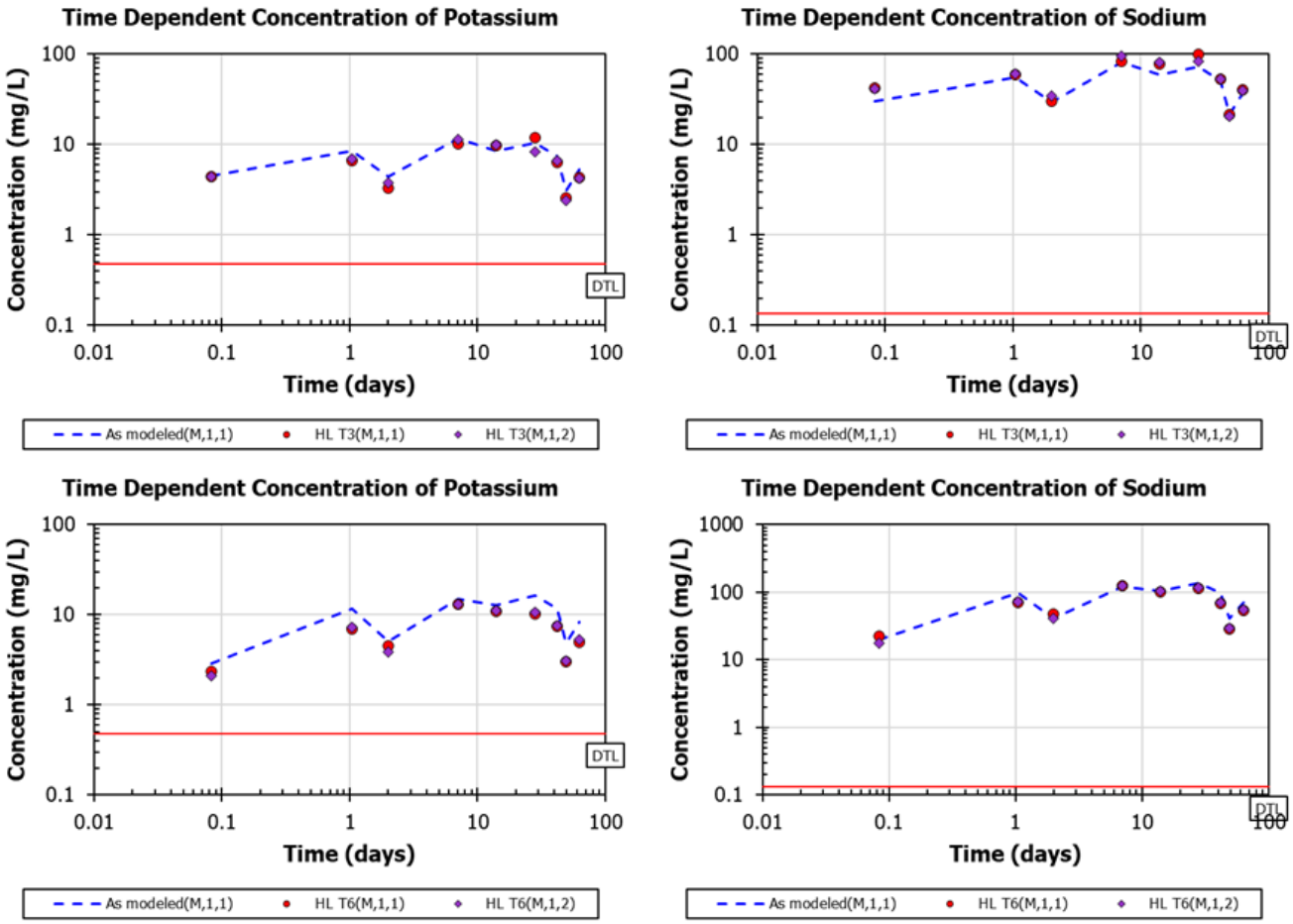

Figure 4.7. LXO simulation results for T3 (top) and T6 (bottom) to determine tortuosity factors of these non-binding species. Red and purple dots are experimental data, and the blue dashed line is simulated concentration.

4.1.5 Path Forward and Integration

4.1.5.1 Year 1 Accomplishments

The work performed in Year 1 of this task has shown the promise of geochemical speciation modeling to replicate leaching behavior of various grout formulations and provide calculated parameters crucial for grout modeling. This tool will form a key component of the *Hanford Grout Modeling Framework* in its development in Year 2. During Year 1, the following accomplishments were made in maturing the geochemical speciation model:

- Results of EPA Method 1313 and 1315 tests for hydrated lime were converted to LXO database formats. The LXO format is planned for the presentation of leaching data relevant for Hanford grouts moving forward.
- pH-dependent simulations for hydrated lime secondary liquid waste grout T3 and T6 samples were developed in LXO.
- LXO simulation was used to develop and calibrate a mineral reaction set for hydrated lime secondary liquid waste grout T3 and T6 samples that can describe the interaction of grouts with the environment under a wide range of pH conditions.

- Mass transfer rate tank leaching simulations were developed in LXO for hydrated lime secondary liquid waste grout T3 and T6 samples.
- Tortuosity factors of hydrated lime secondary liquid waste grout T3 and T6 samples were calibrated using LXO. Tortuosity factors were estimated to be 40 and 61 for T3 and T6, respectively.
- No significant differences were observed in chemistry, but the water-to-dry materials ratio may affect physical properties as such as tortuosity factor and, therefore, affect the effective diffusivity of constituents in the secondary liquid grout waste. This potential effect will be studied further using sensitivity analyses in Year 2.

4.1.5.2 Year 2 Plan

The following tasks are planned for Year 2 of the project.

- ***Subtask 3.1.1 – Continued Geochemical Model Development:*** Efforts similar to those performed for the T3 and T6 samples will be done for the T11 sample. Following this, the mineral reaction set describing Tc LSP for T3, T6, and T11 grout samples will be incorporated, along with these mineral sets, in mass transfer tank leaching simulations for diffusion prediction and further validation of the reactive constituents. The simulations performed to date will be extended beyond 63 days for validation of modeled monolith bulk tortuosity factor to predict "long-term" leaching behavior (in collaboration with H2C staff). An additional grout case will be evaluated using a dataset generated by PNNL and SRNL for the leaching of ultra-high performance grout. These grouts are being considered as waste forms for solid secondary wastes and as barriers due to their low porosity.
- ***Subtask 3.1.2 – Uncertainty:*** This task will begin to construct the uncertainty component of the *Hanford Grout Modeling Framework* with an approach taken for the estimation of mineral network uncertainty by using uncertainties associated with solid phase K_f values and pH.
- ***Subtask 3.1.3 – Framework Integration:*** This task will target development of a link between eSTOMP and LXO to provide geochemical speciation information in conjunction with Theme 6.

4.2 Theme 3 Task 2: Integration of Key Aging Processes as Spatial Evolution in eSTOMP.

4.2.1 Team Members

Jacob Anderson (PNNL), Xuehang Song (PNNL), Chen Gruber (VU), Christine Langton (SRNL)

4.2.2 Background

In the conceptual models supporting the *Hanford Grout Modeling Framework*, described in Section 1.2, oxidation and carbonation were identified as key processes that needed to be accurately represented. These processes progress from the outer surface of the grout inward to the monolith as reactive species (e.g., carbonate, O_2) are transported to the grout from the near-field environment. Currently, neither process is discretely determined in grout modeling at Hanford, and any changes in material properties induced by these processes are included as bulk step changes for the whole monolith. The parameter most impacted by these changes is contaminant retention, which in current modeling is represented as a static distribution coefficient (K_d, higher K_d is higher retention). Once the grout becomes oxidized, at some point K_d decreases and contaminant release increases. However, oxidation and carbonation have impacts, both beneficial and deleterious, on other grout properties, and this step change approach is overly conservative.

In the SRS PA, oxidation and carbonation are evaluated dynamically using information from pore volume exchanges. With the emergence of geochemical speciation modeling to assess the impacts of oxidation and carbonation on grouts (Chen et al. 2023; Gruber et al. 2022; Chen et al. 2021), contemporary tools are available to evaluate the progression of these processes spatially and dynamically in grouts at Hanford. This task is focused on remediating this significant gap in grout modeling by developing approaches to simulate these two processes in Hanford-relevant materials and disposal environments. This tool will be a direct component of the *Hanford Grout Modeling Framework* for evaluating how the two key processes affect aging. The tool will eventually function by using the reactive transport software to evaluate the ingress of O_2/CO_2 into grouts. Based on the depth, spatially dependent properties of the grout will be determined using geochemical speciation modeling (e.g., contaminant speciation, mineral makeup). In doing so, a dynamic, spatially driven model of oxidation and carbonation will be developed.

4.2.3 Technical Approach

eSTOMP is used for geochemical and reactive transport modeling to simulate the interactions of grout waste forms with the subsurface environment at Hanford. Within this task, eSTOMP simulations assessed the software's ability to reconstruct oxidation processes in grout, using a similar approach to that used in the SRS PA (Kaplan et al. 2005). The case studies evaluated herein focused on the oxidation front's progress into grout waste forms of two different sizes: a B-25 waste box and a waste burial box. The full input files can be found in Appendix C. Table compares the properties of the two case studies.

Table 4.4. Comparison of the properties of the two case studies for oxidation testing in this report.

Property	B-25 Box – 8 High Stack	Burial Box – 8 High Stack
Height (1 waste form/total)	1.19m / 14.52m	1.22m / 14.76m
Length (1 waste form/total)	1.83m / 1.94m	2.44m / 2.55m
Width (1 waste form/total)	1.17m / 1.28m	1.22m / 1.33m
Density (g/cm^3)	2.82	2.82
Porosity	0.557	0.557
Hydraulic Conductivity (cm/s)	1.54×10^{-9}	1.54×10^{-9}
Surface area (m^2)	11.42	14.88
Volume (m^3)	2.55	3.63
Surface Area to Volume (m^{-1})	4.48	4.099

Each input file contains detailed geochemical parameters such as waste form composition, governing equations, and subsurface interactions that influence oxidation and carbonation. These test cases are examples of how current subsurface modeling is done at Hanford without dynamic callouts.

In Appendix C, the two input files for eSTOMP are consolidated into a table format to summarize the parameters used to generate a baseline grout case for oxidation. The models were initialized with a 3.5-mm/yr infiltration rate and have identical density and porosity values for the high-density (HD_BACKF) and low-density (LD_BACKF) backfill while the grout (W1) is both more dense and more porous than the backfills. Other parameters like hydraulic conductivity, saturation functions that define parameters related to van Genuchten models for water retention capabilities, aqueous relative permeability, aqueous species, conservation equations, kinetic equations, and boundary conditions are considered. That is not an exhaustive list, and the rest can be found in Appendix C.

In the simulations, the degree of oxidation is measured by the changes in reduction capacity within the grout. Reduction capacity is the numerical representation of the ability of a material to consume oxidants

and, as such, maintain existing species in reduced states (Abrahmson et al. 2022). Using these input cards, eSTOMP predicts the reduction capacity of certain materials and gives insight into how, when, and why the waste form will leach into the surrounding subsurface. The general redox equation is presented in Eq. 4.3:

$$O + e^- = R \quad \text{Eq. 4.3}$$

where:

O = oxidizing agent, meq e^- L^{-1}
R = reducing agent, meq e^- L^{-1}
e^- = electron

The progression of reduction capacity consumption was defined as follows:

$$O_2(\text{aq}) + \text{R(grout)} = \text{R}O_2(\text{grout}) \quad \text{Eq. 4.4}$$

where:

O_2(aq) = O_2 dissolved in water (meq e^- g^{-1} of the fluid)
R(grout) = reduction capacity of the grout (meq e^- g^{-1} of solid)
RO_2(grout) = oxygenated grout (meq e^- $g^{-1}$of solid; shown in traditional stoichiometric chemistry as a product of the two reactants, rather than as an oxidized species)

The expression used to calculate the rate of oxidation (R_O; meq e^- g^{-1} yr^{-1}) for the above reaction (Eq. 4.3) is:

$$R_o = k \cdot C_{O_2} \cdot C_R \quad \text{Eq. 4.5}$$

where k is the oxidation rate coefficient (meq^{-1} e^- g yr^{-1})), C_{O2} is the concentration of dissolved O_2 (meq e^- g^{-1}), and C_R is the concentration of reductant in the grout (meq e^- g^{-1}) (Kaplan et al. 2005).

The primary goals of model development are to integrate oxidation and carbonation processes into eSTOMP using the methodology from SRS in Year 1 and then in Year 2 work toward creating communication between eSTOMP and ORCHESTRA for dynamic updates to oxidation and carbonation parameters. Good progress has been made running simulations in eSTOMP for multiple cases of grout disposal for oxidation

4.2.4 Results to Date

The current step change, static K_d approach limits the model's ability to accurately predict long-term behavior and the impact of oxidation and carbonation. Preliminary simulations of an oxidation process of CS grout using the B-25 and waste burial box cases have shown that while the models run successfully under these static assumptions, they fail to capture the changes in the waste forms that would naturally occur in response to subsurface conditions. As a result, the predicted leaching rates are likely to be inaccurate, since dynamic changes in waste form chemistry are not considered. This highlights the need to incorporate dynamic processes for a more realistic representation of grout behavior in long-term disposal scenarios.

Previous work was done to recreate the SRS PA waste burial method. A comparison between the SRS PA and the PNNL model revealed that the PNNL model predicted a reduction capacity of ~ 16% while the

SRS model predicted 16%. This difference could be explained by the differing amounts of salt solution between the models.

Figure shows the baseline model setup for each test case. The waste burial box has a slightly longer waste form than the B-25 waste box, which is the main difference between the two as both have the waste form surrounded similarly by low- and high-density backfill.

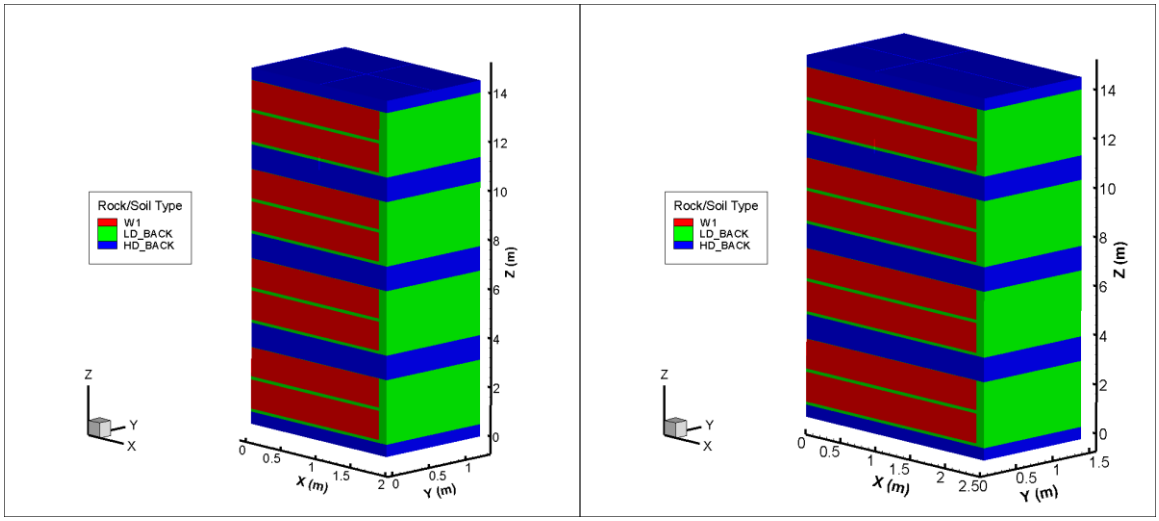

Figure 4.8. Low- and high-density fill around the grout waste form in the B-25 waste box (left) and the waste burial box (right).

Figure 4.9 and Figure 4.10 present some of the results for each test case. In most cases, box size has no discernable effect on the reduction capacity consumed by the salt solution and the residual reduction capacity. However, there is a slight decrease in the reduction capacity consumed by dissolved oxygen (DO). The waste burial box also seems to have more solution product, O_2, slag, and slightly more O_2 product than the B-25 waste box. These findings signal that larger box size provides more byproducts from oxidation with comparable reduction capacity to the B-25 waste box and could be more susceptible to oxidation reactions because it has more solute mass present. Figure 4.11 shows the consumption of the reduction capacity with a 3-D visualization of the B-25 waste form. This shows the regions with higher consumption of reduction capacities.

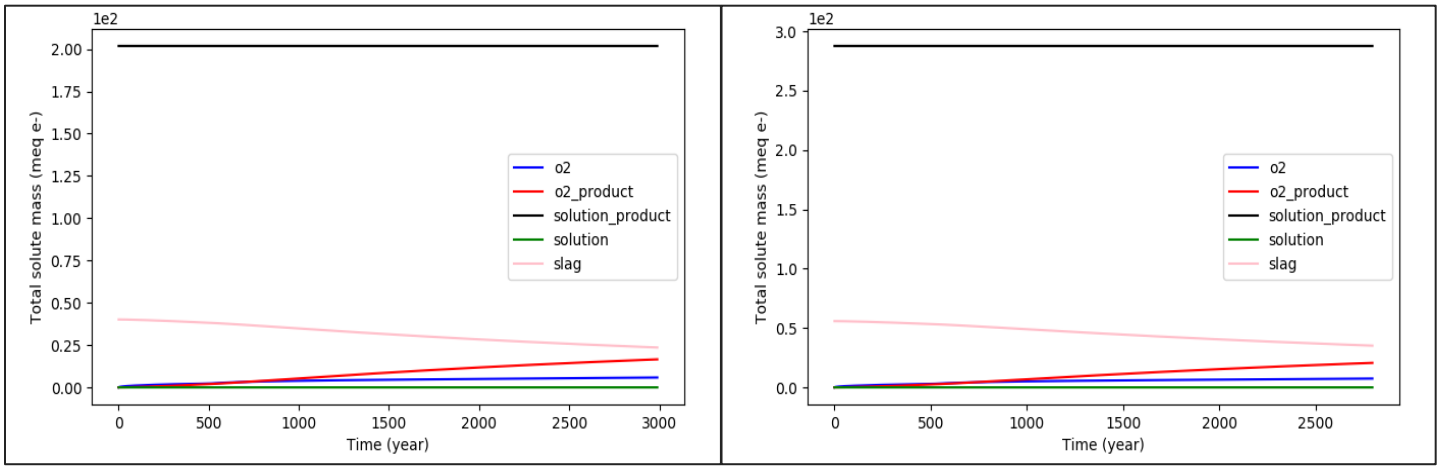

Figure 4.9. Total solute mass (meq e-) for the B-25 waste box (left) and the waste burial box (right).

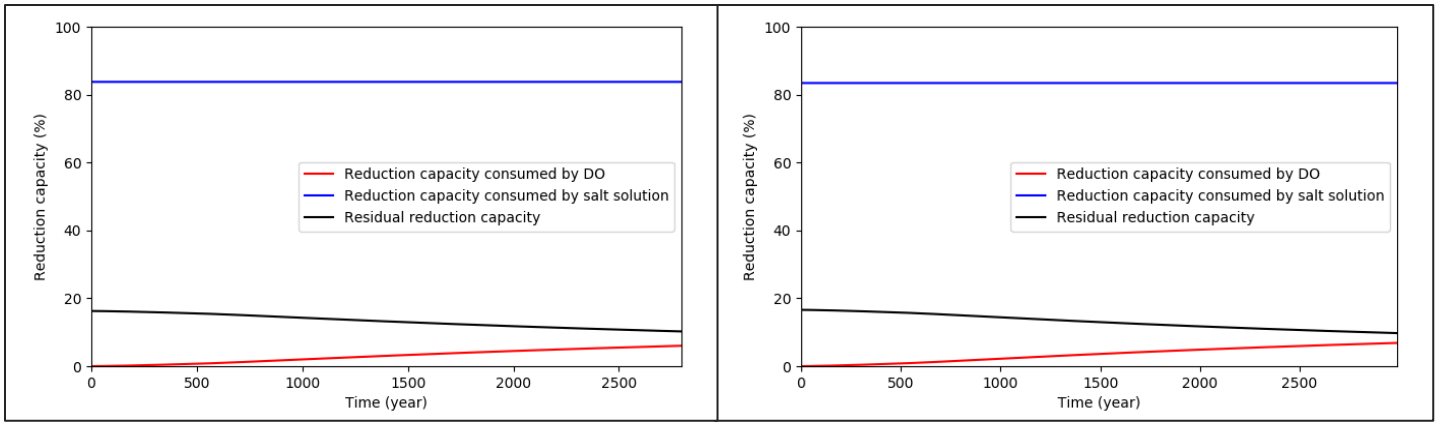

Figure 4.10. Reduction capacity (%) for the B-25 waste box (left) and the waste burial box (right).

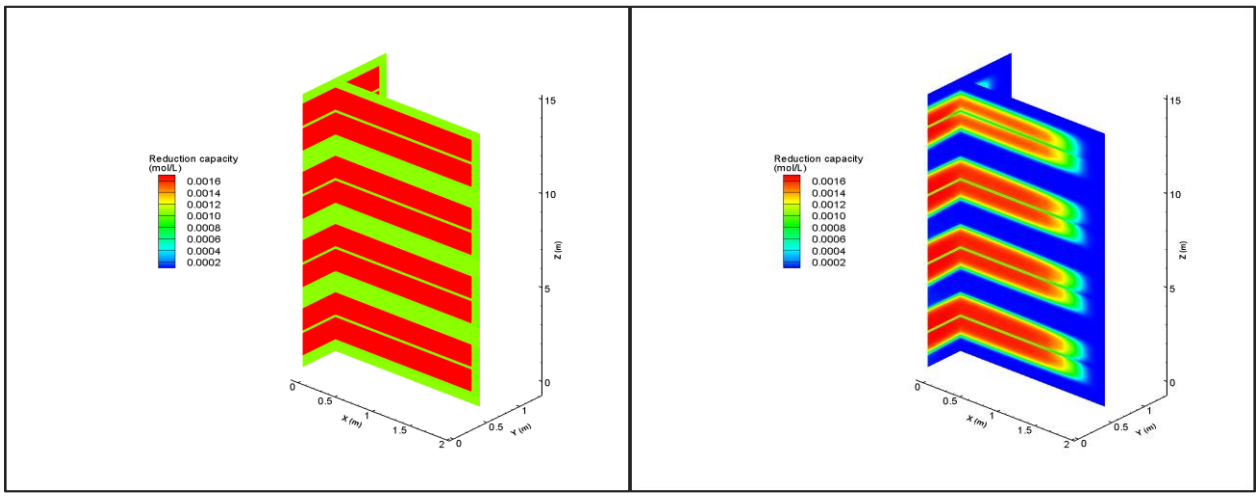

Figure 4.11.B-25 waste box reduction capacity consumption.

4.2.5 Path Forward and Integration

The Year 1 effort has shown that eSTOMP is capable of tracking oxidation processes spatially using previously established approaches for saltstone. Moving forward, the task will focus on linking the impacts of oxidation and carbonation on grout properties through geochemical speciation modeling and developing models for carbonation.

- ***Subtask 3.2.1 – Oxidation Modeling:*** This task will continue to mature the modeling of oxidation processes in Hanford grout. This will be done by carrying out simulations similar to those presented using other grout formulations. This effort will include verification modeling against experimental datasets (Langton and Almond 2013; Chen et al. 2023; Saslow et al. 2024). Oxidation can occur in both the pre-burial (air exposure) and post-burial timeframes, and both will be considered in these efforts.
- ***Subtask 3.2.2 – Carbonation Modeling:*** This task will create baseline simulations for carbonation, similar to the approach for oxidation modeling.
- ***Subtask 3.2.3 – Geochemical Based Impacts:*** This task will update the methods by which oxidation and carbonation are handled in in eSTOMP to reflect the changes that occur over time. A callout between LXO and eSTOMP will be developed by writing a wrapper for eSTOMP to communicate

with LXO and dynamically update parameters affecting oxidation and carbonation. While initial development has begun, there are still questions about the most effective way to implement these dynamic updates without complicating the model excessively. The integration of LXO will be explored to facilitate dynamic updates using the C++ version of LXO. LXO will serve as a control mechanism to interface with eSTOMP, allowing oxidation and carbonation processes to be updated based on geochemical calculations derived from the eSTOMP subsurface model. To incorporate LXO, a code wrapper is being developed to help the eSTOMP and the geochemical calculator communicate and exchange the needed information for these planned dynamic updates, see Figure . Collaboration with Theme 1 Task 1 and Theme 3 Task 1, which focuses on developing specific waste form materials geochemical and mineral information, will ensure that both material properties and environmental interactions are well-represented in the *Hanford Grout Modeling Framework*.

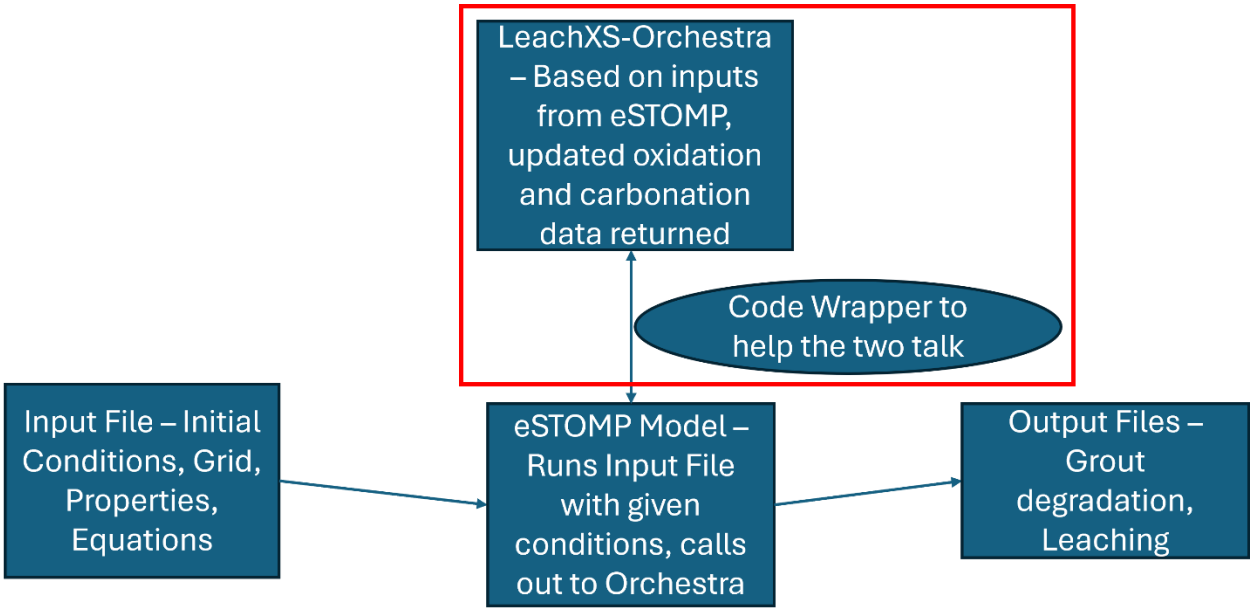

Figure 4.12. High-level design for eSTOMP and ORCHESTRA interaction for dynamically updating oxidation and carbonation.

4.3 Theme 3 Task 3: Contaminant Interactions with Microbial Processes

4.3.1 Background

Within the Hanford subsurface, a range of microbial processes can lead to natural attenuation of contaminants. One such contaminant is nitrate, a major component of LAW, which in a hypothetical disposal scenario of LAW grout in the IDF can contribute significantly to subsurface contamination (Asmussen et al. 2024). Microbial conversion rates for nitrate (and nitrite) are available from prior subsurface models but have yet to be linked with grout leaching behavior. This task will evaluate the influence of nitrate conversion on the overall impact to groundwater from a grouted inventory of LAW in the IDF.

4.3.2 Technical Approach

A simple test model case was performed that considered nitrate transport with both linear adsorption and microbial reduction. These cases simulated the effects of microbial reduction on nitrate leaching using a previous configuration of grouted inventory of LAW in the IDF (USDOE 2018) with waste form size of a B-25 box with dimensions of 6 ft × 4 ft × 4 ft. K_d values are 0.372 mL/g for nitrate in the grout and 0.0 mL/g for nitrate in the backfill. K_d was previously used to evaluate the diffusive release of nitrate from cementitious waste forms. Dissolved organic carbon (CH_2O) is assumed to be initially present in the backfill. As an example, nitrate reduction reaction and rate parameters are taken from Newcomer et al. (2018):

$$(5+\gamma)CH_2O + 4NO_3^- \leftrightarrow +4H^+ + 5CO_3^{-2} + 2N_2(aq) + 2H_2O + \gamma Biomass \qquad \text{Eq. 4.6}$$

where γ is the microbial yield, which is 0.17.

Using dual Monod kinetics, microbial growth was specified as a function of the concentration of nutrient substrates (NO_3^- and CH_2O) and the concentration of microbial mass in the system. Dual-Monod maximum growth rate coefficients is 10^{-7} (M_{DOC} M_{NO3}^{-1} $Mbio^{-1}$). The half saturation constants of CH_2O and NO_3^- are 10^{-4} M and 8.064×10^{-6} M, respectively. Microbial biomass decay was given a constant rate of 10^{-7} s^{-1}.

4.3.3 Results to Date

Initially, the concentration of CH_2O was set to 1.0 mM in the backfill, and total nitrate in the waste form was 1 mole. Figure compares the cumulative release of nitrate from the IDF. Microbial reduction decreases the amount of nitrate released from the IDF. The results are sensitive to the substrate concentrations and where they are located.

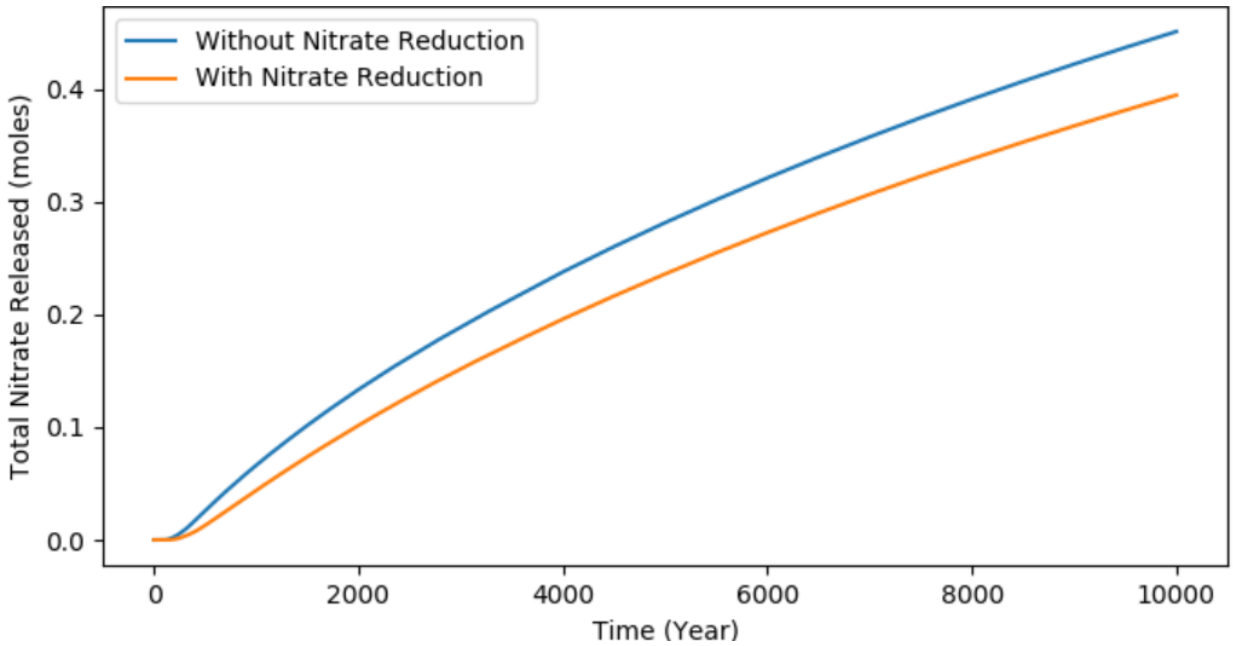

Figure 4.13. Comparison of the model results of nitrate release within the IDF from a grouted inventory with and without nitrate reduction.

4.3.4 Path Forward and Integration

Year 1 of this work showed that there can be an impact at the transport timescales of interest for nitrate remediation. Updated calculations will be performed to integrate other aspects of the *Hanford Grout Modeling Framework* once complete. Integration of the microbial process into reaction network scenarios will be straightforward. One significant gap in testing and validating the nitrate conversion model is the lack of relevant experimental data. There is currently a task funded by H2C looking at microbial conversion rates of nitrate and nitrite in these simulations.

5.0 Theme 4: Modeling of Cracking in Grout

5.1 Theme 4 Task 1: Peridynamics Modeling

5.1.1 Team Members

Jessica Rimsza (Sandia National Laboratories, Sandia), Jeremy Trageser (Sandia), Mark Rigali (Sandia), Naveen Karri (PNNL), Jon Lapeyre (PNNL), Suraj Rahmon (PNNL)

5.1.2 Background

Cracking remains the prominent mechanism that can drive failure of grout and can be caused by several processes. Yet, predicting and representing cracking in cements in general remains a challenge and has rarely been pursued for grouts used in waste management applications. PD modeling has potentially beneficial features for the modeling of grouts used in waste disposal, such as ease of implementation and an intrinsic ability to represent brittle fracture, which makes this effort distinct from previously employed classical continuum methodologies. With the success of PD application to the aging of hardened cement pastes (Jones et al. 2021), this task will be focused on a novel effort integrating PD modeling into the prediction of physical properties of grouts used in waste management. The goal of this tool development is to provide predictions of the degree of cracking (and possible failure modes) of various grouts in this disposal/closure application. In the current modeling, the grouts can be assumed to lose all structural integrity in short timeframes. The goal is to develop a model with PD to predict the degree of cracking at certain times to define how cracking in grout is handled in the *Hanford Grout Modeling Framework* as a change in surface area and transport pathways.

5.1.3 Technical Approach

This task was designed with two components: (1) preparing laboratory samples with different formulations and exposure conditions that can provide cracking test cases for PD and (2) modeling of these grout samples using PD. Year 1 was focused on constructing first-of-its-kind PD modeling of Hanford tank floors that have experienced varied thermal histories. In Year 2, this work will target waste form grouts.

5.1.3.1 Sample Fabrication, Thermal Treatment, and Testing

Three different cementitious mix designs were fabricated at PNNL to provide data to assess against PD modeling predictions. These mixtures included two conventional construction binders of an OPC concrete and an OPC mortar. Additionally, CS, a highly studied grout at Hanford for solidification and encapsulation, was fabricated to provide an initial waste form dataset. Unlike the previous two conventional mix designs, CS is a ternary blend of BFS, FA, and OPC at 47, 45, and 8 wt%, respectively. Unlike the conventional binders, the CS was mixed with a LAW simulant instead of deionized water (conforming to Type II reagent water in ASTM 1193-24) to fabricate a mix at a water-to-binder ratio of 0.5. The water-to-binder ratio for the mortar and concrete was also 0.5.

Table collates the mix design for the concrete and mortar samples. The source for the Type I/II OPC was Exshaw and the coarse and fine aggregate (i.e., gravel and sand) was sourced from American Rock Products (ARP) in Richland, WA. The fine aggregate was dried at 110 °C in an oven before fabrication of concrete or mortar. The gravel was used as-is. The gravel size deviated from the original mix design in Daniel et al. (1982) by having a maximum diameter of 9.53 mm (3/8 in.) rather than 19.05 mm (3/4 in.); this is due to changes in aggregate availability. The CS mix design is reported in Table , with the cement

manufacturer being Exshaw while both BFS and FA were sourced by Lafarge as the NewCem product for the BFS and FA from a powerplant in Centralia, WA. The simulant was a highly alkaline 5.6 M Na LAW simulant fabricated in 2024 without hexavalent chromium [i.e., Cr(VI)] with 30% dissolved solids by mass.

Table 5.1. Original and fabricated mix design for concrete and mortar samples.

Constituent (source)	Original Concrete Design[(a)] (lb/yd^3)	Concrete Batch 1 (g)	Concrete Batch 2 (g)	Mortar Batch 1 (g)	Mortar Batch 2 (g)	Mortar Batch 3 (g)
Cement (Exshaw)	494	476.16	476.75	475.64	475.69	475.68
Sand (ARP)	1,154	1,096.38	1,096.21	1,095.10	1,095.26	1,095.56
Gravel (ARP)	2,000	1,905.34	1,906.21		N/A	
Water	267	256.50	256.50	256.76	256.11	256.87
Water-to-cement ratio (w/c)	0.54	0.5387	0.5380	0.5398	0.5384	0.5400
% Fine aggregate to total aggregate	36.6	36.5	36.5		N/A	

(a) Sourced from Table 4 of Daniel et al. 1982.

Table 5.2. Fabricated mix design for Cast Stone samples.

Constituent	Source	Batch 1 Cast Stone (g)	Batch 2 Cast Stone (g)
Cement	Exshaw	172.58	172.96
Blast furnace slag	Lafarge NewCem	1,020.79	1,013.56
Fly ash	Lafarge Centralia	172.58	970.04
5.6 M Na LAW simulant	FY24-5.6M LAW-COMB-02292024-1 No Cr	1,652.84	1,652.69
Simulant dissolved solids (% mass)	0.3		
Water-to-binder ratio (w/b)	0.5	0.53	0.54

The fabrication and mixing varied depending on the mix design. For the concrete samples, the cement and fine aggregate were mixed mechanically following ASTM C305-20, followed by hand-mixing of the coarse aggregate for 2 minutes. The resulting mix was placed into 50 mm ∅ × 100 mm molds and tapped to remove air pockets. Excess vibration was avoided to prevent segregation of the coarse aggregate. The same-sized molds were used for all three mixtures. Preparation of the mortar samples also followed the directions of ASTM C305-20. After homogenizing and mixing, the samples were poured into molds at half-capacity, and the molds were subsequently tapped and vibrated, followed with a second pour to fill the mold. After filling the mold, the samples were tapped and vibrated a second time. A total of 10 concrete specimens (split between two batches) and 12 mortar samples (split between three batches) were measured. The CS samples were mixed using an overhead mixer instead of a planetary mixer. The CS dry mix was added to the simulant and mixed at up to 300 rpm for 15 minutes. After mixing, the CS grout was poured into molds and like the mortars were poured halfway, agitated to remove air bubbles, then poured into the mold with a second vibrating/agitation stage. Between two batches, 17 CS specimens were tested. The completed molds were placed into a 45-L (10-gal) bucket with a small volume of water to ensure a humid environment for the cementitious materials. The curing stage lasted for 28 days.

Comparisons of the PD modeling to the conventional mortar and CS will be available at the beginning of Year 2.

After the curing and demolding stage, the mass, height, and diameter of all the monoliths were measured. Following these measurements, the subsequent testing for the conventional samples and CS diverged. The conventional concrete and mortar mixtures were divided into three groups: a room temperature group serving as the control, a 93 °C heat treatment, and a 149 °C heat treatment. The samples were heated at a rate of 1 °C/min, followed by the isothermal hold at the target temperature in a conventional oven, and subsequently heated for 7 days. This heat treatment was based on thermal history of tanks reported in Giever (2018). The highest temperature reached was within the tank center corresponding to ~149 °C (300 °F). An additional temperature 94 °C (200 °F) was chosen as an intermediate temperature. The heat rate was calculated by using the slope of tank center bottom line estimated from 1965 to 1971 (~6 years). The resulting heating rate was very slow, on the order of µ°C/min; therefore, a heating rate of 1 °C/min was chosen since higher rates may lead to spalling of the concrete or mortar. After the heating period, the oven was turn off and the samples were passively cooled.

Conversely, the CS samples were tested immediately without a heat treatment. To ensure a parallel cross-sectional area, samples were cut with a slow-speed saw followed by wet grinding with 100 grit silicon carbide paper. This was done before physical testing (i.e., after the heat treatment for the respective samples), and the height was measured for the subsequent displacement and axial engineering strain calculations. The room temperature and cooled concrete monoliths were tested for compressive strength (σ) following ASTM C39/C39M-21. The elastic modulus (*E*) was calculated as the slope of the elastic region in the stress vs. axial engineering strain (ε) curve. The reported compressive strength was the maximum compressive stress in the elastic region. Figure is a representative example of a stress-strain curve annotated with the elastic region, the linear fit, and the reported strength.

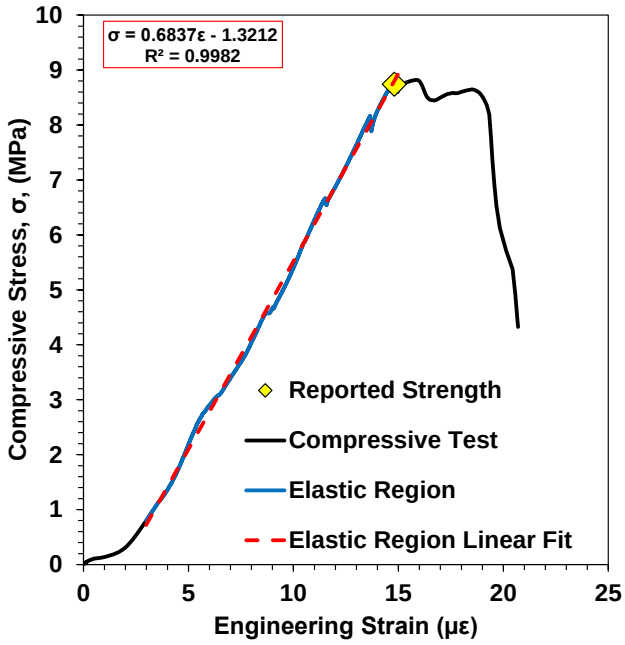

Figure 5.1. Representative compressive test curve of CS sample nine from batch one. The slope of the elastic region is used as the elastic modulus (*E*), and the reported compressive strength (σ) is the maximum of that elastic region.

Since the CS specimens were not heat treated, the dataset only contains 28-day room temperature physical property measurements. To provide a more robust analysis of the failure of the samples, statistical treatment via Weibull distribution statistics was conducted. In the context of materials, Weibull statistics assume that a given volume of material under a uniform stress will fail at the greatest flaw (i.e., material is limited by its the weakest link). For cementitious waste forms, this would provide the stress that would initiate a crack, reducing the transportation distance for contaminants and significantly diminishing the immobilization performance. The PDF and CDF of the two-parameter Weibull distribution are given by the following equations:

$$p(\sigma) = \left(\frac{m}{\sigma_0}\right)\left(\frac{\sigma}{\sigma_0}\right)^m \exp\left[-\left(\frac{\sigma}{\sigma_0}\right)^m\right] \quad \text{Eq. 5.1}$$

$$P(\sigma) = 1 - \exp\left[-\left(\frac{\sigma}{\sigma_0}\right)^m\right] \quad \text{Eq. 5.2}$$

Here, $p(\sigma)$ is the probability of the occurrence of a specific stress (σ), whereas σ_0 and m are the scale and shape parameters. Conversely, the CDF or $P(\sigma)$ is the probability that the specific stress is greater than population data or, in other words, the probability of failure. The σ_0 is greater than 63.2% of the population of stresses, whereas the latter parameter, m, represents the data scatter of the distribution so that a lower value of m corresponds to a broad distribution whereas a higher value represents a sharp transition at σ_0. In material science and failure analysis fields, this term m is often referred to as the Weibull modulus.

The CDF can be linearized into a two-point linear equation to estimate the two parameters: σ_0 and m. This can be done by taking the complement of the probability of failure and the probability of success $S(\sigma)$, and through rearranging and simplification using the properties of logarithms, Eq. 5.4 is obtained. In the linearized formula, the left side of the equation is treated like a dependent variable whereas the Weibull modulus, $\ln(\sigma)$, and $\ln(\sigma_0)$ are the slope, independent variable, and x-intercept of the line, respectively. The term $P(\sigma_i)$ is the probability of failure for a stress sample i, which is determined based on the estimator formula from ASTM C1239-13 (2024), Eq. 5.5. Here, the term N is the total number of specimens, each assigned a number i. The individual strengths are ordered from weakest to strongest, so the weakest specimen is assigned the number one whereas the greatest number is assigned the number N. Once the "x" and "y" data are calculated, the subsequent m and σ_0 parameters can be calculated:

$$S(\sigma) = 1 - P(\sigma) = 1 - \left(1 - \exp\left[-\left(\frac{\sigma}{\sigma_0}\right)^m\right]\right) \quad \text{Eq. 5.3}$$

$$\ln[-ln[1 - P(\sigma)]] = m\ln(\sigma) - m\,ln(\sigma_0) \quad \text{Eq. 5.4}$$

$$P(\sigma_i) = \frac{i - 0.5}{N} \quad \text{Eq. 5.5}$$

5.1.3.2 Software Development and Simulations

PD is a relatively recent reformulation of continuum mechanics (Silling 2000). Unlike traditional methods where material points interact over infinitesimal distances, PD allows interactions through bonds over finite distances. This is exhibited in material models where the material response is described by integral operators rather than spatial derivatives. A major benefit of this approach is the reduction in the regularity requirements imposed on the solution, allowing for the natural evolution of fractures and other discontinuities.

PD has been used successfully to describe a variety of phenomena such as crack branching (Bobaru and Zhang 2015), sintering (Silling et al. 2017), spalling (Silling et al. 2023), and chemomechanical failure (Jones et al. 2021; Chen and Bobaru 2015). The aim of this project is to develop PD capabilities for Hanford grout applications. To facilitate the exploration and validation of relevant models, the project team used the massively parallel open-source PD code Peridigm, which was originally developed at Sandia (Parks et al. 2012; Littlewood et al. 2024). This project has yielded several important enhancements to Peridigm, such as the implementation of a new solver and material models.

Many of the applications of interest at Hanford for PD require long timescales and recognize the need for capabilities to solve quasi-static problems. While Peridigm has built-in implicit solvers, these solvers currently experience significant challenges when damage is encountered and were not suitable for the test cases here in their current form. To address this, a dynamic relaxation solver was integrated into Peridigm, permitting quasi-static analysis. Several material models were also implemented into Peridigm.

For initial validation of material models, the aim was to compare simulation results with experimental data. The first experiment considered involved a grout cylinder composed of coarse and fine aggregates (OPC concrete from the previous section) subjected to uniaxial compression. Due to the relatively small dimensions of the cylinders in the study, the grout was expected to behave as a quasi-brittle material. The team considered several existing quasi-brittle PD material models from the literature (Gerstle et al. 2005; Zaccariotto et al. 2015; Lai et al. 2018; Niazi et al. 2019), ultimately focusing on the bilinear model proposed by Zaccariotto et al. (2015) due to its simplicity, ability to match model parameters to commonly measured engineering quantities, and capacity to represent softening as an irreversible process – features not shared by all models.

The first test case considered involved the changing properties of the concrete used in the Hanford tanks and any changes in properties due to the thermal history of the concrete while in service. Due to the environmental conditions expected in grouted material at Hanford, relevant material models must consider variations in material properties in response to factors such as material degradation, temperature variations, and heterogeneity. Previous work developed a model with this potential into Peridigm (Jones et al. 2021; Trageser et al. 2022; Torrence et al. 2022); however, the model did not include softening, making it less applicable to simulating material response in grout. Taking inspiration from Zaccariotto et al. (2015), softening was incorporated into the model. This enhanced model allows for parameter changes due to various phenomena, including temperature variation, degradation, heterogeneity, and softening, which are essential for accurately describing material response in grout under the desired environmental conditions. The corresponding material model was then implemented into Peridigm.

5.1.4 Results to Date

5.1.4.1 Experimental Results – Conventional Concrete

The concrete mixing produced adequate samples. Open porosity was observed on the outside façade of all the samples. Size varied from “pinhole” to larger – on the order of a few millimeter – cavities. Heat treatment of the concrete samples appeared to have minimal effects on the specimens. Representative photos in Figure 5.2 of the control as well as the specimens before and after firing show the fired samples change color to a dull gray. No other color changes were observed, such as red/orange coloring due to oxidized aggregate. Additionally, no cracks after the heat treatment were observed.

(a)

(b)

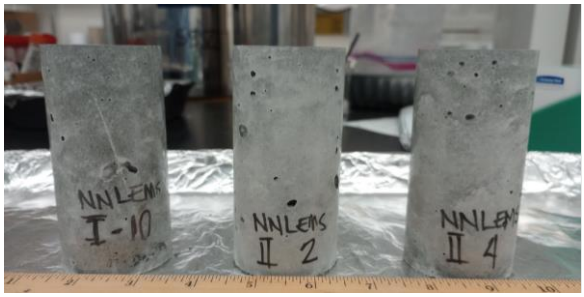

(c)

(d)

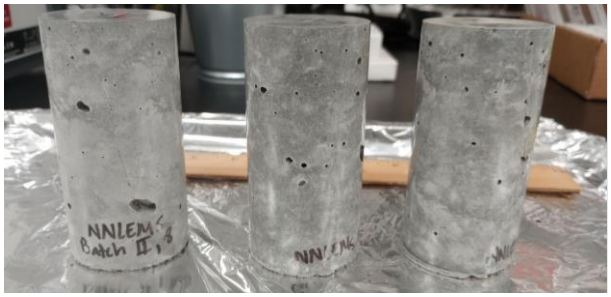

(e)

Figure 5.2. Photos of (a) control (i.e., non-heat treated) concrete samples, (b,c) samples before and after firing at 94 °C, and (d,e) samples before and after firing at 149 °C. Examples of pinhole porosity (solid) and larger cavities (dashed) are circled in panel (a).

Increasing the heat treatment temperature had limited effect on the compressive strength (all three heat treatment temperatures exhibited similar compressive strength within the standard deviation), as shown with the goodness-of-fit 0.0909 R^2 for a linear model, while the elastic modulus of the concrete exhibited a slight decrease with temperature treatment R^2 0.7715, as shown

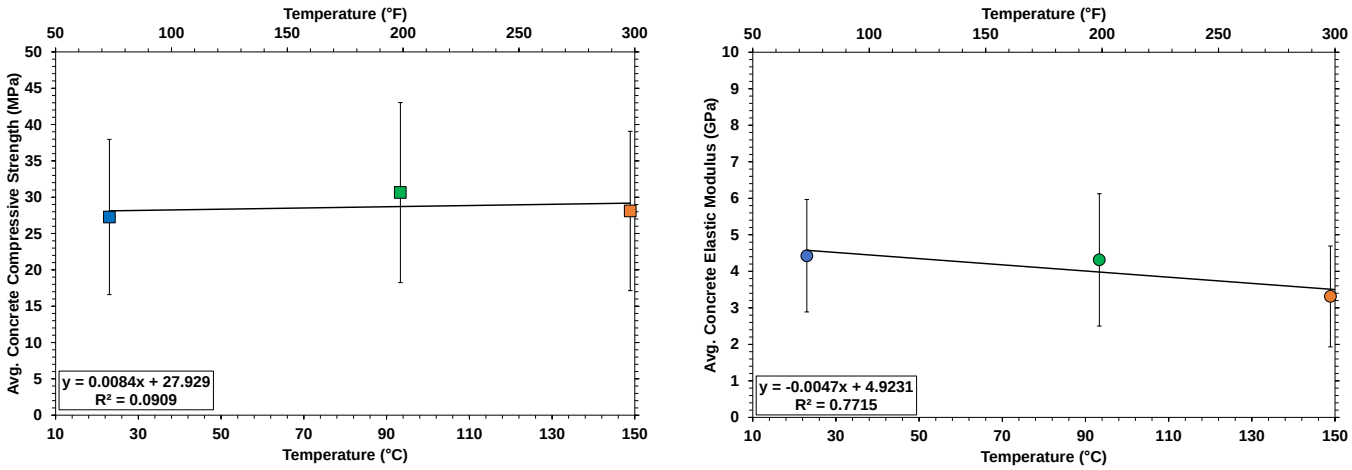

(a) (b)

Figure 5.3 and tabulated in Table 5.3. This did not lead to any changes in the fracture patterns, with patterns 2 and 3 being prevalent in all three temperature regimes.

Table 5.3. Summary of the concrete physical properties: 28-day avg. compressive strength, 28-day avg. elastic modulus, and the fracture patterns measured and observed during testing.

Temperature	Avg. 28-day Compressive Strength (MPa)	Avg. 28-day Elastic Modulus (GPa)	Fracture Patterns
Control	30.28 ± 7.64	4.51 ± 1.59	2,3,2
94 °C (200 °F)	31.58 ± 11.22	4.40 ± 1.77	2,2,4
150 °C (300 °F)	29.84 ± 8.53	3.57 ± 1.16	3,2,2

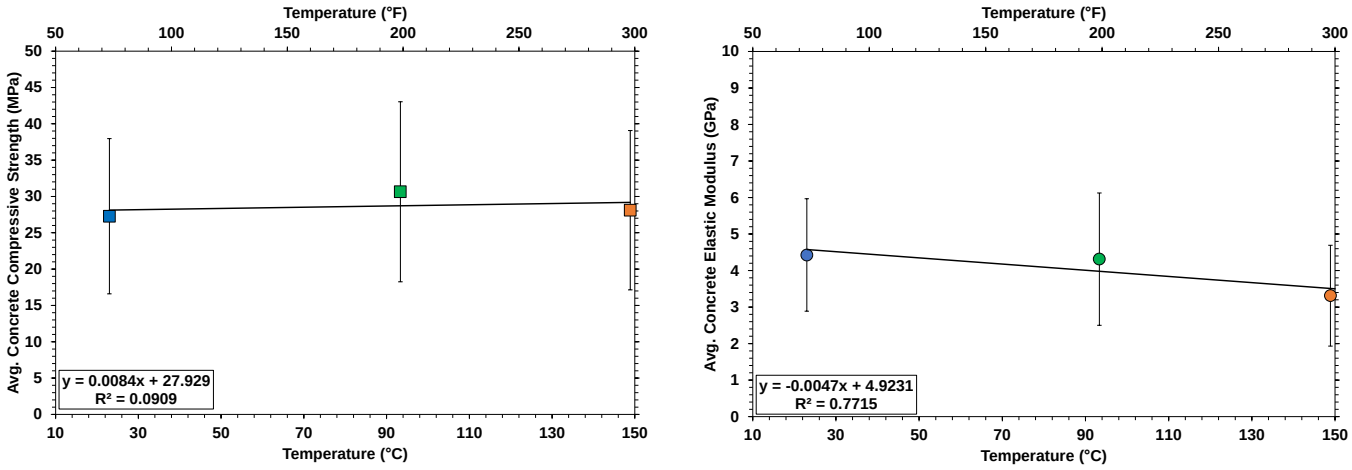

(a) (b)

Figure 5.3. (a) Average 28-day compressive strength and (b) average elastic modulus of concrete as heat treatment temperature increases. The standard deviation is represented by the error bars.

These results align with the scientific literature examining how heat exposure can damage concrete (Khoury 2000). The hydrates in concrete only begin to decompose above 100 °C and, given the

temperature data, the concrete likely experienced dehydration of free water and loosely bound water within certain hydrates such as ettringite and calcium silicate hydrate gel. However, the extent of damage was less than for worst-case conditions such as temperatures above 300 °C (572 °F), where catastrophic strength loss and explosive spalling may occur. Likewise, the lack of cracks disqualifies thermal expansion mismatch at 150 °C or, similarly, any volume changes due to phase changes (e.g., α-quartz to β-quartz). From the physical testing, three types of facture patterns were observed. Typical fracture pattern adapted from ASTM C39/C39M-24 are included in Figure 5.4 with corresponding examples from concrete specimens included in Figure 5.5.

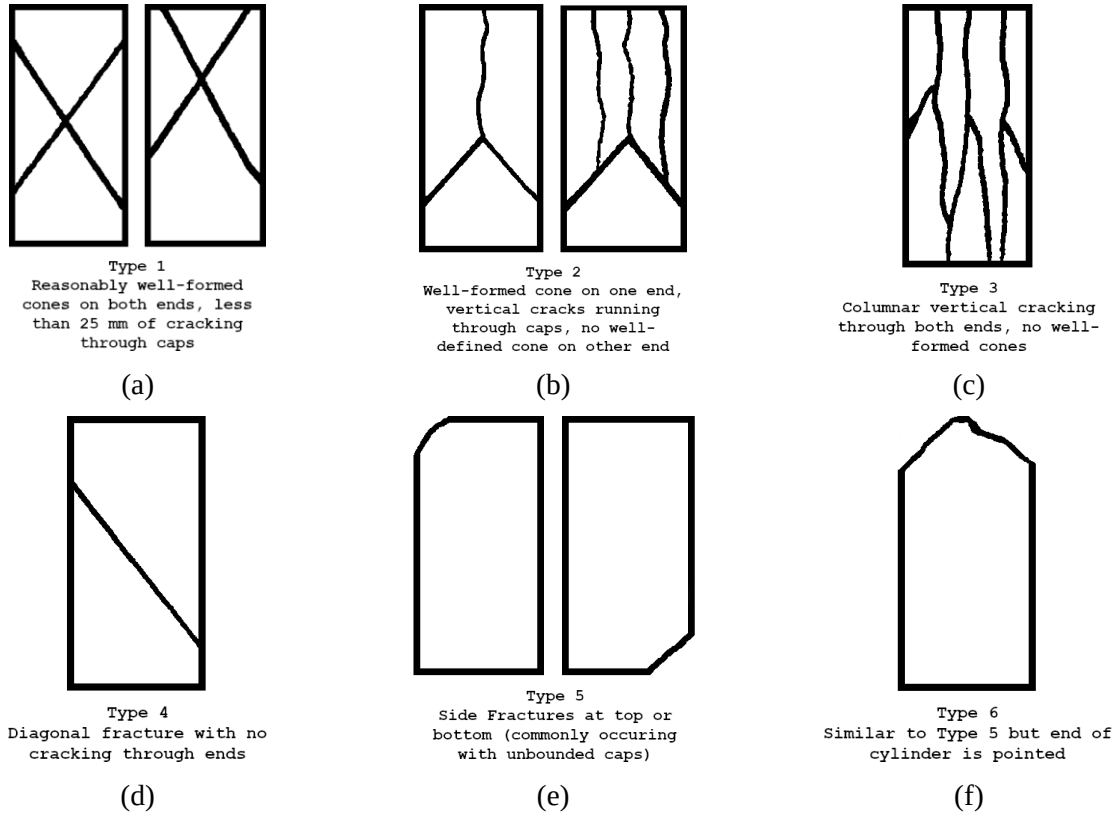

Figure 5.4. Cartoons of typical fracture patterns based on ASTM C39/C39M-24. Here, “caps” are secondary materials like neoprene, sulfur mortar, or high-strength gypsum plaster placed at the ends of samples to facilitate C39/C39M planeness requirements. These secondary materials were not used for these tests. Fracture is not limited to these patterns.

Generally, the cementitious binder matrix was the source of failure rather than any large aggregate. The inclusion of large aggregate, while within the recommendations of ASTM C192/C192M-24 of being less than three times the mold diameter, appeared to affect the propagation of the crack during testing, leading to a mismatch in fracture pattern in the results compared to experimental results. This finding prompted the batching of mortar samples. These observations are used to compare against PD modeling in the section that follows.

(a) (b) (c)

Figure 5.5. Photographs of representative concrete specimens depicting the different fracture patterns from Figure 5.4. (a) Batch 1 Sample 10 fired at 94 °C pattern 2, (b) Batch 1 Sample 1 fired at 149 °C showing pattern 3, and (c) Batch 2 Sample 2 fired at 94 °C. Patterns 2 and 3 were as prevalent as the resulting pattern, whereas pattern 4 only occurred once during testing. Note: The photo in panel (a) is rotated to better show the fracture pattern.

5.1.4.2 Experimental Results – Conventional Mortar

Similar to the concrete samples, there were open cavities and “pinhole” pores on the surface of the monoliths; however, the porosity was not as prevalent compared to the concrete samples. The coloring of the mortar samples varies; it was generally lighter compared to the concrete samples. After firing, independent of temperature, the color transformed into a uniform buff gray. No cracking was observed after the firing process. Figure 5.6 presents representative photographs of the control and comparison samples.

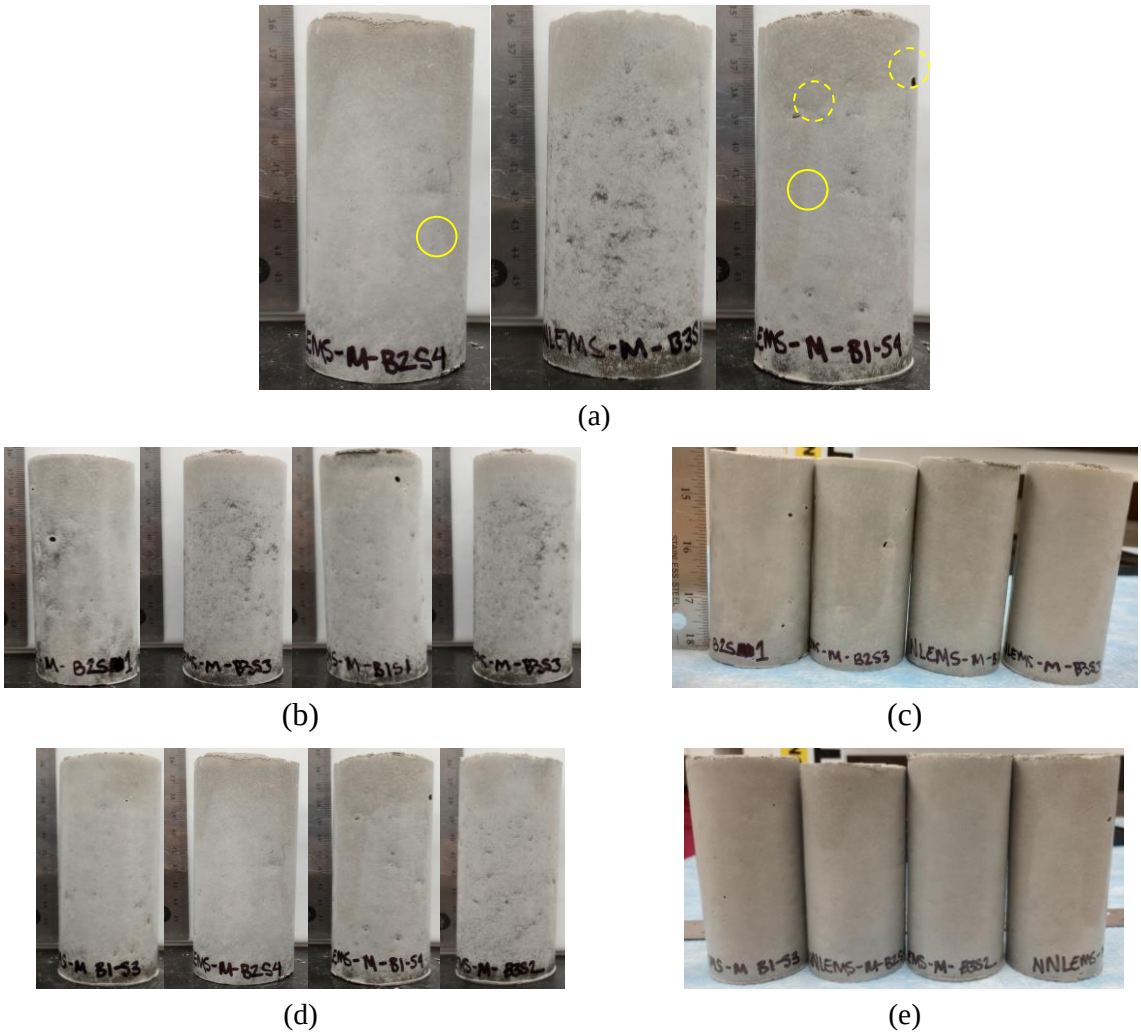

Figure 5.6. Photos of (a) non-heat-treated mortar samples, (b,c) samples before and after firing at 94 °C, and (d,e) samples before and after firing at 149 °C. Examples of pinhole porosity (solid) and larger cavities (dashed) are circled in panel (a).

The effect of increasing the heat treatment temperature on the mortar's 28-day compressive strength and 28-day elastic modulus was again limited, Table 5.4 and Figure 5.7. Other than one sample, the fracture patterns observed were mostly 2 and 3 (4 out of 10 and 5 out of 10, respectively). However, unlike the concrete sample, where increasing the temperature led to a slight *decrease* in performance, the mortar physical properties exhibited slight *increases* as the heat-treatment temperature increased.

Table 5.4. Summary of the concrete physical properties: 28-day avg. compressive strength, 28-day avg. elastic modulus, and the fracture patterns measured and observed during testing. Note: Two control specimens broke prematurely before testing.

Temperature	Avg. 28-day Compressive Strength (MPa)	Avg. 28-day Elastic Modulus (GPa)	Fracture Patterns
Control	21.58 ± 6.34	2.81 ± 1.15	4,3
94 °C (200 °F)	33.39 ± 14.96	4.56 ± 1.87	2,3,3,3
150 °C (300 °F)	29.20 ± 3.32	3.62 ± 1.06	2,3,2,2

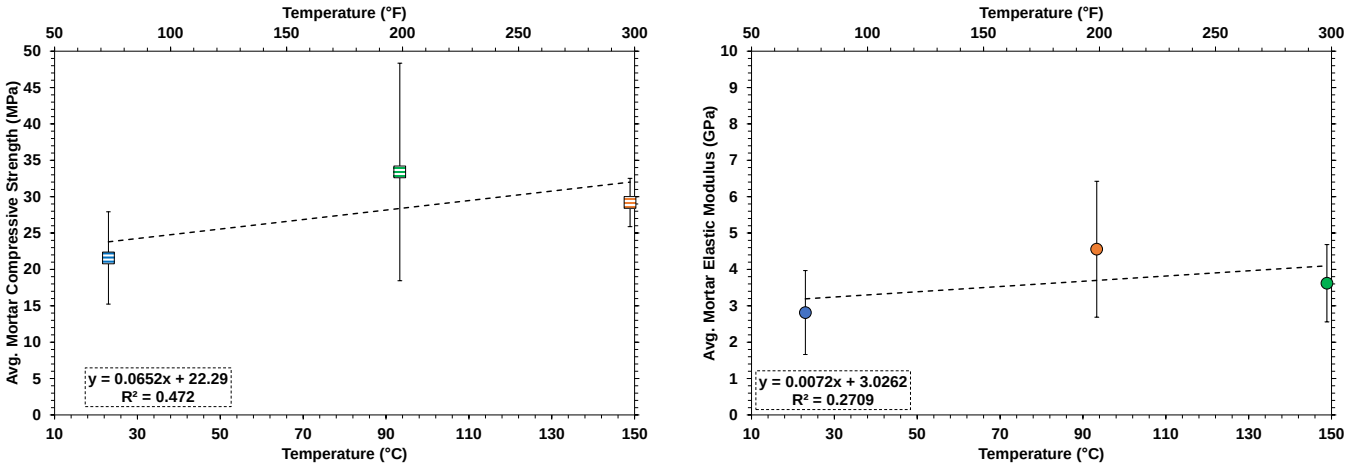

(a) (b)

Figure 5.7. (a) Average 28-day compressive strength and (b) average elastic modulus of mortar samples as heat-treatment temperature increases. The standard deviation is represented by the error bars.

While certain factors like a more controlled mixing regime likely homogenized the mortar more than hand-mixing the concrete, there were likely additional factors that could have caused this difference. As previously seen in the concrete samples and in mortar samples in Figure 5.8, the cement matrix was the weaker phase regardless of temperature treatment. Many cracks deflect around the fine aggregate in Figure 5.8, although one crack transverses one larger aggregate. Regardless of the type of cementitious material, cement matrix is the “glue” that contains the fine and/or coarse aggregate to create the mortar or concrete composite. However, within the monolith volume, the concrete samples would be expected to contain a smaller volume of cement compared to the mortar due to the inclusion of coarse aggregate in the mix design. Therefore, if there is less cement and that cement is the weakest link, especially with increasing heat treatment, those effects would be magnified compared to the mortar.

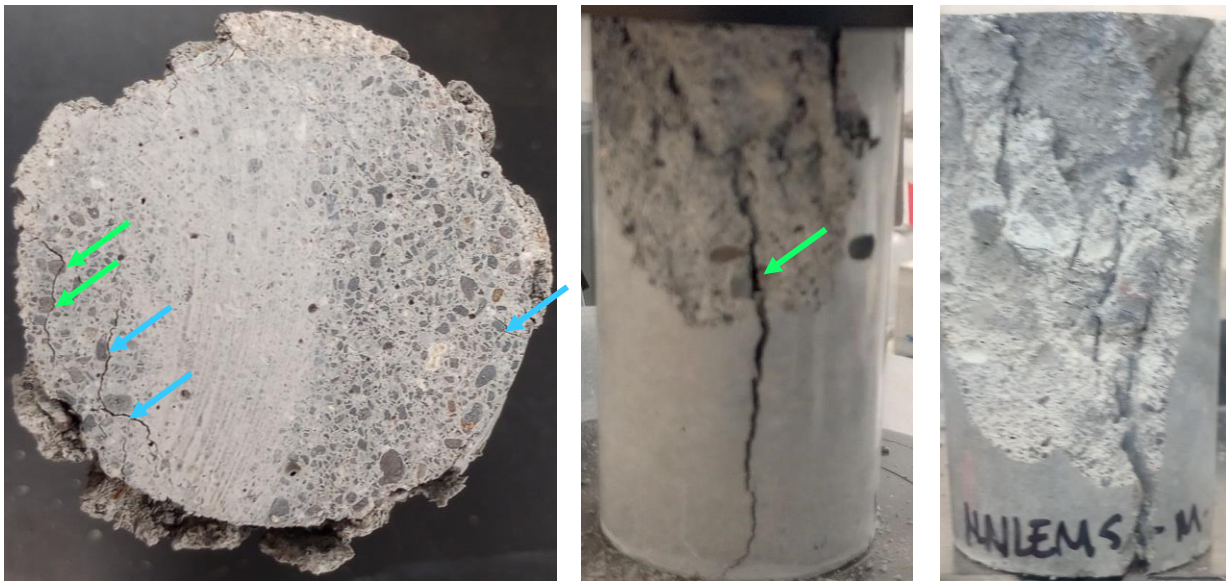

(a) (b) (c)

Figure 5.8. (a) Top surface of control mortar (Batch 1 Sample 2). (b) Fracture surface Batch 2 Sample 3, (c) Fracture surface Batch 2 Sample 1. Blue arrows show fine aggregate deflecting the propagation of a crack whereas green arrows show a crack traversing an aggregate.

5.1.4.3 Experimental Results – Cast Stone

Figure 5.9 shows a photograph of a representative CS sample (Batch 1 Sample 9) before and after crushing. The surface is smooth and has a gray-white color. After fracture, the green-blue color commonly observed in BFS-containing mixtures is observed. Literature sources have determined that sulfur chromophore(s) such as S_3^- and S_2^- significantly contribute to the blue and green coloring (Chaouche et al. 2017; Le Cornec et al. 2017).

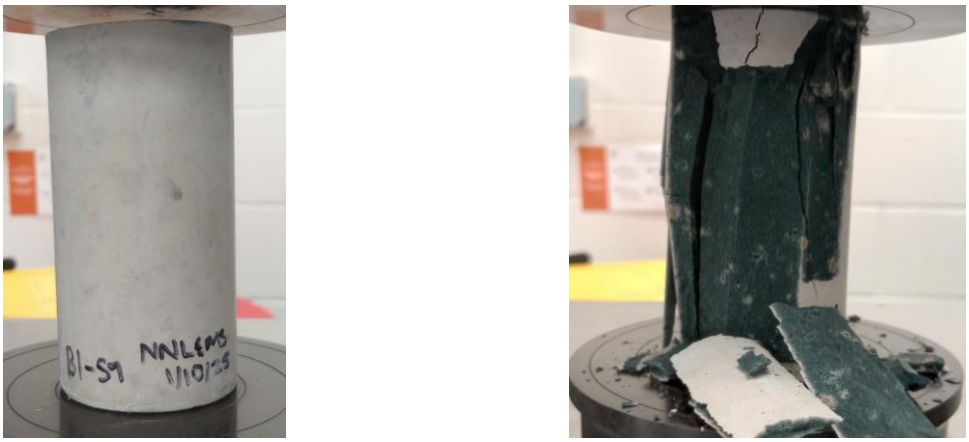

(a) (b)

Figure 5.9. Representative photos of the 50 mm Ø × 100 mm CS cylinder (a) before and (b) after type 3 fracture. The green-blue color is commonly observed in BFS-containing mixtures.

The strength and elastic modulus were 8.527 MPa ± 3.744 MPa and 1.170 GPa ± 0.679 GPa, respectively. This is less than the conventional concrete and mortar samples. Since many samples were fabricated, additional failure analysis was conducted using Weibull statistics. Figure 5.10 shows the linearized data as well as the calculated *m* and σ_0 values: 2.548 and 12.44 Mpa, respectively. Although the R^2 value is near unity at 0.9523, deviation from linearity indicates different flaw populations within the tested samples contributing to the failure of the material.

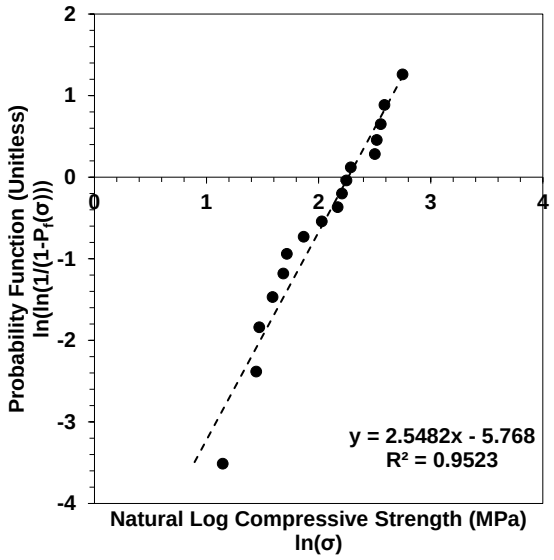

Weibull Modulus *m* (unitless)	Scale Parameter σ_0 (MPa)
2.548	12.44

Figure 5.10. Probability function vs. natural log of CS compressive strength (i.e., Weibull plot). The *m* and σ_0 parameters (slope and x-axis intercept) were calculated from the linearized dataset. Seventeen samples were tested.

These parameters were used to create the 28-day compressive strength CDF shown Figure 5.11. Within the population data, the average strength of failure is 11.04 MPa. The upper, median, and lower quartiles are 14.15, 10.77, and 7.64 Mpa, respectively, with a standard deviation of 4.66 MPa. Additionally, the probability failure was calculated for thresholds of interest. The Nuclear Regulatory Commission has a technical requirement of 3.45 MPa (500 psi), which for the CS 50 Ø mm × 100 mm specimen had a 3.7% probability of failure at 28 days, whereas the IDF threshold is 0.5 MPa, which for the same samples at 28 days had a 0.028% probability of failure.

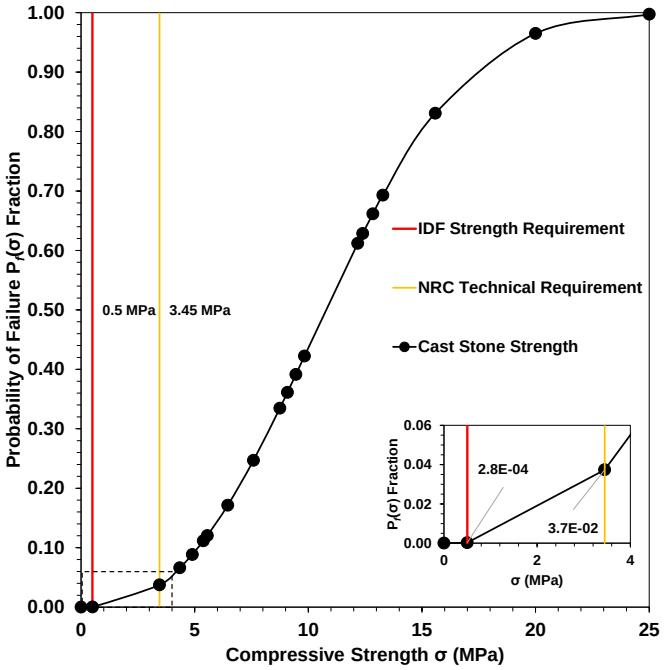

Figure 5.11. Cumulative probability distribution of the tested CS specimens annotated with IDF and Nuclear Regulatory Commission thresholds. The inset (bottom right) is an enlarged image the intersection of the probability function and the regulatory thresholds.

There are limitations to the analysis of the dataset. First, the dataset was relatively small, and this leads to inaccurate estimations of the true Weibull modulus. The literature varies on the number of samples necessary, with recommended sample sizes of 30, 60, or even 100+ for a "sufficient" experiment (Quinn and Quinn 2010; Nohut 2014). No attempt was made to characterize the origin of the flaw (e.g., surface flaw or volume flaw) that led to the failure of the material through forensic fractography.

Finally, it is not immediately clear that a Weibull distribution would be sufficient to describe the effect of flaw distribution. Vu et al. (2022) showed that the Weibull distribution does NOT scale to larger volumes of concrete. This is likely due to differences in sample scale such as the proportion of aggregate, the interface between aggregate and paste, the amount of porosity, porosity connectivity, and processing parameters such as mixing affecting the type and distribution of flaws within their samples. While CS does not have aggregate, the microstructure could change due to differences in simulant concentration or composition. These changes can impact the activating reaction, leading to the differences in the reaction products and consequentially physical performance.

5.1.4.4 Computational Results

With the implementation of the necessary solver and material model capabilities into Peridigm, the next phase of the project focused on describing material response in grouts. PNNL conducted several experiments to be used for validation of material models of interest. These results are presented in Section 5.1.3.1. The observations of lab samples under compression can be compared to the predictions of failure pattern in Peridigm.

The simulations were conducted with Peridigm, which uses a meshless discretization of the domain. An example discretization of the domain can be seen in Figure . A no-slip boundary condition where the caps come into contact with the grouted cylinder was applied. The bottom cap is stationary while the top cap

compresses the cylinder up to an engineering strain of 0.01. The team explored a wide range of parameter permutations, such as percentage of aggregate packing as well as varying material parameters, as some uncertainty exists, particularly for the interface between aggregates and grout.

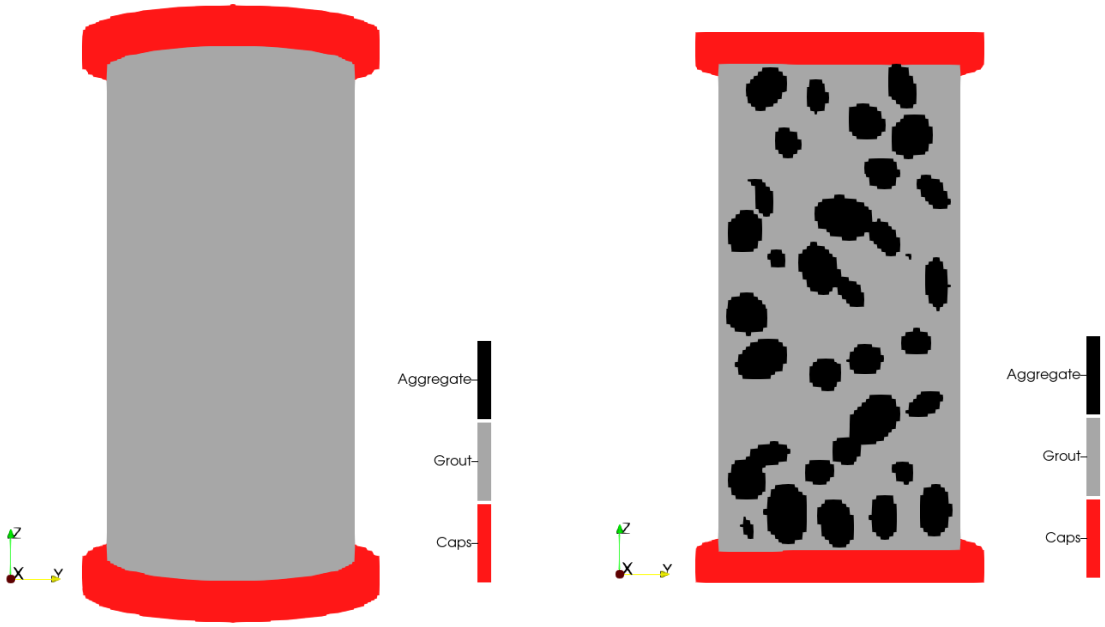

(a) Discretization for the uniaxial compression geometry

(b) Cross-section of the discretization for the uniaxial compression geometry

Figure 5.12. Discretization for the uniaxial compression test geometry with 20% aggregate packing.

Qualitatively, some of the expected behavior is observed. For instance, in Figure a, the characteristic x pattern appears, which is often seen in uniaxial compression tests when the material is more homogeneous. The larger aggregates used in the experiment do play a significant role in the resulting fracture patterns. In particular, from Figure b, Figure c, and Figure d, it was observed that the configuration of aggregates may prevent deeper penetration of the fracture into the cylinder, which is what was seen in the experimental results, see Figure 5.5a-c, where much of the damage is concentrated at the surface of the cylinder rather than the interior. These differences will be refined in Year 2.

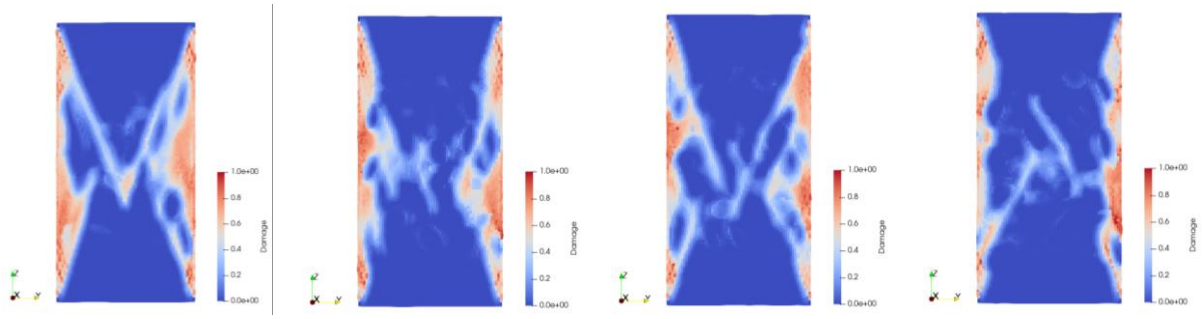

(a) 5% aggregate packing.

(b) 10% aggregate packing.

(c) 15% aggregate packing.

(d) 20% aggregate packing.

Figure 5.13. Fracture pattern cross-section for various aggregate packings.

From a more quantitative perspective, the damaged bonds in the system will also show when damage initiates in the simulations. Figure compares the percentage of broken bonds to the engineering strain. Interestingly, the aggregate packing percent did not appear to play a large role in the initialization of damage. The amount of aggregates did, however, slow the accumulation of damage in the structure, allowing a larger strain before complete failure. The engineering strain at failure is reasonable when compared to experimental results where the engineering strain was observed between 0.007 and 0.0015. Small perturbations to the strength of the interface between the grout and aggregate did not yield significantly different results. The configuration of the aggregates was seen as far more important in determining the resulting fracture network and strength of the cylinder.

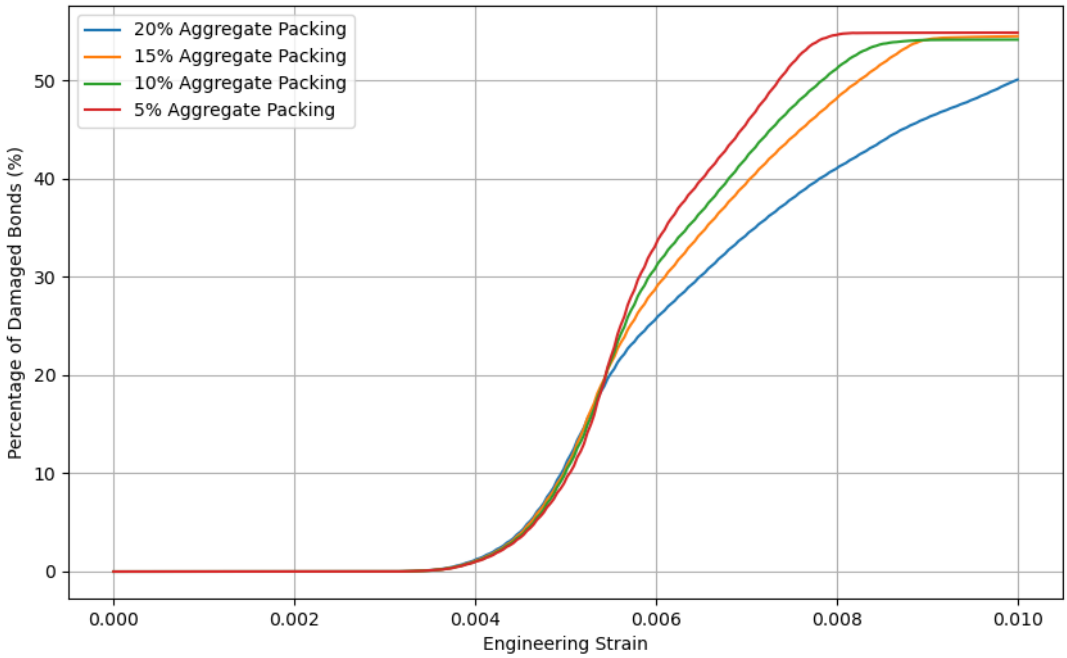

Figure 5.14. Comparison of percent of broken bonds in the cylinder against the engineering strain for 5%, 10%, 15%, and 20% aggregate packings.

5.1.5 Path Forward and Integration

5.1.5.1 Experimental Path Forward and Integration

In Year 2, additional samples will be evaluated and compared against PD modeling. Both OPC mortar bars will be characterized that will are likely a better representation of the PD model since the fine aggregate is expected to cause less deviation than the larger gravel. Likewise, the ASTM mixing method and equivalent sample distribution is expected to limit any differences between batches and heat treatments. The CS samples will be tested to measure strength and elastic modulus without any heat treatment and provide data for a waste form case in the PD models. Unlike the conventional binders, the large number of samples can provide insight into the average performance of the CS monolith.

5.1.5.2 Computational Path Forward and Integration

Year 1 efforts were primarily focused on model selection and validation as well as code development. Although early results look promising, model validation is still ongoing.

- ***Subtask 4.1.1 – Continued Validation:*** The data PNNL is generating for mortar cylinders is expected to be easier to replicate with PD simulations due to the reduced dependence on aggregate configuration. Once the model is further validated, material response will be explored in relation to perturbations of material parameters due to environmental changes, loading conditions, and geometry.
- ***Subtask 4.1.2 – Waste Form PD Modeling:*** Year 2 efforts will shift toward PD modeling of grout waste forms. Model validation with material degradation present is of particular interest. There is also strong interest in leveraging other modeling efforts within the team, particularly the mesoscale modeling from Section 4.2. The PD framework is especially well-suited for upscaling from other material models such as those found in molecular dynamics (Seleson et al. 2009; You et al. 2022). It is anticipated that the mesoscale models will provide valuable insights and contribute to an improved PD model of grout waste forms.

5.2 Theme 4 Task 2: Maturation of Mesoscale Models for Hanford Grout

5.2.1 Team Members

Shenyang Hu (PNNL), Yulan Li (PNNL)

5.2.2 Background

As grouts age, there are spatial changes in the bulk material properties due to natural evolution of hydration products and interactions with the near-field environment. These bulk properties can directly impact the migration behavior of contaminants within the porous network of the grout. As such, one key grout property is porosity, which dictates the flow of water within the grout and associated diffusion of aqueous species. While geochemical speciation modeling (Theme 3 Task 1) can derive properties such as tortuosity changes, the micro-scale features of the porous grout network (e.g., connectivity) are not replicated. As such, a gap remains between the grout's chemo-mechanical processes occurring on the microscale and the bulk properties. This task aims to begin to bridge this fundamental gap in grout modeling by developing mesoscale models of a Hanford grout system and assessing a migratory process in this network.

Mesoscale modeling holds promise for investigating the microstructural processes within grouts that combine to dictate bulk material behavior. Prior development of mesoscale models occurred in the Center for Hierarchical Waste Form Materials Energy Frontier Research Center (EFRC) (Li et al. 2022a; zur Loye et al. 2018), where the aim was to develop advanced nuclear waste form materials through advanced synthesis, characterization, and multiscale modeling. Within this EFRC, a generic mesoscale model of ion exchange and leaching in multiphase porous structures was developed, as shown in Figure . The mesoscale model takes into account multi-physics coupling such as ion diffusion, interface reaction, porous media flow, elastic and electric interactions, phase transition, and microstructure evolution in a representative volume using a grout base case (geopolymer / zeolite particle composites) (Li et al. 2022b). During grout waste form aging, similar physics are expected, including diffusion in porous structures, microstructure change associated with oxidation and carbonation, deformation and cracking due to phase transition-induced volume change, leaching, and interface reaction (Li et al. 2022a). This multi-physics

coupling may be key to linking chemo-mechanical processes within the grout to bulk properties, providing technical defense-in-depth for the processes captured in the *Hanford Grout Modeling Framework*.

The mesoscale modeling outputs are (1) the time and spatial evolution of species concentrations, stresses, and microstructures; (2) the effect of evolving microstructures on leaching kinetics; and (3) the effect of evolving microstructures on material properties such as effective diffusivity. These results can be directly compared with microstructures and material properties obtained from experiments. The mesoscale simulations can also generate a huge amount of virtual data on material performance and property degradation.

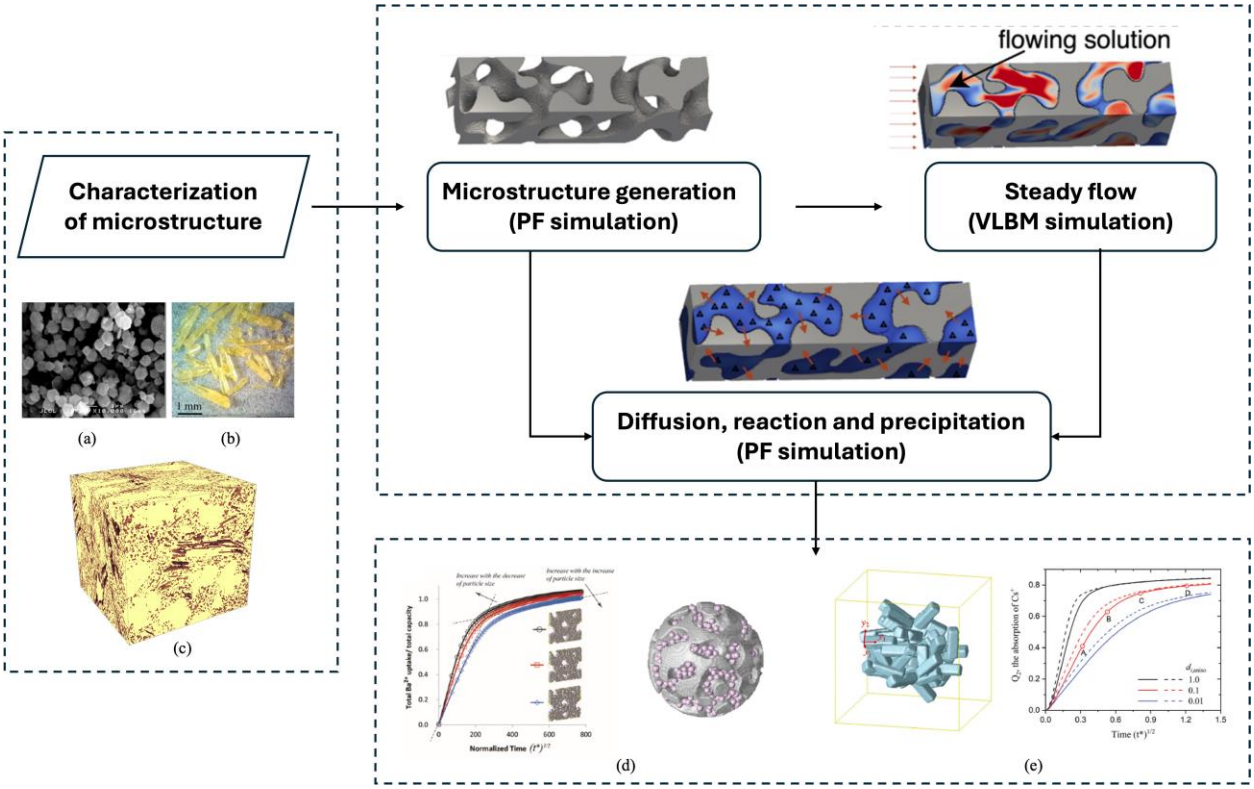

Figure 5.15. A mesoscale model of adsorption and/or desorption in porous structures during batch and column processes (Li et al. 2022a; Proust et al. 2024). (a) Scanning electron micrograph (SEM) of LTA-zeolite particles, (b) optical images of salt inclusion single crystals, (c) focused ion beam (FIB)-TEM image of geopolymer-based waste-form materials, (d-e) effect of microstructures on radionuclide absorption.

The mesoscale models developed in this work are first of their kind for contaminant behavior in grout waste forms. The results presented utilize the best available data from the literature, but material-specific data will replace specific inputs in future iterations. The target of this tool would be a complementary approach to the *Hanford Grout Modeling Framework* that can link chemo-mechanical processes.

5.2.3 Technical Approach

The target system to develop the first Hanford-based mesoscale grout models was a grouted solid secondary waste, specifically a silver mordenite (AgM) particle stabilized in the CS formulation (Fujii Yamagata et al. 2022). This system is of interest as it has been reported that during leaching, the Ag

contained on the zeolite migrates through the grout matrix, providing a “barrier” against iodine migration through the matrix and out of the waste form. However, there are no modeling estimates of this process based on the fundamental physics and chemistry, and as such, this presents an opportunity to develop a mesoscale model.

Figure illustrates the microstructure and elemental distribution in the CS matrix with AgM granule particles (Fujii Yamagata et al. 2022). Figure e shows that Ag dissolved from AgM particles has very inhomogeneous distribution. Ag segregates mostly at the interface between AgM and CS; and Ag concentration in the unreacted FA and BFS particles is very low. The inhomogeneous Ag distribution indicates inhomogeneous electrochemical potential as well as inhomogeneous reaction/dissolution rate in this multiphase microstructure. The goal of this effort is to develop a mesoscale model that accounts for the effect of inhomogeneous microstructures on the kinetics of dissolution, diffusion, reaction and precipitation; improve the understanding of the physics and kinetics behind the microstructure and property evolution; identify when approximating grout as a homogeneous material fails; and determine the relationship between microstructures and properties such as effective diffusivity for macroscale grout performance models.

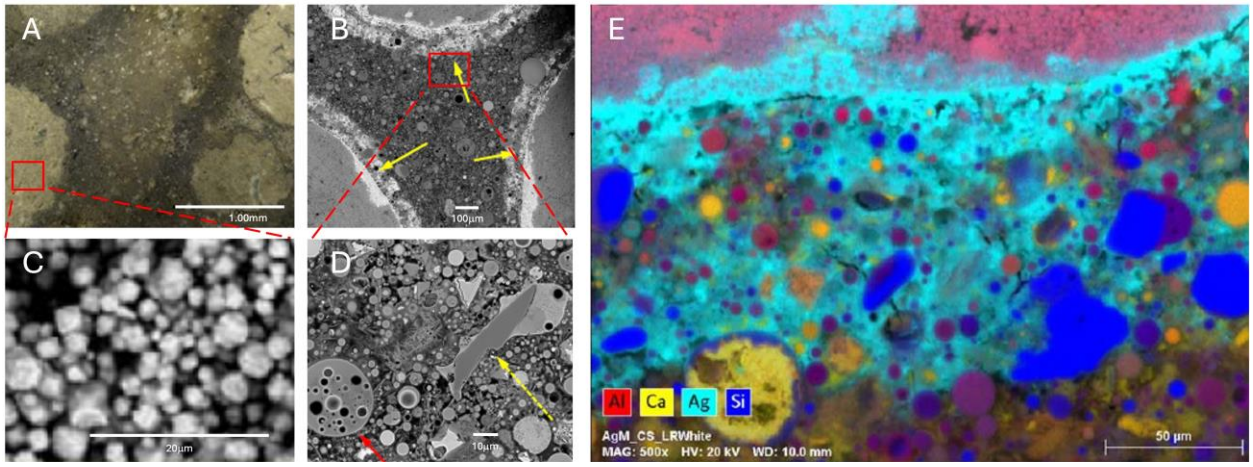

Figure 5.16. (a-d) SEM backscattered electron images of microstructures at magnification levels in the CS matrix with AgM granules. (a) CS matrix with AgM particles; (b) the yellow arrow points to the AgM-CS interface; (c) enlarged image of the AgM particle with mesoscale pores and AgM polycrystalline grains; (d) enlarged image of porous CS with macroscale pores, FA, and BFS particles; the red arrow points to a spherical FA particle while the dashed yellow arrow to a BFS particle; and (e) elemental energy dispersive X-ray spectroscopy dot map near the interface between an AgM granule and CS shown in (c).

5.2.3.1 Description of Mesoscale Model

Based on the microstructure shown in Figure , the mesoscale model of Ag dissolution considers the primary microstructure features, including the average sizes of AgM, FA, and BFS particles; their volume fractions; and the porosity in the CS matrix and AgM particles. The model assumes five phases co-exist: AgM, FA, BFS, porous CS matrix, and Ag precipitate (ppt). In the framework of a mesoscale phase-field approach (Chen 2002; Li et al. 2017), two sets of field variables are used to describe the temporal and spatial evolution of chemistry and microstructures. One set of field variables is the concentration of diffusive species, and the other set is about the order parameters. The concentration field $c_i(\boldsymbol{r},t), i = Ag^+,\ Ag,$ and pore water (PW) describe the evolution of Ag^+ ion, Ag^0, and groundwater concentrations, respectively. The order parameter field $\eta_p(\boldsymbol{r},t), p = AgM, FA, BFS,$ porous $CS,$ and Ag ppts describe the morphology evolution of different phases, respectively. $\boldsymbol{r} = (x,y,z)$ and t are the spatial coordinate and

time, respectively. In the model, the lattice of AgM phase is taken as the reference, i.e., the Ag concentration is $c_{Ag^+}(\boldsymbol{r}, 0) = 0.5$ inside AgM at initial stage. The equilibrium concentrations of Ag and Ag ion and PW in different phases are denoted as $c_{p,i}^{eq}$, $p =$ AgM, FA, BFS, porous CS, and Ag ppts, $i = Ag^+, Ag,$ and PW. For example, in AgM particles, the equilibrium concentrations are $c_{AgM,Ag^+}^{eq} = 0.5, c_{AgM,Ag}^{eq}$, and $c_{AgM,PW}^{eq}$, respectively. In Ag ppts, the equilibrium concentrations are $c_{Ag,Ag^+}^{eq}, c_{Ag,Ag}^{eq}$, and $c_{Ag,PW}^{eq}$, respectively. $c_{p,i}^{eq}$ are thermodynamic properties of phases that depend on local environment or experimental conditions such as temperature, pH, Eh, and chemistry. The measured sorption and desorption coefficients k_d in batch experiments can be used to calculate the equilibrium concentrations (Fujii Yamagata et al. 2022). The order parameter field $\eta_p(\boldsymbol{r}, t)$ is equal to 1 inside the phase p and to 0 outside the phase p, while it varies smoothly from 0 to1 across the interface.

The microstructure evolution is driven by the minimization of the total free energy of the system. The governing equations of the non-conserved order parameters $\eta_p(\boldsymbol{r}, t)$ and the conserved concentration $c_i(\boldsymbol{r}, t)$ follow the Allen-Cahn equations and Cahn-Hilliard equations (Cahn 1961; Allen and Cahn 1979), respectively.

$$\frac{\partial \eta_p}{\partial t} = -L_p \frac{\delta F}{\delta \eta_p} = -L_p \left(\kappa_p \nabla^2 \eta_p + m\left[\eta_p^3 - \eta_p + \eta_p \sum_{q \neq p} \lambda_{qp} \eta_q^2\right] + \sum_q \frac{\partial h_q(\boldsymbol{\eta})}{\partial \eta_p} f_q(\boldsymbol{c}) \right), \quad p = AgM, FA, BFS, \text{ porous CS and } Ag \text{ precipitate} \qquad \text{Eq. 5.6}$$

$$\frac{\partial c_i}{\partial t} = -\nabla \cdot \boldsymbol{J}_i = \nabla \cdot \left(M_i \nabla \frac{\delta F}{\delta c_i} \right) = \nabla \cdot [M_i \nabla(\mu_i)] + \dot{R}_{i,react} + \dot{R}_{i,disol}, \quad i = Ag^+, Ag, \text{and } GW \qquad \text{Eq. 5.7}$$

where F is the total free energy of the system, $\mu_i$is the chemical potential of species i with the unit of [J/m^3]. $f_p(\boldsymbol{c})$ is the chemical free energy density of phase p with the unit of [J/m^3]. $\dot{R}_{i,react}$ is the reaction rate for the reaction $Ag^+ + PW \rightarrow Ag$. $\dot{R}_{i,disol}$is the dissolution rate for the dissolution reaction $Ag \rightarrow Ag^+ + e$. L_p is the interface mobility. M_i is the mobility of species i.

The total free energy F of the system is formulated as a functional of the order parameter field $\boldsymbol{\eta} = \{\eta_p(\boldsymbol{r}, t)\}$ and concentration field $\boldsymbol{c} = \{ c_{\mathrm{i}}(\boldsymbol{r}, t)\}$ as:

$$F(\boldsymbol{\eta}, \boldsymbol{c}) = \int_V \left[f_{intf}(\boldsymbol{\eta}) + f_{bulk}(\boldsymbol{\eta}, \boldsymbol{c}) \right] dV \qquad \text{Eq. 5.8}$$

where V is the volume of the simulation domain. $f_{intf}(\boldsymbol{\eta})$ and $f_{bulk}(\boldsymbol{\eta}, \boldsymbol{c})$ are the interfacial free energy density and bulk chemical free energy density, respectively. The interfacial free energy density and the bulk chemical free energy density are expressed by the phase field variables as (Moelans et al. 2008; Moelans 2011):

$$f_{intf}(\boldsymbol{\eta}) = m f_0(\boldsymbol{\eta}) + \sum_p \frac{\kappa_p}{2} (\nabla \eta_p)^2, f_0(\boldsymbol{\eta}) = \sum_p \left(\frac{\eta_p^4}{4} - \frac{\eta_p^2}{2} + \frac{1}{2} \sum_{q \neq p} \lambda_{pq} \eta_p^2 \eta_q^2 \right) + \frac{1}{4} \qquad \text{Eq. 5.9}$$

$$f_{bulk}(\boldsymbol{\eta}, \boldsymbol{c}) = \sum_p h_p(\boldsymbol{\eta}) f_p(\boldsymbol{c_p}), \; h_p(\boldsymbol{\eta}) = \frac{\eta_p^2}{\sum_q \eta_q^2} \qquad \text{Eq. 5.10}$$

$$f_p(\boldsymbol{c_p}) = \sum_i \frac{1}{2} A_{p,i} \left(c_{p,i} - c_{p,i}^{eq} \right)^2 \qquad \text{Eq. 5.11}$$

where $h_p(\boldsymbol{\eta})$ is a shape function that presents the volume fraction of each phase at point $\boldsymbol{r}$. κ_p is the gradient coefficient with unit of [J/m], and m is the energy density coefficient with the unit of [J/m^3]. λ_{pq} is a dimensionless model parameter. $\boldsymbol{c_p}$ is the concentration field $\boldsymbol{c_p} = \{c_{\mathrm{p,i}}(\boldsymbol{r}, t)\}$ in phase p. Any complicated chemical free energy functional $f_p(\boldsymbol{c_p})$ valid in the thermodynamic database could be used. For simplicity, a parabolic function of species' concentration $\boldsymbol{c_p}$is employed in the current model. The concentration variables at point $\boldsymbol{r}$ is the summation of that in different phases as:

$$\boldsymbol{c} = \sum_p h_p(\boldsymbol{\eta})\boldsymbol{c_p} \qquad \text{Eq. 5.12}$$

It is assumed that $f_p(\boldsymbol{c_p})$ satisfies the following relationship (i.e., having the same chemical potential of species i in different phase p and q):

$$\frac{\partial f_p(\boldsymbol{c_p})}{\partial c_{p,i}} = \frac{\partial f_q(\boldsymbol{c_q})}{\partial c_{q,i}} = \mu_i, \quad p \neq q \qquad \text{Eq. 5.13}$$

All these coefficients or parameters ($\kappa_p, m, \lambda_{pq}, A_{p,i}\ and\ c_{p,i}^{eq}$) can be determined by the thermodynamic properties, including common tangent, equilibrium concentrations, interfacial energy, interface thickness of any two different phases, the energy barriers of phase transition, and driving forces of phase nucleation.

5.2.3.2 Inhomogeneous Thermodynamic and Kinetic Properties

The thermodynamic and kinetic properties of species i in the CS should be inhomogeneous due to the inhomogeneous microstructures. For instance, the mobility of PW in porous CS and meso-pores inside the AgM particle might be much greater than that in FA, BSF, and AgM grains. Species' mobility might be different in different phases. The chemical potential of species at the interface might be different from that inside bulk phases because the interface defects may affect the formation energy. The reaction and dissolution rates might also be spatially dependent. With the order parameters $\boldsymbol{\eta}$, two shape functions $h_p(\boldsymbol{\eta})$ and $g_{pq}(\boldsymbol{\eta})$ are used to define the phase p and the interface between phase p and q. $h_p(\boldsymbol{\eta})$ is defined in Eq. 5.10. $g_{pq}(\boldsymbol{\eta})$ is defined as $g_{pq}(\boldsymbol{\eta}) = 2(1 - \eta_p^2 - \eta_q^2)$, which is zero inside phase p and phase q and varies from 0 to 1 to 0 across the interface. With the mixture rule (Kim 2007), the inhomogeneous thermodynamic and kinetics properties in the multiphase materials can be described by:

$$M_{\mathrm{i}} = \sum_p M_{p,i} h_p(\boldsymbol{\eta}) + \sum_{p \neq q} \Delta M_{pq,i} g_{pg}(\boldsymbol{\eta}) \qquad \text{Eq. 5.14}$$

$$D_{\mathrm{i}} = \sum_p D_{p,i} h_p(\boldsymbol{\eta}) + \sum_{p \neq q} \Delta D_{pq,i} g_{pg}(\boldsymbol{\eta}) \qquad \text{Eq. 5.15}$$

$$\mu_i = \sum_p \mu_{p,i} h_p(\boldsymbol{\eta}) + \sum_{p \neq q} \mu_{pq,i} g_{pq}(\boldsymbol{\eta}) \qquad \text{Eq. 5.16}$$

$$\begin{aligned} \dot{R}_{i,react} = {} & \textstyle\sum_p r_{p,Ag^+}(c_{p,Ag^+} - c_{p,Ag^+}^{eq})\big(c_{p,PW} - c_{p,PW}^{eq}\big)h_p(\boldsymbol{\eta}) \\ & + \textstyle\sum_{p \neq q} \Delta r_{pq,Ag^+}(c_{p,Ag^+} - c_{p,Ag^+}^{eq})(c_{p,PW} - c_{p,PW}^{eq}) g_{pq}(\boldsymbol{\eta}) \end{aligned} \qquad \text{Eq. 5.17}$$

$$\dot{R}_{i,disol} = \sum_{p} r_{p,Ag}(c_{p,Ag} - c_{p,Ag}^{eq})h_p(\boldsymbol{\eta}) + \sum_{p \neq q} \Delta r_{pq,Ag}(c_{p,Ag} - c_{p,Ag}^{eq})g_{pq}(\boldsymbol{\eta}) \quad \text{Eq. 5.18}$$

where $\psi_{p,i}$ is the property of species i inside phase p, and $\Delta\psi_{p,i}$ is the increment of property at the interface between species p and q. In geochemical models (Fang et al. 2003; Chen et al. 2021, the reactions are assumed to reach equilibrium immediately, i.e., the reaction rates are infinite. In Eq. 5.17 and Eq. 5.18, r_{p,Ag^+} is the reaction rate coefficient for the reaction $Ag^+ + PW \rightarrow Ag$ in phase p, $r_{p,Ag}$ is the reaction rate coefficient for the reaction $Ag \rightarrow Ag^+ + e$ in phase p, and $\Delta r_{pq,Ag^+}$ and $\Delta r_{pq,Ag}$ describe the inhomogeneous reaction rates at the interface. The reaction rate (Eq. 5.17 and Eq. 5.18) depends on local concentration and microstructure. The reaction rates could be modified by adding local fields such as local pH and Eh.

5.2.3.3 Nucleation Scheme

Ag ppts are described by the order parameter $\eta_{Ag}(\boldsymbol{r}, t)$ and the concentration $c_{Ag,i}(\boldsymbol{r}, t)$. At the initial stage, $\eta_{Ag}(\boldsymbol{r}, 0) = 0$ is assigned, which means there are no Ag ppts inside the simulation cell. The nucleation of ppts could be homogeneous or heterogeneous . For homogeneous nucleation, thermal fluctuations cause the formation of different size clusters of Ag atoms. When the size of clusters exceeds the critical nucleus size, clusters grow and form Ag ppts. Thermal fluctuations and ppt nucleation can be mimicked by introducing a random fluctuation of order parameter $\eta_{Ag}(\boldsymbol{r}, t)$ and concentration field $c_{Ag,i}(\boldsymbol{r}, t)$. For heterogeneous nucleation, the inhomogeneous chemical potentials result in segregation of species at extended defects such as interfaces, which may promote nucleation at defects. The fact that Ag ppts are mostly present at the interface between AgM and CS indicates that Ag precipitation occurs via heterogeneous nucleation. The simulations use two model parameters (i.e., the critical concentration c_{Ag}^* and the frequency of nucleation searching N_{Nuclt}^*) to mimic the heterogeneous nucleation process. The nucleation scheme is described as follows: (1) search for the nucleation sites where the concentration is larger than c_{Ag}^* and $\eta_{Ag}(\boldsymbol{r}, t) = 0$ at every nucleation step N_{Nuclt}^*; (2) assign $\eta_{Ag}(\boldsymbol{r}, t) = 1$ at the nucleation sites; and (3) repeat steps 1 and 2. With this nucleation scheme, the nuclei of Ag ppt can be continuously introduced at the nucleation sites. The introduced nuclei may grow or shrink depending on the driving force for local phase transition.

5.2.3.4 Model Parameters

In solving the equations, Eq. 5.6 and Eq. 5.7, all the thermodynamic and kinetic properties are normalized by the characteristic energy density m_0, characteristic length l_0, and characteristic time t_0, respectively. The following normalization is used:

$$t^* = \frac{t}{t_0},\ M_i^* = \frac{M_i}{M_c},\ \nabla^* = l_0\nabla = l_0\left(\frac{\partial}{\partial x}, \frac{\partial}{\partial y}, \frac{\partial}{\partial z}\right),\ \kappa_p^* = \frac{\kappa_p}{m_0 l_0^2},\ L_p^* = \frac{L_p}{L_0}, \text{ and } A_{p,i}^* = \frac{A_{p,i}}{m_0},$$
$$\text{where } t_0 = \frac{l_0^2}{M_c m_0}, \text{ and } M_c = \frac{V_{mol} D_0}{RT_0},\ L_0 = M_c/l_0^2 = \frac{1}{m_0 t_0}. \quad \text{Eq. 5.19}$$

where V_{mol} is the molar volume and D_0 is the diffusion coefficient of diffusive species that has the maximum diffusivity; m_0 is usually set to RT_0. R is the gas constant; T_0 is the absolute temperature of a reference state. Generally, the mobility of species depends on temperature and material structure, so the following expression is assumed:

$$M_{p,i} = \frac{D_{p,i}V_{p,i}}{RT} \quad \text{Eq. 5.20}$$

$$D_{p,i} = D_{p,i}^{0}\, exp(-\frac{\Delta Q_{p,i}}{RT}) \quad \text{Eq. 5.21}$$

where $D_{p,i}^{0}$ is the diffusion coefficient, $V_{p,i}$ is the molar volume, and $\Delta Q_{p,i}$ is the active energy of the considered species in phase p, respectively. T is the temperature. Similarly, the interface mobility, L_p, depends on temperature and is expressed as $L_p = L_p^0\, exp\left(-\frac{\Delta Q_p}{RT}\right)$.

The free energy coefficients κ_p, m, and λ_{pq} can be assessed by the interface energy, σ, and interface thickness, $l_{thickness}$ as $\sigma = \frac{\sqrt{2}}{3}\sqrt{m\kappa_p}$ and $l_{thickness} = \sqrt{\frac{8\kappa_p}{m}}$ when the dimensionless model parameter λ_{pq}=1.5 (Moelans et al. 2008). The normalized coefficients are calculated by $\kappa_p^* = \frac{3\sigma l_{thickness}}{4m_0 l_0^2}$ and $m^* = 6\sigma/(l_{thickness}m_0)$. The chemical free energy coefficient $A_{p,i}$ and equilibrium concentration $c_{p,i}^{eq}$ can be determined by measured absorption coefficient $k_{d(adsorb)}$ and desorption coefficient $k_{d(desorb)}$ in absorption and desorption batch experiments of different pure phases (AgM, FA, BFS, CS) with PW. For a given temperature, pH, E_h, chemistry in the PW, and the measured coefficient at equilibrium have the relationship with equilibrium concentration $k_{d(adsorb)} = c_{p,i}^{eq}/c_{PW,i}^{eq}$, and/or $k_{d(desorb)} = c_{p,i}^{eq}/c_{PW,i}^{eq}$. These measured coefficients can be used to develop the chemical free energy functional $f_p(\boldsymbol{c_p})$. The $A_{p,i}$ is associated with the second derivative of $f_p(\boldsymbol{c_p})$ with respect to concentration $c_{p,i}$ at equilibrium concentrations $c_{p,i}^{eq}$. The chemical potential increment $\mu_{pq,i}$ of species i at the interface of phase p and q is related to the formation energy increment of species i at the interface and the bulk reference phase. The diffusivity $D_{p,i}$ of species i in phase p can be calculated by density functional theory and molecular dynamics simulation. Leaching experiments are often used to measure the effective diffusivity of species i in different phases. For example, measured effective diffusivity of iodine in CS and CS with AgM particles was about $5.8 \times 10^{-13} \sim 5.0 \times 10^{-17} m^2/s$ (Cantrell et al. 2016). The reaction rate coefficient $r_{p,i}$ can be calculated by the energy barrier of the reaction. All the model parameters can be assessed by the thermodynamic and kinetics properties of species in the system. This report aimed to develop and validate the model capability with parametric studies. Model parameters were therefore estimated. Hence, all the results are qualitative. The normalized model parameters are given in Table .

Table 5.5. Non-zero model parameters used in the mesoscale simulations which employed equations 5.6 through 5.21 .

Symbols	Value	Symbols	Value
m_0	$10^7 J/m^3$	κ_p^*	0.12
l_0	$5.7\mu m$	m^*	0.12
D_0	$1.5 \times 10^{-16} m^2/s$	L_p^*	10.0
V_{mol}	$7.85 \times 10^{-5} m^3/mol$	$A_{p,i}^*$ $i = Ag, Ag^+, PW$	100, $p = AgM, FA, BFS$ 0.2, $p = Ag, CS$
$T = T_0$	$423K$	$c_{p,PW}^{eq}$	0.1, $p = AgM, CS$ 0.0001, $p = FA, BFS, Ag$
dt^*	0.000002	$c_{p,Ag}^{eq}$	0.0001, $p = AgM, CS, FA, BFS$ 0.8, $p = Ag$
$D_{CS,i}^*$	10	c_{p,Ag^+}^{eq}	0.001, $p = AgM, CS, FA, BFS, Ag$
$\Delta D_{pq,i}^*$ $p, q = AgM, CS$	4,2,1,0.1 $i = Ag, Ag^+$	$\Delta\mu_{pq,i}^*$	0.65,0.3,0, $p = AgM, q = CS$ 0.65,0.3,0, $p = Fa, BFS, q = CS$
c_{Ag}^*	0.4	$r_{p,Ag}^*$	0.05,0.1,0.15,0.2, $p = Ag$
N_{Nuclt}^*	6000	r_{p,Ag^+}^*	0.05,0.1,0.2,0.3,0.4, $p = AgM, CS$

5.2.3.5 Simulation Cell, Initial and Boundary Conditions

For given microstructure features, including the volume fraction of different phases and average particle size, a phase-field model of multiphase grain growth is used to generate the initial microstructure for the developed model (Moleans et al. 2011). Figure illustrates the simulation cell with a large AgM and some small FA and BFS particles embedded in a CS matrix. The developed mesoscale model of Ag dissolution is generic in three dimensions. For the sake of computer resource, the simulations are carried out in quasi three dimensions. There is a small dimension in the y-direction and a larger dimension in x- and z-dimensions, and periodic boundary conditions are applied in the x-, y- and z- directions. The physical dimension of the simulation cell is $256l_0 \times 4l_0 \times 256l_0$, where l_0 is the characteristic length.

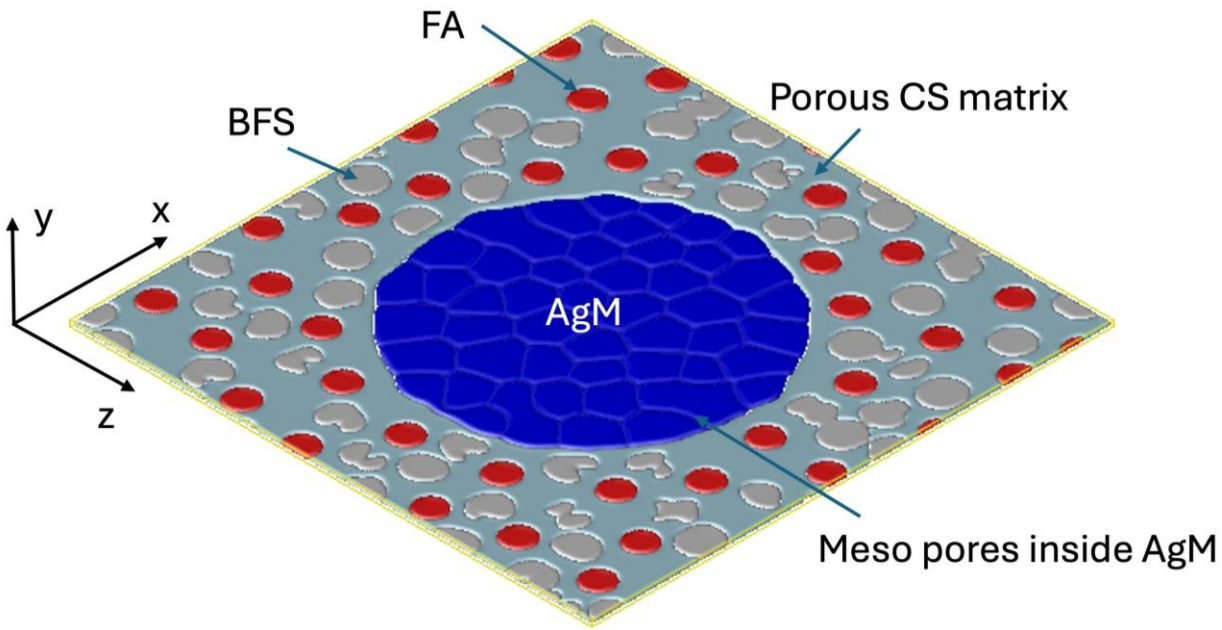

Figure 5.17. Schematic of the simulation cell including AgM, FA, BFS particles, porous CS matrix, and meso-pores inside AgM. The AgM particle is viewed as a cluster of small AgM grains.

To simulate Ag dissolution under batch experiment conditions, it is assumed that PW in the porous CS matrix quickly reaches a saturated concentration $c^0_{CS,PW}$. This should be true if the pore volume fraction in CS matrix is high and pores are well connected. In that case, the material has closed pores which can be viewed as a uniform phase with identical thermodynamic and kinetic properties. The large AgM particle is made of small AgM grains (polycrystalline zeolite) (Fujii Yamagata et al. 2022). The pores between the small AgM grains are small, about tens to hundred nanometers, and are called meso-pores. The effective diffusivity should depend on the average size of AgM grains and meso-pores. During Ag dissolution, it is assumed that PW diffuses into the meso-pores and microchannel in AgM grains; reacts with AgM and produces Ag; Ag diffuses, segregates, and forms Ag ppts; and Ag may be oxidized depending nonlocal chemistry. The dissolution mechanisms are discussed in literature (Inagaki et al. 2008). Table lists the initial and equilibrium concentrations used in the simulations, which are assigned for the validation of model capability. More accurate data is required to predict leaching experiments for setting the initial and boundary conditions, which will be targeted in Year 2.

Table 5.6. Initial concentrations of species in the AgM-CS mesoscale model

Initial concentration	Porous CS	FA	BFS	AgM	Ag
$c^0_{p,PW}$	0.5	0.001	0.001	0.001	0.001
c^0_{p,Ag^+}	0.001	0.001	0.001	0.001	0.001
$c^0_{p,Ag}$	0.001	0.001	0.001	0.001	1.0

5.2.3.6 Numerical Method

With the mesoscale model of Ag dissolution in CS with AgM particles, an in-house FORTRAN code was developed. In the simulations, the normalized Eq. 5.6 and Eq. 5.7 are solved by the Fastest Fourier Transform in the WEST (FFTW) with semi-explicit scheme (Chen and Shen 1998). For Ag precipitation,

a nucleation scheme is used to introduce nuclei when the local Ag concentration is higher than a critical value. Solving the equations, the temporal and spatial evolution of concentration fields $c_i(\boldsymbol{r}, t)$ and order parameter fields $\eta_j(\boldsymbol{r}, t)$ are obtained, hence, Ag segregation and precipitation.

5.2.4 Results to Date

In Year 1, a mesoscale model of Ag dissolution in CS with AgM particles was developed. The model considers the effect of microstructures and inhomogeneous thermodynamic and kinetics properties on Ag dissolution and Ag precipitation. In particular, the model has the following capabilities:

1. For given microstructure features, including the volume fractions of different phases and average particle sizes, the model can generate a 3-D microstructure to mimic the CS grout.
2. The model takes into account the physics processes: (a) multi species diffusion (i.e., Ag^+, Ag and PW) driven by chemical potential gradient; (b) two non-equilibrium reactions: $Ag^+ + PW \rightarrow Ag$ and $Ag \rightarrow Ag^+ + e$; (c) Ag segregation at interface and nucleation/growth of Ag ppts
3. The model considers inhomogeneous thermodynamic properties, including microstructure dependence of chemical potential and energy barrier of reactions.
4. The model considers inhomogeneous kinetic properties, including microstructure dependence of species diffusivity and reaction rates

A comprehensive parametric study was carried out to validate the model capability. The project team defined two quantities [i.e., $w_{Ag,ppt}(t)$ and $w_{Ag,Matrix}(t)$] to capture the Ag dissolution kinetics. $w_{Ag,ppt}(t)$ is the percentage of Ag in Ag ppts. $w_{Ag,Matrix}(t)$ is the percentage of Ag in the matrix. They are described as:

$$w_{Ag,ppt}(t) = \int_{V_{Ag}} c_{Ag,Ag}(t)dV \Big/ \sum_p \int_{V_p} [c_{p,Ag}(0) + c_{p,Ag^+}(0)]dV \qquad \text{Eq. 5.22}$$

$$w_{Ag,Matrix}(t) = \{\sum_p \int_{V_p} [c_{p,Ag}(t)]dV - \int_{V_{Ag}} c_{Ag,Ag}(t)dV\} \Big/ \sum_p \int_{V_p} [c_{p,Ag}(0) + c_{p,Ag^+}(0)]dV \qquad \text{Eq. 5.23}$$

The denominators in Eq. 5.22 and Eq. 5.23 are the total Ag and Ag^+ in the simulation domain at initial stage $t = 0$. The numerators in Eq. 5.22 and Eq. 5.23 are the amount of Ag in ppt and in the matrix at time t, respectively.

5.2.4.1 Effect of Ag Chemical Potential at the Interface on Ag Dissolution

The chemical potentials of Ag at the interfaces among AgM, FA, BFS, and porous CS may be different from their chemical potentials in different phases. At the initial stage, Ag is present in the AgM particles. With time, Ag diffuses and precipitates. Figure (a) and (b) show the evolution of percentage of Ag ppt, i.e., $w_{Ag,ppt}(t)$, and the percentage of Ag dissolving into the matrix, i.e., $w_{Ag,Matrix}(t)$. In Figure , $\Delta\mu^*_{pq,Ag}$ represents the chemical potential increment of Ag at interface of phase $p_1 = CS$ and $q_1 = FA$ and BFS. It is clear there is no Ag segregating to form Ag ppt at the interface of phase $p = AgM$ and $q = CS$ if $\Delta\mu^*_{pq,Ag} = 0$. Figure (b) shows the Ag segregation at the interface of phase $p_1 = CS$ and $q_1 =$

FA and BFS with the decrease of $\Delta\mu^*_{p_1q_1,Ag}$. All Ag is dissolved in the CS matrix and interfaces as shown in Figure (b). The large increase in the percentage of Ag in ppt shown in Figure (a) indicates the nucleation of Ag ppts at the specified conditions.

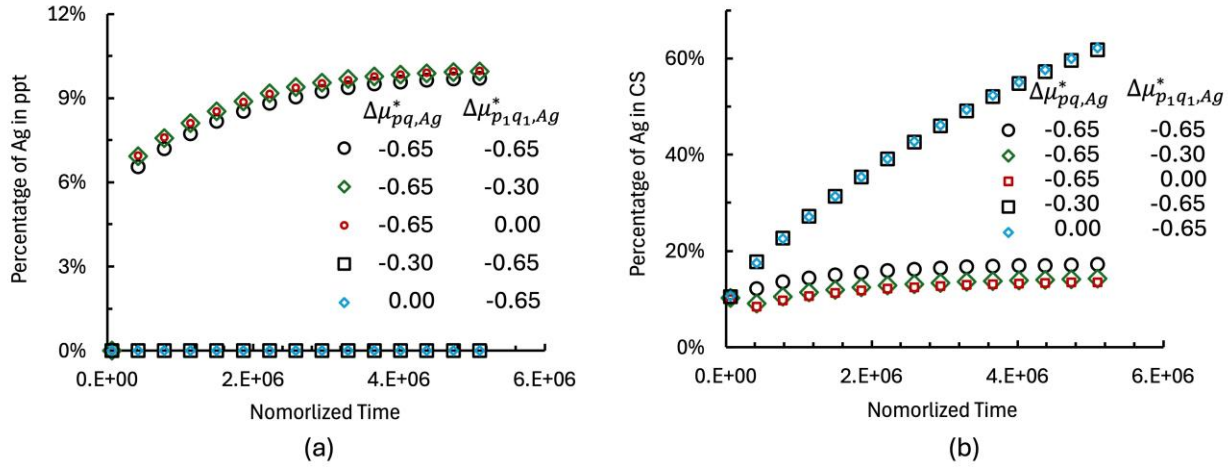

Figure 5.18. Temporal evolution of Ag content inside the Ag precipitates and CS matrix. (a) $w_{Ag,ppt}(t)$, and (b) $w_{Ag,Matrix}(t)$.

The distribution of Ag is very inhomogeneous due to the variation in chemical potentials at interfaces in the microstructure. Figure a,c show the distribution of overall Ag concentration. It is seen in Figure a that Ag has a high concentration at the interface between AgM and CS if $\Delta\mu^*_{pq,Ag} = -0.65$ and $\Delta\mu^*_{p_1q_1,Ag} = 0.0$. Figure c shows that Ag has a low concentration on the interface of AgM and CS, while it has a higher concentration on the interface among FA, BFS, and CS if $\Delta\mu^*_{pq,Ag} = 0.0$ and $\Delta\mu^*_{p_1q_1,Ag} = -0.65$. The lower chemical potential $\Delta\mu^*_{pq,Ag} = -0.65$ causes Ag ppt to form at the interface of AgM and CS, while the lower chemical potential $\Delta\mu^*_{p_1q_1,Ag} = -0.65$ results in Ag segregation on the interface among FA, BFS, and CS. To illustrate more clearly the distribution of the low Ag concentration in the CS matrix, the concentration was assigned to be zero inside Ag ppt. Figure b,d show the distribution of Ag concentration resulting from the Ag ppt. There is a diffusion field in CS matrix, and no Ag segregation at the interfaces among Fa, BFS, and CS was observed because of $\Delta\mu^*_{p_1q_1,Ag} = 0.0$. Figure d shows that Ag diffuses much further than that shown in Figure b because more Ag is available when $\Delta\mu^*_{pq,Ag} = 0.0$ and Ag segregation at the interfaces among FA, BFS, and CS due to $\Delta\mu^*_{p_1q_1,Ag} = -0.65$. The results demonstrate that Ag distribution strongly depends on the chemical potential of Ag on interfaces, and the model can capture the effect of inhomogeneous chemical potentials on dissolution and precipitation.

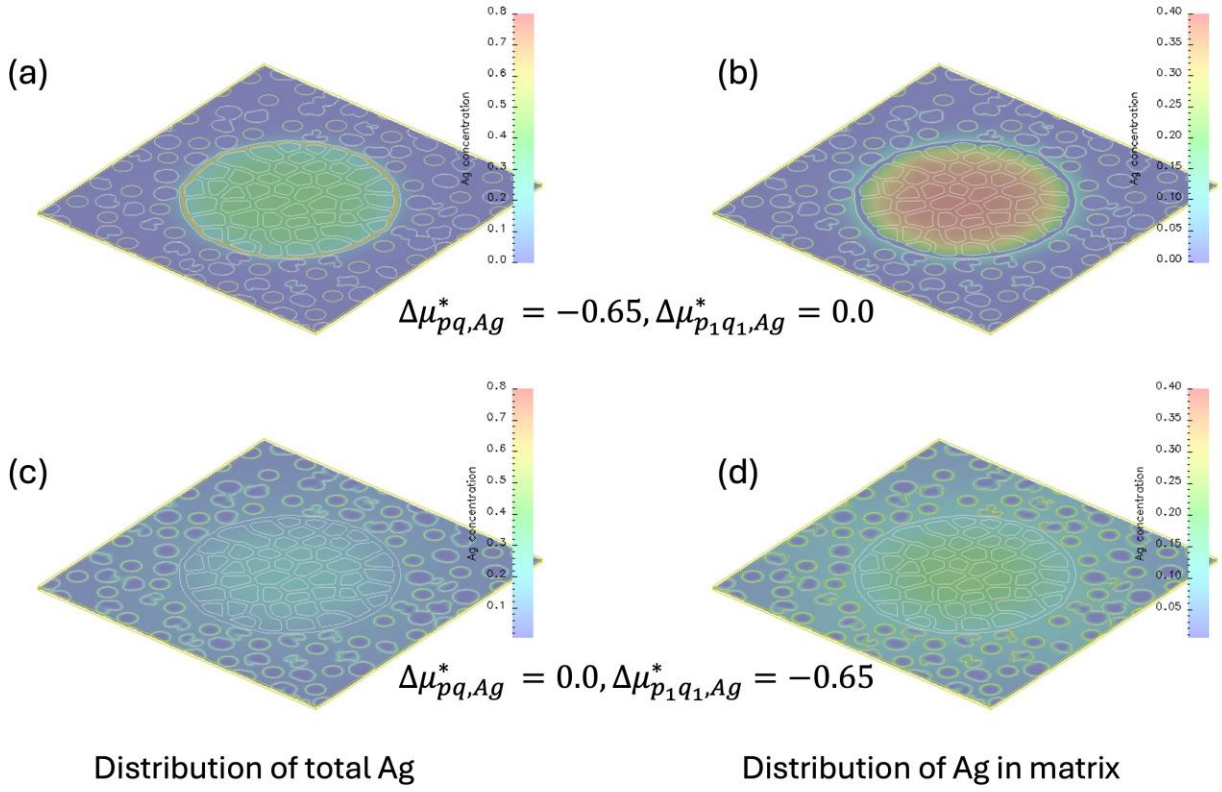

Figure 5.19. Distribution of Ag concentration inside the Ag ppt and CS matrix at normalized time 5820000. (a-b) for $\Delta\mu^*_{pq,Ag} = -0.65$ and $\Delta\mu^*_{p_1q_1,Ag} = 0.0$, and (c-d) for $\Delta\mu^*_{pq,Ag} = 0.0$ and $\Delta\mu^*_{p_1q_1,Ag} = -0.65$, respectively.

5.2.4.2 Effect of Reaction Rate on Ag Dissolution

The rates of reactions $Ag^+ + GW \rightarrow Ag$ and $Ag \rightarrow Ag^+ + e$ depend on the local concentrations of Ag^+ and GW and their energy barrier as well as pH and Eh. Figure presents the evolution of the percentage of the overall Ag formed as Ag ppt and the percentage of Ag that dissolves in the CS matrix under different reaction rates. With a smaller reaction rate $r^*_{p,Ag^+} = 0.1$ and $r^*_{p,Ag} = 0.0$, more Ag^+ dissolves into that CS matrix, which delays the nucleation of Ag ppt at the interface of AgM and CS. The dashed lines in Figure a,b indicate the nucleation of Ag ppt. Increasing the reaction rate $r^*_{p,Ag^+}$from 0.1 to 0.4 promotes the nucleation and growth of Ag ppt and reduces the amount of Ag dissolving into CS matrix as shown in Figure b. Figure shows the temporal evolution of Ag and Ag^+ concentrations for the two cases (a) $r^*_{p,Ag^+} = 0.4$ and $r^*_{p,Ag} = 0.2$, and (b) $r^*_{p,Ag^+} = 0.05$ and $r^*_{p,Ag} = 0.2$. The same color bars are used for overall Ag and Ag^+ concentrations. Comparing the results shows that reaction rate has an important impact on Ag ppt growth and the distribution of Ag and Ag^+concentrations.

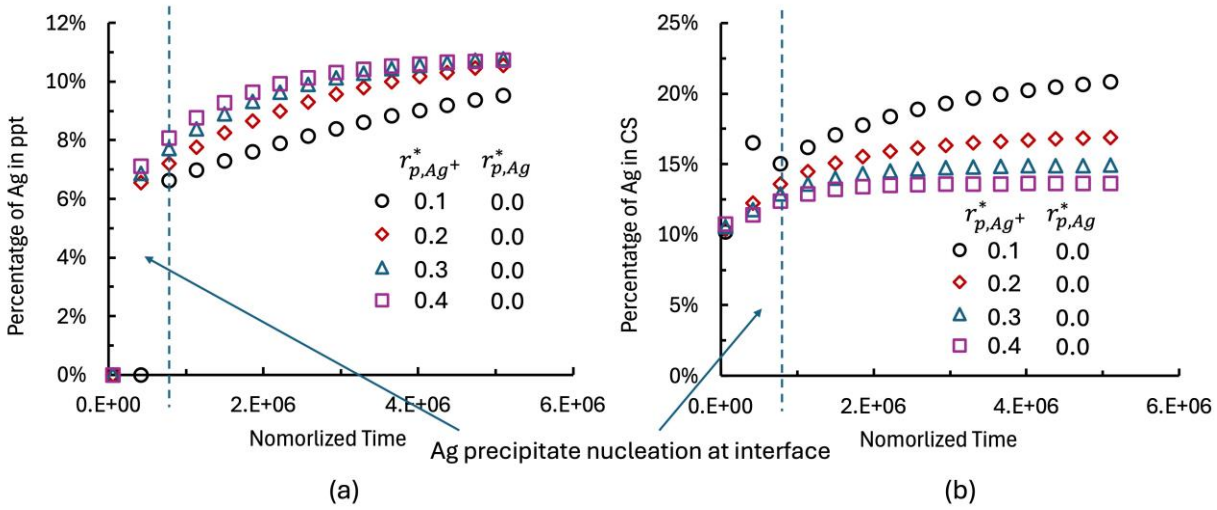

Figure 5.20. Effect of reaction rates on the temporal evolution of Ag content inside Ag precipitate (ppt) (a) and CS matrix (b).

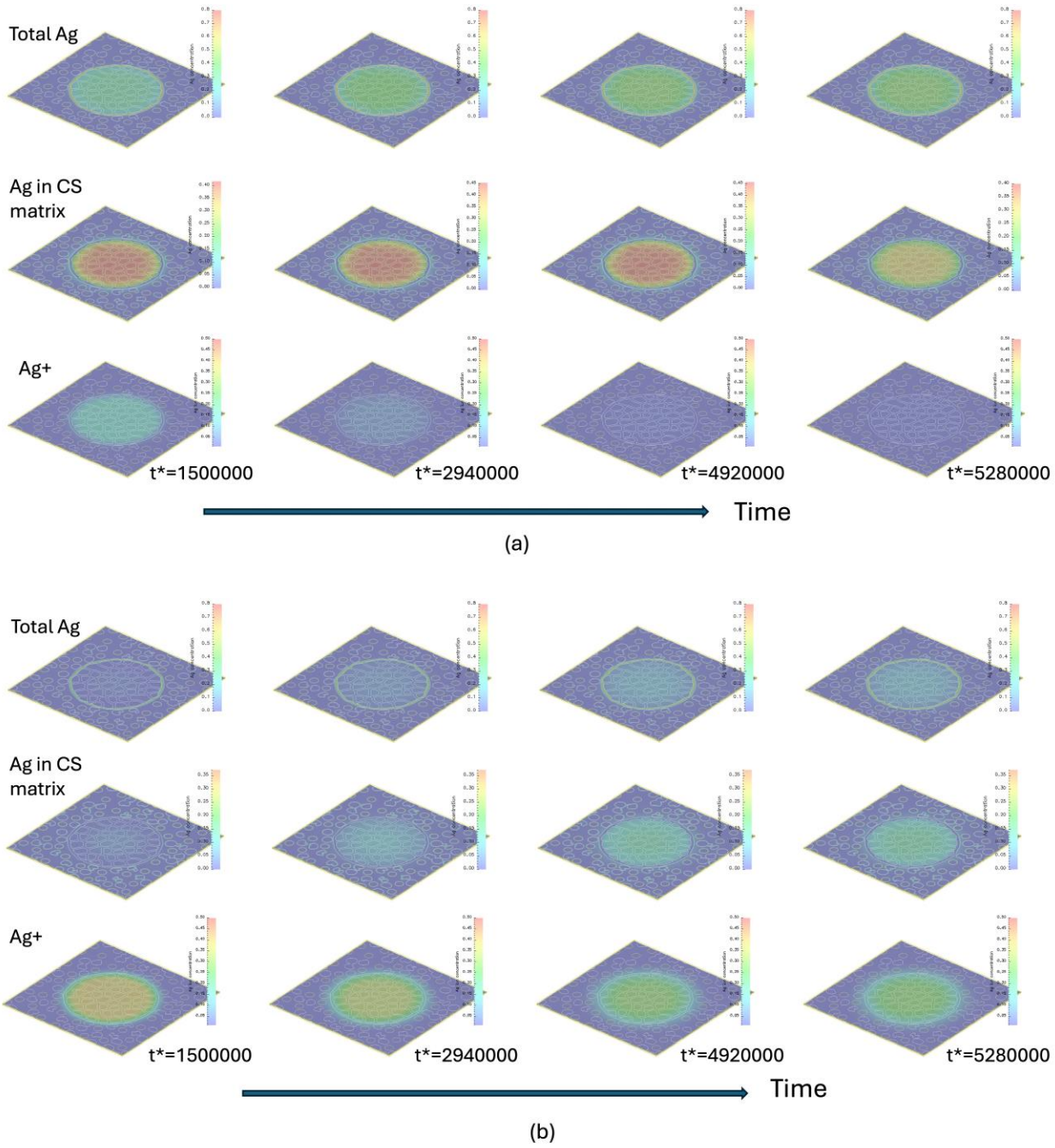

Figure 5.21. Temporal evolution of Ag and Ag^{+} concentrations (a) for $r^{*}_{p,Ag^{+}} = 0.4$ and $r^{*}_{p,Ag} = 0.2$ and (b) for $r^{*}_{p,Ag^{+}} = 0.05$ and $r^{*}_{p,Ag} = 0.2$.

5.2.4.3 Effect of Ag and Ag+ Diffusivity on Ag dissolution

The diffusivity of Ag and Ag^{+}could be different inside phase p. Figure presents the effect of the diffusivity $D^{*}_{p,i}$, where $p = AgM, FA, BFS$, and porous CS, and $i = Ag$ and Ag^{+}. The general conclusions are (1) larger $D^{*}_{p,Ag}$ and $D^{*}_{p,Ag^{+}}$ speeds up the nucleation of Ag ppt as well as Ag dissolution into CS and (2) smaller $D^{*}_{p,Ag^{+}}$delays the nucleation of Ag ppt.

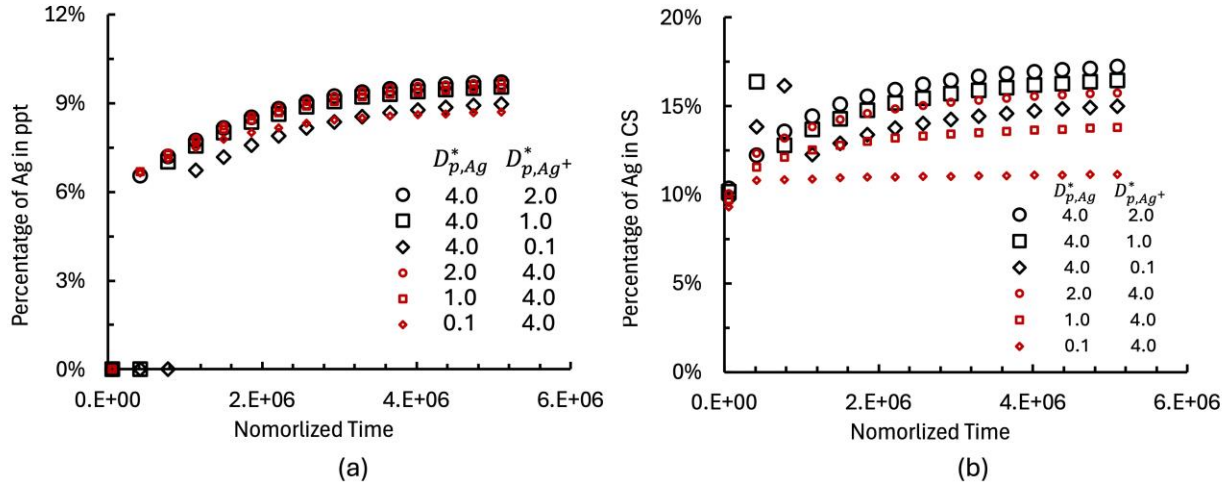

Figure 5.22. Effect of Ag and Ag+ diffusivity on the temporal evolution of Ag content inside Ag precipitate (ppt) (a) and CS matrix (b).

5.2.4.4 Effect of AgM Particle Size on Ag Dissolution

AgM particle size affects the distance of Ag diffusion during dissolution. Figure summarizes the effect of AgM particle size on Ag dissolution. The radius R_0 of AgM particle is normalized by the simulation domain size as $R = R_0/(256l_0)$. The results demonstrate that (1) decreasing the AgM particle size delays the nucleation of Ag ppt, and (2) decreasing the AgM particle size results in more Ag segregating in ppt as well as in CS. This implies that reducing the AgM size increases the Ag dissolution kinetics as expected due to the increased surface area to accessible Ag.

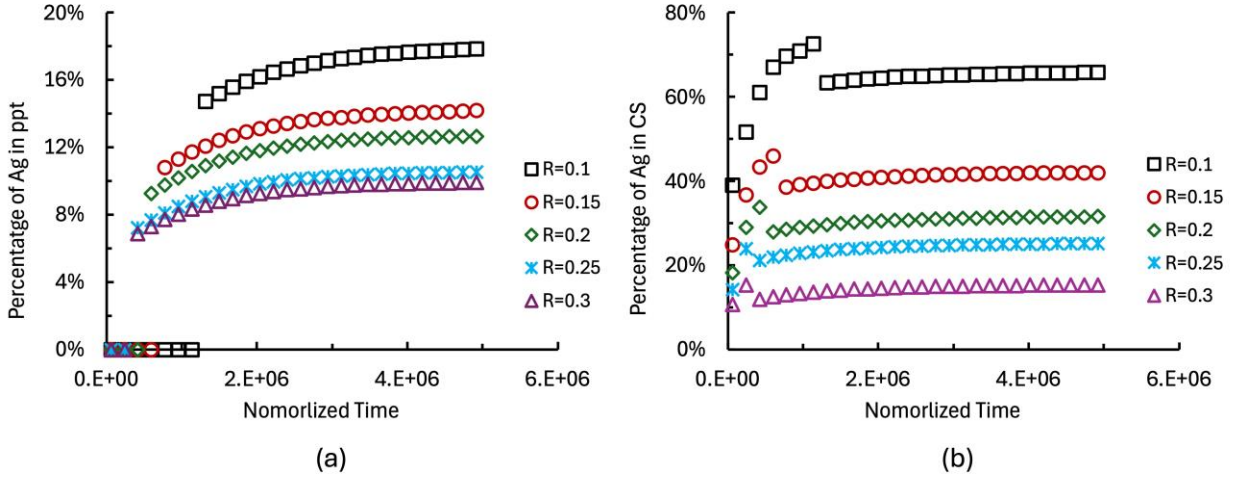

Figure 5.23. Effect of AgM particle size on the temporal evolution of Ag content inside Ag precipitate (ppt) (a) and CS matrix (b).

In summary, the inhomogeneous thermodynamic and kinetics properties of species due to the inhomogeneous microstructures dramatically affect the nucleation and growth of Ag ppt and Ag dissolution kinetics into the CS matrix. The results demonstrated that the developed mesoscale model of Ag dissolution enables one to assess the effect of microstructure and thermodynamic and kinetic properties on Ag dislocation kinetics.

5.2.5 Path Forward and Integration

In Year 1, a first-of-its-kind mesoscale model was developed for an example Hanford grout system. This mesoscale model was able to predict Ag migration into a CS matrix over time based on input values compiled from the literature. In Year 2, the mesoscale model efforts will focus on refining and publishing this original model while also targeting integration with two other efforts.

Subtask 4.2.1 – Complete Ag Model: The developed mesoscale model has a number of model parameters that are associated with the microstructure features and thermodynamic and kinetic properties. In principle, absorption and desorption experiments, lower length scale simulations such as density functional theory and molecular dynamics simulations, and thermodynamic calculations such as phase diagram calculations can provide all the data to determine the model parameters. This will be attempted using existing data. In addition, the thermodynamic and kinetic properties used in geochemical speciation models (Chen et al. 2021) can also be used to assess the model parameters. The output of local fields such as chemistry, pH, and Eh in the geochemical speciation modeling can be used as boundary conditions in the mesoscale model. The mesoscale modeling can be used to determine when mean field methods fail and when the microstructure of the grout material needs to be considered in predictions of macroscopic properties. Therefore, the path forward and integration include the following tasks:

1. Assess the model parameters with thermodynamic and kinetics properties used in geochemical speciation models and absorption/desorption experiments for Ag and radionuclide dissolution in CS with AgM particles.
2. Assess an expanded test case where iodine is also present and leaching from the AgM particle.
3. Predict the dissolution kinetics and effective diffusivity, study the effect of inhomogeneous microstructures on effective material properties, and develop the effective properties for macroscale performance models.
4. Improve the understanding of dominant physics and/or mechanisms behind the observed phenomena.
5. Extend the model by adding more physics such as the effects of pH, Eh, deformation, and cracking on radionuclide dissolution and material property degradation.

- ***Subtask 4.2.2 – Integration with Geochemical Modeling of Grout Phases:*** This task will link with Theme 1 Task 2 to develop a mesoscale model of a slag particle reacting long-term within a grout matrix. This effort will be supported with characterization of slag particles at VU. This effort will be the first attempt to link long-term phase evolution in grouts. The long-term goal would be to expand this effort to phases present to enhance contaminant retention (e.g., iron oxides).
- ***Subtask 4.2.3 – Integration with Peridynamic Modeling:*** This task will attempt to build a chemo-mechanical link between processes in the microstructure with bulk property changes predicted by PD modeling. Local strength and hardness measurements will be made on select grout phases (e.g., nano-indentation) and any resulting softening measured near particles will allow for a mesoscale model to be constructed to predict the local physics, while similar information could be used to build the foundation of a PD model. This effort would lay the groundwork for a modeling tool to link local properties at the microscale to bulk properties in the grout, a capability long sought-after in the cement and concrete research community.

6.0 Theme 5: Grout Database

6.1 Theme 5 Task 1: Grout Database

6.1.1 Team Members

Sarah Saslow (PNNL), Xiaonan Lu (PNNL), Chloe Curry (PNNL), Mayra Diaz-Acevedo (PNNL), Jacob Anderson (PNNL), Dewei Wang (PNNL), Mirina Enderlin (PNNL), Wyatt Kiff (PNNL, now WSU)

6.1.2 Background

To assess grout waste forms of various types in the *Hanford Grout Modeling Framework*, a database that presents available data in a consistent format is required. To date, information on the performance, aging, and degradation of waste forms relevant to Hanford is only present in individual reports, journal articles, and a set of data packages supporting the 2018 IDF PA (which themselves only consider a small subset of samples). Theme 5 is dedicated to developing a comprehensive grout database (GDB) to (1) facilitate future modeling updates (e.g., conceptual models, *Hanford Grout Modeling Framework*, PA simulations, predictive tools), (2) provide a centralized database of grout data curated for general use, (3) capture quality assurance (QA) status of the data to define use limits, and (4) offer training and test datasets for future ML predictive model development for grout properties based on formulation and waste composition inputs. The database will incorporate successes and lessons learned from an in-development online database for glass properties that is farther along in the development process (publication in progress).[1]

The GDB will be available as an online resource for future grout efforts of interest.

6.1.3 Grout Database Objectives and Approach

The overarching goal of the GDB is to improve Hanford grout waste form performance data curation, accessibility, and interpretation for long-term efficiency and use consistency. Specific objectives include:

- ***Evaluation of existing resources:*** Assess reports, data formats, and existing datasets to identify gaps, standardization needs, and test data that is most useful for capturing overall grout waste form performance.
- ***Database format transition:*** Replace the current Excel-based data files with a file format better suited for databases and data analysis to enhance efficiency, scalability, and maintainability.
- ***Data entry standardization:*** Develop a user-friendly data entry interface to ensure consistency and accuracy in future data collection.
- ***Literature search and organization:*** Conduct comprehensive literature reviews, implement efficient methods for downloading and managing papers and reports, and organize them for easy access.
- ***Artificial intelligence (AI) integration for data curation:*** Evaluate and modify existing AI tools for automated data scraping, improving data acquisition efficiency.

[1] A beta version of the online tool for glass waste form properties can be found at https://srnl.mcdc.cecas.clemson.edu/general/glass-database.

6.1.4 Grout Waste Form Data Needs

Based on the project's June 2024 contributors' workshop (Asmussen 2024) and the first iteration of the GDB, developed in Microsoft Excel between June 2021 and June 2024, grout waste form formulation, characteristics, and performance qualification data have been identified as useful for downstream modeling, data visualization, and analysis efforts. Table 6.1 presents the information recommended for entry into the GDB. Section 6.1.8 describes how this data is entered into the GDB.

Table 6.1. Recommended grout waste form data for entry into the GDB.

Information Need	Purpose	Examples
Documentation	Provide information needed to locate the source of the data entered into the database.	• Document title • Authors and lead institution • Digital object identifier (DOI) • Publication date • Web link • Quality assurance program or code • Public availability
Sample Fabrication	Describe the basic conditions used to fabricate the grout waste form batch or individual sample.	• Sample or batch ID • Targeted waste stream, e.g., LAW, liquid secondary waste, solid secondary waste, real waste streams, or water • Conventional grout waste form name, e.g., Cast Stone, Hanford Grout Mix 5, unknown, other. • Water-to-dry-mix ratio • Curing time • Dry ingredients and the amount added of each • Liquid waste composition
Slurry Properties	Determine the workability of a freshly made grout slurry and determine if certain storage, handling, and transportation criteria are met.	• Reabsorption time of residual free liquids • Initial and final set times • Flowability
Cured Properties	Understand how the grout waste form may withstand external stress.	• Compressive strength • Saturated hydraulic conductivity to describe the passage of water through the grout waste form • van Genuchten parameters that capture water retention in the grout waste form
Contaminant Leachability	Quantify grout waste form performance for immobilizing, sorbing, and releasing contaminants of interest.	• Toxicity characteristic leaching procedure contaminant concentrations • Sorption and desorption partition coefficient (K_d) values • Observed/effective diffusivity values

6.1.5 Data Sourcing from Published Literature

6.1.5.1 Literature Inputs

The primary literature search engines used to generate a list of candidate publications for GDB entry were those hosted by the DOE Office of Science and Technology Information (OSTI) and peer-reviewed publisher, Elsevier. Both resources offer an Application Programming Interface (API) that allows users to query their publication database based on keywords and other search criteria (publication date, institution, etc.). Other search engines were used, like Web of Science, but Elsevier accounted for over 50% of the peer-reviewed publications returned in our queries. Other publications not published by Elsevier were mostly captured in searches on OSTI; therefore, these two APIs were used to generate an initial list of candidate publications for GDB entry.

In addition to capturing most relevant literature for this effort, access permissions established between PNNL and Elsevier and OSTI allowed full text files to be downloaded and exported from each search. With Elsevier, an Extensible Markup Language (XML) file is downloaded. This file type is advantageous for data extraction because it retains the file data structure encountered in tables, making it both human and machine readable. PNNL secured a memorandum of understanding with OSTI for an API key that allows the team to export the publication's full text file, e.g., PDF, and associated metadata, for data entry efforts. The API key is limited to PNNL use to support the aims of this project and is not intended for external or other project use. To the team's knowledge and as of the time of this publication, Web of Science does not offer a tool to extract full text documents.

An initial search in the OSTI and Elsevier search engines for keywords "Hanford" and "Cast Stone" mentioned in Elsevier publications returned 19 records in OSTI and only 15 records in Elsevier. Therefore, OSTI was used to generate the first list of candidate records for entry into the GDB because it was more inclusive. After removing the filter for Elsevier-specific records, an OSTI search for entries mentioning both "Hanford" and "Cast Stone" returned 279 records. To date, the team has determined that at least 105 of these records do not contain data of interest to the GDB; 24 records have been determined to contain test data of interest and 16 have been successfully entered into the GDB. After all records have been considered in this OSTI search, the search terms will be expanded to include other terms, like other grout waste form formulations and legacy waste sites.

6.1.5.2 AI/ML for Data Extraction from Published Reports and Papers

Manually evaluating the content of candidate publications for GDB entry is time-consuming. Therefore, one of the first needs identified by the GDB team was to evaluate AI/ML tools that could be used to extract relevant data from candidate reports. However, the tools used to extract data depend on the file type the publication was saved as. The file types most commonly encountered included XML files and PDF files formatted as text, an image, or an image-Optical Character Recognition (OCR). The tools evaluated to extract data from these file types are described in the subsections below.

Overall, these extraction tools are useful for performing a first pass on available data contained within candidate publications. Often though, the data desired for entry into the database is found in the main text, not the supporting tables. How the data was analyzed and the conditions for data use are also commonly found in the main text, which still requires human interpretation before database entry.

6.1.5.3 Data Extraction from XML Files

XML files retain the data structure in a document, which makes it easier to retain the format in which data is presented in a publication. This is especially important when navigating data tables with merged or empty data cells and/or tables that are inserted into a document formatted to have two text columns. The script provided in Appendix A was used to read an input XML file, create an Excel file with a sheet for each identified data table, and export the structured table data to the respective sheet. After generating the Excel file, it is essential for users to review the data extracted because embedded images and complex formatting (e.g., tables without column titles or more than one header) can cause some extracted data to be formatted incorrectly in the Excel file.

6.1.5.4 Data Extraction from PDF Files

The most common PDF files are formatted as a text, an image, or an image-OCR. Text-formatted PDFs contain text and/or data that is selectable and can be copied and pasted into another document. These files allow readers to search for keywords without additional document processing. Image-formatted PDFs present the content as images rather than actual text. Attempts to select specific text result in the entire page being highlighted. Image-based files are often encountered with older reports and scanned publications. Finally, image-OCR formatted PDFs are image-based files that have undergone OCR conversion, which allows the reader to search and select text contained in the document. Each file type poses different challenges when extracting data tables. For this effort, the team primarily focused on data extraction from text-formatted PDF files.

One of the most effective tools tested for extracting data tables from text-formatted PDF files was PNNL's AI-Incubator API, which leverages the OpenAI API. A script provided in Appendix B was written to use this API. With an active Project-Use API key, the script reads PDF files placed in a designated "pdf" folder and extracts table data while also summarizing non-table text. The extracted and summarized data is saved to text (.txt) or Excel (.xlsx) files. Tables identified in a PDF are summarized in a spreadsheet, with each table on a separate sheet. Several Python-based PDF extraction packages were evaluated for similar use in this project, but faced some challenges. Table 6.2 presents the benefits and challenges of the extraction packages tested.

Table 6.2. Evaluated PDF data table extraction methods and packages.

Extraction Package	Benefits	Challenges
PDFplumber	• Ideal for single-column formatted text • Works best for tables that have solid lines	• Struggles with multi-column layouts • Extracts extra text due to its top-to-bottom, then left-to-right reading order
PyMuPDF	• Exports clean tables • Detects all data tables during testing	• Often misses the column titles and first data row • Some tables are not written to the created Excel file • Challenges handling rotated tables • May split a single table into two tables
Tabula	• Eliminates extra text during extraction • Allows user to select tables for extraction	• Requires user to manually select table area for extraction, not ideal for documents with multiple tables/pages and/or multiple PDF files • Templates are specific to each PDF
pdf2image + pytesseract	• Can be used on image-formatted pdfs • Includes a prebuilt feature of searching for tables	• Inconsistent accuracy in detecting tables • Often captures extra text from the document
pdf2image + TATR + pytesseract	• Effective for image-based pdfs • Highly accurate in recognizing standard tables • Efficient as it processes cropped table regions	• May miss non-standard tables (e.g., rotated tables) • Cannot extract information from the surrounding text

6.1.6 Data Organization

The first version of the GDB was developed in Microsoft Excel due to the familiarity of staff, site contractors, and stakeholders with this software and its ease of use. However, with Excel and similar file formats like comma separated values (.csv) and Parquet file types, the amount of data that can be stored in a single file is much lower compared with SQLite Database (.db) or Pandas Hierarchical Data Format version 5 (HDF5; .hf) file types. As the database grows, the time required to load and enter data would increase due to increased demand on processing power.

A .db or .hf file is designed to organize large amounts of data within a single file and allow researchers to quickly query the entire dataset or subsets of data. The difference between these file types is how the data is organized. A .db file is a compilation of structured tables, where each table row and column represent fields of interest. Using Structured Query Language (SQL), the data can be queried similar to how one might index data in Excel but can support more complexity. This organization structure is ideal for correlating datasets. A HDF5 file can stores data in a hierarchical structure that can consist of multiple datasets and groups of data akin to a directory. This organization approach is better for very large data sets but has limited data query functionality when compared to .db files queried by SQL. Since identifying relationships within the GDB is a primary aim of this effort, the team chose to transfer the existing database to a SQLite database file and continue data entry and GDB entry with this organization structure.

6.1.7 Database Access

Currently, the GDB is only accessible to PNNL staff as development and troubleshooting efforts continue. A GitLab group was created for internal sharing of the GDB and supporting data entry files. Contributing staff use assigned access tokens to collaborate on the GDB. In Year 2, this will be expanded to project partners with the goal of hosting the GDB on an online platform by the end of Year 2. The online tool aims to incorporate data analysis and visualization tools that will guide user interpretation of available data for application-specific needs.

6.1.8 Data Entry

Figure 6.1 offers a view of the GDB entry form after launching from the Python script. This form is intended to be used for test data pertaining to a single test condition, e.g., formulation, curing time, liquid waste data. After filling out the report information and general sample formulation information, the user continues by using the data entry buttons at the bottom of the form for capturing liquid waste composition, slurry properties and flowability, compressive strength, saturated hydraulic conductivity, water characteristic curve, contaminant leachability according to EPA Methods 1315 and 1311, as well as contaminant sorption and desorption partition coefficients (K_d values). Figure 6.2 through and Figure 6.4 provide examples of how data is entered into the corresponding window that pops up when a data entry button is selected. After a user is done entering data into a window, they save the data and the window will close. If the user reopens a window for entering data, the fields will no longer be populated but that data has not been lost. If changes need to be made, the user enters the new data and clicks save to overwrite the previous values. Future modifications to the GDB entry form will allow users to return to previously entered values after saving data, but not after submitting data to the GDB. When the user is done entering data into the entry form, they must click the “Submit Data” button to upload it to the GDB.

Controls have been put in place to help maintain uniformity in how data is imported into the GDB. For instance, the format of the publication date (YYYY-MM-DD) is checked, and if the entered text does not match this format, a warning message appears that states “Date published must be a date in YYYY-MM-DD format.” Similarly, text appears when entering the dry ingredient weight percent values to indicate if the sum is equal to 100 wt% (Figure 6.5 top) Once this criterion, and other formatting criteria, are met, the data can be submitted to the GDB (Figure 6.5 bottom).

If a paper or report tested multiple sample conditions, formulations, and/or waste types, an option is also provided to upload data from an Excel document. Bulk data entry is standardized using an Excel template; however, data formatting controls put in place for the grout data entry form are not available. The purpose of this functionality is to make data entry faster at the beginning of this effort. When the GDB is released for public access and contribution, a bulk entry form that incorporates these data formatting controls would be required or the option to submit data using Excel will be removed from the entry form.

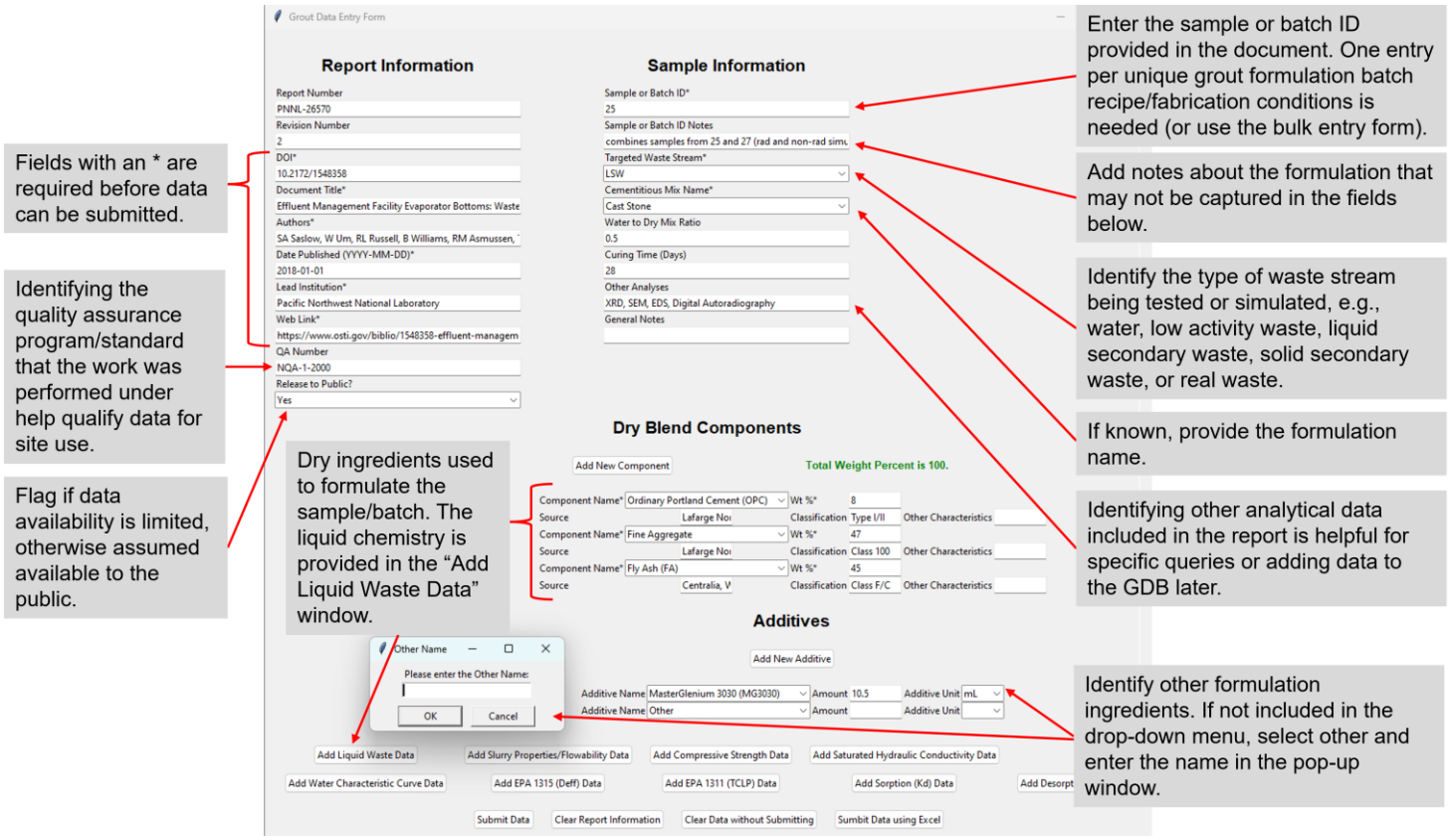

Figure 6.1. The GDB entry form used when entering single sample or batch data into the GDB. This main window is where document information and sample formulation and curing conditions are logged, except for the liquid composition, which has its own pop-up window that is accessed by the "Add Liquid Waste Data" button at the bottom. Annotations are overlayed describing the type of information being logged for key entry fields.

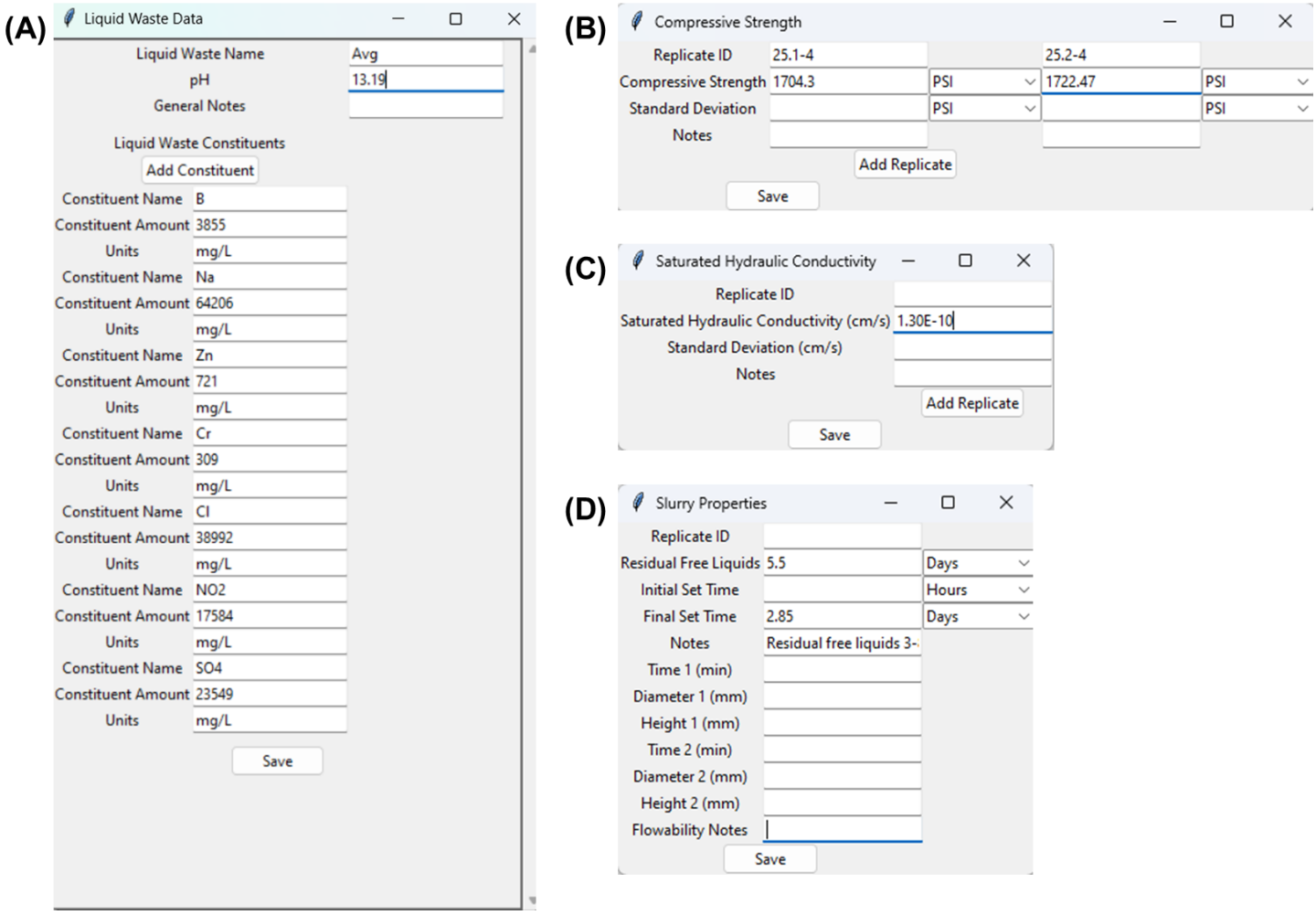

Figure 6.2. Examples of the pop-up windows that appear for entering relevant sample or batch test data. (A) The composition of the aqueous (liquid) phase used to formulate the respective batch identified in the main GDB entry form window. (B) The compressive strength of the respective sample or test batch, which can be entered as an average value with the standard deviation identified or as replicate samples with their individual compressive strength values provided. (C) Saturated hydraulic conductivity value(s), entered as an average with a standard deviation or single replicate values. (D) Slurry properties of the formulated batch or sample, including the number of days required to reabsorb residual free liquids, initial and final set times, and flowability measurements using the adapted procedure from Harbour et al. (2005).

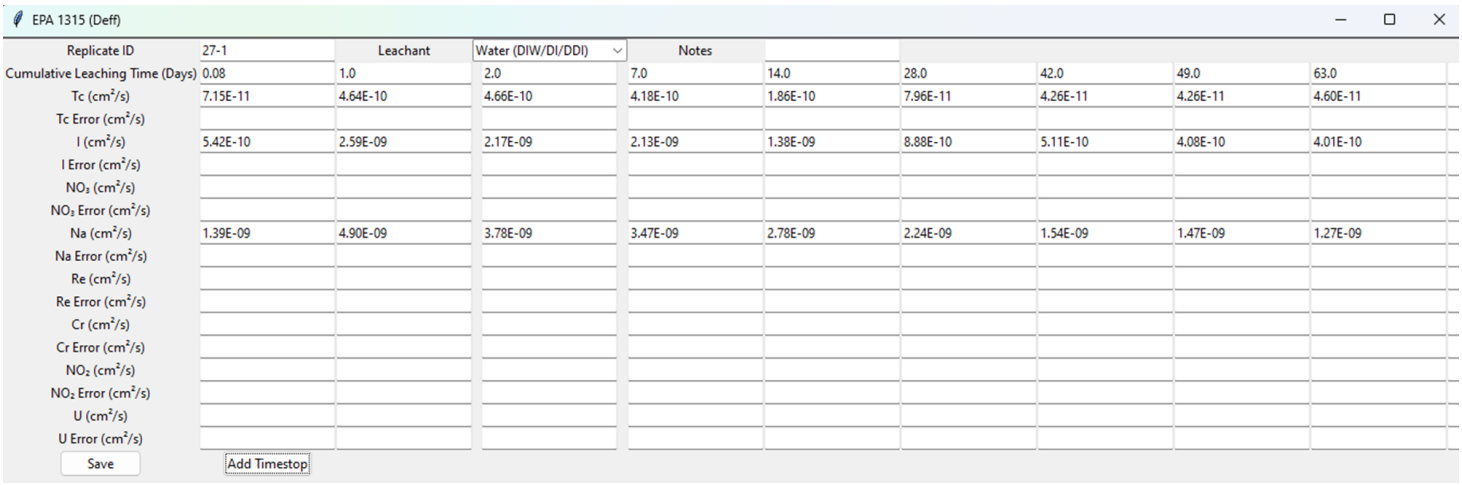

Figure 6.3. Pop-up window for logging EPA 1315 effective diffusivity values.

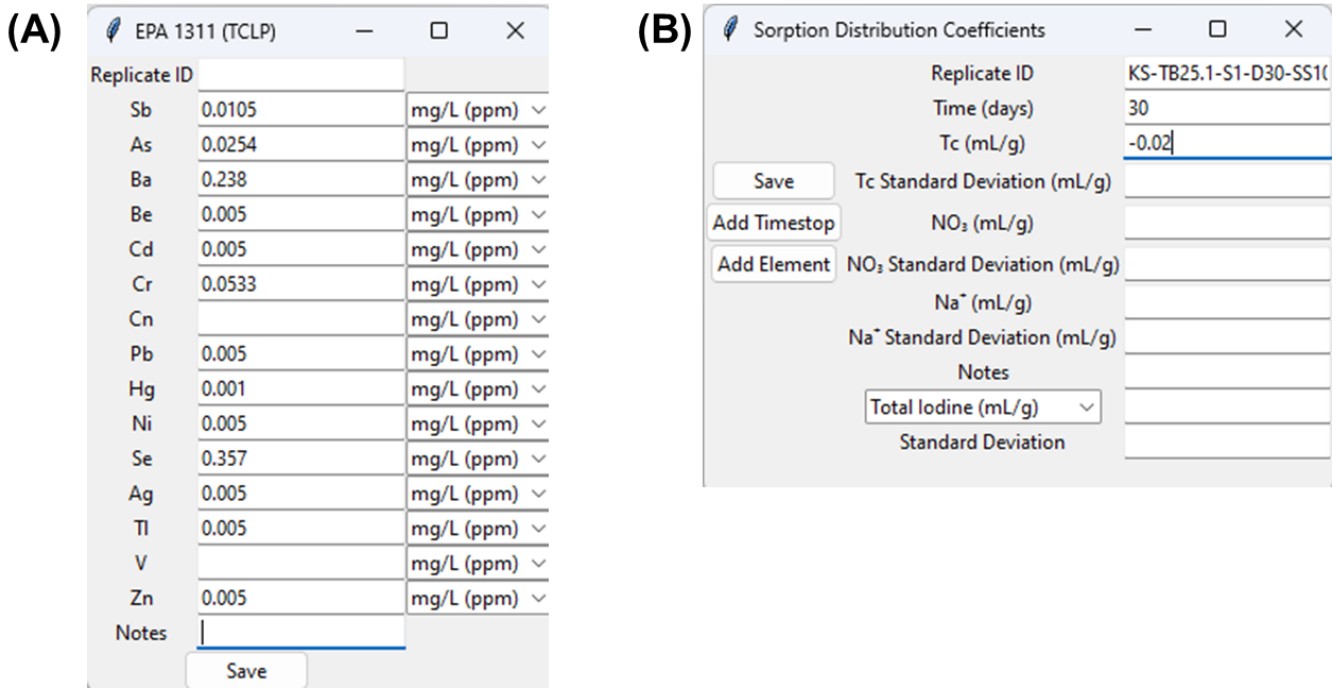

Figure 6.4. Pop-up windows for entering (A) Toxicity Characteristic Leaching Procedure (TCLP) concentrations for RCRA metals and (B) sorption partition coefficient test data. Note that the desorption coefficients data entry window (not shown) has the same data entry format used for sorption coefficients.

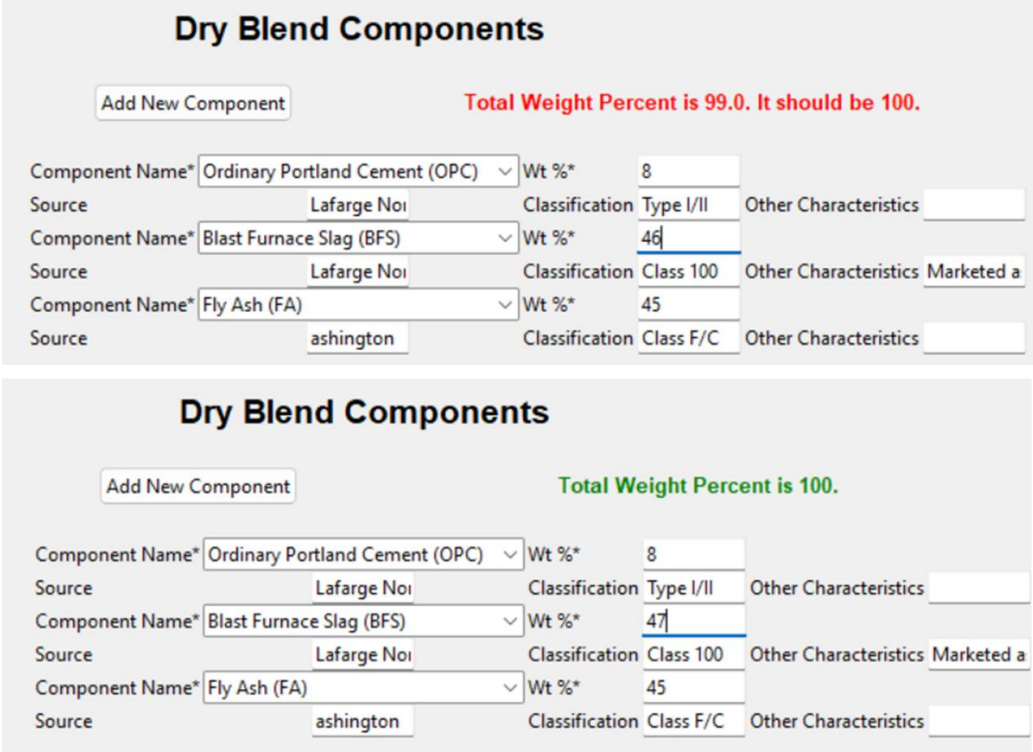

Figure 6.5. One control incorporated into the GDB entry form is that the dry blend components' weight percent values must sum to 100 weight percent. (top) Red text appears indicating the current weight percent total and (bottom) turns to green text when the criterion is met.

6.1.9 Path Forward to Integration

Year 1 GBD efforts primarily focused on establishing a database structure that positions the project for future efforts involving data visualization and AI/ML model development. Database population efforts are ongoing, and lessons learned help refine the user interface that will eventually be opened for external user contributions. As these efforts continue, the following aims have been identified for Year 2 efforts considering what has been learned in Year 1.

- ***Subtask 6.1.1 – Efficient Data Entry:*** As previously mentioned, scripts written and tested for extracted data from tables often neglects key data provided and described in the main text; this missing information can limit the completeness of the built dataset. As Large Language Models (LLMs) improved recently, many models have the potential to bridge this gap by extracting relevant data from both publication tables and report text, providing a more comprehensive dataset. Several promising tools, like PNNL's AI-Incubator, OpenSearch, and LLMWhisperer, were identified in Year 1 for this purpose. PNNL AI-Incubator, powered by the OpenAI, can conduct complex text analysis, summarization, and interpretation of unstructured text. OpenSearch can offer real-time data access and analysis. LLMWhisperer is known for its accurate speech-to-text conversion capabilities, providing a potential for capturing spoken contents into a text-based dataset. Efforts in Year 2 will explore implementation of these advanced tools to help build the GDB dataset more efficiently and effectively.
- ***Subtask 6.1.2 – GDB Expansion:*** A pathway for database expansion without disrupting existing GDB entries will be defined in Year 2 in anticipation of evolving and growing needs and use of the GDB. Select GWF properties and performance data are currently being entered in the GDB (Table 6.1); however, many reports and journal articles include other test data that may be of interest or

relevant to modeling efforts in the future. To date, most reports with data entered in the database have not included test results from EPA Method 1313. This test method evaluates contaminant retention in grout waste forms as a function of pH and is used in some modeling efforts. As data entry is expanded to include grout waste form formulations that are not Hanford specific, more EPA Method 1313 data may come available and warrant inclusion in the database.

- ***Subtask 6.1.3 – Quality Assurance:*** To effectively use the database for developing models applicable to plant design and operation, certain data must be collected or meet specific nuclear quality assurance requirements. However, consolidating this information presents challenges due to varying QA standards across different property types. For example, product-quality-related properties often have stricter requirements compared to processing-related properties. Additionally, some reports reference internal documents for QA statements, requiring extra efforts to obtain and verify these documents. QA statements are often presented in text format within reports, making manual extraction inefficient. Integrating AI-based text scraping tools can streamline the extraction and organization of QA information, enhancing data accessibility and ensuring compliance with relevant standards.
- ***Subtask 6.1.4 – External Access:*** The ultimate goal is to create a hosting website that consolidates all project developments, including the existing database, data entry interface, data scraper tools, and ML models. This platform will provide a centralized, consistent, and open-access resource for the broader community to use, contribute to, and enhance. A user guide will be authored and published with the site. Data export functions may also be incorporated so custom modeling tools can use the assembled data. Eventually, data visualization and ML functionality will be incorporated into the online tool to make it easier to work with and understand data relevant to specific application needs.

By sharing these tools and data, this project aims to support external researchers in developing models, adding their data, and advancing knowledge in the field. A unified, freely accessible platform ensures data consistency, fosters collaboration, and maximizes the impact of these efforts on plant design and operation.

6.2 Theme 5 Task 2: Completing Data Gaps

6.2.1 Team Members

Jon Lapeyre (PNNL), Suraj Rahmon (PNNL), Miroslava Peterson (PNNL), Joelle Reiser (PNNL)

6.2.2 Background

Based on the evaluation of the current information in the GDB, significant data gaps exist for information that is crucial to successful modeling of grout using the *Hanford Grout Modeling Framework*. These gaps are due to the continued improvement in understanding of processes key to grout aging that have not been a focus in previous Hanford-related testing and are a result of sporadic grout development at Hanford over the last three decades. This task will be initiated in Year 2 and will seek to fill some of the most pressing data gaps to support development of the *Hanford Grout Modeling Framework*. However, a focused program guided to fill these data gaps will be required to achieve complete fidelity of the *Hanford Grout Modeling Framework*.

6.2.3 Target Experiments and Task Integration

- ***Slag dissolution testing:*** This experiment will support Theme 1 Task 2 to study the dissolution of slag in different simulated cement pore waters to represent different ages of grouts to allow expansion of the geochemical modeling approach to longer timeframes. This testing will also assess

slag dissolution in simulated waste environments to replicate the early-age hydration processes. It will be supported by ongoing characterization of slag containing samples at VU.

- ***Carbonated grout for peridynamics:*** One of the most prominent aging processes related to the physical characteristics of grout is carbonation. This task will fabricate grout samples for carbonation tests of long timeframes to assess physical changes for data to be fed into the PD modeling in Theme 4 Task 1.
- ***Aged grout leaching:*** Geochemical speciation models have been developed for the CS formulation on samples that have been oxidized and carbonated to assess their impact on leaching. This experiment will provide data on aged alternative grout formulations to support expansion of the geochemical speciation modeling in Theme 3 Task 1.
- ***Chemo-mechanical links through local hardness:*** This task will take hardness measurements (e.g., nano-indentation) across a grout sample to assess any changes locally to specific microstructure components. This information can be used in the design of mesoscale models in Theme 4 Task 2 to predict cracking and link to the PD models in Theme 4 Task 1.

7.0 Summary

Year 1 development of the *Hanford Grout Modeling Framework* has laid the groundwork for formation of the full system tool and provided substantial advancement of new tools in the modeling of grout. Based on conceptual models of the three main applications of grout at Hanford, liquid waste immobilization, solid waste stabilization/encapsulation, and tank closure are the main processes and mechanisms that control grout properties during aging. Five original themes were defined to support the development of the *Hanford Grout Modeling Framework*, and the associated subtasks were initiated during Year 1. The significant developments in each subtask presented in this report are as follows.

- ***Theme 1 Task 1 – Hanford Mineral Network:*** A main component of the *Hanford Grout Modeling Framework* was developed in which the mineral composition of grouts is now defined using a geochemical speciation model. A software link between eSTOMP and LXO was developed to facilitate this information transfer.
- ***Theme 1 Task 2 – Geochemical Modeling of Reactive Grout Phases:*** Predictive dissolution models developed originally for glass waste forms have been successfully applied to predict the early-life dissolution of BFS, showing promise for a long-term predictive tool of dissolution of key phases in the grout microstructure.
- ***Theme 2 Task 1 – Integration of Variably Saturated Flow Modeling to eSTOMP:*** This task was able to demonstrate that previous predictions of moisture pathways and transport times in the disposal facility using Variably Saturated Flow modeling can be replicated in eSTOMP. These calculations will provide the bases for reaction times in modeling in the Hanford Grout Modeling Framework.
- ***Theme 2 Task 2 – Integration of Variably Saturated Flow Modeling to Field Experimental Data:*** This task was a first step of validating the Hanford Grout Modeling Framework against field data by comparing moisture content models against measurements in the Hanford field lysimeter test.
- ***Theme 3 Task 1 – Application of Geochemical Speciation Modeling to Other Hanford Grout Examples:*** This task further evaluated geochemical speciation models for predicting the behavior of grout components and contaminants. Prior demonstration of this tool was on a single grout formulation, and this has now shown success on other Hanford grouts. This tool will provide a key component to predict the chemical state of the grout.
- ***Theme 3 Task 2 – Application of Geochemical Speciation Modeling to Other Hanford Grout Examples:*** This task demonstrated for the first time a reactive transport representation of oxidation of grout in a Hanford disposal environment, laying the groundwork for spatial and dynamic aging processes to be captured in the Hanford Grout Modeling Framework.
- ***Theme 3 Task 3 – Contaminant Interactions with Microbial Processes:*** This task developed an approach within eSTOMP to represent microbial conversions in grout leachates in disposal using nitrate as an example.
- ***Theme 4 Task 1 – Peridynamic Modeling:*** This task successfully built, for the first time, a PD model of a Hanford-relevant grout (using tank concrete as an example) and compared failure predications against experimental data.
- ***Theme 4 Task 2 – Maturation of Mesoscale Models for Hanford Grout:*** This task built a Hanford-relevant mesoscale model for the first time of a silver zeolite solid waste in a grout waste form to model silver migration in the grout matrix that will be expanded to contaminant migration and physical evolution.

- ***Theme 5 Task 1 – Grout Database:*** An online hosting tool has been developed for a database of Hanford-relevant grout data and population with data has been ongoing.

8.0 References

Abramson, JE, NM Avalos, AL Bourchy, SA Saslow, and GT Seidler. 2022. "An exploration of benchtop X-ray emission spectroscopy for precise characterization of the sulfur redox state in cementitious materials." *X-Ray Spectrometry* 51(2):151-162.

Arnold, J, R Duddu, K Brown, and DS Kosson. 2017. "Influence of multi-species solute transport on modeling of hydrated Portland cement leaching in strong nitrate solutions." *Cement and Concrete Research* 100:227-244.

Asmussen, R, CE Bagwell, DR Dixon, L Hare, S Johansen, C Johnson, PD Meyer, CI Pearce, AE Plymale, S Saslow, JE Szecsody, and GL Smith. 2024. *Nitrate and Nitrite at Hanford - From Tanks to Natural Attenuation*. PNNL-35629, Rev. 0. Pacific Northwest National Laboratory, Richland, WA.

Asmussen, R, S Saslow, GL Smith, AL Bourchy, JJ Neeway, AL Fujii Yamagata, R Nichols, CA Langton, R Mabrouki, JK Bernards, RS Skeen, and DJ Swanberg. 2021. *Evaluation of Degradation Mechanisms for Solid Secondary Waste Grout Waste Forms*. PNNL-32458. Pacific Northwest National Laboratory.,Richland, WA.

Asmussen, RM. 2024. *Summary of Developing a Hanford Grout Modeling Framework Initial Workshop*. PNNL-36945. Pacific Northwest National Laboratory, Richland, WA.

Asmussen, RM, JJ Neeway, AR Lawter, W Lukens, and NP Qafoku. 2015. "Technetium and iodine getters to improve Cast Stone performance-15420." Waste Management Symposia, Phoenix Arizona

Asmussen, RM, S Saslow, JJ Neeway, JH Westsik Jr, K Rod, C Lonergan, and B Johnson. 2020. *Development and Characterization of Cementitious Waste Forms for Immobilization of Granular Activated Carbon, Silver Mordenite, and HEPA Filter Media Solid Secondary Waste*. PNNL-28545, Rev. 1. Pacific Northwest National Laboratory, Richland, WA.

Bates, WF. 2022. *Follow-on Report of Analysis of Approaches to Supplemental Treatment of Low-actiivty Waste a the Hanford Nuclear Reservation Vol I and II*. SRNL-STI-2023-00007. Savannah River National Laboratory, Aiken, SC.

Bobaru, F and G Zhang. 2015. "Why do cracks branch? A peridynamic investigation of dynamic brittle fracture." *International Journal of Fracture* 196:59-98.

Bourchy, A, SA Saslow, BD Williams, NM Avalos, W Um, NL Canfield, L Sweet, GL Smith, and RM Asmussen. 2022. "The evolution of hydrated lime-based cementitious waste forms during leach testing leading to enhanced technetium retention." *Journal of Hazardous Materials* 430:128507.

Cantrell, KJ, JH Westsik, RJ Serne, W Um, and AD Cozzi. 2016. *Secondary Waste Cementitious Waste Form Data Package for the Integrated Disposal Facility Performance Assessment*. PNNL-25194. Pacific Northwest National Laboratory, Richland, WA.

Chaouche, M, XX Gao, M Cyr, M Cotte, and L Frouin. 2017. "On the origin of the blue/green color of blast-furnace slag-based materials: Sulfur K-edge XANES investigation." *Journal of the American Ceramic Society* 100(4):1707-1716.

Chen, L-Q. 2002. "Phase-field models for microstructure evolution." *Annual Review of Materials Research* 32(1):113-140.

Chen, LQ and J Shen. 1998. “Applications of semi-implicit Fourier-spectral method to phase field equations.” *Computer Physics Communications* 108(2-3):147-158.

Chen, Z and F Bobaru. 2015. “Peridynamic modeling of pitting corrosion damage.” *Journal of the Mechanics and Physics of Solids* 78:352-381.

Chen, Z, P Zhang, KG Brown, JL Branch, HA van der Sloot, JC Meeussen, RC Delapp, W Um, and DS Kosson. 2021. “Development of a Geochemical Speciation Model for Use in Evaluating Leaching from a Cementitious Radioactive Waste Form.” *Environmental Science & Technology* 55(13):8642–8653.

Chen, Z, P Zhang, KG Brown, HA van der Sloot, JC Meeussen, AC Garrabrants, X Wang, RC Delapp, and DS Kosson. 2023. “Impact of Oxidation and Carbonation on the Release Rates of Iodine, Selenium, Technetium, and Nitrogen from a Cementitious Waste Form.” *Journal of Hazardous Materials* 449:131004.

Daniel, J, C Stark, and P Kaar. 1982. *Long-Term Effects of Waste Solutions on Concrete and Reinforcing Steel*. RHO-RE-CR-8 P. Portland Cement Association, Skokie, IL.

Eary, L and EA Jenne. 1992. *Version 4. 00 of the MINTEQ geochemical code*. Pacific Northwest National Laboratory, Richland, WA.

EPA. 2017a. “Liquid-solid partitioning as a function of extract pH using a parallel batch extraction procedure.” Method 1313. U.S. Environmental Protection Agency, Washington, D.C.

EPA. 2017b. “Mass transfer rates of constituents in monolithic or compacted granulated materials using a semi-dynamic tank leaching procedure.” Method 1315. U.S. Environmental Protection Agency, Washington, D.C.

Fujii Yamagata, A, SA Saslow, JJ Neeway, T Varga, LR Reno, Z Zhu, KA Rod, BR Johnson, JA Silverstein, and JH Westsik. 2022. “The behavior of iodine in stabilized granular activated carbon and silver mordenite in cementitious waste forms.” *Journal of Environmental Radioactivity* 244:106824.

Gerstle, W, N Sau, and S Silling. 2005. “Peridynamic modeling of plain and reinforced concrete structures.” In 18th International Conference on Structural Mechanics in Reactor Technology (SMiRT 18). 7-12 August 2005, Beijing, China.

Giever, P. 2018. *Single-Shell Tank Structural Integrity Assessment Report*. RPP-IQRPE-50028. Washington River Protection Solutions, Richland, WA.

Gong, W and IL Pegg. 2022. *Development of Improved Grout Waste Forms for Supplemental Low Activity Waste Treatment.* VSL-21R-5000-1. The Catholic University of America, Washington, D.C.

Gruber, C, M Steen, KG Brown, R Delapp, EN Matteo, O Klein-BenDavid, G Bar-Nes, JC Meeussen, JC Ayers, and DS Kosson. 2022. “Cement-carbonate rock interaction under saturated conditions: From laboratory to modeling.” *Cement and Concrete Research* 160:106899.

Haase, CS, KL Von Damm, and SH Stow. 1987. “Closure of the Oak Ridge National Laboratory Hydrofracture Facility: An opportunity to study the fate of radioactive wastes disposed of by subsurface injection.” In International Symposium on Class V Injection Well Technology. 22 September 1987, Washington, D.C.

Harbour, J, T Edwards, E Hansen, and V Williams. 2005. *Variability Study for Saltstone*. WSRC-TR-2005-00447. Westinghouse Savannah River Company, Aiken, SC.

Inagaki, Y, T Imamura, K Idemitsu, T Arima, O Kato, T Nishimura, and H Asano. 2008. "Aqueous dissolution of silver iodide and associated iodine release under reducing conditions with FeCl2 solution." Journal of Nuclear Science and Technology 45(9):859-866.

Jones, R, J Rimsza, J Trageser, and J Hogancamp. 2021. "Simulation of hardened cement degradation and estimation of uncertainty in predicted failure times with peridynamics." *Construction and Building Materials* 286:122927.

Kaplan, D, T Hang, and S Aleman. 2005. *Estimated Duration of the Reduction Capacity within a High-Level Waste Tank*. WSRC-RP-2005-01674, Rev. 0. Washington Savannah River Company, Aiken, SC.

Khoury, GA. 2000. "Effect of fire on concrete and concrete structures." *Progress in Structural Engineering and Materials* 2(4):429-447.

Kim, SG. 2007. "A phase-field model with antitrapping current for multicomponent alloys with arbitrary thermodynamic properties." *Acta Materialia* 55(13):4391-4399.

Lai, X, L Liu, S Li, M Zeleke, Q Liu, and Z Wang. 2018. "A non-ordinary state-based peridynamics modeling of fractures in quasi-brittle materials." *International Journal of Impact Engineering* 111:130-146.

Langton, C and P Almond. 2013. *Cast Stone Oxidation Front Evaluation: Preliminary Results For Samples Exposed To Moist Air*. SRNL-STI-2013-00541. Savannah River Site, Aiken, SC.

Le Cornec, D, Q Wang, L Galoisy, G Renaudin, L Izoret, and G Calas. 2017. "Greening effect in slag cement materials." *Cement and Concrete Composites* 84:93-98.

Li, Y, S Hu, FW Hilty, R Montgomery, KC Park, CR Martin, NB Shustova, Y Liu, and SR Phillpot. 2022a. "Leaching model of radionuclides in metal-organic framework particles." *Computational Materials Science* 201:110886.

Li, Y, S Hu, R Montgomery, A Grandjean, T Besmann, and H-C zur Loye. 2022b. "Effect of charge and anisotropic diffusivity on ion exchange kinetics in nuclear waste form materials." *Journal of Nuclear Materials* 572:154077.

Li, Y, S Hu, X Sun, and M Stan. 2017. "A review: applications of the phase field method in predicting microstructure and property evolution of irradiated nuclear materials." *npj Computational Materials* 3(1):16.

Littlewood, DJ, ML Parks, JT Foster, JA Mitchell, and P Diehl. 2024. "The peridigm meshfree peridynamics code." *Journal of Peridynamics and Nonlocal Modeling* 6(1):118-148.

Lorier, TH and CA Langton. 2019. *Review of Cementitious Materials Development and Applications That Have Supported DOE-EM Missions: Waste Treatment, Conditioning, Containment Structures, Tank Closures, Facility Decommissioning, Environmental Restoration, and Structural Assessments*. Savannah River National Laboratory, Aiken, SC.

Lothenbach, B, DA Kulik, T Matschei, M Balonis, L Baquerizo, B Dilnesa, GD Miron, and RJ Myers. 2019. "CEMDATA18: A chemical thermodynamic database for hydrated Portland cements and alkali-activated materials." *Cement and Concrete Research* 115:472-506.

Mackin, JE and RC Aller. 1983. "The infinite dilution diffusion coefficient for A1 (OH) 4− at 25 C." *Geochimica et Cosmochimica Acta* 47(5):959-961.

Meeussen, J and K Brown. 2018. *ORCHESTRA Manual and Documentation*. Netherlands, NRG (Ed.) Petten.

Meeussen, JC. 2003. "ORCHESTRA: An object-oriented framework for implementing chemical equilibrium models." *Environmental Science & Technology* 37(6):1175-1182.

Mehta, S, W Kozak, N Hasan, R Khaleel, D Morgans, WJ McMahon, B Sun, MP Bergeron, JG Field, MJ Singleton, and MP Connelly. 2016. *Performance Assessment of Waste Management Area C, Hanford Site, Washington*. RPP-ENV-58782. Washington River Protection Solutions, Richland, WA.

Meyer, PD, RM Asmussen, GL Smith, JJ Neeway, J Thomle, H Emerson, JT Reiser, Y Fang, O Garayburu, S Warnick, Z Vincent, and S Phillips. 2024. *Field-scale Lysimeter Studies of Low-Activity Waste Forms Degradation – Implementation and Status*. PNNL-36443, Rev. 2.0. Pacific Northwest National Laboratory, Richland, WA.

Meyer, PD, P Saripalli, and VL Freedman. 2004. *Near-Field Hydrology Data Package for the Integrated Disposal Facility 2005 Performance Assessment*. PNNL-14700. Pacific Northwest National Laboratory, Richland, WA.

Moelans, N. 2011. "A quantitative and thermodynamically consistent phase-field interpolation function for multi-phase systems." *Acta Materialia* 59(3):1077-1086.

Moelans, N, B Blanpain, and P Wollants. 2008. "Quantitative analysis of grain boundary properties in a generalized phase field model for grain growth in anisotropic systems." *Physical Review B—Condensed Matter and Materials Physics* 78(2):024113.

Newcomer, ME, SS Hubbard, JH Fleckenstein, U Maier, C Schmidt, M Thullner, C Ulrich, N Flipo, and Y Rubin. 2018. "Influence of hydrological perturbations and riverbed sediment characteristics on hyporheic zone respiration of CO2 and N2." *Journal of Geophysical Research: Biogeosciences* 123(3):902-922.

Niazi, S, Z Chen, and F Bobaru. 2021. "Crack nucleation in brittle and quasi-brittle materials: A peridynamic analysis." *Theoretical and Applied Fracture Mechanics* 112:102855.

Nichols, R and D Kaplan. 2021. *Ultra-High-Performance Grout for Encapsulation of HEPA Filters*. SRNL-STI-2020-00563. Savannah River National Laboratory, Aiken, SC.

NNLEMS. 2022. *R&D Roadmap for Hanford Tank Waste Mission Acceleration*. U.S. Department of Energy Office of Environmental Management, Washington, DC.

Nohut, S. 2014. "Influence of sample size on strength distribution of advanced ceramics." *Ceramics International* 40(3):4285-4295.

Pabalan, RT, FP Glasser, DA Pickett, GR Walter, S Biswas, MR Juckett, LM Sabido, and JL Myers. 2009. *Review of Literature and Assessment of Factors Relevant to Performance of Grouted Systems for Radioactive Waste Disposal*. CNWRA-2009-001. Center for Nuclear Waste Regulatory Analyses, San Antonio, TX.

Parkhurst, DL and C Appelo. 2013. "Description of input and examples for PHREEQC version 3—a computer program for speciation, batch-reaction, one-dimensional transport, and inverse geochemical calculations." US Geological Survey Techniques and Methods 6(A43):497.

Parks, ML, DJ Littlewood, JA Mitchell, and SA Silling. 2012. "Peridigm users' guide. V1. 0.0." SAND2012-7800. Sandia National Laboratories, Albuquerque, NM, and Livermore, CA.

Proust, V, A Leybros, A Gossard, T David, Z Mao, Y Li, S Hu, A Grandjean, and H-C Zur Loye. 2024. "Influence of porous aluminosilicate grain size materials in experimental and modelling Cs+ adsorption kinetics and wastewater column process." *Journal of Water Process Engineering* 66:106066.

Quinn, JB and GD Quinn. 2010. "A practical and systematic review of Weibull statistics for reporting strengths of dental materials." *Dental Materials* 26(2):135-147.

Richards, LA. 1931. "Capillary conduction of liquids through porous mediums." *Physics* 1(5):318-333.

Samson, E, J Marchand, and J Beaudoin. 1999. "Describing ion diffusion mechanisms in cement-based materials using the homogenization technique." *Cement and Concrete Research* 29(8):1341-1345.

Sanford, WE, TS Steenhuis, J-Y Parlange, JM Surface, and JH Peverly. 1995. "Hydraulic conductivity of gravel and sand as substrates in rock-reed filters." *Ecological Engineering* 4(4):321-336.

Saslow, S, K Rue, S Rahmon, R Anguish, J Lapeyre, NM Escobedo, RM Asmussen, and GL Smith. 2024. *Measuring the Spatial Rate of Grout Waste Form Oxidation*. PNNL-36409, Rev. 0. Pacific Northwest National Laboratory, Richland, WA.

Seleson, P, ML Parks, M Gunzburger, and RB Lehoucq. 2009. "Peridynamics as an upscaling of molecular dynamics." *Multiscale Modeling & Simulation* 8(1):204-227.

Silling, SA. 2000. "Reformulation of elasticity theory for discontinuities and long-range forces." *Journal of the Mechanics and Physics of Solids* 48(1):175-209.

Silling, SA, F Abdeljawad, and KR Ford. 2017. Peridynamic Theory as a New Paradigm for Multiscale Modeling of Sintering. SAND-2017-10313R; 657247. Sandia National Laboratory, Albuquerque, NM.

Silling, SA, DP Adams, and BA Branch. 2023. "Mesoscale model for spall in additively manufactured 304L stainless steel." *International Journal for Multiscale Computational Engineering* 21(3).

Šimůnek, J. 2005. "Models of Water Flow and Solute Transport in the Unsaturated Zone." *Encyclopedia of Hydrological Sciences*. Wiley.

Skeen, RS, KG Brown, N Adams, DS Kosson, DJ Swanberg, GL Smith, and RM Asmussen. 2025. "Alternative Methods to Analyze EPA Method 1315 Leach Data; Implications to Performance Assessment Modeling - 25076." In *Proceedings of Waste Management Symposium 2025*, Phoenix, AZ.

Torrence, C, J Trageser, R Jones, and J Rimsza. 2022. “Sensitivity of the strength and toughness of concrete to the properties of the interfacial transition zone.” *Construction and Building Materials* 336:126875.

Trageser, JE, CA Mitchell, RE Jones, EN Matteo, JM Rimsza, and LJ Pyrak-Nolte. 2022. “The effect of differential mineral shrinkage on crack formation and network geometry.” *Scientific Reports* 12(1):22264.

Trivelpiece, CL and MC Hsieh. 2021. *Blast Furnace Slag Reactions in Various Solutions (Interim Report).* SRNL-STI-2021-00097. Savannah River Site, Aiken, SC.

Um, W, BD Williams, MM Valenta Snyder, and G Wang. 2016. *Liquid Secondary Waste Grout Formulation and Waste Form Qualification*. PNNL-25129, Rev. 1. Pacific Northwest National Laboratory, Richland, WA.

USDOE. 2016. *Two-Dimensional, Two-Phase Flow Model Calculations for the Integrated Disposal Facility Performance Assessment*. RPP-CALC-61029. US Department of Energy, Office of River Protection, Richland, WA.

USDOE. 2018. *Performance Assessment for the Integrated Disposal Facility, Hanford Site*. RPP-RPT-59958, Rev. 1. Washington River Protection Solutions, Richland, WA.

van Beek, JE and DD Wodrich. 1990. *Grout Disposal System for Hanford Site Mixed Waste*. WHC-SA-00694. Westinghouse Hanford Company, Richland, WA.

Van der Sloot, H, P Seignette, J Meeussen, O Hjelmar, and D Kosson. 2008. “A database, speciation modelling and decision support tool for soil, sludge, sediments, wastes and construction products: LeachXS™-Orchestra.” Second International Symposium on Energy from Biomass and Waste, Venice.

van Genuchten, MT. 1980. “A closed‐form equation for predicting the hydraulic conductivity of unsaturated soils.” Soil Science Society of America Journal 44(5):892-898.

Vanysek, P. 2018. “Ionic Conductivity and Diffusion at Infinite Dilution.” *CRC Handbook of Chemistry and Physics*. CRC Press/Taylor & Francis, Boca Raton, FL.

Vu, C-C, N-K Ho, and T-A Pham. 2022. “Weibull statistical analysis and experimental investigation of size effects on the compressive strength of concrete-building materials.” *Case Studies in Construction Materials* 17:e01231.

Westsik, JH, GF Piepel, MJ Lindberg, PG Heasler, TM Mercier, RL Russell, A Cozzi, WE Daniel, RE Eibling, EK Hansen, MM Reigel and DJ Swanberg. 2013b. "Supplemental Immobilization of Hanford Low-Activity Waste: Cast Stone Screening Tests". PNNL-22747; SRNL-STI-2013-00465. Pacific Northwest National Laboratory, Richland, WA (United States).

Yuan-Hui, Li, and Sandra Gregory. "Diffusion of ions in sea water and in deep-sea sediments." Geochimica et cosmochimica acta 38, no. 5 (1974): 703-714.

Yeh, TCJ and DJ Harvey. 1990. “Effective unsaturated hydraulic conductivity of layered sands.” *Water Resources Research* 26(6):1271-1279.

You, H, Y Yu, S Silling, and M D’Elia. 2022. “A data-driven peridynamic continuum model for upscaling molecular dynamics.” *Computer Methods in Applied Mechanics and Engineering* 389:114400.

Zaccariotto, M, F Luongo, and U Galvanetto. 2015. “Examples of applications of the peridynamic theory to the solution of static equilibrium problems.” *The Aeronautical Journal* 119(1216):677-700.

Zhang, P, JB Lewis, O Klein-BenDavid, AC Garrabrants, R Delapp, HA van der Sloot, and DS Kosson. 2022a. “The role of environmental conditions on the carbonation of an alkali-activated cementitious waste form.” *Cement and Concrete Research* 151:106645.

Zhang, Y, E Schlangen, and O Çopuroğlu. 2022b. “Effect of slags of different origins and the role of sulfur in slag on the hydration characteristics of cement-slag systems.” *Construction and Building Materials* 316:125266.

zur Loye, H-C, T Besmann, J Amoroso, K Brinkman, As Grandjean, CH Henager, S Hu, ST Misture, SR Phillpot, and NB Shustova. 2018. “Hierarchical materials as tailored nuclear waste forms: a perspective.” *Chemistry of Materials* 30(14):4475-4488.

Appendix A – Python Script to Extract Table Data from XML Files

The purpose of this script is to extract all table data from a publication's XML file to a new Excel file, with each sheet being a different table in the paper.

```
import pandas as pd
import requests
from bs4 import BeautifulSoup
import os
from datetime import datetime
import numpy as np
import re

papers_path = 'C:\\[User defined path]\\Unique File Name.xlsx'
download_path = 'C:\\ [User defined path]'

folder_name = f'{datetime.now().strftime('%Y-%m-%d')}_ [User Name]_XML'


PDF_folder = os.path.join(download_path, folder_name, 'PDF')
XML_folder = os.path.join(download_path, folder_name, 'XML')
data_folder = os.path.join(download_path, folder_name, 'DATA')

os.makedirs(PDF_folder,  exist_ok =True)
os.makedirs(XML_folder,  exist_ok =True)
os.makedirs(data_folder,  exist_ok =True)

api_key = '[User specific API Key]'
headers_xml = {
'x-els-apikey': api_key,
'User-Agent': 'Mozilla/5.0'
}

headers_pdf = {
'x-els-apikey': api_key,
'accept': 'application/pdf'
}

def get_table_body(body, num_cols):
all_rows = []
more_rows = [0] * num_cols
for row in body:
entries = row.find_all_next('entry')
row = []
i = 0
while i < len(more_rows):
        if more_rows[i]!= 0:
        row.append('')
```

```
            more_rows[i] -= 1
            else:
            entry = entries.pop(0)
            text = (''.join(entry.text.strip('\n')))
            # if text == '–':   looses semantic meaning without the - i think :/
            #     text = np.nan
            row.append(text)
            if entry.attrs != None:
                        if 'namest' in entry.attrs:
                        start = int(entry['namest'].strip('col')) - 1
                        end = int(entry['nameend'].strip('col')) - 1
                        num_fill = end - start
                        for j in range(num_fill):
                        row.append('')
                        if 'morerows' in entry.attrs:
                        more_rows[i] = int(entry['morerows'])
                        i+=1
            if 'morerows' in entry.attrs:
                        more_rows[i] = int(entry['morerows'])
            i+=1
all_rows.append(row)

return all_rows

def get_column_titles(head, num_cols):
all_rows = []
more_rows = [0] * num_cols
for row in head:
entries = row.find_all_next('entry')
row = []
i = 0
while i < len(more_rows):
            if more_rows[i] != 0:
            row.append("")
            more_rows[i] -= 1
            else:
            if len(entries) != 0:
                        entry = entries.pop(0)
                        col_text = ' '.join(entry.text.split('\n')).strip()
                        row.append(col_text)
                        if 'namest' in entry.attrs:
                        start = int(entry['namest'].strip('col')) - 1
                        end = int(entry['nameend'].strip('col')) - 1
                        num_fill = end - start
                        for j in range(num_fill):
                        row.append(f'{col_text}')
                        if 'morerows' in entry.attrs:
                        more_rows[i] = int(entry['morerows'])
                        i+=1
                        if 'morerows' in entry.attrs:
                        more_rows[i] = int(entry['morerows'])
```

```
            i+=1
all_rows.append(row)

col_titles = []
for col in range(len(all_rows[0])):
combined_column = ''
for row in all_rows:
            if row[col] != '':
            combined_column = combined_column + ' ' + str(row[col])
col_titles.append(combined_column)

if len(col_titles) != len(set(col_titles)):
counts = {}
result = []

for item in col_titles:
            if item in counts:
            counts[item] += 1
            result.append(f"{item}{counts[item]}")
            else:
            counts[item] = 0
            result.append(item)
col_titles = result
return col_titles

def get_tables(tables):
all_tables = {}
errors = []
for i in range(len(tables)):
table = tables[i]
try:
            title = table.find("ce:label").text
except:
            title = "Unnamed table {}".format(i)
print(title)
try:
            num_cols = table.find_all('tgroup')
except:
            errors.append(title)
try:
            col_titles = []
            heads = table.find_all("thead")
            for i in range(len(heads)):
            head = heads[i].find_all("row")
            col_titles.append(get_column_titles(head,int(num_cols[i].get('cols'))))
except Exception as e:
            col_titles = [i for i in range(num_cols)]
try:
            table_data = []
            bodies = table.find_all("tbody")
            all_tables[title] = []
```

```
            for i in range(len(bodies)):
            body = bodies[i].find_all("row")
            table_data.append(get_table_body(body, int(num_cols[i].get('cols'))))
            for i in range(len(col_titles)):
            table_df = pd.DataFrame(table_data[i], columns=col_titles[i])
            all_tables[title].append([table_df])

            captions = table.find_all("ce:caption")
            captions.extend(table.find_all("ce:legend"))
            captions.extend(table.find_all("ce:table-footnote"))
            if len(captions) != 0:
            captions = [' '.join(caption.text.split('\n')) for caption in captions]
            captions_df = pd.DataFrame(captions, columns=["captions"])
            all_tables[title].append(captions_df)
except Exception as e:
            errors.append(title)
if len(errors) != 0:
all_tables['ERROR'] = [pd.DataFrame(errors, columns=['ERROR'])]
return all_tables

def num_check(val):
try:
#remove comma from number
val_num = ''.join(str(val).split(','))

#replace − with -
val_num = val_num.replace('−', '-')

# if scientific notation (ie 1X10-1)
if re.search('[  ]?[Xx×][  ]?10', val_num):
            val_num = re.sub("[  ]?[Xx×][  ]?10", "e", val_num)

return float(val_num)
except:
return val

def format_df(df):
new_columns = {}
percent_columns = []
for col in df.columns:
#convert to float if digit
df[col] = df[col].apply(lambda val: num_check(val))

#plus or minus symbol
if df[col].astype(str).str.contains('±').any():
            #split columns
            expansion = df[col].astype(str).str.split('±', expand=True)
            #strip whitespace and convert to numbers, replace NA with 0
            expansion = expansion.map(lambda x: str(x).strip())
            expansion = expansion.map(lambda val: '-' if val == 'None' else val)
            expansion = expansion.map(lambda val: num_check(val))
```

```
            #name columns
            if '±' in str(col):
            expansion.columns = [col.strip() for col in col.split('±')]
            else:
            columns = [col]
            for i in range(len(expansion.columns)-1):
                        columns.append(f'(error{i}){col}')
            expansion.columns = columns
            new_columns[col] = expansion

            df = df.drop(columns=col)
#replace column with new columns
for col, exp_cols in new_columns.items():
col_idx = len(df.columns)  # By default, add at the end if column not found
if col in df.columns:
            col_idx = df.columns.get_loc(col)
df = pd.concat([df.iloc[:, :col_idx], exp_cols, df.iloc[:, col_idx:]], axis=1)
return df

def download_papers(papers_df):
summary = "Title,num_tables,has_supps,errors\n"
for index, paper in papers_df.iterrows():
doi = paper["DOI"].strip('https://doi.org/')
paper_title = re.sub(r"(<.[^>]*>)|([\\\/:|?*$#\".,;\'\(\)]|(\s(CH2MHILL)))", "",
paper['Title'])[0:245].strip()
authors = paper["Authors"]
date = paper['Publication Date'].split('T')[0]

metadata = {
            "DOI": doi,
            "Title": paper_title,
            "Authors": authors,
            "Publication Date": date
}
api_url = f'https://api.elsevier.com/content/article/doi/{doi}'
xml_response = requests.get(api_url, headers=headers_xml)
pdf_response = requests.get(api_url, headers=headers_pdf)
if xml_response.status_code != 200:
            print("ahh! {}: {}".format(xml_response.status_code, xml_response.content))
            break
soup = BeautifulSoup(xml_response.content, 'lxml')

article_info = soup.find('xocs:articleinfo')
has_sup_data = False

if 'appendices' in str(article_info):
            has_sup_data = True

tables = soup.find_all('ce:table')

summary += f'{paper_title},{len(tables)},{str(has_sup_data)},'
```

```
print(f'**********{paper_title}**********')

if len(tables) != 0:
        all_tables = get_tables(tables)

        if('ERROR' in all_tables.keys()):
        summary += 'True'
        else:
        summary += 'False'

        metadata_df = pd.DataFrame(metadata, index=[0])
        with pd.ExcelWriter(os.path.join(data_folder, f'{paper_title}.xlsx')) as writer:
        for table in all_tables:
                data = all_tables[table]

                startrow = 0
                for i in range(len(data) - 1):
                data[i] = format_df(data[i][0])
                data[i].to_excel(writer, sheet_name=table, startrow=startrow, startcol=0,
                index=False)
                startrow += data[i].shape[0]+1
                data[-1].to_excel(writer, sheet_name=table, startrow=0,
                startcol=len(data[0].columns)+2, index=False)

        metadata_df.to_excel(writer, sheet_name="metadata", index=False)
else:
        print("No tables found in paper {}".format(index))
with open(os.path.join(XML_folder, f'{paper_title}.xml'), 'wb') as file:
        file.write(xml_response.content)
with open(os.path.join(PDF_folder, f'{paper_title}.pdf'), 'wb') as file:
        file.write(pdf_response.content)
summary += '\n'

with open(os.path.join(download_path, folder_name,
'summary_{}.csv'.format(datetime.now().strftime("%Y-%m-%d_%H-%M"))), 'w') as file:
file.write(summary)


if __name__ == '__main__':

papers_df = pd.read_excel(papers_path, "Records")
papers_df = papers_df[papers_df['XML?'] == 'Y']
download_papers(papers_df)
```

Appendix B – Python Script for Extracting Data Tables from PDF Files Using LLM API Key

The Python script below was used to extract data tables from publication PDF files as output text (.txt) or Excel files. Each table is exported as its own .txt file or in its own sheet within the Excel file created. This script was written by coauthor Dewei Wang for specific use with the Pacific Northwest National Laboratory AI Incubator, which is an internal capability built on the same technology used by OpenAI.

```
# -*- coding: utf-8 -*-
"""
Created on Wed Feb  4 12:45:10 2025

@author: wang109
"""

#%% Import necessary libraries
import numpy as np
import pandas as pd
import os
import PyPDF2
import openai
import re
from src.common_utils import load_environment_variables
load_environment_variables()
API_KEY = os.getenv("OPENAI_API_KEY")
client = openai.OpenAI(
    api_key=API_KEY,
    base_url=os.environ["OPENAI_BASE_URL"]
)

#%%
def aiprocessor(page_no, text):
    print(f"\n\n..AI processing page {page_no}")

    messages = [
        {
            "role": "system",
            "content": """You are a PDF table extractor, a backend processor.
- User input is messy raw text extracted from a PDF page by PyPDF2.
- Do not output any body text, we are only interested in tables.
- The goal is to identify tabular data, and reproduce it cleanly as pipe-separated (|) table.
- Reply with the table data only, no title or summary.
- Reproduce each separate table found in page, separate tables by an empty line."""
        },
        {
            "role": "user",
            "content": "raw pdf text; extract and format tables: " + text
        }
    ]
```

```
    my_ai_model = os.environ["OPENAI_MODEL"]
    api_params = {"model": my_ai_model, "messages": messages, "stream": True}

    try:
        api_response = client.chat.completions.create(**api_params)
        reply = ""
        for delta in api_response:
            # if 'choices' in delta and delta['choices'][0].get('finish_reason') is None:
            if delta.choices and delta.choices[0].finish_reason is None:
                word = delta.choices[0].delta.content or ''
                reply += word
                print(word, end="")
        return reply

    except Exception as err:
        error_message = f"API Error on page {page_no}: {str(err)}"
        print(error_message)
        return error_message

def parse_pipe_table(raw_text):
    lines = raw_text.splitlines()

    clean_rows = []

    for line in lines:
        line = line.strip()

        # 1) Skip empty lines
        if not line:
            continue

        # 2) Skip lines with triple backticks
        if '```' in line:
            continue

        # 3) Skip lines that are just dashes (the header separators)
        if re.match(r'^\|\-+\|$', re.sub(r'\s+', '', line)):
            continue

        # 4) Split on the pipe
        row_parts = line.split('|')

        # 5) Trim leading/trailing empties if the row starts or ends with '|'
        #    e.g. ['', ' Leachant ...', ' Al', ... , '']
        if row_parts and not row_parts[0].strip():
            row_parts = row_parts[1:]
        if row_parts and not row_parts[-1].strip():
            row_parts = row_parts[:-1]

        # 6) Strip each cell; convert repeated dashes or a single dash into None
```

```
            cleaned_cells = []
            for cell in row_parts:
                cell = cell.strip()
                # Convert dash-like cells ("-", "–", "--", "—", "-----", etc.) to None
                if re.match(r'^[-–—]+$', cell):
                    cell = None
                cleaned_cells.append(cell)

            # skip a row that is entirely None
            if all(x is None or x == '' for x in cleaned_cells):
                continue

            clean_rows.append(cleaned_cells)

        if len(clean_rows) < 2:
            # Not enough data to form a header + rows
            return None

        # # First row as header
        # header = clean_rows[0]
        # data = clean_rows[1:]

        # # Create DataFrame
        # df = pd.DataFrame(data, columns=header)

        # Create DataFrame
        df = pd.DataFrame(clean_rows)

        # Drop columns that are entirely None / empty
        df = df.dropna(axis='columns', how='all')

        # Drop rows that are entirely None / empty
        df = df.dropna(axis='rows', how='all')

        return df

    def save_tables_to_excel_ai(tables, output_xlsx):

        with pd.ExcelWriter(output_xlsx) as writer:
            table_count = 0

            for i, table_text in enumerate(tables):

                individual_tables = [t.strip() for t in table_text.strip().split("\n\n") if t.strip()]

                for table in individual_tables:

                    try:
                        df = parse_pipe_table(table)
                        if df is None:
                            print("No valid data was found in the table.")
```

```
                else:
                    print("DataFrame:")
                    print(df)

                # Save each table to a separate sheet
                sheet_name = f"Table_{table_count+1}"
                df.to_excel(writer, sheet_name=sheet_name, index=False, header=False)
            except Exception as e:
                # If DataFrame conversion fails, write as plain text
                sheet_name = f"Table_{table_count+1}_plain_text"
                pd.DataFrame({"Table Text": [table]}).to_excel(writer, sheet_name=sheet_name,
index=False)
                print(f"Warning: Could not convert table to DataFrame. Saved as plain text in {sheet_name}.
Error: {e}")

            table_count += 1

    print(f"Tables saved to {output_xlsx}")

def extract_tables_openai(pdf_path, output_folder="output_ai"):

    tables = []
    if not os.path.exists(output_folder):
        os.makedirs(output_folder)

    # Open the PDF file in binary mode
    with open(pdf_path, 'rb') as pdf_file:
        pdf_reader = PyPDF2.PdfReader(pdf_file)

        # Iterate through each page and extract text
        for page_num in range(len(pdf_reader.pages)):
            page = pdf_reader.pages[page_num]
            page_text = page.extract_text()

            if len(page_text)>20:
                # # Dump unprocessed pages if desired
                # page_text_file = f"{output_folder}/" + pdf_file.name + "-extractedpage" + str(page_num) +
".txt"
                # with open(page_text_file, 'w', encoding='utf-8') as output_file:
                #     output_file.write(page_text)

                # Process with AI
                ai_processed_text = aiprocessor(page_num, page_text)

                # Dump AI pages if desired
                # page_text_file = f"{output_folder}/" + pdf_file.name + "-AIpage" + str(page_num) + ".txt"
                page_text_file = os.path.join(output_folder, f"{os.path.basename(pdf_file.name)}-
AIpage{page_num}.txt")

                with open(page_text_file, 'w', encoding='utf-8') as output_file:
                    output_file.write(ai_processed_text)
```

```
            # Append the AI-processed text to the list
            tables.append(ai_processed_text)

    return tables

#%%
if __name__ == '__main__':

    #%% load PDF for the scrape
    work_path = './pdf/'
    result_path = './excel/'

    #%% for multiple files
    pdf_files = [file for file in os.listdir(work_path) if file.endswith('.pdf')]
    for file_name in pdf_files:

        #%% extract tables containing identifiers
        print('extract tables from ', file_name, ' ...')
        extracted_tables = extract_tables_openai(os.path.join(work_path, file_name))

        #%% save tables to excel
        if not os.path.exists(result_path):
            os.makedirs(result_path)
        print('saving tables from ', file_name, ' ...')
        file_name_output = result_path+file_name[: -4]+'.xlsx'
        save_tables_to_excel_ai(extracted_tables, file_name_output)
```

Appendix C – Oxidation Model Inputs

Table C.1. Waste Burial Box input file.

Card	Parameter	Value
Simulation Title Card	Title	Water mode (STOMP-W)
	Parameters	Solidification, Oxidizing conditions (ACM1), Long term Infiltration 3.5mm/yr
	Researcher	Xuehang Song, Jacob Anderson
	Institution	PNNL
	Date	11/07/2019, 01/2025
Solution Control Card	Method	normal w/petsc
	Convergence Criteria	1.0E-12, 1.0E-25
	Water mode	Water w/ECKEChem w/courant
	Time step	10, s, 1 yr
	Maximum Time Step	1e+30, yr
Rock/Soil Zonation Card	Zonation file	grout.zon
	Zonation Levels	HD_BACKF, LD_BACKF, W1
Mechanical Properties Card	Material	HD_BACKF, LD_BACKF, W1
	Density	2.710 g/cm^3 (for HD_BACKF and LD_BACKF), 2.820 g/cm^3 (W1)
	Porosity	0.35 (HD_BACKF), 0.37 (LD_BACKF), 0.557 (W1)
Hydraulic Properties Card	Hydraulic Conductivity	4.91e-03 hc cm/s (HD_BACKF), 1.86e-02 hc cm/s (LD_BACKF), 1.54E-09 hc cm/s (W1)
Saturation Function Card	Function Model	van Genuchten
	Parameters	6.50e-02 (HD_BACKF), 5.70e-02 (LD_BACKF), 6.03E-06 (W1)
Aqueous Relative Permeability Card	Model	Mualem
Solute/Porous Media Interactions Card	Interaction	0.0 cm (for HD_BACKF, LD_BACKF, W1)
Aqueous Species Card	Species	O2(aq), 0.315 cm^2/yr (Conventional)
Solid Species Card	Species	slag, solution, O2_product, solution_product
	Density	1.7 g/cm^3
Conservation Equations Card	Equations	Total_slag, Total_o2(aq), Total_solution
Kinetic Equations Card	Kinetic Reactions	KnRc-1, KnRc-2
Kinetic Reactions Card	Reactions	Forward-Backward for slag to O2(aq) and solution to solution_product
Output Options Card	Output Variables	Aqueous Saturation, species aqueous conc, species volumetric conc, species integrated mass
	Time Intervals	0 s, 1 yr, 10 yr, 50 yr, etc.
Grid Card	Grid Dimensions	31, 25, 281
	Coordinates	0.0m, 0.01m, 0.025m, etc.
Initial Conditions Card	Parameters	Gas Pressure, Aqueous Pressure, Species Volumetric (slag, solution_product)
	Value	Various pressure and volumetric values for different time steps
Boundary Conditions Card	Boundary Type	Neumann, Dirichlet
	Species	O2(aq)
	Boundary Values	Various values for top, bottom, east, north

Table C.2. B-25 Waste Box input file.

Card	Parameter	Value
Simulation Title Card	Title	1
	Input	Xuehang Song, Jacob Anderson
	Organization	PNNL
	Date	11/07/2019, 01/2025
Solution Control Card	Solver	normal w/petsc
	Tolerance	1.0E-12
	Convergence	1.0E-25
	Water Model	Water w/ECKEChem w/courant
	Time Step	10 s
	Time Interval	10000 yr
	Maximum Iterations	1
	Solver Method	solute diffusion, harmonic
	Diffusion Constant	1e-20
Rock/Soil Zonation Card	File	formatted zonation file, grout.zon
	Zones	HD_BACKF, LD_BACKF, W1
Mechanical Properties Card	HD_BACKF Density	2.710 g/cm³
	HD_BACKF Porosity	0.35
	LD_BACKF Density	2.710 g/cm³
	LD_BACKF Porosity	0.37
	W1 Density	2.820 g/cm³
	W1 Porosity	0.557
Hydraulic Properties Card	HD_BACKF	4.91e-03 hc cm/s
	LD_BACKF	1.86e-02 hc cm/s
	W1	1.54E-09 hc cm/s
Saturation Function Card	HD_BACKF Model	van Genuchten
	HD_BACKF Parameter 1	6.50e-02 1/cm
	HD_BACKF Parameter 2	1.7
	HD_BACKF Parameter 3	0.086
	LD_BACKF Model	van Genuchten
	LD_BACKF Parameter 1	5.70e-02 1/cm
	LD_BACKF Parameter 2	2.8
	LD_BACKF Parameter 3	0.081
	W1 Model	van Genuchten
	W1 Parameter 1	6.03E-06 1/cm
	W1 Parameter 2	1.649
	W1 Parameter 3	0.108
Aqueous Relative Permeability Card	HD_BACKF Model	Mualem
	LD_BACKF Model	Mualem
	W1 Model	Mualem
Solute/Porous Media Interactions Card	HD_BACKF	0.0 cm
	LD_BACKF	0.0 cm
	W1	0.0 cm
Aqueous Species Card	O2(aq) Diffusion	0.315 cm²/yr

Card	Parameter	Value
	O2(aq) Behavior	Constant
	O2(aq) Rate	1.0
Solid Species Card	Slag	1.7 g/cm³, 27.027027 g/mol
	Solution	1.7 g/cm³, 27.027027 g/mol
	O2 Product	1.7 g/cm³, 27.027027 g/mol
	Solution Product	1.7 g/cm³, 27.027027 g/mol
Conservation Equations Card	Total Slag	3 slag, 1 solution_product, 1 O2_product
	Total O2(aq)	2 O2(aq), 1 O2_product
	Total Solution	2 solution, 1 solution_product
Kinetic Equations Card	Kinetic O2 Product	1 O2_product, 1 KnRc-1, 1.0000
	Kinetic Solution Product	1 solution_product, 1 KnRc-2, 1.0000
Kinetic Reactions Card	KnRc-1	Forward Backward, 2 slag, 1 O2(aq), 1 O2_product
	KnRc-1 Rate	1e-3 1/yr, 0 1/yr
	KnRc-2	Forward Backward, 2 slag, 1 solution, 1 solution_product
	KnRc-2 Rate	1e-3 1/yr, 0 1/yr
Output Options Card	1	1, 1, 1
	2	1, 1, yr, m, 6, 6, 6
	13	Aqueous Saturation
	14	species aqueous conc, O2(aq), mol/L
	15	species volumetric conc, O2(aq), mol/L
	16	species volumetric conc, solution, mol/L
	17	species volumetric conc, solution_product, mol/L
	18	species volumetric conc, O2_product, mol/L
	19	species volumetric conc, slag, mol/L
	20	Species Integrated Mass, O2_product, mol
	21	Species Integrated Mass, solution, mol
	22	Species Integrated Mass, solution_product, mol
	23	Species Integrated Mass, slag, mol
	24	Species Integrated Mass, O2(aq), mol
	25	diffusive porosity
Grid Card	Type	Cartesian
	Grid Size	28, 25, 281
	Grid Spacing	0.0 m to 12.75 m (spanning several specific distances)
Initial Conditions Card	Gas Pressure	1.0135e+5 Pa
	Aqueous Pressure	5e5 Pa
	Species Volumetric Slag	0.0010569 mol/liter
	Species Volumetric Solution Product	0 mol/liter
Boundary Conditions Card	Top Boundary	Neumann Aqueous, Aqueous Concentration
	O2(aq) Concentration	1.06e-3 mol/L
	East Boundary	Neumann Aqueous, Aqueous Concentration
	O2(aq) Concentration	1.06e-3 mol/L
	North Boundary	Neumann Aqueous, Aqueous Concentration
	O2(aq) Concentration	1.06e-3 mol/L

Appendix D – Additional Batch Grout Model Output

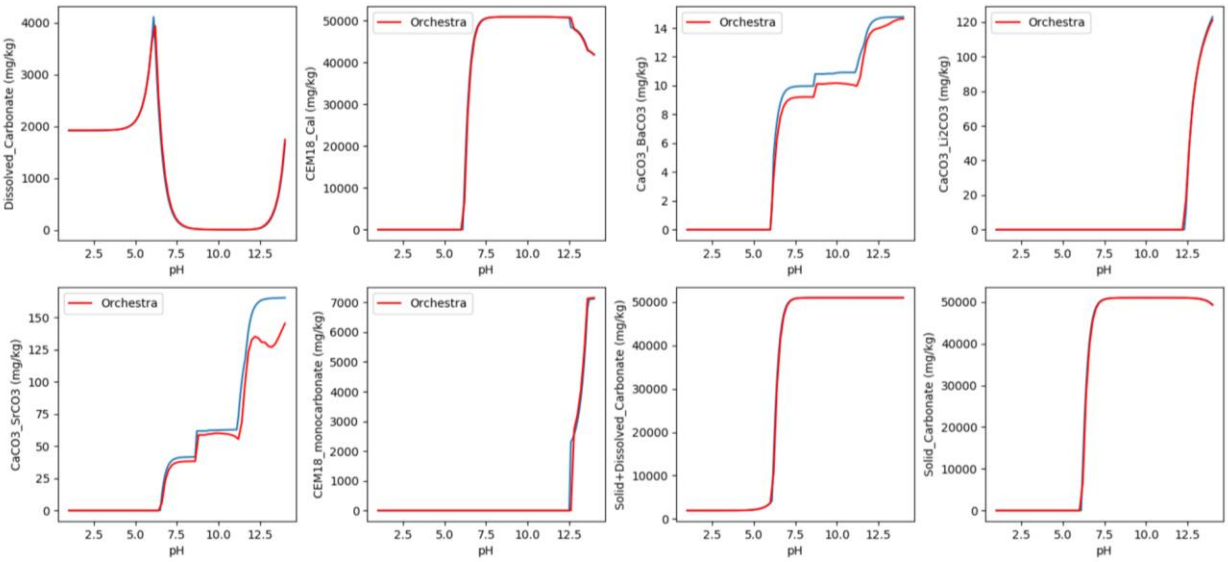

Figure D.1. Comparison between the expected dissolved components controlled by mineral assemblages in grout as predicted by BIOGEOCHEM (blue) and ORCEHSTRA (red) for carbonate species.

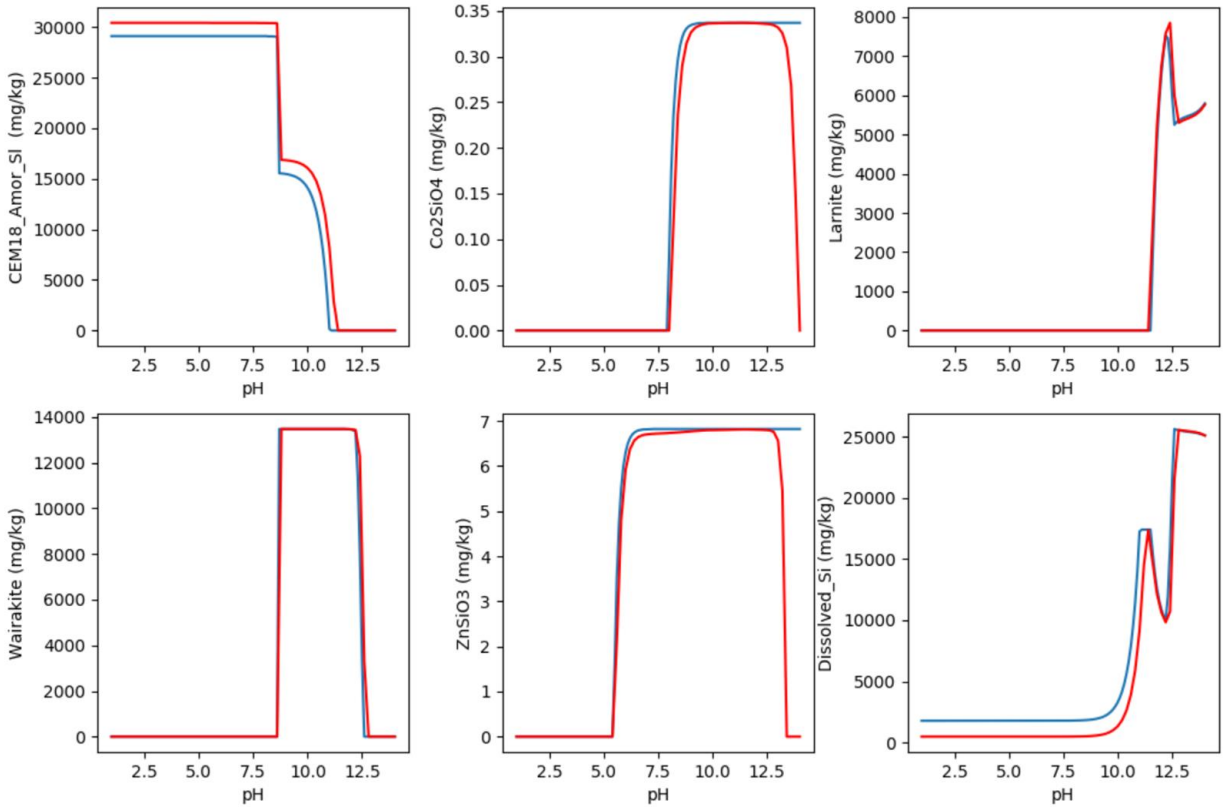

Figure D.2. Comparison between the expected dissolved components controlled by mineral assemblages in grout as predicted by BIOGEOCHEM (blue) and ORCEHSTRA (red) for silicate species.

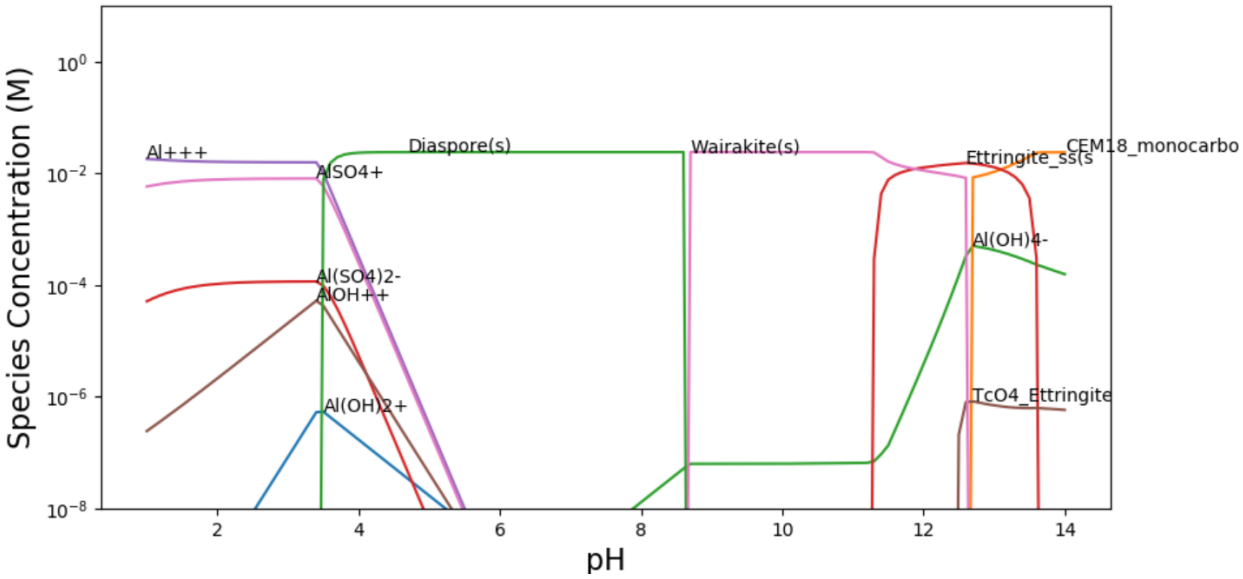

Figure D.3. Aluminum speciation with pH from the batch model BIOGEOCHEM.

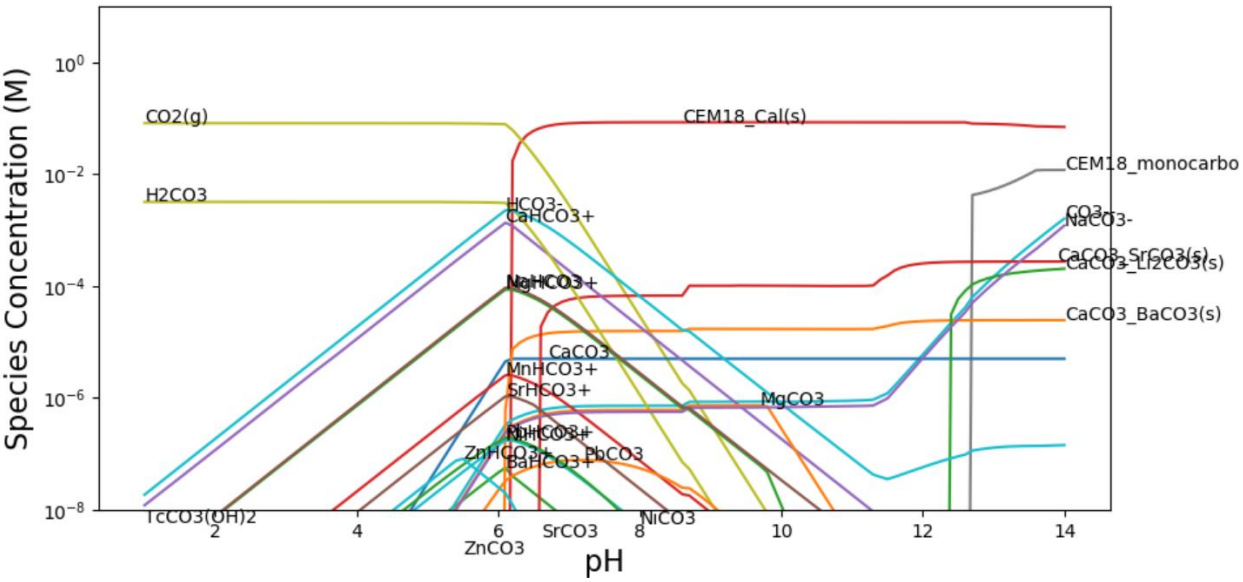

Figure D.4. Carbonate speciation with pH from the batch model BIOGEOCHEM.

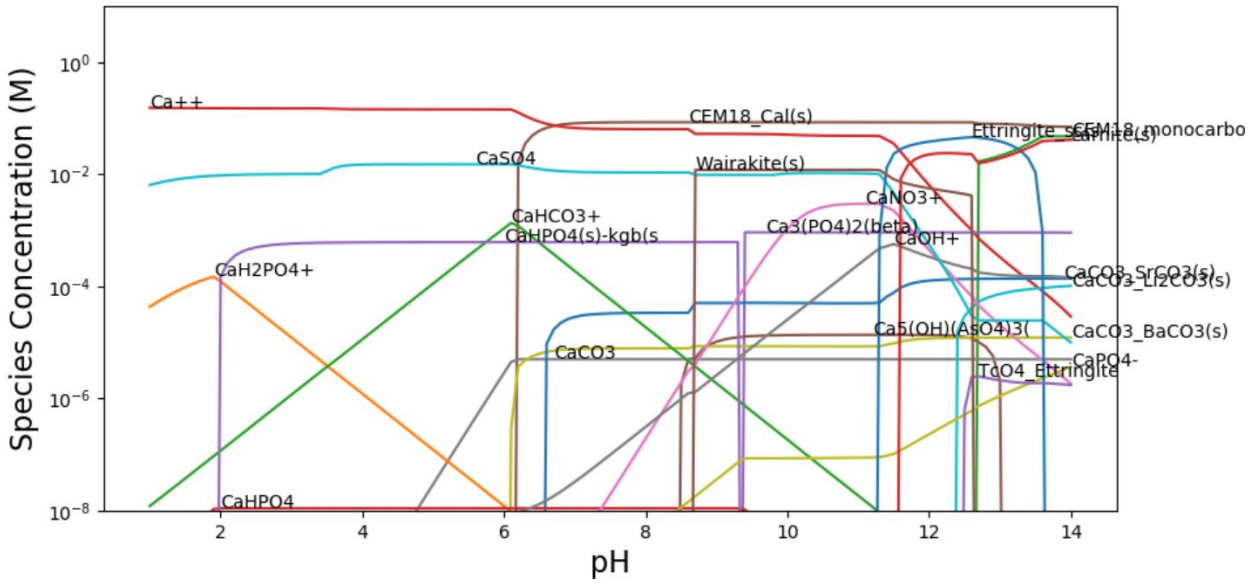

Figure D.5. Calcium speciation with pH from the batch model BIOGEOCHEM.

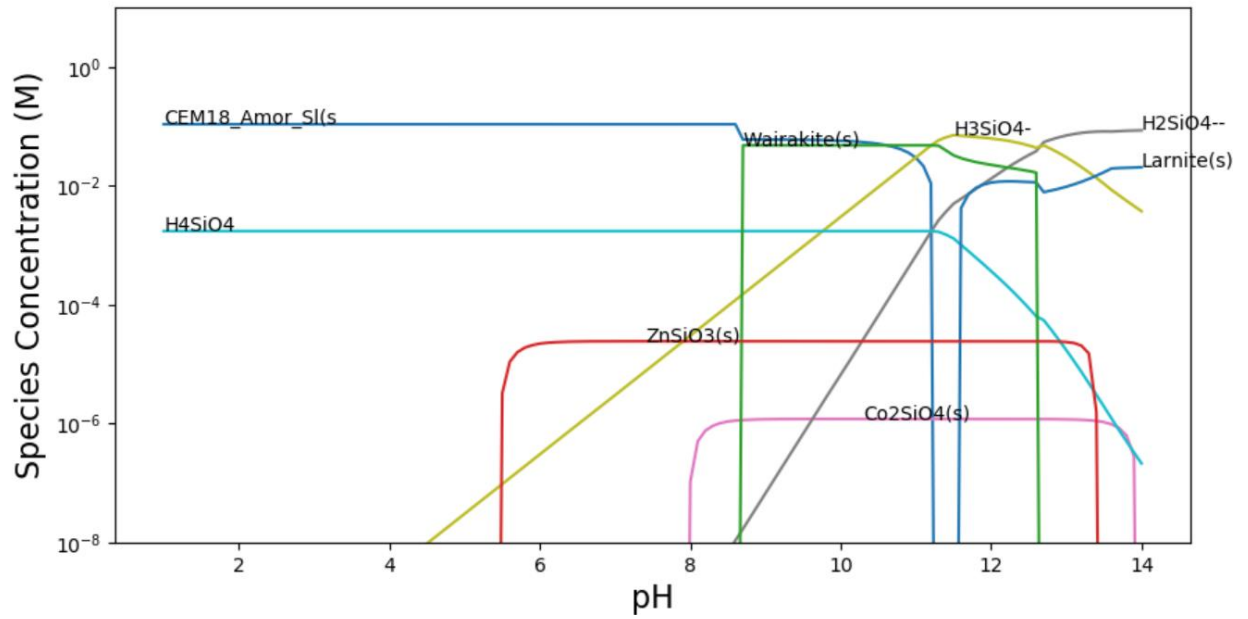

Figure D.6. Silicate speciation with pH from the batch model BIOGEOCHEM.

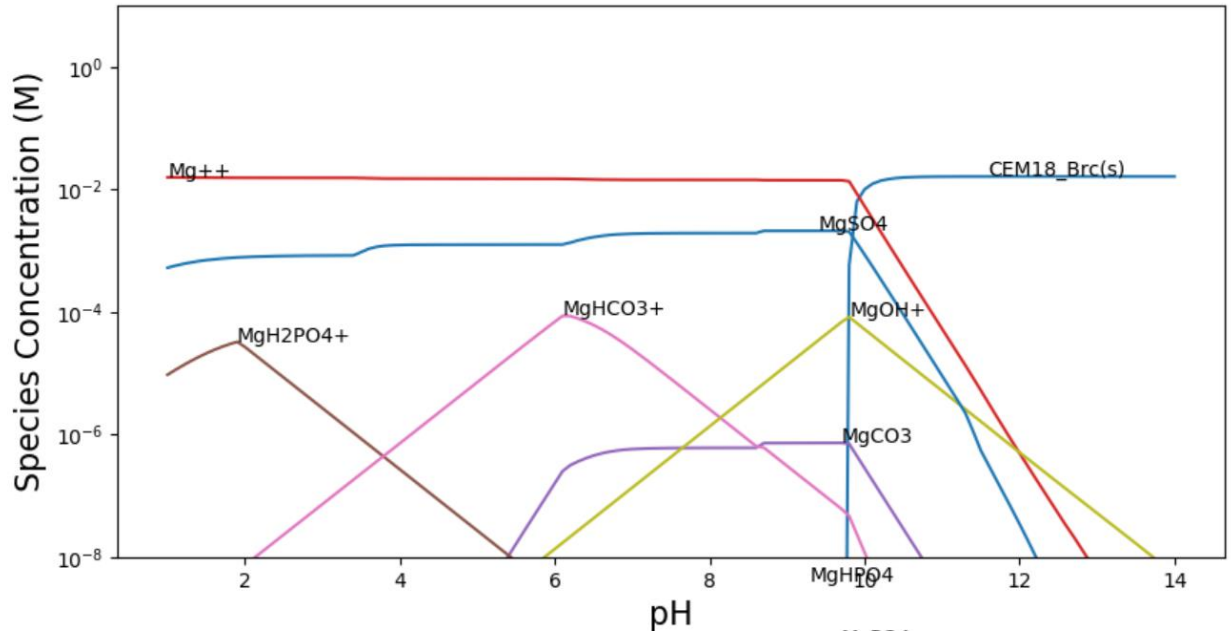

Figure D.7. Magnesium speciation with pH from the batch model BIOGEOCHEM.

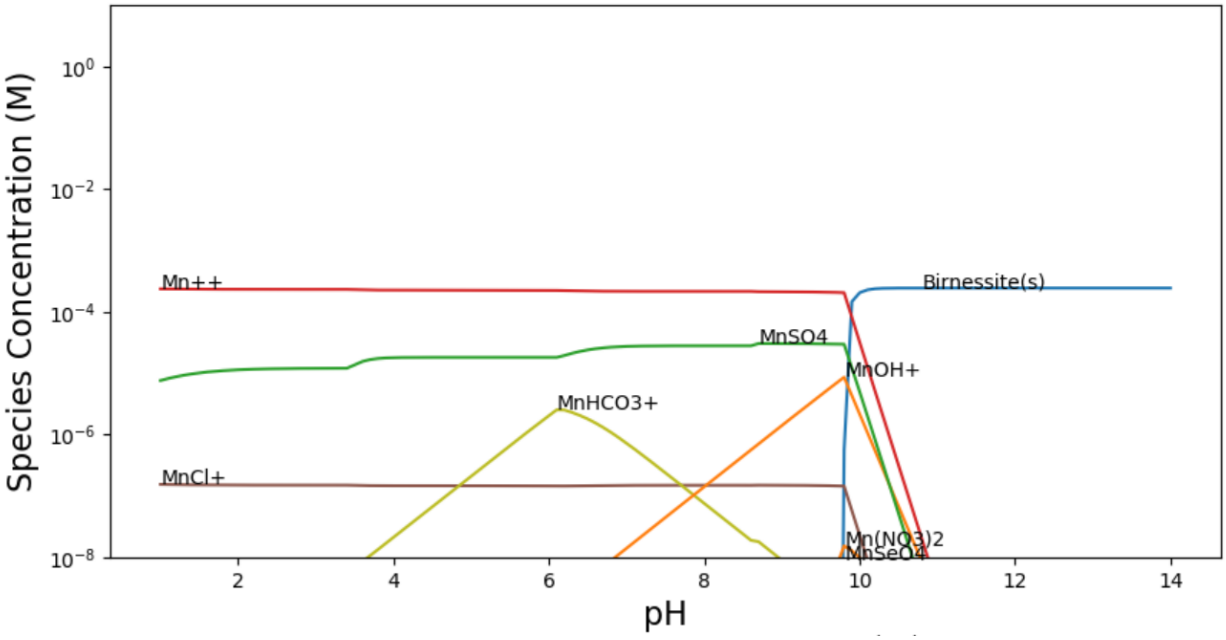

Figure D.8. Manganese speciation with pH from the batch model BIOGEOCHEM.

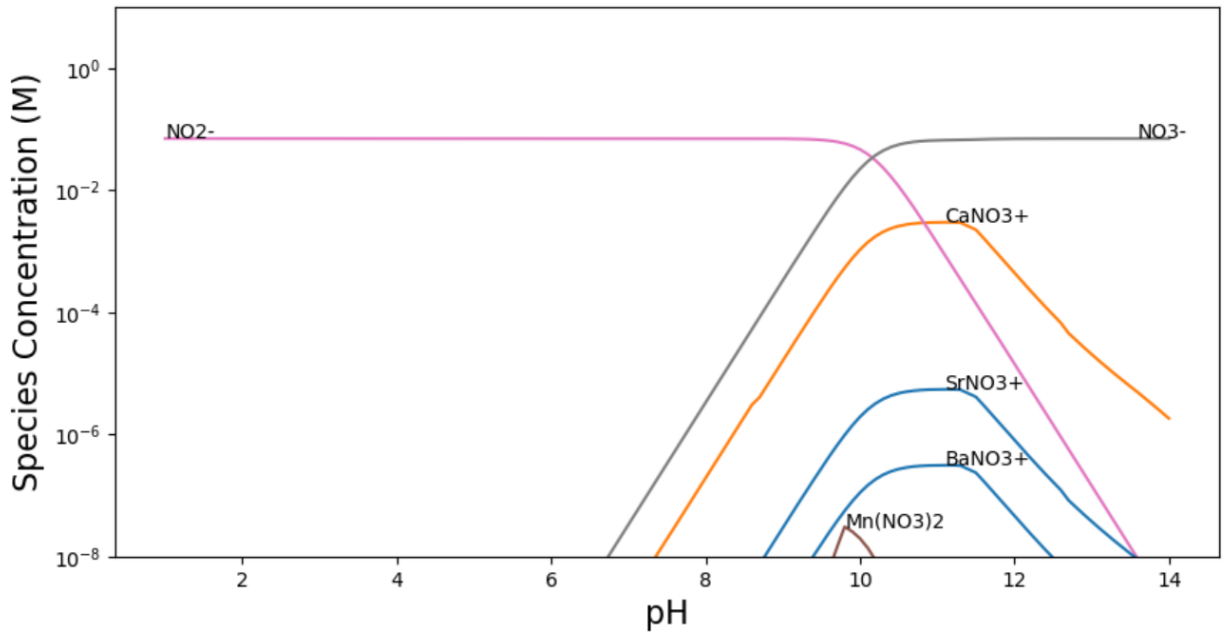

Figure D.9. Nitrogen speciation with pH from the batch model BIOGEOCHEM.

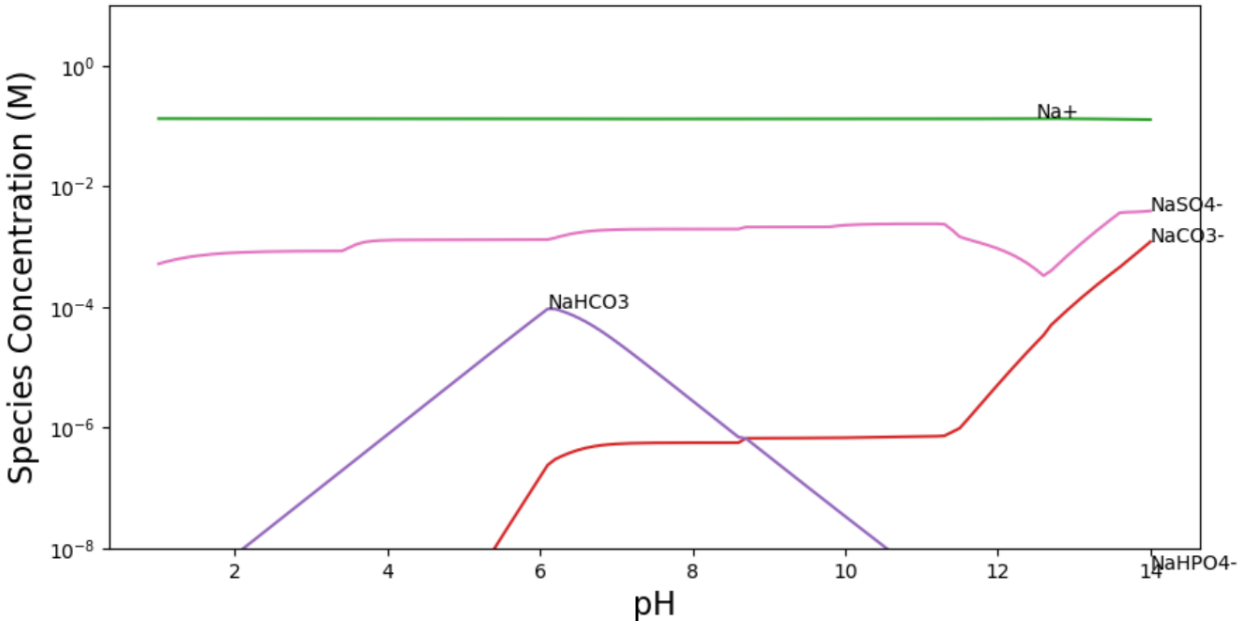

Figure D.10. Sodium speciation with pH from the batch model BIOGEOCHEM.

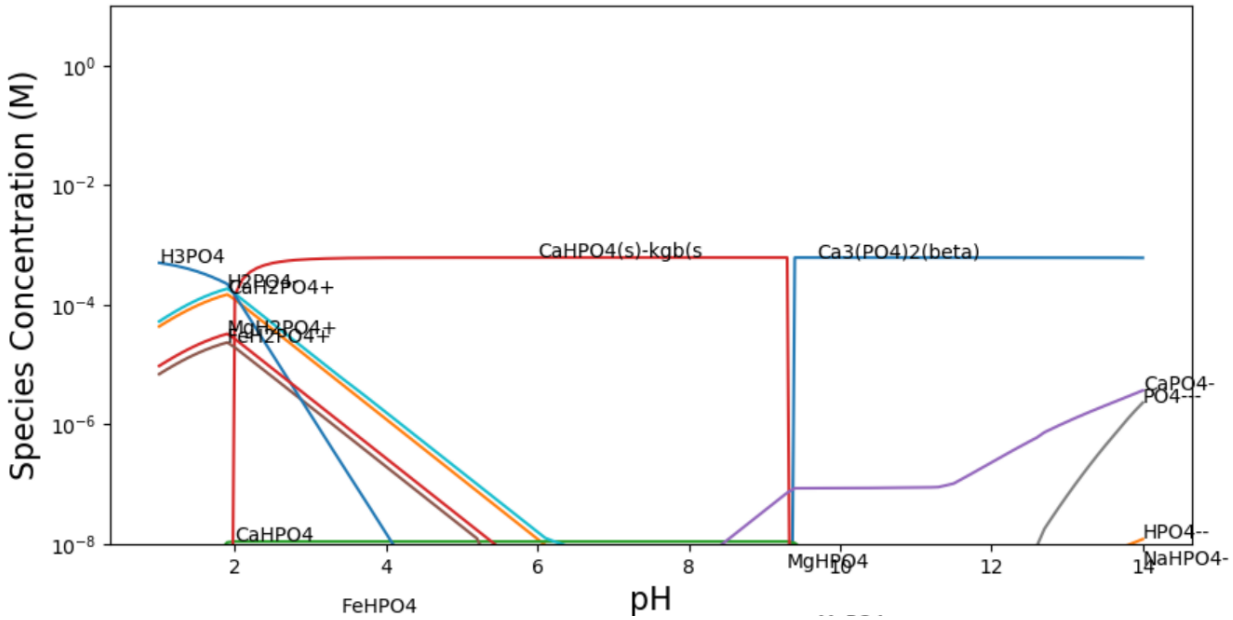

Figure D.11. Phosphorous speciation with pH from the batch model BIOGEOCHEM.

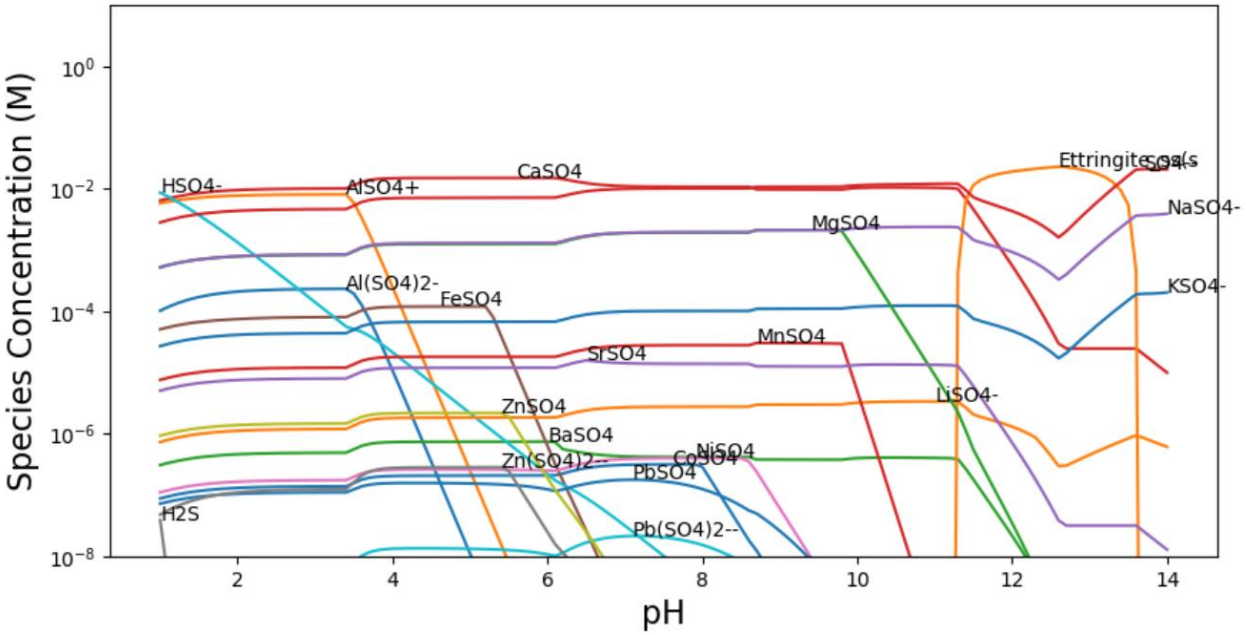

Figure D.12. Sulfate speciation with pH from the batch model BIOGEOCHEM.

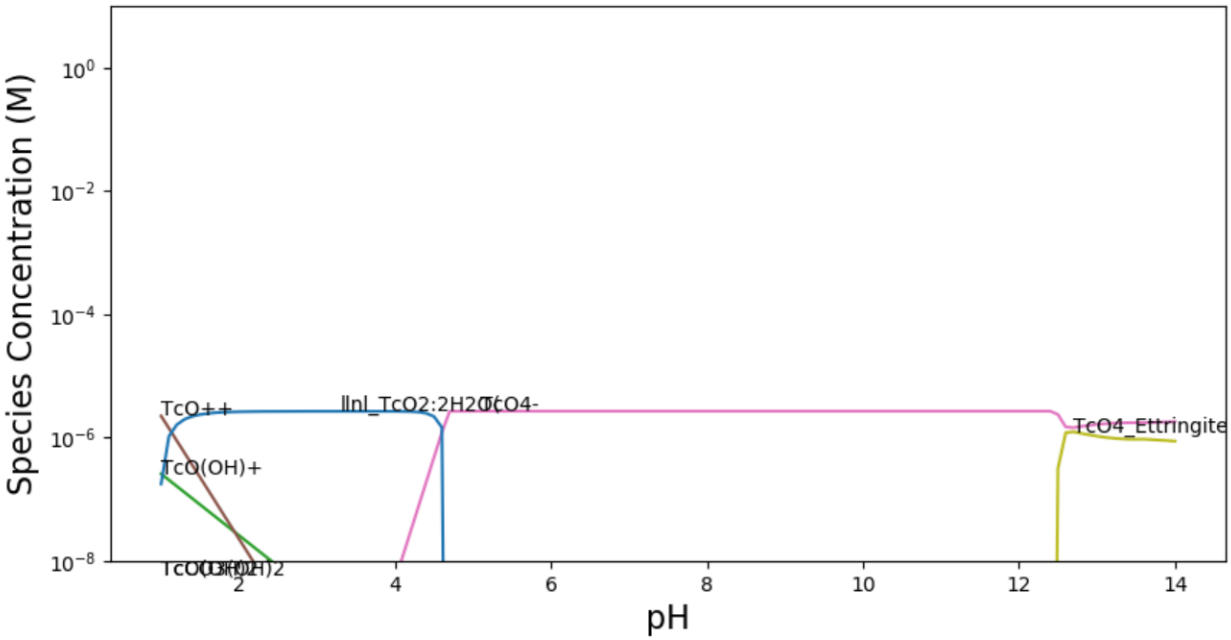

Figure D.13. Technetium speciation with pH from the batch model BIOGEOCHEM.

Pacific Northwest National Laboratory

902 Battelle Boulevard
P.O. Box 999
Richland, WA 99354

1-888-375-PNNL (7665)

www.pnnl.gov